Synthesis of silicon carbide ceramics by novel microwave methods

By

Lucia Carassiti

Submitted in fulfilment of the requirements for the Degree of Doctor of Philosophy

School of Chemistry

College of Science and Engineering

University of Glasgow

September 2011

Abstract

The work described in this thesis was carried out on the synthesis of silicon carbide using microwave processing and aimed to develop procedures to reduce processing complexity and cut processing times.

Si-C/SiO_2-C systems were first studied due to the ready availability at reasonable cost of the starting powders and the excellent microwave absorption properties of carbon. Silicon carbide was synthesised from silicon or silica combined with activated carbon or graphite via microwave heating over timescales from minutes to seconds without the need for inert atmospheres or subsequent purification.

In the reactions performed in a MMC, graphite was found fundamental not only as a microwave susceptor, but also as a reductant, preventing the oxidation of silicon carbide. Another important beneficial factor was water, used as a binder in the pellet making process, it minimised the intergrain void space between particles and possibly acted as a polar liquid microwave susceptor.

It was found the carbide morphology and phase purity can be controlled by the microwave cavity used, the power applied and hence by the heating rate. Short irradiation times (ca. 5 minutes) in a multimode cavity using silicon and activated carbon powders produced single phase β-SiC nanofibres as small as 5 nm in diameter while large crystallites of β-SiC can obtained in ~1 minute using high power, single mode cavity microwave techniques. Furthermore, similar microwave cavity systems shown that the removal of the susceptor, starting from silica and carbon mixtures, is possible and the successful conversion to silicon carbide can be performed using loose powders. This represented a major step with respect to designing a flow process and reducing carbon contamination.

Studies of microwave processing of silicon carbide were then extended to x-aerogels, to probe whether the produced silicon carbide would mimic the porous microstructures offered by the precursor. This indeed resulted in the production of porous silicon carbide (in 15 minutes) and also sintered crystallites of micrometre sizes (after 3.5 minutes) whether MMC or SMC systems were employed.

Contents

Acknowledgments

First of all, I would like to thank WestChem and GRPe for funding and my two supervisors, Professor Duncan H. Gregory and Dr. Phil Harrison for their assistance during my Ph.D. Particularly Duncan, for the past years of support, advice and helpful discussions, it was a pleasure to work with you. I would also like to thank various collaborators who let me try different set ups, Prof. Sam Kingman, Dr. Aled Jones; helped me to gain a better understanding of my samples: Dr. Phil Dobson, Dr. Ian McLaren, Andy Monaghan and gave me interesting samples to work with: Prof. Nick Leventis. Finally, thanks to everyone in Prof. Gregory's group, especially Bob for the support, Donnie for the good laughs and Saleem for being my sidekick.

It has been a long way since the first Google search to find a Ph.D. and I can't help but feeling blessed with all the people I met in Glasgow. A special thanks goes to my flatmates, Caroline and Lynne, for making me feel at home in the past 2 years and being very caring in the past months while I was writing up in the flat.

Finally a heartfelt thanks to my parents, here goes the Italian bit: Un ringraziamento sentito ai miei genitori. A mio padre che mi ha sempre chiesto di scrivere di cosa mi occupo, questa tesi e' per te, buona lettura! Ma soprattutto grazie mamma, per l'amore, la stima e l'incoraggimanto costante.

1 Introduction

1.1 Microwave vs. conventional processing

In the field of materials chemistry the development of new processes for the synthesis of solids is fundamental to establish fast and energy-efficient techniques, which lead to improved materials in shorter times or different products compared to the conventional processes if materials can be heated selectively. Heating is the most common process used in manufacturing industries. It finds applications in food, chemical, textile and engineering industries for drying and promoting a wide variety of chemical and/or physical changes.[1]

Even though it is widely used, conventional heating can be slow and inefficient. All the heat energy required to heat up the sample must pass through its surface and the surface is heated by a complex mixture of radiation, convection and conduction processes. Processing time is then limited by the rate of the heat flow from the surface into the bulk and this heat flow is determined by the physical properties of the sample. Specific heat, thermal conductivity and density are combined into one parameter, the thermal diffusivity, which determines the temperature rise within a material as a function of time and depth from the surface, subject to a given set of conditions at the surface. From equation **(1-1)** it can be seen that the thermal diffusivity α (m s^{-2}) is proportional to the thermal conductivity k (W m^{-1} K^{-1}) and inversely proportional to the volumetric heat capacity, expressed as the product of the specific heat C (J kg^{-1} K^{-1}) and the density of the material ρ (kg m^{-3}):[2]

$$\alpha = \frac{k}{C\rho} \qquad \textbf{(1-1)}$$

It is not only the nature of the sample, but also that of the furnace used that greatly affects the quality of the heating process. Large furnaces can be slow to respond to temperature changes, require long times to warm up and have high heat capacities. This can mean that sudden changes in production requirements cannot easily be met and the quality of the treated sample is often inferior to that which is desired.[1]

One alternative heating method which has raised a lot of interest and has been exploited in the past decades is microwave irradiation. As will be seen in the following sections, this technique has been used very effectively both to heat materials and to drive chemical processes.

1.2 History of microwave processing

The first microwave generator was developed in 1920 by Hull and sparked academic interest in the subject.[3] It was not however until the 2nd World War that the real advantages of microwaves in communications were realised with the development of radar.[4] The advances in techniques and components which took place during the war led to an increase in applications in the following decade. In the late 1940s various patents were issued for microwave industrial heating applications regarding the drying of materials (such as textiles, tires and wood) and for food processing.[5]

In 1946 the Federal Communications Commission in the U.S.A. allotted the 915 and 2450 MHz bands for microwave ovens following the preferences given by the two microwave oven manufacturing companies, Raytheon and GE. Raytheon preferred the higher frequency of 2.45 GHz, arguing small food loads would couple better and the higher number of modes in a cavity would enable the heating profile to be more uniform. GE however, favoured 915 MHz as the radiation would penetrate more and there would be less chance of thermal runaway while defrosting.[6] The first commercial microwave ovens, called Radarange, were introduced in the early 1950s by Raytheon targeting mainly restaurants for heating food. Later in the 1960s domestic microwave ovens were supplied by Tappan.[6]

The first major interest in microwaves from a scientific experimental point of view dates back to 1954 when Von Hippel started collecting dielectric data at the MIT Radiation Laboratory for various materials (including ceramics) at different values of frequency and temperature.[7] The first paper dealing with microwave heating in chemical research was published in the early 1970s,[8] but the microwave branch of synthetic organic chemistry flourished around the 1980s when laboratories could be equipped with inexpensive domestic microwave ovens and chemists started reporting successful reactions. [9]

In most of the early studies, reagents were dissolved in a solvent which couples effectively with microwaves and generates the heat energy required for the reaction to take place. Several reviews reported the continuous progress of microwave assisted organic reactions[10,11,12] which in turn led to solvent-free approaches for organic synthesis. Typically such approaches involve microwave irradiation of liquid reactants in the presence of a catalyst or catalysed by the surfaces of various supports.[13]

Today microwave reactors are still widely used in many synthetic organic laboratories and a recent review, for example, describes the use of microwave irradiation combined with

heterogeneous catalysis to promote transformations of carbohydrates without the aid of solvents.[14]

The first investigations concerning sintering and joining of ceramics under microwave irradiation can be tracked back to the 1960s and work in particular by Bennett,[15] however it was in the 1990s that the vast majority of experimental studies on the microwave synthesis and processing of materials were performed and this period was responsible for many of the reviews that summarised the techniques and benefits of the approach.[6,9,16,17] For example, an overview on the microwave processing of materials was given by Clark and Sutton in 1996. The fundamentals of the microwave/matter interactions and how they influence the characteristics of microwave processing (see next section) are described and some processes are considered from lab scale to potential commercialisation.[9] Some of the seminal reviews in microwave chemistry will be briefly discussed here (chronologically) to illustrate how microwave processing in solid-state chemistry has progressed and flourished expanding to different classes of materials and compounds.

Two fundamental advantages of using microwaves over conventional heating were highlighted in 1992 by Katz regarding the sintering of ceramic materials.[16] First, the high efficiency (as high as 80-90 %) of the microwave heating process could lead to reduced processing costs. In fact, in microwave heating, heat is generated within the sample itself by interaction of microwaves with material and it is volumetric, while as mentioned previously, in conventional heating the surface of the work piece must be heated first and then the heat reaches the bulk of the load by thermal conduction. Second, Katz stresses that the rapid heating rates characteristic of microwave heating significantly reduce processing time, enabling more samples to be processed in less time.

Slightly prior to Katz's paper, Mingos and Baghurst described microwave dielectric heating from a chemical point of view, explaining how the dielectric loss of solvents and solids could be exploited for chemical reactions, reporting examples in the synthesis of polymers and ceramic materials amongst others.[17] While considering the microwave processing of ceramics, aside from the advantage of being an inexpensive process, the authors emphasise the fact that since the heat is generated inside the component, the method could be used to densify materials and given the rapid heating involved, grain growth would be minimised preventing the segregation of impurities to grain boundaries and hence increasing the strength. Also, contamination from the vessel in which the reaction takes place is argued to be reduced since the heat is concentrated in the bulk of the

material. Various early examples of solid state synthesis are presented, all based on the principle that in a mixture of components, if one absorbs microwaves strongly, the heat produced can be used to drive the reaction. Among many important examples, the ferroelectric material potassium vanadate, KVO_3, was synthesised from the strong microwave absorbing vanadia (V_2O_5) and K_2CO_3.[18] Similarly, superconducting $YBa_2Cu_3O_{7-x}$ was synthesised starting from a stoichiometric mixture of CuO, $Ba(NO_3)_2$, and Y_2O_3, taking advantage of the good absorber properties of CuO.[19]

In 1995 Whittaker and Mingos highlighted the importance of the form in which samples are treated.[20] They showed that while bulk metals are excellent microwave reflectors and do not heat significantly, if these same reactants are irradiated in the form of loose powders, they heat and sinter satisfactorily without causing electric discharges. Chromium sulfides and selenides were synthesised starting from the elemental powders and taking advantage of the rapid heating provided by chromium metal powders. In the case of Cr, as the metal reacts, the heat starts to be provided by the semiconducting product that replaces the Cr as a microwave absorber. Microwave heating has been also proved advantageous in the formation of chalcogenides since the high heating rate reduces the evaporation of the chalcogen which reacts quickly with the metal powders.

In 1998, Agrawal published a notable review on the microwave processing of ceramics. The paper highlighted the advantages over conventional processes, but also drew attention to the challenges of treating low microwave absorbing oxides.[21] When sintering tungsten carbide using Co as a binder, the microwave sintering process took 1/6 of the time compared to conventional heating and nearly full density was achieved with minimum grain growth. Also the final product exhibited improved mechanical properties and a uniform microstructure with fine grains. Other ceramic materials successfully treated in the microwave and reported in the review were reduced oxide precursors, in which the low absorbing oxides (such as TiO_2 and Ta_2O_5) were partially reduced prior to microwave irradiation and made oxygen defective so that they could couple better with microwaves.
A decade of significant progresses in experimental knowledge was concluded by a comprehensive review on the synthesis of inorganic solids using microwaves by Rao *et al.*, who however stressed the gaps still present in the understanding of the reaction mechanisms involved in the microwave field.[22]

Since the primary material studied in this thesis is silicon carbide, it is worth mentioning why microwave processing has been proposed as a good alternative to conventional

heating in the case of ceramic materials. The most notable papers on the synthesis of carbides using microwave irradiation are discussed thereafter.

While the most common industrial microwave applications concern rather low-temperature processes, such as food processing, wood drying and rubber vulcanization; Bykov *et al.* published in 2001 a review to stress the benefits of exploiting microwave radiation to activate mass transport mechanisms during the high-temperature processing of inorganic solid materials.[23] Aside from the distinctive characteristics already highlighted previously, such as a decrease in energy expenditure and processing time compared to conventional heating, the authors described how the controllable heating achievable during microwave processing has been exploited for the sintering of ceramic materials. (A more recent review on the advantages of microwave sintering versus conventional sintering can be also found by Oghbaei.[24]) Tuning the heating rate enables the surface diffusion at the first stage of sintering to be retarded, high heating rates are applied subsequently to densify the material while maintaining its fine microstructure and reducing grain growth.

The inverse temperature profile characteristic of microwave heating has been exploited, for example, when reacting a porous solid matrix with a gas. Reaction-bonded silicon nitride starting from silicon powder compacts and nitrogen at temperatures ranging between 1150-1450 °C has been successfully synthesised using microwaves. The temperature distribution and gradient made silicon powders heat up and react faster in the interior. The reaction then propagates outward, where the porosity is still open for the nitrogen to diffuse and react.[25]

Finally, the selectivity of heating that arises from the varying dielectric properties of materials has been successfully exploited in other processes. Joining of ceramic materials can be achieved using a thin layer of a good absorber material between ceramic parts, usually transparent to microwave radiation.[23]

Silicon and boron carbide along with the carbides of the group IV–VI transition metals have extremely high melting points and are commonly referred to as refractory carbides. These materials have sparked interest due to their good physical stability, high thermal conductivity, high hardness and high strength.[26,27,28] For this reason, microwave heating has been applied to promote their synthesis through combustion taking advantage of the dielectric properties of the starting materials, especially the excellent capacity of carbon to absorb microwave energy and transform it into heat.[29] In the combustion method two or

more solids combine and the temperature of the reactants is increased to a value (combustion temperature) where the formation of the product is favourable. At the combustion temperature, the product starts forming and heat generated in the chemical reaction (the reaction chosen needs to be exothermic) drives the remaining unreacted material to conversion. When the heat is supplied through microwave irradiation, ignition and control of the combustion wavefront propagation is possible. Furthermore, using microwaves, the product can be densified by maintaining the microwave power applied.[30]

An aluminium oxide (Al_2O_3)-titanium carbide (TiC) composite has been synthesised through combustion starting from titania (TiO_2), aluminium and graphite by Clark *et al.*[31] The advantage of using microwaves to ignite the combustion lies in the ability to control the propagation of the combustion wave front using the microwave power applied. Furthermore, the inverse temperature profile enables the gradual release of volatile species outward without expansion of the product. The sample ignites in the centre and a combustion wave front propagates outward in a radial manner. Also, as microwaves are absorbed continuously by the material, the ignition temperature is sustained and as the temperature of the material increases, the dielectric properties of materials improve and they become better microwave absorbers. Therefore, microwave energy and combustion synthesis assist each other in sustaining the reaction.

Hassine *et al.* reported the synthesis of two refractory metal carbides, titanium carbide (TiC) and tantalum carbide (TaC), through the carbothermal reduction of the oxides using microwaves.[32] The mixtures of TiO_2 and carbon black were successfully heated as a consequence of the good absorbing properties of carbon powders (by contrast, titanium dioxide is almost transparent to microwaves at room temperature). However, problems still persisted when synthesising TiC, as the reaction yielded exclusively a titaniumoxycarbide ($Ti(O_{0.2},C_{0.8})$ at 1550 °C) phase based on the solid solution between the isotypic suboxide (TiO) and TiC. This result has been attributed to a relatively low reaction temperature (1550 °C as opposed to 2000 °C) and the fact that the reaction has been performed under an atmosphere of argon (possibly containing oxygen as impurity) instead of high vacuum. In the case of the tantalum carbide complete conversion was achieved. Overall, in comparison to conventional heating, faster reaction rates and higher yields were obtained at lower temperatures (measured with an optical fibre thermometer buried in the reaction mixtures) and in shorter times.

The synthesis and sintering of tungsten carbide WC-Co by the carburisation of a mixture of W, Co and C powders has been studied by many different groups through the years. Cheng *et al.* reported a total sintering cycle of less than 90 minutes compared to up to 24 hours

required conventionally with a sintering temperature of only 1300 °C; 150 °C lower than that necessary in the commercial process.[33,34] Enhanced densification of the product, finer WC grains and a more uniform distribution of the Co binder made the material produced 1-5 GPa harder than the conventionally synthesised material, six times more resistant to corrosion and twice as resistant to erosion compared to the conventional product. Working on the same system, Rodiger *et al.* were able to perform the carburisation reaction at temperatures of ca. 930 °C, also reporting a finer microstructure and a more complete densification than that achieved via conventional heating.[35]

While much previous work was focused on the end product, Vallance *et al.* studied the carburisation of tungsten powders with a combination of *in-situ* and *ex-situ* analysis to build an understanding on the mechanism of solid state microwave reactions (specifically the reactions to form transition metal carbides).[36] Phase-pure WC was synthesised in a single mode cavity reactor at 3 kW in 20 seconds. By relating the reaction temperature (measured *in-situ*) to the dielectric properties of various samples (measured *ex-situ*) it was possible to show how temperature, phase fraction and dielectric properties were intimately related. The same technique was applied to study the synthesis of Mo_2C (achieved in 10 seconds from Mo or MoO_3 and C)[37] and of ternary phases in the Nb–Ta–C solid solution system.[38] All materials could be prepared in a fraction of a minute showing a similar trend to that seen in the synthesis of WC. In all the M–C systems, where M= W, Mo, Nb, Ta, at the beginning of the irradiation process, most of the energy is absorbed by the graphite powder susceptor. As the temperature increases it is possible the dielectric properties of the reactants improve up to a critical temperature where the MW interaction is optimum and product formation begins. Once initiated, the formation of the carbides is extremely rapid, phase-pure products are synthesised and the reaction is self-terminating.

As for the other refractory carbides, the synthesis of silicon carbide through direct carburisation of silicon and carbon powders using microwave irradiation has been studied extensively, mostly resulting only in partial conversion. More detailed discussion of these studies will be made in the results chapters to draw comparisons with the studies performed in this thesis. β-SiC has been previously synthesised starting from silicon and amorphous carbon in a commercial microwave oven using different powers and atmospheres.[39,40,41] Alternatively different morphologies of SiC can be achieved by replacing amorphous carbon with organic carbon sources such as phenolic resin.[42]

As will be shown below, the capacity of a material to be heated under microwave irradiation depends on its dielectric properties and ideally, for each material treated, heating should be performed at an optimum microwave frequency. Historically however, frequency allocations and regulations on permitted radiation have been implemented for industrial, scientific, and medical (ISM) applications.[43] The frequency bands at 915 and 2450 MHz are the most developed bands and the only frequencies easily available at useful power levels to process materials, with most microwave ovens operating at 2.450 GHz. Although water and other polar molecules couple well at these frequencies, providing advantages for food processing, the same frequencies are not optimum for other materials, such as polymers and ceramics, leading to practical processing challenges.

Microwave processing is influenced by complex parameters regarding both the setup used and the materials irradiated.[44] The size and shape of the object being irradiated affects how it is heated. Further, the dielectric properties (and so the ability to generate heat inside the material) change as the material processed undergoes chemical and structural transformations. The design of microwave equipment is particularly important as it determines the electromagnetic field. Since the energy is transferred by the electromagnetic field, any non-uniformity in the field will also cause non-uniformity in the heating profile.

1.3 Electrical volumetric heating

Volumetric heating is possible when all the infinitesimal elements of volume in a sample are each heated individually, ideally at the same rate. When an object is heated volumetrically, the heat energy injected into the material does not flow as heat flux, as in conventional heating, but is transferred through the surface electromagnetically. Therefore the rate of heating is no longer limited by thermal diffusivity and surface temperature, the heat distribution is more uniform, and heating times can often be reduced. Any material, which is neither a perfect electrical conductor nor a perfect insulator, can undergo volumetric heating.[45] The choice of the heating method depends on the effective electrical resistivity and physical properties of the sample and not a single electrical technique is effective in all cases.

For example, conduction and induction heating methods (applied widely in metallurgic industries) are used to heat metals with low resistivity and involve passing a heavy current through the sample to cause ohmic heating.[45] Ohmic heating is also used in the case of

liquids and slurries and consists of passing an alternating current through the liquid between electrodes. Aqueous solutions are always sufficiently conductive to permit a high power density to be dissipated because dissolved salts provide ions as charge carriers. It is widely used in food industries, especially for sterilization in aseptic processing.

Additionally, radio frequency (RF) heating is used when a sample has high resistivity. Increasing the frequency helps to lower the voltage required to pass sufficient current for practical power-dissipation density. Typical applications are plastics, wood, textile, paper and board, food and ceramics. The sample is placed between electrodes in the form of plates or rods across which a high voltage is applied (usually several kilovolts) at the chosen high frequency. This structure forms a capacitor in which the sample is part of the dielectric, and the charge/discharge current flows between the electrodes.[45] Most of the materials which can be heated at RF can be also heated at microwave frequencies, together with some others which are difficult under microwave fields because of their low loss factor (see below).[45]

1.3.1 Microwave interaction with dielectric materials

Gases, liquids and solids can interact with microwaves and be heated. Under certain conditions, gases can be excited by microwaves to form plasmas that are also useful for processing.[45,43,9,46] Microwaves can be reflected, absorbed and/or transmitted by materials. Reflection and absorption require interaction of the microwaves with the material, while transmission is the result of partial reflection and incomplete absorption. During interaction, energy in the form of heat is generated in the material primarily through absorption. Microwaves can interact with materials through either conduction or polarisation processes.[17]

Ionic conduction losses are caused by ohmic losses that occur when ions move through a material and collide with other species. Ionic conduction requires long-range charge transport and it decreases with increasing frequency as the time allowed for transport in the direction of the oscillating field decreases (Figure 1-1).

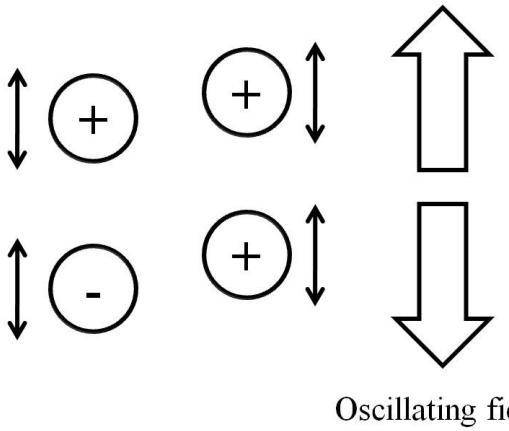

Figure 1-1 Movement of free charge carriers depending on the oscillating field.

Polarization involves the short-range displacement of charge. In particular in the liquid state, dipolar components of molecules in many dielectric substances couple electrostatically to the microwave electric field and rotate to align themselves with it. Since the microwave field is alternating in time, the dipoles will attempt to realign as the field changes direction and by doing so, they are in a constant state of mechanical oscillation at the microwave frequency. Frictional forces within the molecule due to the motion of the dipoles and the lag between the electric field and the polarization cause dissipation of energy as heat inside the material (Figure 1-2).

This effect is clearly frequency sensitive and the rate of dissipation of energy increases as the frequency increases. However, the mechanical displacement of the dipoles changes with a change in frequency. In the microwave region, individual chemical compounds display well defined responses.[45] Mechanical resonances within the molecule result in peaks of power absorption in the frequency spectrum. Many dielectric liquids show polar characteristics, the most common being water which absorbs microwave energy very strongly even when highly pure.

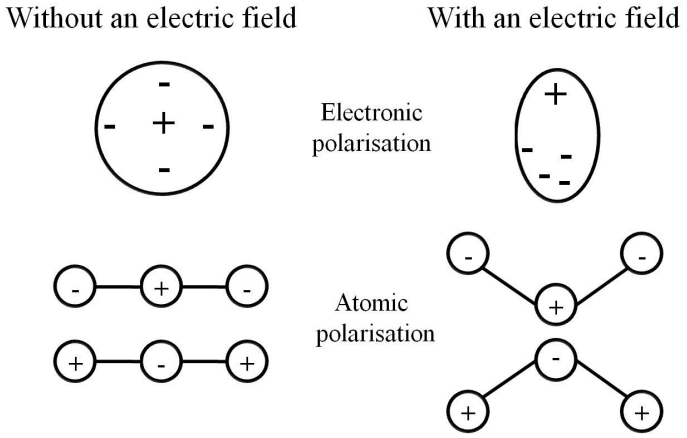

Figure 1-2 Representation of electronic and atomic polarisation arising when the sample is in the presence of an electric field.

Both conduction and polarisation processes give rise to losses in certain frequencies ranges. Generally, the dielectric losses, ε″, are caused by ionic conduction, dominant at low frequencies, and rotation of permanent dipoles at higher frequencies. It is not easy to experimentally distinguish between them however.[45]

A special kind of polarisation, referred to as Maxwell-Wagner or interfacial polarisation, should be mentioned separately for its importance in systems containing both conducting and non-conducting components.[47] Due to the heterogeneous nature of materials systems during processing, sometimes charge carriers can be trapped and are not able to discharge. When this happens, a difference in potential between particles can arise, which leads to uneven charge distribution and subsequent heating (Figure 1-3). This mechanism is very difficult to treat in a simple manner, and is most easily viewed as a combination of conduction and dipolar polarization effects.

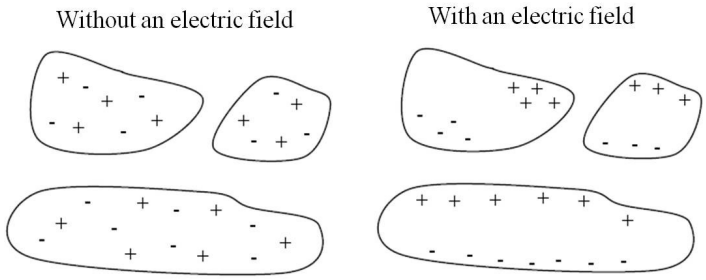

Figure 1-3 Representation of the accumulation of charge at the material interface.

When dealing with poor absorbers, like many ceramics and polymers, several methods can be used to improve coupling with microwaves at 2.45 GHz (and room temperature). Increasing the temperature, adding absorbing constituents (e.g. SiC, carbon, binders), altering their microstructure and defect structure or changing the frequency of incident radiation are some examples.[9] The most common method adopted by many researchers is to increase the temperature (with radiant heat). Once a certain low-loss material is heated to a critical temperature, microwave absorption becomes sufficient to initiate self-heating.[9] This can be done either by using an independent heat source such as a conventional furnace in combination with microwaves (this technique is called hybrid heating) or through the use of an external susceptor, a material that couples well with microwaves. In the latter case, the sample is irradiated simultaneously by heat produced by the susceptor and microwaves.

A sharp increment in the microwave loss begins at temperatures of about 0.4-0.5 T_m in both ionic (e.g. Al_2O_3, ZrO_2) and covalent (e.g. Si_3N_4, AlN) solids (T_m is the melting temperature of the material considered).[23] In this temperature range the bonds between ions in ionic crystals start to break, while in covalent materials the electrons start to populate the conduction bands, improving the dielectric response of the materials to microwaves. Due to the sharp increase in the losses, hybrid heating is often not needed at high temperatures. Ideally, a susceptor system should provide heating at the initial stage, and reflect most of the power at elevated temperatures when microwaves are absorbed directly by the material irradiated. An increase in the local temperature results in an enhancement of microwave energy absorption, which in turn initiates the local acceleration of heating and further growth of temperature. This can cause thermal instabilities, commonly referred to as thermal runaway.[23]

As already explained phenomenologically, in dielectric materials the external electric field polarises the material, by redistributing the internal charges. Dielectric permittivity, ε, represents a measure of such a response to an external electric field. For heat to be generated within the material, the microwaves must be able to enter the material and transmit energy. The relative permittivity (ε′) is the measure of the ability of a material to be polarised by an electric field, while the dielectric loss factor (ε″) quantifies the ability of the material to convert the absorbed microwave power into heat.[24] These components are often expressed in terms of the complex dielectric permittivity (ε*):

$$\varepsilon^* = \varepsilon' - j\varepsilon'' \qquad \textbf{(1-2)}$$

The change of polarization due to the alternating electric field, accompanied by the motion of electric charge generates heat inside the material. The polarisation response to the field is not instant and the greater the imaginary part of the dielectric permittivity, the larger is the lag. Another commonly used term for expressing the dielectric response is the loss tangent. Also called the loss factor, tan δ, characterises the dissipation of electromagnetic energy:

$$\tan\delta = \varepsilon''/\varepsilon' \qquad \textbf{(1-3)}$$

At a macroscopic level, the dielectric properties are involved in the quantitative relationship of absorbed power per unit volume (P) and the depth of penetration (D_p) and regulate the microwave processibility of a wide range of materials. The relative permittivity of free space (ε_0= 8.854 x 10^{-12} F m^{-1}) is a universal constant which defines the mechanical forces between two electrostatic charges spaced apart in a vacuum, for instance between two flat plates constituting a capacitor. If the space between the two flat plates is filled by a dielectric material, the force is increased by a factor, referred to as the relative permittivity for that material. The permittivity, as already mentioned, is generally expressed as complex to reflect loss mechanisms of the dielectric polarisation process. Equation **(1-4)** quantifies the power dissipation in a capacitor comprising a dielectric. The power dissipation density, P (W m^{-3}), is given by:

$$P = 2\pi f \varepsilon_0 \varepsilon'' E_i^2 \qquad \textbf{(1-4)}$$

in which E_i and f are the electric field intensity in volts per metre (V m^{-1}) and its frequency in hertz (Hz) respectively. Equation **(1-4)** is valid for only very thin materials because as energy is absorbed within the material the electric field decreases as a function of the distance from the surface of the material (see penetration depth in the next section). Equation **(1-4)** is also applicable to measure power dissipation in materials and objects of uniform composition adequately described by the simple dielectric parameters.

Some very important features of the dielectric heating can be deduced from this equation.

- The power density dissipated in the sample is proportional to frequency when the other parameters are constant.[45]
- The power density is proportional to the loss factor. The value of ε″ itself changes not only with frequency, but also with temperature, moisture content, physical state (solid or liquid) and composition. For the above reasons, it is important to consider the dielectric parameters as variables during the processing.[45]
- For a constant power dissipation density, the electric field strength E_i decreases with the square root of the frequency. This means that, if ε″ remains constant with frequency, the risk of voltage breakdown decreases as the chosen operating frequency rises (but as discussed above, usually ε″ varies with frequency).[45]
- The electric field E_i is the field within the dielectric material. The electric field just outside the dielectric sample, E_{ext}, is at least equal to E_i and may greatly surpass it, depending on local geometry and ε′.[45] A voltage breakdown will initiate if, even locally, either the internal or the external electric fields reach the critical level. When this occurs, the generated ionised gases form an arc which will then show a low-resistance electrical path. The sample and possibly the equipment can be damaged if considerable power is dissipated locally. Since the field intensity needed to maintain an arc is considerably less than that required to initiate it, it is absolutely necessary to switch off the microwave power to extinguish it. If the sample is damaged, there is a high risk of breakdown recurring at the same location. Before reapplying the microwave power, a few seconds would be needed for the ionised gases to disperse.[45] Therefore, it is very important to know the magnitude of the electric field external to the sample to prevent voltage breakdown of the gases in the vicinity.

1.3.1.1 Penetration depth

As a wave progresses through a dielectric material, its amplitude diminishes due to the absorption of power as heat in the sample. If the waves are not reflected in the material, the field intensity and the associated power flux density fall exponentially with the distance from the surface.[1] Because the power absorbed in a volume of material is proportional to the power flux density flowing through it, even the power dissipation falls exponentially from the surface. Hence the attenuation of the electromagnetic wave can be characterized by a penetration depth, D_p (measured in meters), defined as the depth into the material at which the power flux has fallen to 1/e (= 0.368).

The rate of decay of the power dissipation is a function of both the relative permittivity ε′ and the loss factor ε″. The penetration depth is given by:

$$D_P = \frac{\lambda_0}{2\pi\sqrt{(2\varepsilon')}} \frac{1}{\sqrt{\left[\left\{1+\left(\frac{\varepsilon''}{\varepsilon'}\right)^2\right\}^{0.5} - 1\right]}} \qquad \textbf{(1-5)}$$

Where if ε″≤ ε′, can be simplified, with an error of up to 10 % as:[1]

$$D_P \approx \frac{\lambda_0\sqrt{\varepsilon'}}{2\pi\varepsilon''} \qquad \textbf{(1-6)}$$

The penetration depth gives an immediate indication of the heat distribution within the sample. If the penetration depth of the microwave is much shorter than the thickness of the material, only the surface is heated, while the remainder of the sample will be heated via conduction.

Depending on equation **(1-4)** and equation **(1-6)**, it can be seen which materials are the most suitable for microwave processing. Materials with a high conductance and low capacitance (such as metals), have high dielectric loss factors. As the dielectric loss factor increases, the penetration depth approaches to zero. Materials with this dielectric behaviour are considered reflectors. Materials with low dielectric loss factors have a very large penetration depth. As a result, very little of the energy is absorbed in the material and the material is transparent to microwaves. Because of this behaviour, the materials that transfer microwave energy most effectively are in the middle of the conductivity range (Figure 1-4).[44] In contrast, conventional heating transfers heat most efficiently to materials with high conductivity.

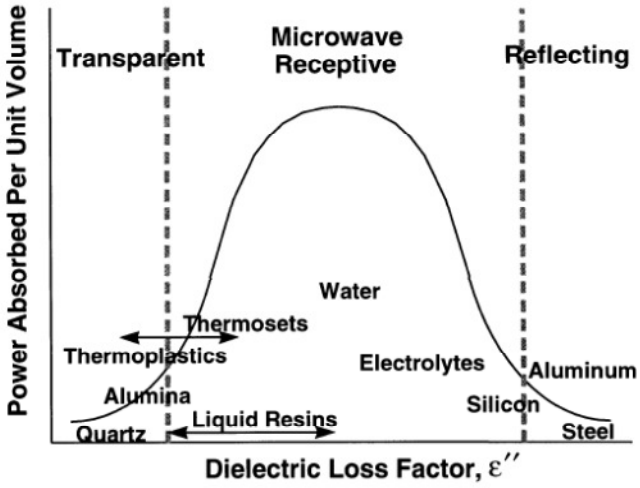

Figure 1-4 Relationship between the loss factor and the ability to absorb MW power.[44]

The mechanisms involved in microwave materials processing are much more complex than in conventional heating since, as previous mentioned, the dielectric properties are dependent on the mobility of the dipoles within the structure, and therefore the dielectric properties depend on a series of parameters and the ability of the material to absorb energy varies during processing. For example, at room temperature, silicon carbide (SiC) has a loss factor of 1.71 at 2.45 GHz. The loss factor at 695 °C at the same frequency is 27.99.[48]

In conventional furnace heating, energy is transferred to the materials by thermal electromagnetic radiation, with its intensity reaching a maximum in the infrared range. The penetration depth of infrared radiation (frequency $\geq 10^{13}$ s^{-1}) is very small (depth $<< 10^{-4}$ m) in the majority of solids. Therefore, conventional heating essentially depends on heat transfer from the hotter near-surface region to the colder bulk of the material. In the microwave frequency range, the absorption properties of non-metallic materials vary greatly.[23] At room temperature, if low-absorption materials, i.e. low ε', are placed in a cavity, the electromagnetic wave passes multiple times within them without being absorbed (Figure 1-5 (a)). However, in the case of highly absorbing materials (with $\tan\delta \geq 10^{-1}$) the effective conductivity is typically so large that a strong reflection of radiation from the surface inhibits microwave heating (Figure 1-5 (b)).

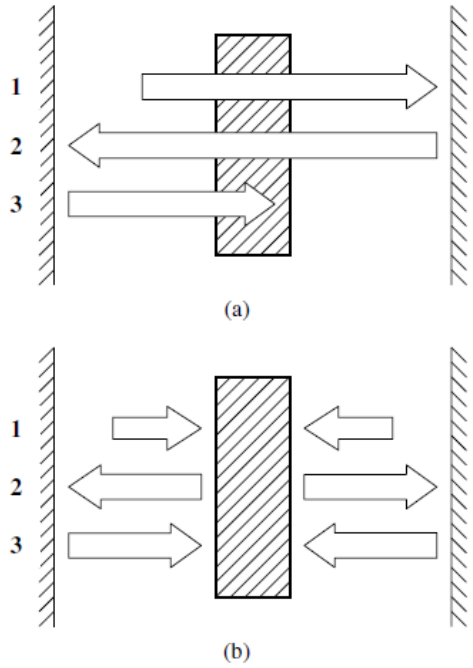

Figure 1-5 Schematic of the behaviour in a microwave cavity of (a) low loss material: 1, incident radiation; 2 and 3, radiation returned to the sample after reflection from walls. (b) high loss material: 1, incident radiation; 2, radiation reflected from the sample; 3, radiation returned to the sample after reflection from resonator walls.[42]

At room temperature the loss factor, tanδ, ranges from 10^{-4} - 10^{-3} (for instance in pure alumina and silicon nitride) up to 1 and higher (in carbides and some oxides and intermetallic compounds).[21] It follows that penetration depth varies inversely from metres to fraction of a millimetre.

Electromagnetic theory, that describes the interaction between microwave electromagnetic fields and materials, gives only qualitative information on the dielectric properties of materials and their frequency dependence. The reason is that the mechanisms of interaction and their effectiveness are strongly interdependent on the frequency, temperature, chemical composition, and microstructure. Furthermore, equations must be modified when a material is magnetic. In these cases, the magnetic dipoles may be able to couple with the magnetic component of the electromagnetic field and provide an additional heating mechanism.[9] Simple theoretical considerations are only able to predict the character of the dependence of ε but fail to calculate the magnitude of the dielectric permittivity at a given frequency. Therefore, the direct measurement of the dielectric properties of materials appears to be the only method to obtain such quantitative information. Furthermore, historically there has been a serious lack of data on dielectric properties of most materials as a function of temperature at microwave frequencies.

1.4 Silicon carbide

Silicon carbide, SiC, is the only stable chemical composition of silicon and carbon. For convention, the term carbide is applied because Si possesses a lower or similar electronegativity to carbon.[27] Both silicon and carbon atoms are tetravalent and since the electronegativity difference between Si and C is small (and the C atom is slightly smaller than the Si atom), the bonding is essentially covalent. The difference in electronegativity following the scale of Pauling[49] is 2.55 - 1.9 = 0.65 and the Si-C bond is considered only 12 % ionic. As evidence of the strongly homopolar bonds, silicon carbide has high hardness and melting point, and pure SiC specimens possess a very high binding energy (the energy to dissociate the solid into separate atoms). Due to its high decomposition point, SiC is listed as a refractory carbide.[27]

In a relatively short time, SiC ceramics have become major industrial materials and have been exploited for their unique high temperature chemical and mechanical properties. The properties measured tend to show a large spread in the values reported,[50] depending strongly on how the SiC sample is synthesised and processed, its purity, polytype and morphology. Nevertheless silicon carbide ceramics show superior mechanical properties such as high hardness and strength, especially at high temperature and extreme resistance to wear and thermal shock,[27] with the only disadvantage of being brittle. Applications of silicon carbide range from cutting and grinding tools, bearings to textile-machinery components, and many others.

Silicon carbide is essentially chemically inert at room temperature and when heated in hydrogen, nitrogen or carbon monoxide, and up to 1000 °C when heated in oxygen. Between 1000 - 1350 °C in air, a silica passivation layer forms on the surface of silicon carbide slowing down oxidation which proceeds quickly only at temperatures higher than 1750 °C. At these high temperatures, silicon carbide is also attacked by water vapour and carbon dioxide. Silicon carbide does not react if boiled in acids, not even with hydrofluoric acid. However, it forms metal silicides when reacted with copper, iron, nickel or manganese oxides at temperatures in the range of 800 - 1370 °C and decomposes by fusion with alkaline hydroxides and molten metals or chlorine at temperatures above 1000 °C.[51, 52]

Silicon carbide is used in refractory and structural ceramic components for harsh environments. SiC is employed in the form of powders for applications such as abrasives in grinding and polishing tools, in shapes as refractory products like heating elements in

electric furnaces, in the form of fibres and whiskers in ceramic composites and as a filler in refractory cements.[53]

Although silicon carbide has long been recognized as a semiconductor, it is with the recent developments in producing high-quality SiC thin films that is now possible to consider silicon carbide for high power and high-frequency electronic devices, capable of operating also at high temperatures and in harsh environments.[54] Compared to the established semiconductor devices based on silicon, cubic SiC has an indirect band gap of 2.39 eV at 20 ºC,[69] double that of Si (1.12 eV) and also shows better thermal conductivity, a large breakdown field (more than an order of magnitude higher than that of Si) and resistance to chemical attack.[55] Further SiC is the only semiconductor compound that can be thermally oxidized to form high-quality SiO_2 films, and has lower defect densities at the interface than films produced from a Si substrate, even though the oxidation rate is considerably lower in comparison.[56] Different types of SiC wafers are now commercially available but they are smaller and more expensive than those made of Si.[57] SiC is also applied in opto-electronic devices working as an emitter in blue LEDs.[58]

1.4.1.1 Polytypic modification of SiC

Silicon carbide is mostly man made. It was found in nature for the first time as crystals in the meteorite from Canon Diablo by Moissan, but it does not occur as a mineral on Earth.[59] In 1912 Bauhauer discovered that SiC crystallises in different structures, purely from optical studies and referred to them as “types”.[60] The discovery of polytypism is therefore attributed to him. Polytypism is classified as a kind of polymorphism, a more general phenomenon which describes the same chemical substance showing different crystal structures. In both cases the polymorphs/polytypes have the same chemical properties, but different physical properties depending on the arrangement of atoms within the structure.[61] However while in polymorphic transition the rearrangement of atoms requires the structural bonds to break and reform during the transition from one structure to another and to obey the laws of thermodynamics, polytypic transformations are more complex, as will be shown subsequently.

The crystalline structures of SiC consist of a close-packed stacking of double layers of Si and C atoms. Each Si or C atom shares a pair of electrons with the other, so that the four hybridized $2sp^3$ orbitals of carbon bond with the four hybridized $3sp^3$ orbitals of silicon. Therefore in all SiC polytypes each Si or C atom is surrounded by four C or Si atoms in a

tetrahedral fashion and differences arise only in the second or higher coordination sphere. The atomic distances are almost the same for the different polytypes and the dependence of the atomic distance on the polytype structure is very weak.[62] Typically the distance between the atoms 1.89 Å.[27]

The polytypism shown by silicon carbide originates from the differences between the closed-packed stacking sequences of the identical double layers of Si and C atoms. The unit cell dimensions of each hexagonal and rhombohedral polytype are the same in the two directions in the plane parallel to the stacked layers (the same tetrahedral arrangement of C and Si atoms), and differ in the direction perpendicular to these layers (the *c*-axis direction).[63] The dimension of the unit cell varies between polytypes according to an integral multiple of a value determined by the distance between successive double layers of Si and C atoms. As a consequence of the low formation energy of stacking faults in the silicon carbide structure, modifications are very common and more than 74 polytypic phases are known.[64] All SiC polytypes are chemically ordered probably due to the fact that incorporating Si-Si and C-C bonds in the structure would introduce strain since the atomic radius of silicon is approximately 1.5 times bigger than the carbon radius.[65] The description of cubic and hexagonal close packing of Si atoms, with C atoms at the centres of the tetrahedra were reported by Hull who first found the correct structure of β-SiC, described as a diamond-type structure, with half of the C atoms replaced by Si.[66] Subsequently, Hull found evidence of a close-packed hexagonal structure of SiC from powder photographs.[67]

The crystal structure of SiC corresponds to either face-centred cubic ZnS zincblende (the cubic SiC variation), or is based on hexagonal ZnS, wurtzite (2H-SiC, hexagonal polymorph). In the cubic zincblende variation (Figure 1-6a), the structure consists of Si and C atoms that exhibit identical interpenetrating close packing, one displaced relative to the other along the *c*-axis by one-quarter of the layer spacing. Furthermore, Si and C layers are stacked alternately, each occupying half the tetrahedral voids between the layers. Because the cubic modification of SiC is isomorphic with β-ZnS (sphalerite) and was believed to be a low-temperature modification, it was named as "β-SiC".

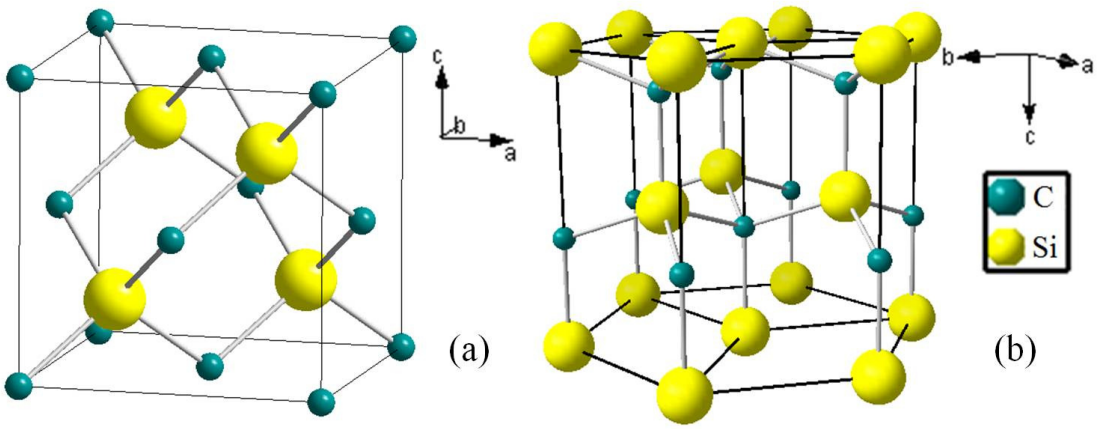

Figure 1-6 Crystal structure of cubic (a) and hexagonal (2H-SiC) (b) polytypes of SiC.

The stacking of the Si-C bilayer follows one of three possible configurations and these are arbitrarily assigned with the notation A, B or C. A convenient and simple method to refer to each polytype is the Ramsdell notation.[68] In this nomenclature system, a number followed by a letter is associated with each polytype. The number represents the repeat stacking sequence of the Si-C layers in the unit cell and the letter is relative to the crystal system (C for cubic, H for hexagonal, and R for rhombohedral). For instance, β-SiC is expressed as 3C because it has a stacking sequence of ABCABCABC… (along the body diagonal). The hexagonal (H) and rhombohedral (R) varieties are collectively called "α-SiC". Of these, 2H-SiC has an ABABAB stacking sequence (see Table 1-1). The 2H polytype has the wurtzite structure and is considered a metastable modification that transforms to the 3C and 6H polytypes above 1400 °C.[27] The 6H structure, the most common α-SiC modification, has a unit cell which is hexagonal and contains six formula weights with a stacking sequence of ABCACBABCACB…

Polytypes	Structure	Sequence
3C (β-SiC)	Cubic	ABCABCABC
2H (α-SiC)	Hexagonal	ABABAB
4H (α-SiC)	Hexagonal	ABACABAC
6H (α-SiC)	Hexagonal	ABCACBABCACB
15R (α-SiC)	Rhombohedral	ABCACBCABACABCB

Table 1-1 Stacking sequences of Si-C double layers in SiC polymorphs.

As mentioned previously, although the potential of silicon carbide as a semiconductor material has been long recognized, the difficulty to control polytypes during crystal growth and the issues with producing high-quality and large size SiC crystals, has prevented electronic applications. The technologically most important polytypes are 3C-, 4H-, and 6H-SiC. Single crystals wafers are commercially available for polytypes 4H-SiC and 6H-SiC, where the electronic band gap is 3.27 eV and 3.02 eV respectively (considerably higher than Si).[69] SiC is also more rigid than Si with a Young's modulus ranging from 360 GPa to 450 GPa depending on the synthetic conditions, morphology and microstructure.[84] SiC can also be doped to create an n- or p-type material and the substitutional dopant added is reported to influence the SiC polytype formed.[69] When elements from groups III, electron acceptors such as Al and Ga, substitute for Si in the SiC lattice, SiC is doped p-type. While if elements from group V of the periodic table, electronic donors like N and P are added, they replace C atoms in the lattice and SiC is doped n-type.

1.4.1.2 Si-C binary phase diagram

The Si-C binary phase diagram (Figure 1-7) shows thermodynamic equilibrium conditions between different phases, but does not distinguish between β-SiC and metastable α-SiC. Nevertheless, the Si-C binary phase diagram can be used as a guide as to how SiC could be synthesised in a conventional furnace. Two invariant points are present in the phase diagram, a peritectic point at 2545 ± 40 °C and an eutectic transformation at 1404 ± 5 °C, representing a three phase equilibrium between liquid Si, solid Si and SiC.

A number of studies have emphasised that silicon carbide has no congruent melting point and rather it decomposes into a Si-rich liquid in equilibrium with graphite. Experiments at high temperatures and pressures performed by Scace and Slack concluded that a peritectic point occurred at 2830 °C ± 40 °C in 35 atm of argon.[70] Knippenberg found from evaporation experiments performed in an atmosphere of argon that the total vapour pressure above evaporating SiC is 1 atm at 2757 °C ± 20 °C.[71] The most abundant species found under these conditions were Si, SiC_2, and Si_2C.

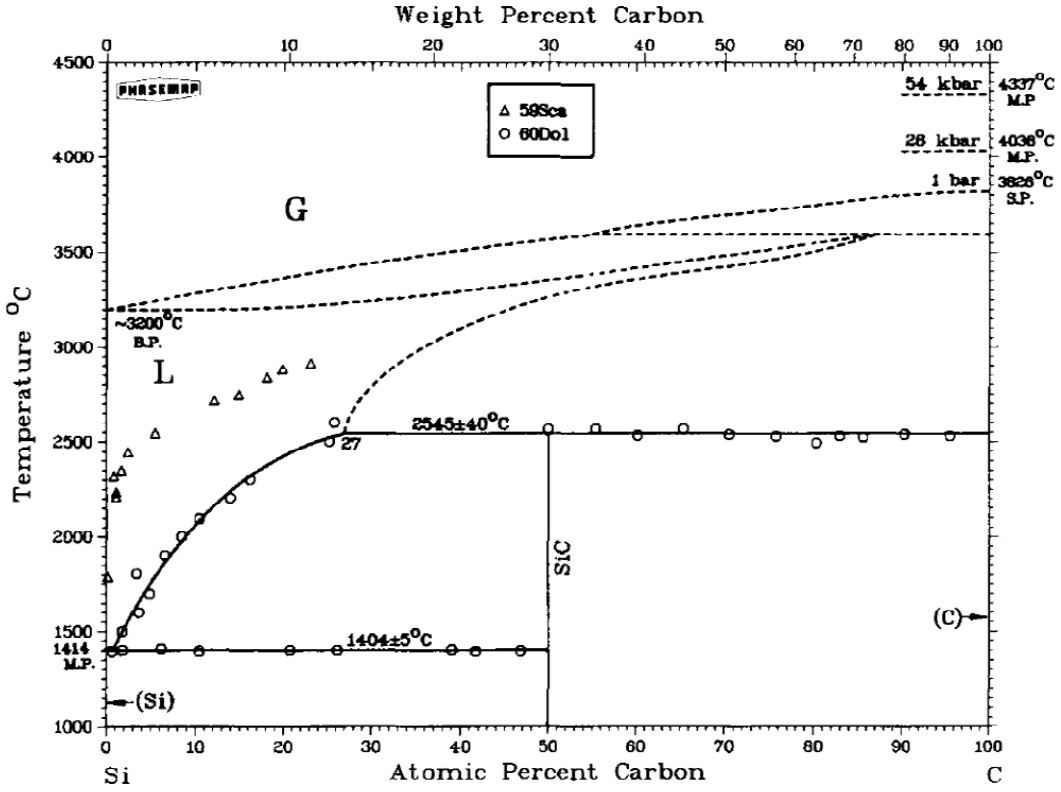

Figure 1-7 Phase diagram of the Si-C system[72] With kind permission from Springer Science+Business Media: Journal of Phase Equilibria, The C–Si (Carbon-Silicon) system, 5, 1984, 486, R.W. Olesinski and G.J. Abbaschian, Figure 1.

Different polymorphic modifications possess unique physical properties and it has been already mentioned that the various SiC polymorphs usually crystallise at different temperature and pressure conditions, depending on their range of thermodynamic stability. This normal situation for polymorphic transformations appears to be completely different for each of the SiC polymorphs however, many SiC polytypes appear to form under the same conditions of temperature and pressure, with the exception of the 2H and 3C polytypes.[73] Transitions from one α-SiC polytype to another are not even affected by pressure, since all α-modifications possess the same density of 3.217 gm cm^{-3}. In general, β-SiC is known as a low-temperature polytype, and 4H- and 6H-SiC are high-temperature polytypes. In particular, β-SiC is obtained when silicon carbide is synthesized below 2100 °C and is thought to be more stable than α-SiC at any temperature below the peritectic point.[27]

6H and 3C are by far the most common polytypes, followed by 15R and 4H, while all the other modifications are mostly found coexisting with these more common polytypes. Many studies have been carried out to assign the transition temperature between the 3C and 6H

modifications, but the small energy differences between the crystals at high temperatures has made this difficult.[74] The cubic phase (β-SiC or 3C) has been always considered as the low temperature modification, since it is usually found in the cooler parts of the electric furnace (forming at temperatures of about 1800 °C).[75,76] Starting from mixtures of silica and carbon, Baumann found that the conversion to β-SiC from silica and carbon mixtures started above 1500 °C and was complete at 1800 °C. Further, β-SiC was observed to begin to transform to α-SiC slowly at 2100 °C, but conversion was rapid at 2300 °C. However contrasting observations were made by Scace and Slack who found that both cubic and hexagonal crystals could be grown alongside one another from the vapour phase at 2600 °C, and also by Knippenberg who confirmed the existence and formation of β-SiC at high temperatures.[71] Therefore it has been concluded that β-SiC is not the low-temperature modification of silicon carbide, but it is metastable at all temperatures.[77] There appears to be no definite transition temperature from β-SiC to α-SiC, since the transformation was reported by Knippenberg to occur irreversibly above 2000 °C, while apparently contradictory studies by Scace and Slack reported β-SiC could be heated approximately to 2830 °C with no transformation taking place. Also the fact that cubic SiC has a higher chemical reactivity than α-SiC even at temperatures below 1000 °C, again would indicate that the cubic modification is probably a metastable modification at all temperatures.

1.4.1.3 History of SiC: from Acheson to modern synthetic methods

Silicon carbide was first made accidentally in 1891 by Edward Goodrich Acheson when he melted carbon and clay in an electric furnace.[78] Thinking the crystals were a compound of carbon and alumina from the clay, he called the material “carborundum”, derived from a combination of carbon and corundum, the crystalline form of alumina. In 1893 Acheson published a patent and since the new material was hard enough to scratch glass, it was commercialised as an abrasive soon afterwards.[79] The commercial Acheson process is essentially unaltered after more than a century; a reaction between high purity silica sand and carbon in an electric furnace.[80] The Acheson furnace can have different geometries, but it is usually composed of a central core of graphite and coke that works as an electrical heater (Figure 1-8, the electrode arrangement is labelled B). The reaction mixture (D) is filled around the core (C). The walls of the furnace (A) comprise of bricks loosely gained together to allow gases produced in the reaction to escape hence the walls are removable and the reaction is not usually sealed from air. The temperature cycles can vary, however the temperature of the central core reaches a maximum temperatures of ca. 2700 °C and is then lowered and maintained for about 30 hours at ca. 2000 °C. Subsequently, the furnace

is allowed to cool and the silicon carbide produced is removed, purified and graded according to size. The best quality samples are found near the core where the temperatures are higher and the reaction that takes place inside the furnace is:

$$SiO_2\ (s) + 3\ C\ (s) \rightarrow SiC\ (s) + 2\ CO\ (g) \qquad \textbf{(1-7)}$$

Sawdust is added (ca. 5 %) to make the mixture porous to help CO and gaseous impurities produced in the reaction to escape. Common salt is also added (ca. 1.5 %) to improve the quality of the samples. In fact, during reaction the common salt is converted to chlorine, which reacts with metal impurities and form volatile chlorides which escape. Further purification is sometimes done by crushing and treating the product with sulfuric acid.[81]

The Acheson process is the most common route for the industrial production of SiC, typically using SiO_2 and carbon black as raw materials to reduce costs. The product, with grains ranging in dimensions and quality, is often impure with a relatively high oxygen content and finds applications mostly as an abrasive, while the preparation of high-performance SiC ceramics requires added purification steps and ball milling.[82]

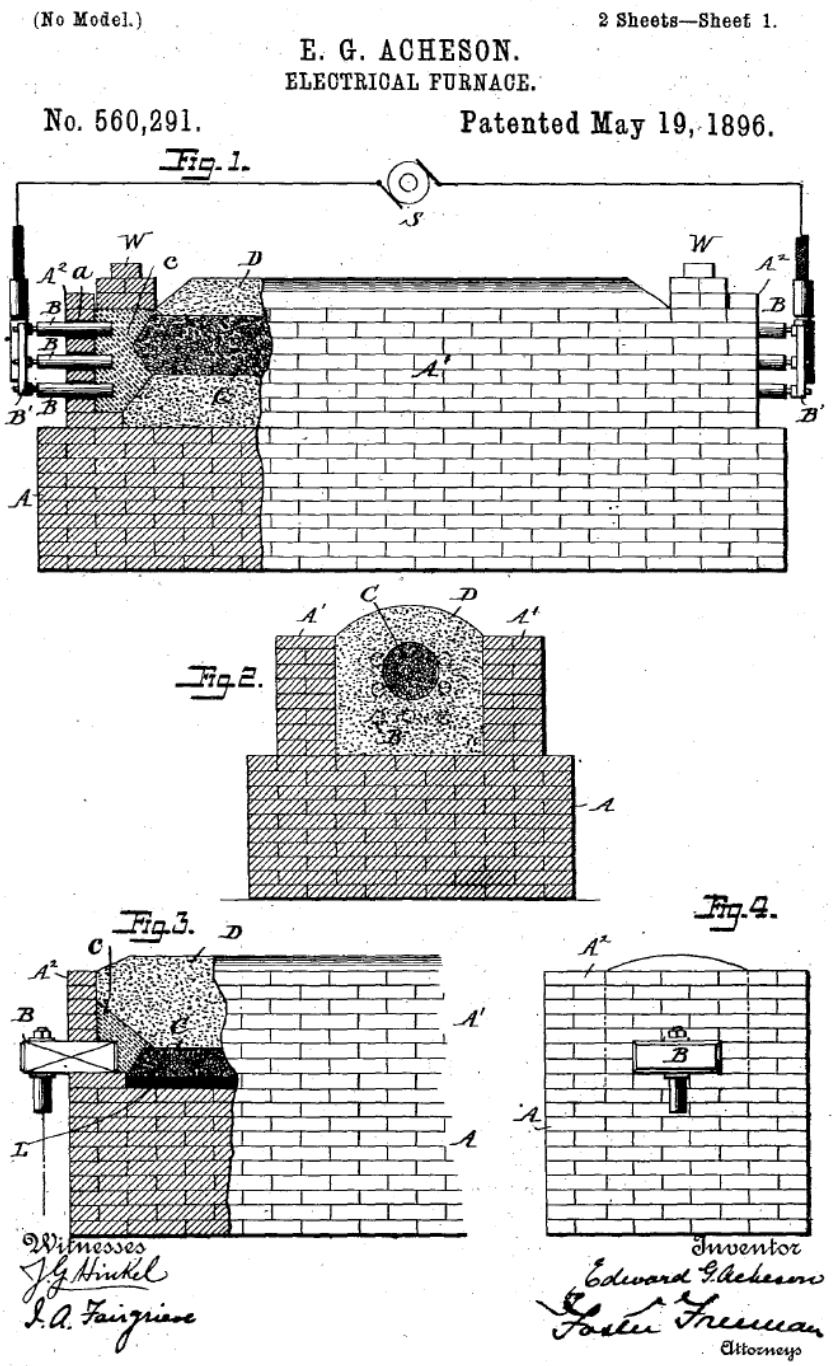

Figure 1-8 Schematic of the Acheson furnace.[83]

Because of the limitations of the conventional Acheson approach, a number of different synthetic routes have been developed to optimize the production and quality of SiC. These can be classified into mainly three categories: sol-gel processing, pyrolysis of preceramic polymers and conversion of biological precursors. Studies of the mechanism of the carbothermal reduction of silica have shown the reaction rate is controlled by both diffusion and gas phase processes.[84] Therefore reaction mixtures prepared by the sol-gel

technique have been employed as fine starting materials. Pure silicon carbide powders have been synthesised using colloidal dispersed mixtures of silica and carbon black[85] and mixtures of pyrolised sugar in silica sol.[86] Conversion to silicon carbide has been performed either under vacuum or an argon pressure of 180 kPa, at temperatures up to 1800 °C. Macroporous silica infiltrated with resin has been also used as SiC precursor,[87] and SiC nanowires have been prepared from mesoporous silica and carbon mixtures using Fe nanoparticles as a catalyst.[88]

Organosilicon polymers, mostly polysilanes or polycarbosilanes, have been used as SiC precursors. These preceramic polymers can be successfully converted to amorphous ceramics when heated at temperatures above 800 °C and crystallized to silicon carbide above 1200 °C leading to a range of different products.[89] Silicon carbide fibres were fabricated in 1975 by Yajima using polycarbosilane fibres heat treated up to 1000° C in vacuum[90] and laser pyrolysis has been used to convert polycarbosilane to SiC films.[91] Also porous silicon carbide ceramics have been produced from polysiloxane with the aid of hollow microspheres as sacrificial templates, showing how polymer processing techniques can be employed to tailor the morphology of the product.[92]

Finally, silicon carbide ceramics have also been produced starting from naturally derived materials either as a new sustainable way of processing or to achieve a biomorphic microstructure. Amongst biomaterials used for the synthesis of silicon carbide, plants containing a considerable amount of colloidal amorphous silica, such as rice husk or horse-tail, have been used to synthesise SiC.[84] SiC powders/whiskers have been produced from rice husk by pyrolysis under nitrogen atmosphere at temperatures around 1100 - 1400 °C.[93] Otherwise bamboo has been used as source of carbon, either as charcoal powders to reduce amorphous silica sol at 2100 - 2200 °C for 2 h in an Ar atmosphere,[94] or also as a porous template for nanocatalyst particles (and a carbon precursor) for the synthesis of SiC nanowires.[95] Biological carbon preforms have been fabricated from different wood structures, such as pine,[96] oak,[97] Tilia amurensis,[98] and beech[99] by high-temperature pyrolysis (up to 1800 °C) and used as templates for infiltration with gaseous or liquid silicon. The direct reaction between porous carbonized wood and silicon was then used to synthesise silicon carbide ceramics and mimic the distinctive open porous structure of wood itself.[100] This process has the advantage of leading to morphologies containing uniaxial pore structures and anisotropic mechanical properties difficult to obtain by usual processes and of interest for applications such as micro filters or catalyst supports.[103]

1.4.1.4 Properties and applications of silicon carbide

The mechanical properties of SiC often show a large spread in reported values, depending mainly on how it has been produced. In general SiC is one of the hardest materials, although extremely brittle. It has been given a value of 9.15 in Mohs' scale of hardness, between diamond and corundum.[59] Due to these characteristics, silicon carbide powders with coarse sizes are used, as already mentioned, as abrasives in grinding and polishing applications, while powders with finer grains are used as fillers in refractory cements, ceramic composites and in shapes as refractory products.[101] Due to its very high thermal stability; silicon carbide is also used to make crucibles for melting metals and electric heating elements and resistors in industrial furnaces.[102]

When looking at silicon carbide synthesis, it becomes clear that control of both crystal structure and morphology is crucial. Recently, porous SiC ceramics have attracted interest as supports in catalysis, as a good alternative to commercial oxide and carbon based supports and catalysts, due to their low density, chemical inertness, thermal and mechanical stability and most of all higher thermal conductivity. This is particularly important to avoid localized hot spots when SiC is used as a support in exothermic catalytic reactions.[103,104] SiC porous ceramics also find applications as filters for molten metals and particles from diesel engine exhaust gases and membrane supports for hydrogen separation.[105]

The density of all SiC modifications has been reported as 3.217 g cm^{-3},[106,107] while electrical conductivity depends on the polytype and the band gap for cubic or β-SiC has been measured at 20 °C as 2.39 eV, while the 6H and 4H polytypes have gaps of 3.02 eV and 3.26 eV respectively.[69] Therefore silicon carbide is a high temperature semiconductor whose characteristics depend on the presence of impurities. Due to the range of wide band gaps, SiC devices have the advantage of working even at high operating temperatures (where the intrinsic carrier concentration is still low).[108]

1-dimensional SiC nanostructures, such as nanowires, have attracted interest due to their high aspect, surface to volume ratio and absence of 3-dimensional growth related defects (such as dislocations). They are used to fabricate nanoelectronic devices for chemical/biochemical sensing and high-temperature, high-power, high-frequency and aggressive environment semiconductor devices.[109] β-SiC single-crystalline nanowires have been used as field emitters due to a strong green light emission.[110]

SiC whiskers and nanowires have also been used as fibrous reinforcements in nanocomposite materials to improve fracture tolerance and/or strength of monolith ceramics.[111,112]

Despite these attractive properties, there are technological difficulties to synthesise single crystals of SiC, mainly due to the fact that the well-known technologies used to produce silicon wafers are not applicable since silicon carbide does not melt congruently at atmospheric pressure.[70,71] The best commercial grades of silicon carbide are almost colourless or pale green, but various green and blue shades as well as black samples are common. The differences in colours of pure cubic and hexagonal crystals are probably due to this difference in the band gap and impurities have also been said to be to affect both the optical absorption and the conductivity.[71]

1.5 Aims and scope of this work

An existing collaboration between Prof. Duncan H. Gregory and Prof. Sam Kingman has led to radical new ultrarapid and sustainable microwave processing routes to materials.[36,37,38] Among the synthesis methods available, carbothermal reduction is the traditionally chosen route for the production of SiC but as already mentioned, it is energy intensive, demanding extreme temperatures and long treatment times, and it leads to coarse and not very pure powders. Therefore synthetic routes that are energy efficient and sustainable have become a high priority in the 21st century. Microwave processing is one alternative approach and the aim of this thesis project is to develop and study microwave (MW) preparations of SiC, to reduce processing complexity (and cost) and cut processing times. Si-C/SiO_2-C systems have been investigated in this thesis as potentially good bases for microwave-based synthesis. The driver behind this approach lies in the ready availability at reasonable cost of the starting powders, but, most importantly, the excellent microwave absorption properties of carbon.

Following a discussion of the experimental techniques employed, Chapters 3 and 4 describe studies pursued on the synthesis of SiC starting from either Si or silica as sources of silicon. Different microwave approaches are described and the effects these have on reaction mechanism, phase composition and material properties discussed. Chapter 5 then goes on to demonstrate how similar microwave processing routes can be extended to conversion of precursors with bespoke porous microstructures, x-aerogels, to silicon

carbide thanks to a collaboration with Prof. Nicholas Leventis, Missouri University of Science and Technology, Department of Chemistry.

[1] R. Meredith, *Engineers' Handbook of Industrial microwave heating*, The Institution of Electrical Engineers, 1998, Chap.1.

[2] D. Annaratone, *Transient Heat Transfer*, SpringerBriefs in Applied Sciences and Technology, 3, Springer, Heidelberg, NY, 2011.

[3] R. L. Wathen, *J. Franklin Inst.*, 1953, **255**, 271.

[4] D. K. Barton, *IEEE Trans. Microwave Theory Tech.*, 1984, **32**, 1161.

[5] H. Sobol and K. Tomiyasu, *IEEE Trans. Microwave Theory Tech.*, 2002, **50**, 594.

[6] J. M. Osepchuck, *IEEE Trans. Microwave Theory Tech.*, 1984, **32**, 1200.

[7] A. R. v. Hippel, *Dielectric Materials and Applications*, Wiley, New York, 1954.

[8] S. W. Liu and J. P. Wightman, *J. Appl. Chem. Biotechnol,* 1971, **21**, 168.

[9] D. E. Clark and W. H. Sutton, *Annu. Rev. Mater. Sci.*, 1996, **26**, 299.

[10] S. Caddick, *Tetrahedron*, 1995, **51**, 10403.

[11] P. Lidström, J. Tierney, B. Wathey and J. Westman, *Tetrahedron*, 2001, **57**, 9225.

[12] C. O. Kappe, *Angew. Chem. Int. Ed.,* 2004, **43**, 6250.

[13] R. S. Varma, *Pure Appl. Chem.*, 2001, **73**, 193.

[14] A. Richel, P. Laurent, B. Wathelet, J.-P. Wathelet and M. Paquot, *Catal. Today*, 2011, **167**, 141.

[15] C. E. G. Bennett, N. A. McKinnon and L. S. Williams, *Nature*, 1968, **217**, 1287.

[16] J. D. Katz, *Annu. Rev. Mater. Sci.,* 1992, **22,** 153.

[17] D. M. P. Mingos and D. R. Baghurst, *Chem. Soc. Rev.,* 1991, **20**, 1.

[18] D. R. Baghurst and D. M. P. Mingos, *J. Chem. Soc., Chem. Commun.,* 1988, 829.

[19] D. R. Baghurst, A. M. Chippindale and D. M. P. Mingos, *Nature*, 1988, **332**, 311.

[20] A. G.Whittaker and D. M. P. Mingos, *J. Chem. Soc. Dalton. Trans.*, 1995, 2073.

[21] D. K. Agrawal, *Curr. Op Solid State Mater. Sci.,* 1998, **3,** 480.

[22] K. J. Rao, B. Vaidhyanathan, M. Ganguli and P. A. Ramakrishnan, *Chem. Mater.*, 1999, **11**, 882.

[23] Y.V. Bykov, K.I. Rybakov and V.E. Semenov, *J. Phys. D: App. Phys.*, 2001, **34**, R55.

[24] M. Oghbaei and O. Mirzaee, *J. Alloy. Compd.*, 2010, **494**, 175.

[25] J. J. Thomas, R. J. Christensen, D. L. Johnson and H. M. Jennings, *J. Am. Ceram. Soc.*, 1993, **76**, 1384.

[26] T. Y. Kosolapova, *Carbides: Properties, Production and Applications,* Plenum Press, New York, 1971.

[27] H. O. Pierson, *Handbook of Refractory Carbides and Nitrides*, William Andrew Publishing, Norwich, NY, USA, 2001.

[28] E. K. Storms, *The Refractory Carbides*, in Refractory Materials, A Series of Monographs, J. L. Margrave, Ed, Academic Press, New York, NY, USA, 1967, p. 94.

[29] J. A. Menendez, A. Arenillas, B. Fidalgo, Y. Fernandez, L. Zubizarreta, E.G. Calvo and J.M. Bermúdez, *Fuel. Process. Technol.*, 2010, **91**, 1.

[30] I. Ahmad, R. C. Dalton and D. E. Clark, *J. Microw. Power Electromagn. Energy,* 1991, **26**, 128.

[31] D. E. Clark, I. Ahmad and R. C. Dalton, *Mater. Sci. Eng. A,* 1991, **144,** 91.

[32] N. A. Hassine, J. G. P. Binner and T. E. Cross, *Int. J. Refractory Metals & Hard Mater.*, 1995, **13**, 353.

[33] J. P. Cheng, D. K. Agrawal, S. Komarneni, M. Mathis and R. Roy, *Mat. Res. Innovat.*, 1997, **1**, 44.

[34] E. Breval, J. P. Cheng, D. K. Agrawal, P. Gigl, M. Dennis, R. Roy and A. J. Papworth, *Mater. Sci. Eng. A,* 2005, **391**, 285.

[35] K. Rodiger, K. Dreyer, T. Gerdes and M. Willert-Porada, *Int. J. Refractory Metals & Hard Mater.*, 1998, **16**, 409.

[36] S. R. Vallance, S. Kingman and D. H. Gregory, *Adv. Mater.*, 2007, **19**, 138.

[37] S. R. Vallance, S. Kingman and D. H. Gregory, *Chem. Commun.*, 2007, **7**, 742.

[38] S. R. Vallance, D. M. Round, C. Ritter, E. J. Cussen, S. Kingman and D. H. Gregory, *Adv. Mater.*, 2009, **21**, 4502.

[39] P.D. Ramesh, B. Vaidhyanathan, M. Ganguli and K. J. Rao, *J. Mater. Res.*, 1994, **9**, 3025.

[40] J. Peng, J. Binner and S. Bradshaw, *J. Mater. Synth. Proces.*, 2001, **9**, 6.

[41] L.N. Satapathy, P.D. Radamesh, D. Agrawal and R. Roy, *Mater. Res. Bull.,* 2005, **40**, 1871.

[42] B. Lu, J.X. Liu, H.W. Zhu and X.H. Jiao, *Mat. Sci. For.*, 2007, **561-565**, 1413.

[43] K. Othmer, *Kirk-Othmer Encyclopedia of chemical technology*, John Wiley&Sons, 5th Ed., 16, 2006, 509-37.

[44] E. T. Thostenson and T.-W. Chou, *Compos. Part A*, 1999, **30**, 1055.

[45] R. Meredith, *Engineers' Handbook of Industrial microwave heating*, The Institution of Electrical Engineers, 1998, Chap.2, 19-52.

[46] K. J. Rao, B. Vaidhyanathan, M. Ganguli and P. A. Ramakrishnan, *Chem. Mater.*, 1999, **11**, 882.

[47] A. R. v. Hippel, *Dielectrics and waves*; MIT Press: Cambridge, Mass, 1954.

[48] W. H. Sutton, *Microwave Processing of Materials III*; San Francisco, California; USA; 27 Apr.-1 May 1992, 3.

[49] L. Pauling, *Nature of the chemical bond*, Cornell University Press, Ithaca, 1950.

[50] K. Othmer, *Kirk-Othmer Encyclopedia of chemical technology*, John Wiley&Sons, 5th Ed., 22, 2007, 524.

[51] J. W. Mellor, *A comprehensive treatise on inorganic and theoretical chemistry*, 5, Longmans, Green and Co., London, 1924, 883-4.

[52] J. L. Smialek and N. S. Jacobson, *J. Am. Ceram. Soc.*, 1986, **69**, 741.

[53] W. Yang, H. Araki, C. Tang, S. Thaveethavorn, A. Kohyama, H. Suzuki and T. Noda, *Adv. Mat.*, 2005, **17**, 1519.

[54] S. G. Sundaresan, A. V. Davydov, M. D. Vaudin, I. Levin, J.E. Maslar, Y.-L. Tian and M. V. Rao, *Chem. Mater.*, 2007, **19**, 5531.

[55] H. Morkoc, S. Strite, G. B. Gao, M. E. Lin, B. Sverdlov and M. Burns, *J. Appl. Phys.,* 1994, **76**, 1363.

[56] C. Virojanadara and L. I. Johansson, *J. Phys.: Condens. Matter.*, 2004, **16**, S1783.

[57] B. Bhushan (Ed.), *Springer Handbook of Nanotechnology*, Springer-Verlag, Chapt.7, 212

[58] H. Matsunami, M. Ikeda, A. Suzuki and T. Tanaka, *IEEE T. Electron Dev.*, 1977, **ED-24**, 7.

[59] A. R. Verna, P. Krishna, *Polymorphism and Polytypism in crystals*, Wiley & Sons, 1966, 81.

[60] H. Baumhauer, *Z. Krist.*, 1912, **50**, 33-9;

[61] A. R. Verna, P. Krishna, *Polymorphism and Polytypism in crystals*, Wiley & Sons, 1966, Chapter 1.

[62] S. Nakashima, H. Harima, T. Tomita and T. Suemoto, *Phys. Rev. B*, 2000, **62**, 24.

[63] P. Krishna and D. Pandey, International Union of Crystallography Commission on Crystallographic Teaching, Pamphlet 5 Close-packed structures by, International Union of Crystallography, University College Cardiff Press, Cardiff, Wales.

[64] Y. Chiang, D. Birnie III and W. Kingery, *Physical Ceramics: Principles for Ceramics Science and Engineering*, John Wiley & Sons, 1997, 30-31.

[65] P. Melinon, B. Masenelli, F. Tournus and A. Perez, *Nature Mater.*, 2007, **6**, 479.

[66] A. W. Hull, *Phys. Rev.*, 1919, **13**, 292.

[67] A. W. Hull, *Phys. Rev.*, 1920, **15**, 545.

[68] L. S. Ramsdell, *Am. Mineralogist*, 1947, **32**, 64.

[69] W. J. Choyke and G. Pensl, *MRS Bull.*, 1997, **22**, 25.

[70] R. I. Stace and G. A. Slack, *J. Chem. Phys.*, 1959, **30**, 1551.

[71] W. F. Knippenberg, *Philips Research Reports*, 1963, **18**, 161.

[72] R. W. Olesinski and G.J. Abbaschian, *Bull. Alloy Phase Diagrams*, 1984, 5, 486.

[73] A. R. Verna and P. Krishna, *Polymorphism and Polytypism in crystals*, Wiley & Sons, 1966, Chapter 4, 62.

[74] J. R. O'Connor and J. Smiltens, *Silicon carbide, a high temperature semiconductor*, Pergamon Press, Oxford, 1960.

[75] A. Taylor and D. S. Laidler, *Br. J. Appl. Phys.*, 1950, **1**, 174.

[76] H. N. Jr. Baumann, *J. Electrochem. Soc.*, 1952, **99**, 109.

[77] A. R. Verna and P. Krishna, *Polymorphism and Polytypism in crystals*, Wiley & Sons, 1966, 81.

[78] E. G. Acheson, *J. Franklin Inst.*, 1893, **136**, 279.

[79] E. G. Acheson, *Production of Artificial Crystalline Carbonaceous Materials*, Patent 492767. 28 Feb. 1893.

[80] G. S. Gupta, P. V. Kumar, V. R. Rudolph and M. Gupta, *Metall. Trans. A,* 2001, **32**, 1301.

[81] A. R. Verna, P. Krishna, *Polymorphism and Polytypism in crystals*, Wiley & Sons, 1966, Chapter 5.

[82] R. Koc and S. V. Cattamanchi, *J. Mater. Sci.*, 1998, **33**, 2537.

[83] E. G. Acheson, *Electric furnace*, Patent 560291. 19 May. 1896.

[84] G. Roewer, U. Herzog, K. Trommer, E. Müller and S. Frühauf, *High Performance Non-Oxide Ceramics I, Structure & Bonding,* 2002, **101**, 59.

[85] V. M. Kevorkijan, M. Komac and D.Kolar, *J. Mater. Sci.*, 1992, **27**, 2705.

[86] H.-P. Martin, R. Ecke and E. Müller, *J. Eur. Ceram. Soc.*, 1998, **18**, 1737.

[87] C. Vix-Guterl, B. McEnaney and P. Ehrburger, *J. Eur. Ceram. Soc.*, 1999, **19**, 427.

[88] C. H. Liang, G. W. Meng, L. D. Zhang, Y. C. Wu and Z. Cui, *Chem. Phys. Lett.*, 2000, **329**, 323.

[89] G. A. Danko, R. Silberglitt, P. Colombo, E. Pippel and J.Woltersdorf, *J. Am. Ceram. Soc.*, 2000, **87**, 1617.

[90] S. Yajima, K. Okamura and J. Hayashi, *Chem. Letters*, 1975, 1209.

[91] P. Colombo, A. Martucci, O. Fogato and P. Villoresi, *J. Am. Ceram. Soc.*, 2001, **84**, 224.

[92] J.-H. Eom, Y.-W. Kim, I.-H. Song and H.-D. Kim, *J. Eur. Ceram. Soc.*, 2008, **28**, 1029.

[93] R. V. Krishnarao, Y. R. Mahajan and T. J. Kumar, *J. Eur. Ceram. Soc.*, 1998, **18**, 147.

[94] G. Xingzhong, Z. Lingjie, Y. Liqing, Y. Hui and Z. Lin, *Mater. Lett.*, 2010, **64**, 331.

[95] X. Tao, Y. Li, J. Du, Y. Xia, Y. Yang, H. Huang, Y. Gan, W. Zhang and X. Li, *J. Mater. Chem.*, 2011, **21**, 9095.

[96] J. Locs, L. Berzina-Cimdina, A. Zhurinsh and D. Loca, *J. Eur. Ceram. Soc.*, 2009, **29**, 1513.

[97] J. Qian, J. Wang and Z. Jin, *Mater. Sci. Eng. A*, 2004, **371**, 229.

[98] J.-M. Qian, J.-P. Wang, G.-J. Qiao and Z.-H. Jin, *J. Eur. Ceram. Soc.*, 2004, **24**, 3251.

[99] A. Herzog, R. Klingner, U. Vogt and T. Graule, *J. Am. Ceram. Soc.*, 2004, **87**, 784.

[100] H. Sieber, C. Hoffmann, A. Kaindl and P. Greil, *Adv. Eng. Mater.*, 2000, **2**, 105.

[101] S. Galvagno, S. Portofino, G. Casciaro, S. Casu, L. D'Aquino, M. Martino, A. Russo and G. Bezzi, *J. Mater. Sci.*, 2007, **42**, 6878.

[102] N. A. Likhomanova and V. F. Kutukov, *Powder. Metall. Met. Ceram.*, **18**, 116.

[103] A.-M. Alexander and J. S. J. Hargreaves, *Chem. Soc. Rev.*, 2010, **39**, 4388.

[104] M. J. Ledoux and C. Pham-Huuet, *Cattech,* 2001, **5**, 226.

[105] J.-H. Eom, Y.-W. Kim, I.-H. Song and H.-D. Kim, *J. Eur. Ceram. Soc.*, 2008, **28**, 1029.

[106] N. W.Thibault, *Amer. Mineral.*, 1944, **29**, 249.

[107] N. W.Thibault, *Amer. Mineral.*, 1944, **29**, 327.

[108] P. A. Ivanov and V. E. Chelnokov, *Semicond. Sci. Technol.*, 1992, **7**, 863.

[109] S. G. Sundaresan, A. V. Davydov, M. D. Vaudin, I. Levin, J. E. Maslar, Y.-L. Tian and M. V. Rao, *Chem. Mater.*, 2007, **19**, 5531.

[110] G. Xi, Y. He and C. Wang, *Chem. Eur. J.*, 2010, **16**, 5184.

[111] L. Wang, H. Wada and L. F. Allard, *J. Mater. Res.*, 1992, **7**, 148.

[112] W. Yang, H. Araki, C. Tang, S. Thaveethavorn, A. Kohyama, H. Suzuki and T. Noda, *Adv. Mater.*, 2005, **17**, 1519.

2 Experimental Theory and Methods

2.1 Microwave radiation and instrumentation

Microwaves belong to the portion of the electromagnetic spectrum between radiowave frequencies and infrared frequencies. Their frequencies lie in the range of 0.3 - 300 GHz and wavelengths in a range of 1 mm - 1 m (Figure 2-1).

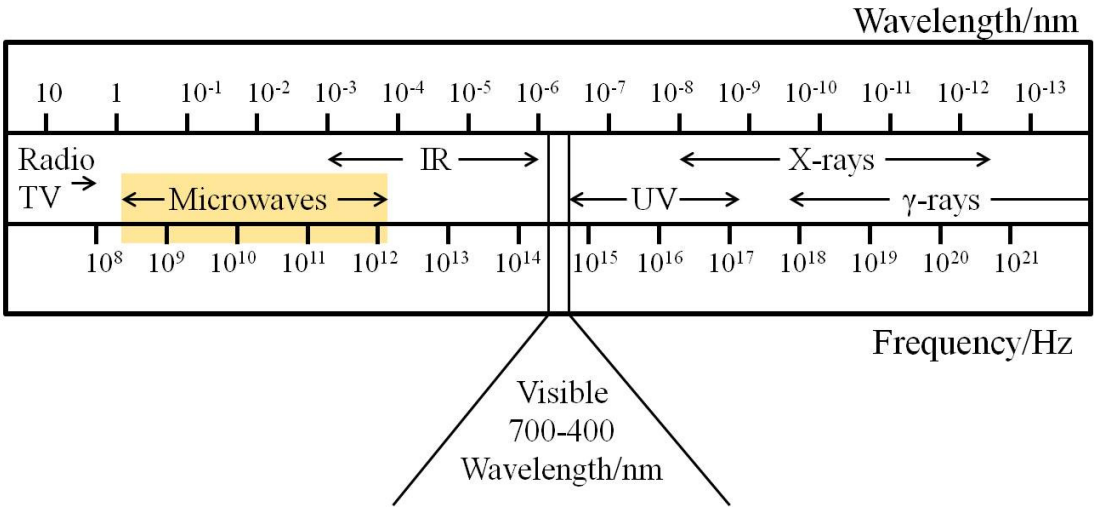

Figure 2-1 The electromagnetic spectrum.

Since the electrical energy involved is the same as that used for services such as broadcasting, television, radar and satellite communications; great care has been used to avoid interference between them. A large part of the microwave spectrum is used for communication purposes and only narrow frequency windows centred at 900 MHz and 2450 MHz are allowed for microwave heating purposes. The main difference is that while the purpose in communications is to radiate power into space, in microwave processing it must be contained within the sample treated.

Microwaves are electromagnetic waves, comprising of an electric and magnetic portion which propagate perpendicular to each other (Figure 2-2). Microwave heating is very rapid as the material is heated by energy conversion rather than by energy transfer, like in conventional heating and almost 100 % of the electromagnetic energy converts into heat (see Chapter 1, section 1.3.1). How well a material will be heated under microwave irradiation is a function of the material being processed.[1]

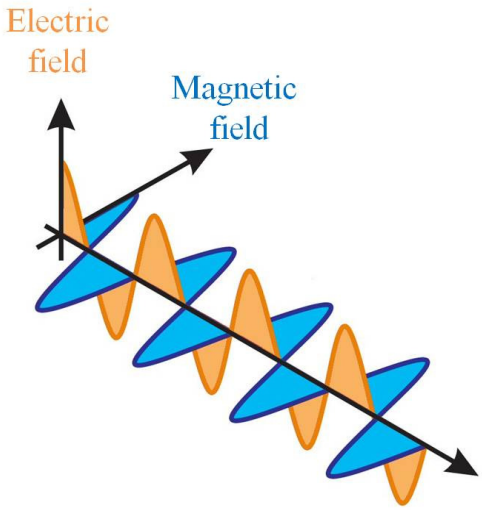

Figure 2-2 Electromagnetic wave components from [2].

A microwave system typically consists of a generator to produce the microwaves, a waveguide to transport the microwaves, an applicator (usually a cavity) to manipulate the microwave field for a specific purpose and a control system (tuning, temperature, power, etc.).[3] Depending on their interaction with microwaves (see Chapter 1, section 1.3.1), different materials are used for different equipment parts (Figure 2-3).[4] Microwave reflectors, mostly bulk metals and alloys, are used in making waveguides and the applicator. Microwave transmitters, such as fused quartz, several glasses and ceramics (not containing transition elements), Teflon, etc., are transparent to microwaves (they are not polar and have high values of DC resistivity); therefore they are used for making containers for chemical reactions.[4]

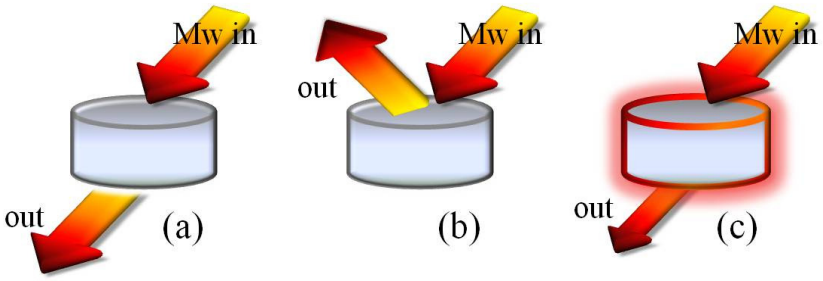

Figure 2-3 Materials' interaction with microwaves: (a) transparent, (b) reflector and (c) absorber.

Magnetrons are the most commonly used source of microwave radiation; they enable the high powers and frequencies required to produce microwaves. In a magnetron (Figure 2-4), the circular anode is concentric and surrounds the cathode. The potential difference between the two electrodes is very high (2 - 20 kV)[5] and produces a strong electromagnetic

field. The cylindrical heated cathode emits electrons which are accelerated radially toward the anode by the electric field. An external magnet at the top and bottom of this assembly is used to create a magnetic field orthogonal to the electric field that causes the electrons to spiral in a circular path rather than moving directly to the anode. As electrons pass the resonant cavities on the anode, the cavities set up oscillations in the electron cloud and the frequency of the oscillations depends on the size of the cavities. Electrons bunch into groups and a portion of this electromagnetic field is extracted and channelled into a waveguide to the cavity.

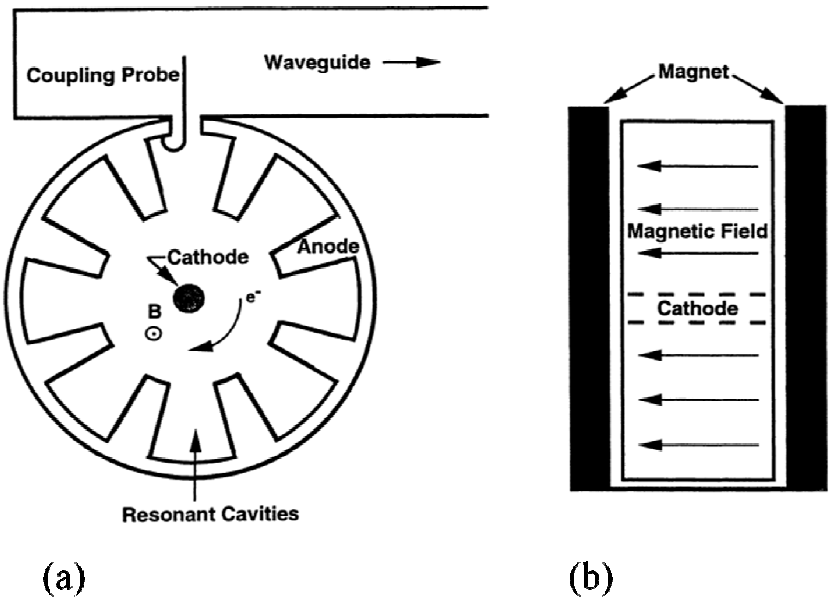

Figure 2-4 Schematic diagram of a magnetron: (a) top view, (b) side view.[3]

Commonly, two methods are applied to adjust the average power output of magnetron sources. The output power of the magnetron can be controlled by either adjusting the period of operation or adjusting the cathode current or magnetic field strength. In domestic microwave ovens, the magnetron always operates at full power. The average power is reduced by simply cycling the current on and off for segments of time, hence the power is time-proportionate. In industrial microwave generators continuous, variable power is provided. In this case, the output power of the magnetron tube can be changed by varying the current amplitude of the cathode or by varying the intensity of the magnetic field. Industrial-scale magnetrons measure and display both the power generated (forward power) and the amount of microwave energy reflected by the system components and/or sample back to the magnetron (reflected power). They also comprise a sink for reflected power and a water-cooled jacket to prevent damage to the magnetron by high reflected

power (if the chamber contains materials that are weakly absorbing or reflect microwave radiation).

Microwaves are transported from the magnetron to the target (in the applicator, or microwave cavity) via so-called waveguides. In low power systems, such as domestic microwave ovens, the transmission lines are often coaxial cables, similar to cables used in televisions. At high frequencies and output power, waveguides are often the transmission line chosen in microwave systems to reduce losses that would occur in coaxial cables. Waveguides are typically thin-walled rectangular metal conduits specifically designed so that a specific pattern of electromagnetic radiation, also called mode of microwaves, is propagated. The waveguides transport the microwaves to the cavity, which is designed to heat the material most efficiently and uniformly.

Two modes of microwave propagation are possible in waveguides: transverse electric (TE) and transverse magnetic (TM). For the TE mode, used in the studies described in this thesis, the electric intensity in the direction of propagation is zero and the most common TE waveguide configuration is the TE_{10} mode (the capital letters specify the mode of propagation and the subscript indicates the number of maxima and minima of the electromagnetic field in a waveguide).[3] The size of the waveguide determines the mode of microwaves that are propagated, so the optimum size for a specific frequency band is a compromise of minimising power loss and consequent heating, requiring a large cross-section size and avoiding possible excitation of higher-order modes.[6] An international standard of waveguide sizes exists, which specifies the optimum waveguide size for operation at specified frequencies throughout the microwave spectrum. All these waveguides have a 2:1 aspect ratio, which conveniently satisfies the above compromise criteria.[6]

Waveguides usually exist in flanged sections and metal-to-metal joints are used to prevent microwave leakage. The choice of materials is mainly a compromise between high conductivity (to minimise losses), corrosion resistance, temperature resistance and ease of manufacture. Aluminium is relatively low cost and has high electrical and thermal conductivity; therefore it is widely used for waveguides transmitting high power. Most alloys have high conductivity and the choice is determined by mechanical issues. Stainless steel is not used for power transmission because it has a low electrical conductivity and is usually responsible for hot spots and wasted power, but can be employed occasionally in short sections for use in high temperature ovens where aluminium would distort. Although

it can be allowed to run hotter, the power-handling capability of stainless steel for the same surface temperature is only about 25 % that of aluminium.[6]

The power transmitted through waveguides is a balance of two components: power transmitted forward towards the sample and power reflected back to the generator. Even a well designed system of waveguide and applicator will reflect some microwaves. A stub tuner is a component that reduces microwave reflection by creating destructive interference. The stubs are brass threaded bolts mounted in a flanged waveguide section. A stub tuner is widely used at low power and comprises a set of manually adjustable screws set in a thick block forming the broad face of the waveguide, allocated along the longitudinal centre line. Simply by setting the screws for minimum net reflected power from the load/tuner combination, it is possible to generate a reflection of any amplitude and phase.[7]

The final fundamental component of the microwave transmission system is the applicator (or cavity). Its function is to send the microwaves efficiently into the heating chamber in the mode that supplies the desired uniform heating.[8] The applicator is mounted inside the heating chamber and one design used for a long cylindrical heating chamber utilizes numerous slots along the length of the applicator. The most common types of applicators used in materials processing are multimode (MMC) and singlemode cavities (SMC) systems. Travelling wave applicators are also employed, but their use is mainly for continuous flow systems which are not applicable to the work discussed in this thesis.

MMC applicators are capable of sustaining a number of high order modes at the same time (Figure 2-5). The various modes result in nonuniformity inside the cavity, where regions of high and low electric fields are present. This causes disadvantages in using domestic microwave ovens (DMOs) with multimode cavities for synthesis and processing including unpredictable mode patterns, poor reproducibility in the synthetic results and the incapability to modulate the power output, which is simply time-averaged as already mentioned. However, multimode cavities have advantages in that they are cheap and readily accessible. The design of multi-mode applicators is often based on trial and error, experience and intuition.[9] The presence of different modes results in multiple hot spots within the microwave cavity and the number of these possible resonant modes increases with the size of the microwave cavity. For cooking, domestic microwave ovens (usually operating at 2.45 GHz) use turntables that rotate during operation, so that the food passes through areas of high and low power and is therefore subject to time-averaged, uniform

heating. Another technique for improving field uniformity is to use mode stirrers. These are reflectors which resemble fans and rotate within the cavity near the waveguide input. These mode stirrers reflect waves off the irregularly shaped blades and constantly redistribute the magnetic field; creating time-averaged uniformity in a similar way to turntables.[9]

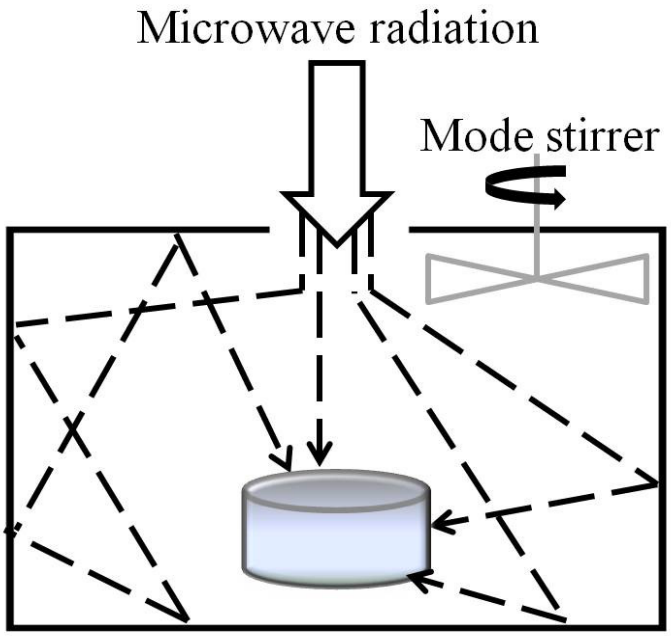

Figure 2-5 Scheme of a MMC with sample.

The design of single mode applicators is made to support only one resonant mode. Consequently, the size of single mode applicators is of the order of approximately one wavelength and to maintain the resonant mode, these cavities require a microwave source with little variation in the frequency output.[9] Areas of high and low electromagnetic field are present, and even though single mode applicators have a nonuniform electromagnetic field distribution like multimode cavities, their configurations are predictable using computational methods. In general, single mode cavities have one "hot spot" where the microwave field strength is high. The main advantage of a single mode cavity is that through proper design, the microwave field can be focused at a given location.[9] Also, precise knowledge of the electromagnetic field distribution enables materials to be placed in the position of highest field strength for optimum coupling. Therefore, these cavities have been used for laboratory-scale studies, while multimode cavities are typically more versatile for batch operations and processing of large, complicated shaped objects because of less stringent spatial requirements.[3]

Single mode cavities consist of a metallic cage in which a microwave signal of the correct electromagnetic field polarization will undergo multiple reflections. The superposition of the reflected and incident waves gives rise to a standing wave pattern that is very well defined in space. Since the microwave power density (equation (1-4) in Chapter 1) is proportional to the electric field strength inside the material squared, such cavities offer extremely rapid heating rates and present the opportunity to heat materials transparent to microwaves in ordinary multimode cavities. Single mode cavities have been available to use in this project thanks to a standing collaboration with Prof. Sam Kingman at the University of Nottingham. Two different single mode cavity reactors were used, both operating at a microwave frequency of 2.45 GHz. It has been possible to position the sample accurately in the electric field within such cavities and regulate parameters such as the power applied, which has enabled a degree of control over the process.

One of the SMC reactors used was a Sairem 3 -15 kW GMP 150SM microwave generator, connected through a WR430 waveguide to an automatic E-h tuner for impedance matching purposes. The tuner was connected to an 82 mm internal diameter TE_{10n} single mode cavity (Figure 2-6). The waveguide was terminated by a short circuit tuner.

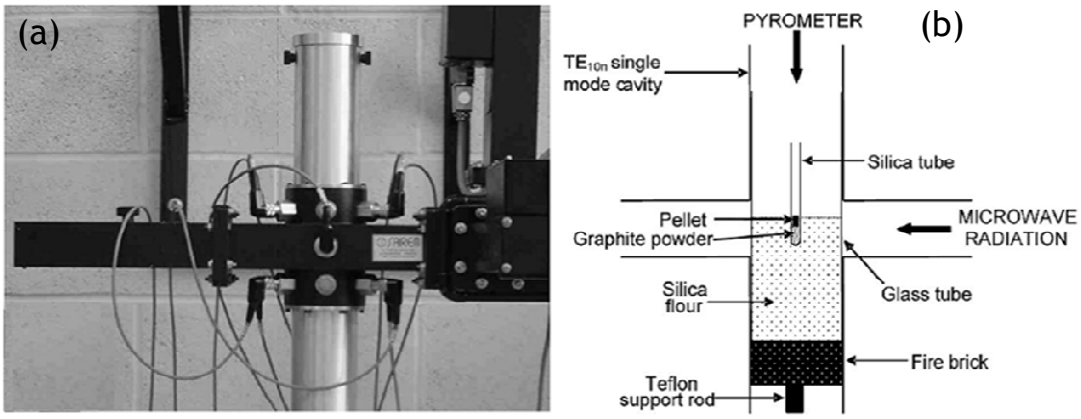

Figure 2-6 Photographic (a) and schematic (b) representation of the 3 – 15 kW applicator SMC.[10]

The other SMC reactor used in this thesis work was based on a 0 - 2 kW microwave generator produced by Sairem and operating at a 2.45 GHz frequency. This system was also equipped with a s-team Homer autotuner. The autotuner is of particular relevance because it allowed the best heating profile without manually using a 3 stub tuner to maximise the absorbed power (Figure 2-7).

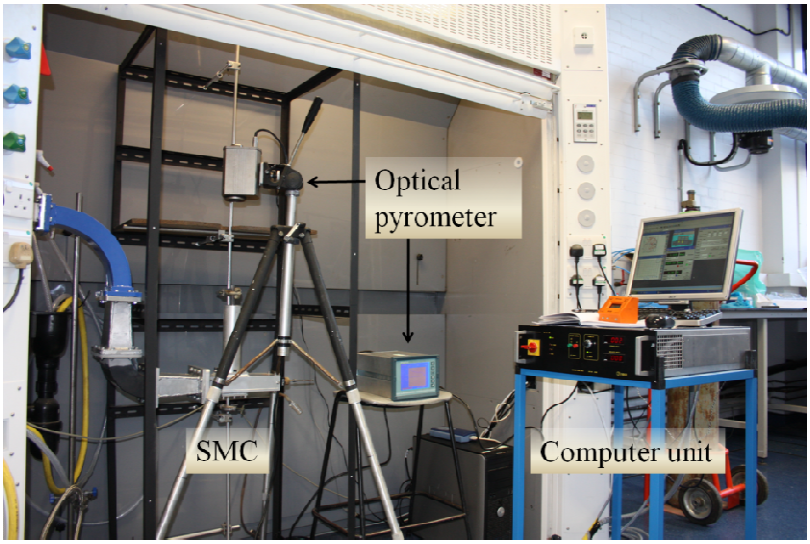

Figure 2-7 Photographic representation of 0 – 2 kW SMC.

Measuring temperatures is another complicated issue in microwave processing.[11,12] Thermocouples are the most simple and cost effective method to measure temperatures. A thermocouple directly reads the temperature when touching the sample. The need for thermocouples to make contact to the sample, often make them act as a heat sink, causing errors or uncertainties in the measurements. More importantly, being an electric conductor, it is probable that the thermocouple probe will change the local electromagnetic field pattern and therefore heat pattern in the microwave cavity. Additionally, when irradiated with microwaves thermocouples normally act as antennae or "self-heat", causing errors or uncertainties in the temperature measurement. Infrared temperature sensors (optical pyrometers) are now commonly used in microwave processing. All materials give off infrared energy depending on their temperature and an infrared sensor consists of a lens to focus this infrared (IR) energy to a detector. The detector then converts the energy to an electrical signal that can be displayed in units of temperature. The advantage of infrared temperature sensors is that they employ a non-contact method to read temperature, so they do not need to be located inside the cavity. Important factors must be taken into account in order to read the temperature accurately. These include the field and angle of view (target size and distance), the type of surface being measured (emissivity considerations) and the temperature range under consideration. To obtain an accurate temperature reading, the target being measured should completely fill the field of view of the instrument. Since the infrared device determines the average temperature of all surfaces within the field of view, it tends to average local hot and cool spots. Emissivity is defined as the ratio of energy radiated by an object at a given temperature to the energy emitted by a perfect radiator, or black body, at the same temperature. The emissivity of a black body is 1.0. All values of

emissivity fall between 0.0 and 1.0. If the emissivity of the sample measured is different from that which is calibrated in the sensor, an error can occur. For most applications a factory setting is usually sufficient. These infrared temperature sensors tend to have a limited temperature range that they can sense, making them limited in the reaction temperatures they can measure.

It is possible to estimate the energy absorbed by the sample irradiated with microwaves using water. In fact, the energy absorbed by water (Q) can be quantified by multiplying the mass of water used by the temperature change (ΔT) and the specific heat of water (C):

$$Q = mass * \Delta T * C$$

The temperature change is proportional to the energy absorbed; therefore to compare the energy absorbed by water when using either a MMC or a SMC (applied power of 800 W in both cases), the temperature vs the time of irradiation profile was reported using a fixed amount of water. The set up used in the thesis work (see following section) has been employed, using a silica tube filled with 10 ml of distilled water. In the case of the MMC test, a thermocouple was used to measure the temperature difference before and after the microwave irradiation (Figure 2-8, squares); while for the SMC test, a fibre optic recorded continuously the temperature signal (Figure 2-8, bold line).

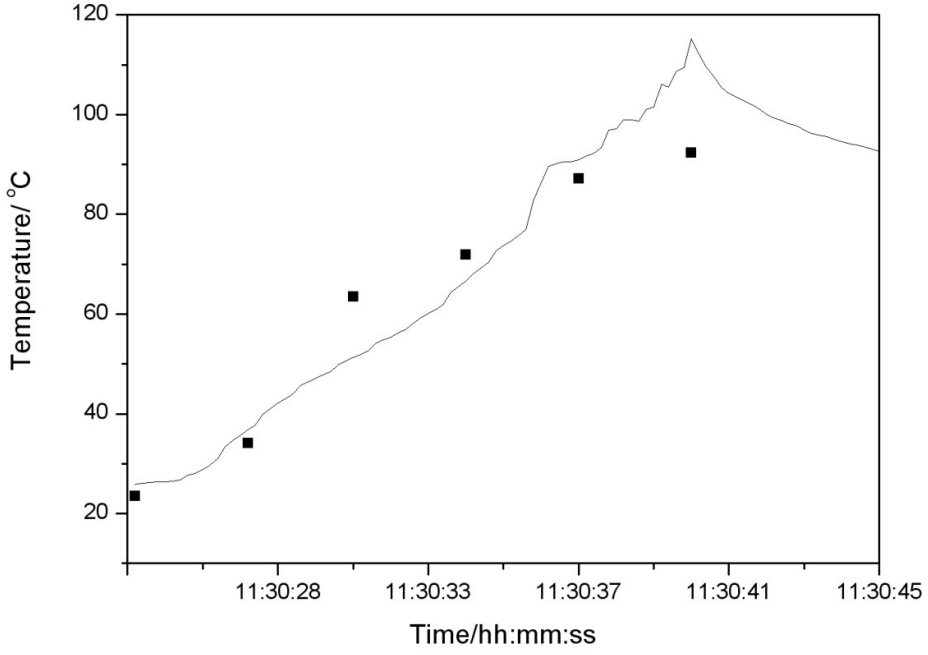

Figure 2-8 Temperature profile of 10 ml of water in a MMC (squares) and SMC (bold line).

From the graph (Figure 2-8), it is possible to note the profile temperature when using a SMC is steeper, meaning more energy is absorbed by water using a SMC and the boiling temperature is reached in shorter times.

Microwaves are not sufficiently energetic to be classified as ionizing radiation and therefore have not been shown to cause cancer.[13] Exposure to microwaves caused localized heating of the tissue exposed. Therefore, any industrial use of microwave must take precautions to prevent microwave leakage and it is important to verify that the system is microwave tight during operation.

2.2 Synthesis and Processing

Fast synthesis of mainly silicon carbide constituted the majority of this thesis. Although in principle the binary carbides are simple to synthesise using conventional heating, using a microwave system setup proved to be a challenge. Partly this was due to the relative lack of current knowledge about microwave heating in the solid state as well as the need to build on the understanding of the heating mechanism.

The synthesis of silicon carbide was attempted from both the elemental powders, the oxide and in further studies monoliths of polymer-coated silica aerogels were used as precursors. In the case of the solid state reaction starting from powders, starting materials were of a high purity and underwent X-ray diffraction analysis prior to their initial use to check the purity and a stoichiometric amount of starting materials was used each time. Mixtures of powders were ground in a planetary ball mill (Retsch, PM100, ~ 4 g of powders charged in an agate grinding jar with 10 agate balls, 450 rpm for 8 h) to break down powders to the ultimate fineness and make mixtures homogeneous. Since the turning directions of the supporting disc and the jar are opposite, the centrifugal forces alternately are synchronized and opposite and act on the milling balls and powders. In the milling jar, the powders and balls alternatively roll on the inner wall of the jar, and are lifted and then set across the bowl at high speed. Once milled, powders were mixed with distilled water and cold pressed uniaxially using a hydraulic press. Pellets were typically kept under pressure for 10 minutes before being removed. Both the pressed pellets and polymer-coated silica aerogels were embedded in graphite (acting as a microwave susceptor) in an open, 10 mm silica tube (microwave transparent) which was surrounded with low dielectric loss silica flour.

Synthesis was conducted in both multimode and single mode microwave applicators; however development of appropriate experimental configurations required much time and trial and error. For this reason the experimental setup will be reported with more details in the results chapters (Chapters 3, 4 and 5). A summary of the cavities used is presented in the section below.

2.2.1 Synthesis using a multimode microwave cavity (MMC)

Synthesis was conducted in a multimode cavity (MMC) fed with an 800 W magnetron and operating at 2.45 GHz (domestic microwave oven, DMO). No impedance matching device was employed due to the very small sample to cavity volume ratio. All preparations were performed at ambient pressure in air using a quartz tube (12 mm in diameter, 1mm wall thickness) sealed only at one end. After initial preparation of the samples had been completed, the silica (quartz) tube was inserted into ground silica in the centre of a glass beaker (Figure 2-9). The silica flour/beaker was used to provide mechanical support for the quartz tube and to provide thermal insulation for the reaction vessel.

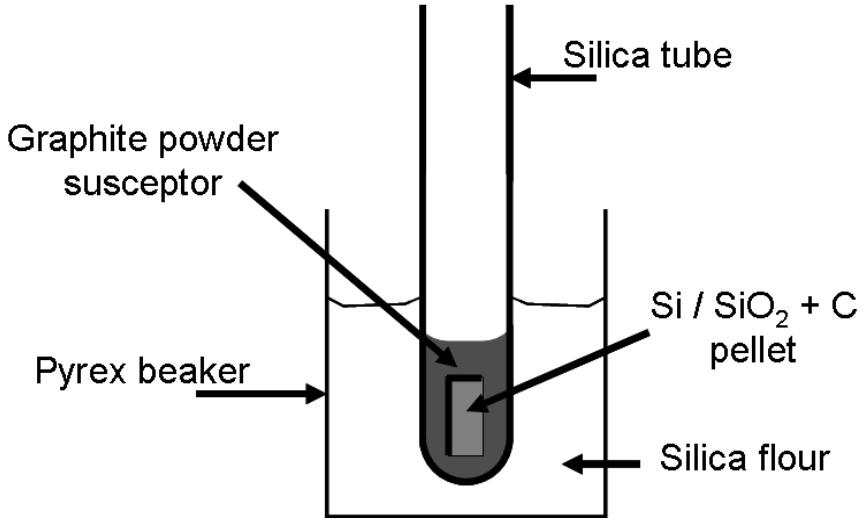

Figure 2-9 Schematic representation of MMC reaction set-up.[14]

The beaker was then placed in the cavity of the DMO in a specific location on top of a heat proof mat (Figure 2-10). This location remained the same to reduce experimental variables; however the modes within a multimode cavity can change position depending on cavity load, temperature and the dielectric properties of the material being heated. A turntable is one method by which the field around the sample could be averaged, but could not be used

here as the high temperature involved in the experiments would melt the plastic components of the turntable mechanism and/or crack the glass turntable.

Figure 2-10 Photo of MMC reaction set-up.

In less than five seconds after the beginning of irradiation, the graphite within the silica tube normally begins to glow indicating that it has been positioned in an appropriate location within the cavity. The overall irradiation time and conditions depend on the sample tested and detail is provided in the following chapters.

2.2.2 Synthesis using a single mode microwave cavity (SMC)

After initial preparation of the samples, as explained above, the quartz tube (12 mm in diameter, 1 mm wall thickness) was loaded into a glass tube, with a fire brick base, containing ground silica. This outer quartz tube is 72 mm in diameter and was designed to fit in the single mode cavity (82 mm diameter) and improve the stability of the experiment. The amount of ground silica added was such to allow embedding of the quartz reaction tube, and ensure efficient heating by positioning the tube within the waveguide. The larger quartz tube was then inserted into the single mode cavity of the 3 - 15 kW Sairem generator and held in place using a (microwave transparent) Teflon rod (Figure 2-11). The setup was similar when employing the 0 – 2 kW Sairem microwave generator, apart from the fact that the SMC was closed at the bottom with an aluminium plate and the glass tube was inserted from the top and held in place by clamping the silica reaction tube.

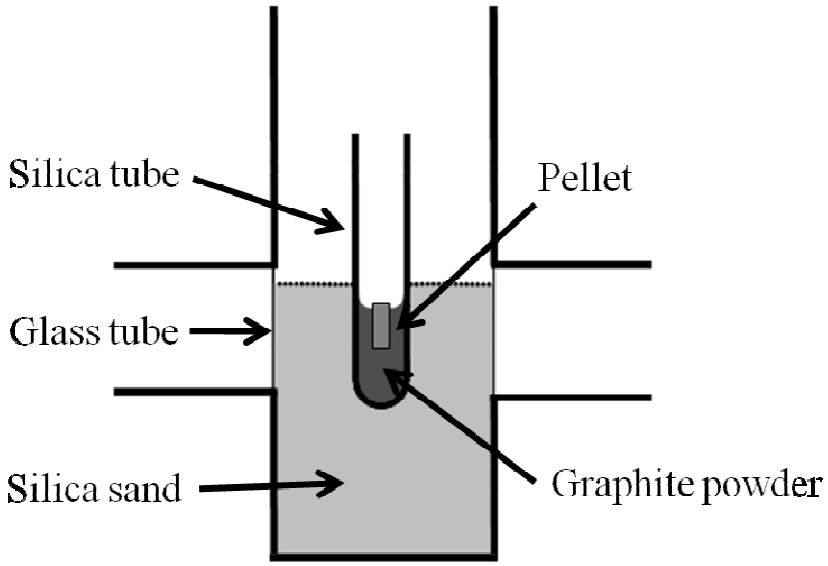

Figure 2-11 Schematic set-up of reaction using a Sairem 0 – 2 kW generator.

Samples were then irradiated with microwaves for a set time and power, varying with each sample. The timing of reactions started once the generator reached the desired power (around 1 second). Reflective power was also monitored on a display to account for any anomalies. When using the Sairem 3 - 15 kW set-up, tuning was necessary prior to a series of experiments. This was done by running a first trial experiment during which the short circuit tuner was adjusted to maximise the energy absorbed by the sample.

An optical pyrometer (LAND System4 Thermometer M1 600/1600 °C; ± 1°C accuracy with a 5 mm diameter spot centred on the sample surface) was supported on top of the cavity by a lighting rig (2 stands and a crossbar manufactured by Manfrotto) and could be manually adjusted. The optical pyrometer was used to monitor the surface temperature of the pellet and provide an estimate of the temperatures involved in the reactions. The temperature measurement during microwave reaction is difficult because emissivity changes as the chemical composition of the pellet changes and emissivity also depends on other factors such as size, shape and granularity of the sample. In addition to the issue of emissivity, due to the mechanisms involved during microwave heating (see Chapter 1, section 1.2) the surface temperature of the pellet measured using the optical pyrometer could be significantly different from the bulk temperature. Furthermore, after reaction at times it was noted the pellet sank in the graphite bed.

2.3 Physical methods to characterise solids

Several techniques have been used to investigate the structures, phase composition and morphology of materials prepared in this thesis. Powder X-ray diffraction (PXD) is suited to elucidating the long-range order of the structure, while Raman spectroscopy is capable of probing both crystalline and amorphous structures in terms of local environment. Scanning electron microscopy (SEM) has been applied to study the morphology of the samples produced and in a few cases transmission electron microscopy (TEM) analysis have been carried to characterize the sample further if nanostructures were present.

2.3.1 Powder X-ray Diffraction

2.3.1.1 Powder X-ray Diffraction theory

Powder X-ray diffraction (PXD) is a rapid and accurate method to identify the crystalline phases present in the sample[15,16,17] and only a relatively small amount of sample is needed to perform the analysis. It is very difficult to grow single crystals of SiC, since it has many polytypes, high melting point and high hardness, hence, powder X-ray diffraction is the technique adopted routinely for characterising the carbide. PXD can also be used to determine atomic positions precisely. Structural models have been refined against diffraction data using the Rietveld method to obtain bond lengths (and bond angles) and accurate phase fractions of sample mixtures and products *ex situ*.

X-ray crystallography generally relies on the fact that the distances between atoms in crystals are of the same order of magnitude as the wavelength of X-rays (1 Å). Hence a crystal acts as a three-dimensional diffraction grating to a beam of X-rays. The resulting diffraction pattern can be interpreted to give an insight into the crystal structure of the sample produced. The unit cell is the fundamental “building block” which constructs a crystal and continuously repeats in all directions, in a perfect regular manner. The common way to describe a crystal is to define the size, shape and symmetry of its unit cell, and the position of the atoms within it. All the possible unit cell shapes that can fill a three-dimensional space are listed in Table 2-1 and are associated with the seven possible crystal systems.

System	Unit cell	Essential symmetry
Triclinic	No special relationships	None
Monoclinic	$a \neq b \neq c$ $\beta \neq \alpha = \gamma = 90°$	2-fold axis or mirror plane (inverse 2-fold axis)
Orthorombic	$a \neq b \neq c$ $\alpha = \beta = \gamma = 90°$	Three orthogonal 2-fold axis or inverse 2-fold axis
Tetragonal	$a = b \neq c$ $\alpha = \beta = \gamma = 90°$	One 4-fold axis or inverse 4-fold axis
Rhombohedral	$a = b = c$ $\alpha = \beta = \gamma \neq 90°$	One 3-fold axis or inverse 3-fold axis
Hexagonal	$a = b \neq c$ $\alpha = \beta = 90°, \gamma = 120°$	One 6-fold axis or inverse 6-fold axis
Cubic	$a = b = c$ $\alpha = \beta = \gamma = 90°$	Three 3-fold axis

Table 2-1 The seven crystal systems.

In three-dimensional space, any repeated pattern, such as the distribution of atoms in a crystal, can be simplified using a lattice of points. This defines completely the repetition characteristics without reference to the details of the repeated motif or the chemistry or bonding within the crystal. In a three-dimensional space, 14 distinctive lattices are possible, called Bravais lattices.[15] Within the unit cell, the collection of symmetry elements constitutes a point group. Only 32 point groups are possible and these constitute 32 crystal classes and all crystals might be assigned to one of them. If we combine the 32 crystal classes with the 14 Bravais lattices, we find 230 three-dimensional space groups.[15] A space group can be also viewed as the combination of the symmetry operations of the point group plus translational symmetry operations. Crystal structures can only adopt 230 distinctive space-filling arrangements, described by a space group and these are all documented in the International Tables for Crystallography.[18]

The periodic arrangement of atoms in a crystal can be seen in numerous planes running in different directions through the lattice points. All of the planes oriented in a certain direction are parallel and separated from each other by a distance *d*, which varies according to the nature of the material. For any crystal, planes exist in a number of different orientations - each with its own specific *d*-spacing. Miller indices are used to refer to the faces and the planes within a crystal. They depend on a particular unit cell and therefore are not uniquely defined. If a line is drawn parallel to the faces such that the intercepts on the unit cell edges are a/h, b/k, c/l; where h, k and l are integers. The integers are referred to as Miller indices.

W. L. Bragg noted that X-ray diffraction behaves like "reflection" from the planes of atoms within the crystal and that only at specific orientations of the crystal with respect to the source and detector are X-rays "reflected" from the planes. Unlike reflection from a mirror where the angle of incidence equals angle of reflection for all angles, the "reflection" in X-ray diffraction only occurs when the conditions for constructive interference are fulfilled.

In a powder X-ray diffractometer, electrons are emitted by an electrically heated filament, usually tungsten, and accelerated by a high potential difference (20 - 50 kV) to strike a water cooled anode. The anode emits sharp and intense X-ray peaks (K_α, K_β) superimposed to a continuous spectrum of "white" X-radiation. K_α and K_β lines (actually unresolved doublets $K_{\alpha1}$, $K_{\alpha2}$, and $K_{\beta1}$ $K_{\beta2}$) have frequencies characteristic of the metal used as an anode. They depend on the difference of energy between the electron ejected from the innermost K shell (n=1) by the bombarding electrons, and the electron from outer shells to fill this vacancy. Electrons descending from the L shell (n=2) give K_α lines and electrons from the M shell (n=3) give the K_β lines. The target metals most commonly used in X-ray crystallography are copper and molybdenum, chosen because their wavelengths are close to the interatomic distances of crystals (K_α lines at 1.5418 Å and 0.7107 Å, respectively). In X-ray diffraction, monochromatic radiation is often more useful, hence the K_β line is filtered out by using a filter made of a thin metal foil of the previous element (Z-1) in the Periodic Table. For example, nickel effectively filters out the K_β line of copper and niobium is used for molybdenum. Otherwise a single crystal, usually graphite, can be used to select a monochromatic beam of X-rays by reflecting the white radiation off a graphitic plane.

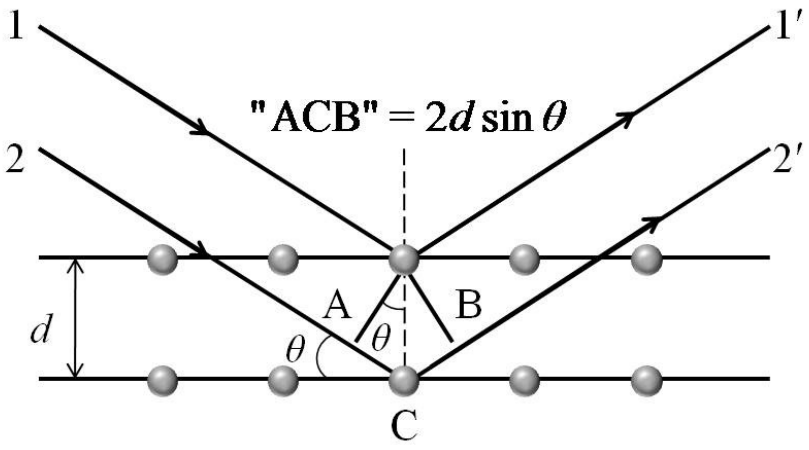

Figure 2-12 Bragg reflection from a set of crystal planes with d_{hkl} spacing.

Figure 2-12 illustrates the Bragg condition for the reflection of X-rays by a crystal. The array of grey points in the diagram represents a section through a crystal and the lines joining the dots mark a set of parallel planes with Miller indices *hkl* and interplanar spacing d_{hkl}. A parallel beam of monochromatic X-rays 1 and 2 is incident to the planes at an angle θ and is scattered giving rays 1', 2'. When parallel X-rays strike a pair of parallel lattice planes, every atom within the planes acts as a scattering centre and emits a secondary wave. All of the secondary waves combine to form a reflected wave. The proportion of the beam that is scattered on the second plane has a path length difference of "ACB" to the proportion of the beam that was scattered at the first plane. For the reflected beams to emerge as a single beam of reasonable intensity, they must arrive in phase with one another. For constructive interference to happen, the path lengths of the interfering beams (in this case "ABC") must differ by a whole multiple of wavelength λ, so the phase difference Δλ is zero or a multiple of the wavelength λ: Δλ=n λ where n=0,1,2,3...

For the definition of sine:

$$\frac{"AC"}{d} = \sin\theta \text{ or } "AC" = d \sin\theta$$

The phase difference "ACB" is twice that, so:

$$"ACB" = 2d \sin\theta$$

And as mentioned, for interference to take place:

$$"ACB" = n\lambda$$

This results in Bragg's Law:

$$n\lambda = 2d_{hkl} \sin\theta \qquad \textbf{(2-1)}$$

The equation relates the d-spacing, d_{hkl}, to the particular Bragg angle, θ at which reflections from these planes are observed. When n=1, the reflections are called first order, when n=2 the reflections are second order and so on. However, the Bragg equation for a second order reflection from a set of planes *hkl* is

$$2\lambda = 2d_{hkl} \sin\theta$$

Which can be rewritten as:

$$\lambda = 2\frac{d_{hkl}}{2} \sin\theta \qquad \textbf{(2-2)}$$

(2-2) represents a first order reflection from a set of planes with interplanar spacing *2h 2k 2l*. Therefore, the second order reflection from *hkl* is indistinguishable from the first order reflection from *2h 2k 2l*, and the Bragg equation can be rewritten simply as

$\lambda = 2d_{hkl} \sin\theta$.

2.3.1.2 Powder X-ray diffraction sample preparation

Samples analysed were prepared by grinding a synthesised pellet using an agate pestle and mortar to ensure random orientation of crystallites.

When using a flat plate, Bragg-Brentano geometry, reflection configuration (see following section), part of the pulverized sample was then spread uniformly over an indented glass sample holder (18mm x 0.8 mm), assuring a flattened upper surface using a glass slide. This is done to prevent displacement errors in the X-ray beam that happen if the sample sits above the surface of the slide.

The sample preparation using a Debye-Scherrer geometry, transmission configuration (see following section) requires that a very small amount of powdered material is sealed into a glass capillary tube of 0.5 or 0.7 mm in diameter. The specimen is aligned on a holder using an external goniometer and then the holder is fixed at the centre of the Debye-Scherrer setup.

2.3.1.3 Powder X-ray diffraction data collection and analysis

In the Bragg-Brentano geometry, the flat plate sample is irradiated using a stationary source and a moving detector to measure the intensity of the diffracted X-rays (Figure 2-13). In particular the sample holder is put on one axis of the diffractometer and tilted by an angle θ while a detector rotates around it on an arm at twice this angle. In this geometry the lattice planes measured are the ones parallel to the sample surface. The X-rays penetrate to a certain depth into the sample, where they are diffracted. The Bragg-Brentano geometry is a type of reflection configuration where the source and detector of X-rays are positioned at the same angle in respect to the sample.

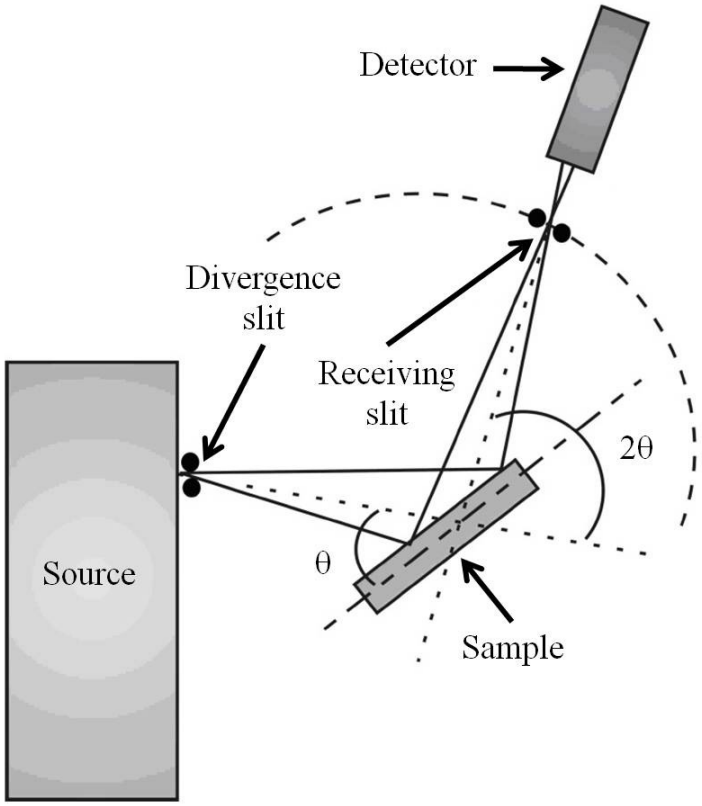

Figure 2-13 Bragg-Brentano geometry.

Some measurements were performed using an X'Pert PRO MPD diffractometer, configured with Cu $K_{\alpha 1}$ radiation (λ = 1.54056 Å) X-ray source and the fast X'Celerator solid-state detector. The standard operating power for the X-ray tube was 40 kV and 40 mA. The X-ray beam was collimated using a 10 mm beam mask, 0.04 rad Soller slits, 1/2° divergence slit and a 1/2° anti-scatter slit on a standard run, in order to prevent both horizontal and vertical divergence of the X-ray beam. Two types of scan were run, a standard 1 hour phase identification scan or a 12 hour overnight scan to have better data that could be used for structural refinement. The standard scan was run between 5° and 85° 2θ, step size of 0.0167° 2θ whereas the overnight scan was run between 10° and 120° 2θ, step size of 0.0167° 2θ and time per step 1120.14 s $step^{-1}$.

The second diffractometer, a Bruker D8 Advance diffractometer, works in a transmission configuration, using a Debye-Scherrer geometry (Figure 2-14).

The Debye-Scherrer configuration is one of the oldest known powder diffraction geometries; it uses a near-parallel incident beam of X-rays with sufficient cross-section to irradiate the whole powder-sample. The powder diffracts the X-rays in accordance with Bragg's law to produce cones of diffracted beams. Arcs of the cones are intercepted by a detector.

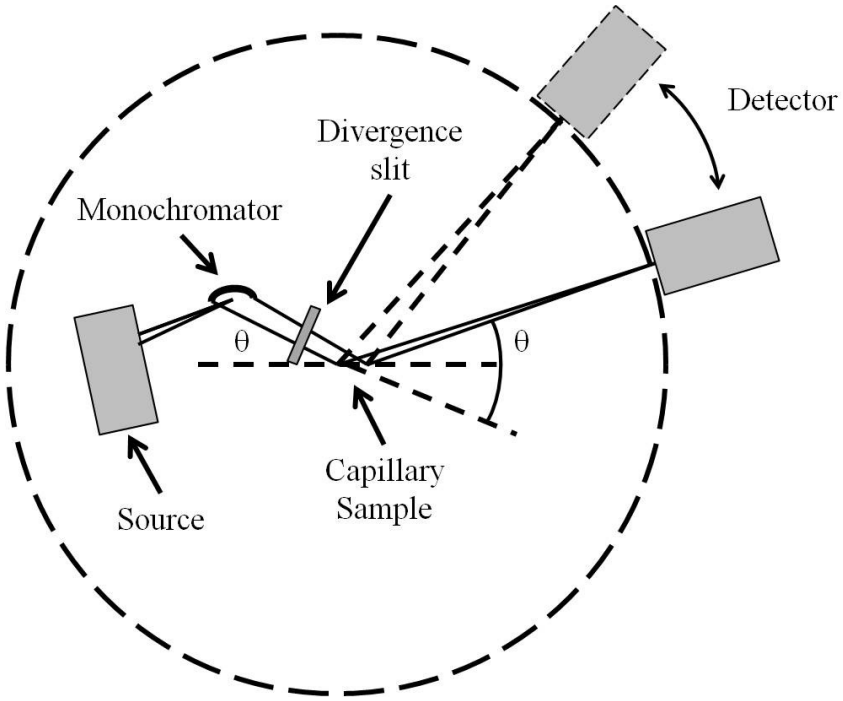

Figure 2-14 Debye-Scherrer geometry.

In this case scans have been carried out using the Bruker D8 Advance diffractometer, configured with a Cu $K_{\alpha 1}$ radiation (λ = 1.54056 Å) X-ray source and VÅNTEC detector.
A divergence slit of 1 mm has been used to collect the scans. The standard scan was run between 5° and 85° 2θ, step size of 0.0167° 2θ for 1 h.
After the scan was complete, the PANalytical program Xpert HighScore Plus was used to search and match unknown reflections using the JCPDS database from ICDD.[19] This is done in order to identify qualitatively any crystalline phase present and check the purity of the sample analysed. The powder diffraction patterns were then plotted as intensity against 2θ using PowderCell 2.3 software[20] and matched against the patterns of known structures downloaded from the Inorganic Crystal Structure Database (ICSD).[21]

2.3.2 Rietveld refinement

One drawback of the PXD method compared to single crystal diffraction is that data are reduced from distinct spots in three dimensions to a one dimensional slice through a diffraction cone. The result is that the diffraction maxima (peaks) in the pattern may overlap preventing proper determination of the structure. The Rietveld method[22,23] has been developed to solve a structure from powder diffraction data. It uses the full information content of an experimental scan to extract detailed crystal structure information and it also

allows phase fractions in multi-phase mixtures to be determined quantitatively. Rietveld analysis uses fundamental analytical profile functions and a least-squares approach to refine a theoretical line profile until it matches the measured profile.[24] Rietveld analysis involves an interpretation of the overall line profile, not only the line position, but also the intensities.

The process of structural refinement starts by taking a good starting model, calculating a powder diffraction profile from it and then comparing it with the measured profile. If the structure to refine is a slight modification of a known structure from a similar crystal system, the latter can be used as trial structure, for instance. Having a good starting model is fundamental because Rietveld analysis is a structure refinement method rather than structure solution one. The trial structure can then be gradually modified and refined by simultaneously changing parameters in the model for structure and for other specimen and instrument effects that modify the calculated diffraction pattern until the best fit with the entire observed powder diffraction pattern is achieved.

In general, the parameters refined fall into two groups. The structural parameters describe the contents of the unit cell and include the atomic temperature factors, co-ordinates and occupancies of each atom. The other group of variables includes the profile parameters like position, shape and full-width-at-half-maximum of each peak. The refinement process is a least squares, best fit method. The quantity minimised during the least squares refinement is the function M.

$$M = \sum_i w_i (y_i^{obs} - y_i^{calc})^2 \qquad \textbf{(2-3)}$$

The sum is across all data points (i) in the profile and the parameters involved are:

- w_i: a weighting factor given by $1/y_i^{obs}$,
- y_i^{obs}: the observed intensity at each step/point i ($2\theta_I$ for PXD), and
- y_i^{calc}: the calculated intensity at each i^{th} step.

The calculated intensities y_i^{calc} are determined from the $|F_K|^2$ values calculated from the structural model, summing the calculated contributions from Bragg reflections within a specified range k with the background, b_i :

$$y_i^{calc} = s\sum_k L_k |F_k|^2 \phi(2\theta_i - 2\theta_k) P_k A + y_{bi} \qquad \textbf{(2-4)}$$

where s is the scale factor, L_k contains Lorentz polarisation and multiplicity factors, ϕ is a reflection profile function, F_k is the structure factor for the k^{th} Bragg reflection, P_k is the preferred orientation function, A is an absorption factor and y_{bi} is the background intensity at i^{th} step.

Looking at Equation **2-4** it can be seen the relationships between the variable parameters and the intensities are not linear. This is why the starting model must be close to the correct one or the non-linear least squares procedure will either diverge or lead to a false minimum instead of the global minimum.

From Equation **2-4** also:

- ϕ, the reflection profile function approximates the effects of both instrumental features and possible specimen features such as aberrations due to absorption, specimen displacement and specimen-caused broadening of the reflection profiles.
- A, the effective absorption factor, differs with instrument geometry. It is usually taken to be constant for the Bragg-Brentano geometry, the most commonly used.
- y_{bi}, the background intensity, can be obtained in different ways: from an operator-supplied table of background intensities; linear interpolation between operator-selected points in the pattern; or a specific background function. When the last of these is used, usually y_{bi} is a cosine Fourier series with a leading constant term[26]:

$$y_{bi} = B_l + \sum_{j=2}^{N} B_j \cos[P * (j-1)] \qquad \textbf{(2-5)}$$

For X-ray diffraction, P is the position of the step in 2θ. Values of B_l and B_j are determined during the least squares refinement.

In Rietveld analysis, scale factors and background parameters are usually the first to be refined as they involve coefficients of ordinary or orthogonal polynomials, that make the problem linear and quick to converge. Accurate determination of the Bragg reflection positions is then accomplished by variation of sample displacement, lattice parameters and the zero-point correction. From this point it is also possible to start refining the peak shape parameters. Subsequently, atom positions are varied to fit the peak intensities and temperature factors can be refined to define thermal motion of the atoms.

The pseudo-Voigt function is normally used to fit the observed peak shapes. It is a linear combination of a Lorentzian and a Gaussian function and is described as:

$$\eta L + (1 - \eta) G \qquad \textbf{(2-6)}$$

where L and G are the Lorentzian and Gaussian contributions to the peak shape and η is the mixing parameter refinable as a linear function of 2θ. The Gaussian (G) and Lorentzian (L) components of the peak shape are represented by the equations:

$$G = \frac{(4\ln 2)^{1/2}}{H_k \sqrt{\pi}} \exp\left(-4\ln 2\left(2\theta_i - 2\theta_k\right)^2 / H_k^2\right) \qquad \textbf{(2-7)}$$

and

$$L = \frac{2}{\pi H_k} 1 \Big/ \left[1 + 4\frac{(2\theta_i - 2\theta_k)^2}{H_k^2}\right] \qquad \textbf{(2-8)}$$

where $2\theta_k$ is the calculated position for the k^{th} Bragg peak corrected for the zero-point and H_k is the full-width-at-half-maximum (FWHM) of the k^{th} Bragg reflection. The full width at half maximum (FWHM), H_k, of a peak has been shown to vary with the scattering angle $2\theta_k$ and is modelled as:[25]

$$H_k^2 = U \tan^2\theta + V \tan\theta + W \qquad \textbf{(2-9)}$$

where U, V and W are the refinable parameters that depend on both instrument and sample. If the instrument contribution can be modelled well through standard samples, peak broadening effects caused by the small particle sizes in the sample can be estimated from this formula. The peak shape can also manifest asymmetry at low scattering angles due to the detector and sample heights and this can be taken into account using a semi-empirical correction factor.

In order to provide an indicator as to whether the refinement is proceeding satisfactorily and ultimately has reached completion, indices, called R-factors, are reported at the end of

each cycle. These reliability factors are $R_{profile}$, $R_{expected}$, $R_{weighted\ profile}$ and R_{Bragg}. The first two are expressed as:

$$R_{profile} = R_p = 100\left[\frac{\sum_i \left| y_i^{obs} - y_i^{calc} \right|}{\sum_i y_i^{obs}}\right] \qquad \textbf{(2-10)}$$

and

$$R_{expected} = R_{exp} = 100\left[\frac{(N-P+C)}{\sum_i \omega_i (y_i^{obs})^2}\right]^{1/2} \qquad \textbf{(2-11)}$$

R_{exp} is defined from the statistics of the refinement and in its expression (Equation **2-11**) N is the number of observations, P the number of refinable parameters and C the number of constraints and ω_i is a weighting factor. From a mathematical point of view, $R_{weighted\ profile}$ (R_{wp}) is the most meaningful of the R-indicators because the numerator is the residual being minimized (Equation **2-3**), making R_{wp} the most appropriate to reflect the progress of the refinement:

$$R_{wp} = 100\left[\frac{\sum_i \omega_i \left[y_i^{obs} - y_i^{calc} \right]^2}{\sum_i \omega_i \left[y_i^{obs} \right]^2}\right]^{1/2} \qquad \textbf{(2-12)}$$

Another useful indicator is the Bragg R factor that measures the agreement between the intensities calculated from the model (I_j^{calc}) and those measured experimentally (I_j^{obs}) over all Bragg reflections (hence summation index *j*). Unlike $R_{profile}$, it depends only on the fit of the structural parameters and not on the profile parameters.

$$R_{Bragg} = R_B = \frac{\sum_j \left| I_j^{obs} - I_j^{calc} \right|}{\left| \sum_j I_j^{obs} \right|} \qquad \textbf{(2-13)}$$

The final measure of the whole fit, minimised during the refinement, is the goodness of fit or chi-squared parameter and is defined as:

$$\chi^2 = \left[\frac{R_{weightedprofile}}{R_{\exp}} \right]^2 \qquad \textbf{(2-14)}$$

Therefore, for a good fit, the $R_{weighted\ profile}$ should approach the statistically expected R factor (R_{exp}).

Graphical criteria of fit can be used as well; the observed and calculated patterns often give immediate clues on the source of the problems one is having while refining. Gross errors in background level, scale factor, peak or lattice parameters, for instance, can be recognized immediately in such plots. Also the goodness of fit can be estimated by examining a difference plot; for a good fit, the difference line between the calculated and observed patterns should be as flat as possible. Structural refinement using the Rietveld method was undertaken with data collected from the majority of the overnight scans, using the General Structure Analysis System (GSAS) and EXPGUI packages.[26,27]

2.3.3 Raman Spectroscopy

Raman spectroscopy is a vibrational spectroscopic technique.[28] Like X-ray diffraction (PXD), Raman spectroscopy is a non-destructive, simple to use and precise method.

When light is scattered from an atom or molecule, most photons are elastically scattered (Rayleigh scattering), such that the scattered photons have the same energy as the incident photons. Raman scattering[29] occurs when light impinges upon a sample and polarizes the electric distribution around the nuclei, deforming the electron cloud with respect to the vibrational coordinate. This creates an unstable state called a “virtual state”, a very short lived distortion of the electron cloud and the photon is quickly re-radiated. When the system relaxes, it returns to a different vibrational state. The difference in energy between the original state and this new state leads to a shift in the emitted photon’s frequency away from the excitation wavelength. This light scattering phenomenon should not be confused with absorption where the molecule is excited to a discrete energy level (for instance, IR absorption is shown in Figure 2-15).

If the final vibrational state of the molecule is more energetic than the initial state, then the emitted photon will be shifted to a lower frequency in order for the total energy of the system to remain balanced and this will be designated as Stokes shift. While in an anti-Stokes shift the final vibrational state is less energetic than the initial state and the emitted photon will be shifted to a higher frequency (Figure 2-15). Since the virtual states are not discrete states (*cf.* IR spectroscopy), but are created when the laser causes polarization in the system analysed, the energy of these states is determined by the frequency of the light source used. Another important thing to consider is that Raman scattering does not require matching of the incident radiation to the energy difference between the ground and excited states.

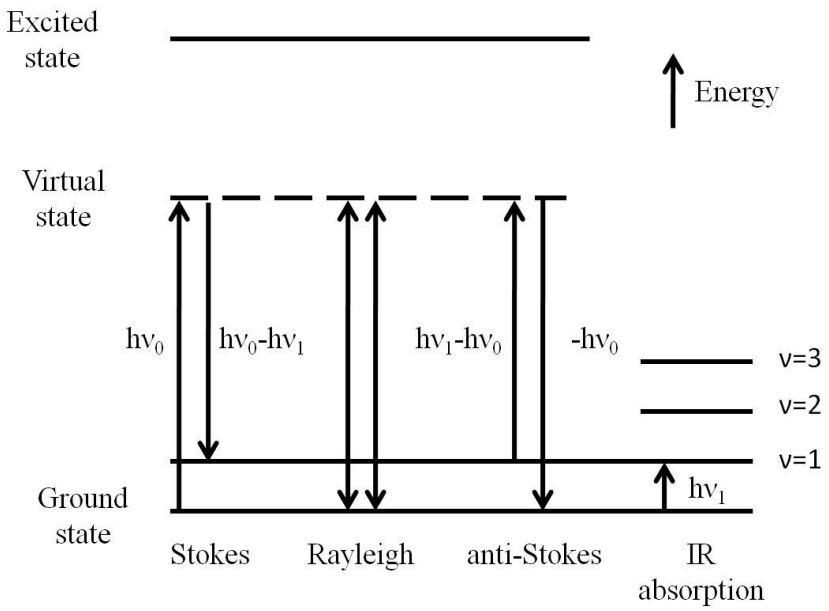

Figure 2-15 Spectroscopic transitions underlying several types of vibrational spectroscopy.

The populations can be determined using the Boltzmann equation, but is clear that at room temperature, the number of molecules expected in another vibrational state than the ground state will be small. Thus, compared to Stokes scattering, anti-Stokes scattering will be weak and will become weaker as the frequency of the vibration increases. Conversely, anti-Stokes scattering will increase relative to Stokes scattering as the temperature increases. Hence the Stokes and anti-Stokes Raman peaks are symmetrically positioned about the Rayleigh peak, but their intensities are very different depending on the population of the various states of the system. The Rayleigh process does not involve any energy change and will be the most intense process. Thus Raman scattering is inherently a weak process. Even though only one in every 10^6–10^8 photons contributes to Raman

scattering,[30] modern Raman spectrometers permit very high power densities to be delivered to very small samples. Issues arise if other processes such as sample degradation and fluorescence can readily occur.[30]

In Raman spectroscopy, the interest is focused on the interaction between radiation (usually characterized by its wavelength (λ)) and the states of the molecule being examined. The units are expressed in wavenumbers (ω), which are linearly related with energy. The relationships between these scales are given below:

$$\lambda = c/\nu \qquad \textbf{(2-15)}$$

$$\nu = \Delta E/h \qquad \textbf{(2-16)}$$

$$\omega = \nu/c = 1/\lambda \qquad \textbf{(2-17)}$$

A Raman spectrum consists of scattered intensity plotted against energy. Strictly speaking, Raman scattering should be expressed as a shift in energy from that of the incident light energy $h\nu_o$ and should be referred to as Δcm^{-1} but it is often expressed for simplicity as cm^{-1}. Also Raman scattering is usually recorded only on the low-energy side to give Stokes scattering.[28]

Typically, a sample is illuminated with a laser beam. Light from the illuminated spot is collected with a lens and sent through a monochromator. Wavelengths close to the laser line, due to elastic Rayleigh scattering, are filtered out while the rest of the collected light is dispersed onto a detector. Given that spontaneous Raman scattering is typically very weak compared to the intense Rayleigh scattered laser light, instrumentation almost universally employs notch or edge filters for laser rejection. On many modern Raman spectrometers, the sample is simply presented to a microscope which is an integral part of the spectrometer. Microscopes can be employed as sampling accessories when using laser sources emitting in the visible region of the spectrum. This means that the scattered Raman radiation can pass efficiently through and be focussed by the glass lenses.

The microscope has many advantages; for example, it is possible to look at extremely small samples and therefore, despite the fact that Raman scattering is weak, to detect very small amounts of material. When using a microscope on small samples, the beam diameter reduces very significantly and is often much smaller than the total size of the sample. The focal point will then determine which part of the sample is being analysed. This means that

to have a reliable analysis of the sample, a number of measurements should be taken across it. Furthermore, using a microscope can discriminate against fluorescence from a sample matrix since only the chosen microscopic feature in the sample is irradiated at high power, particularly when the microscope is set up confocally. The advantages are that coupling visible laser sources to the microscope optics makes the detection system at the sensing points extremely efficient. [31] Figure 2-16 shows a typical arrangement for a microscope.

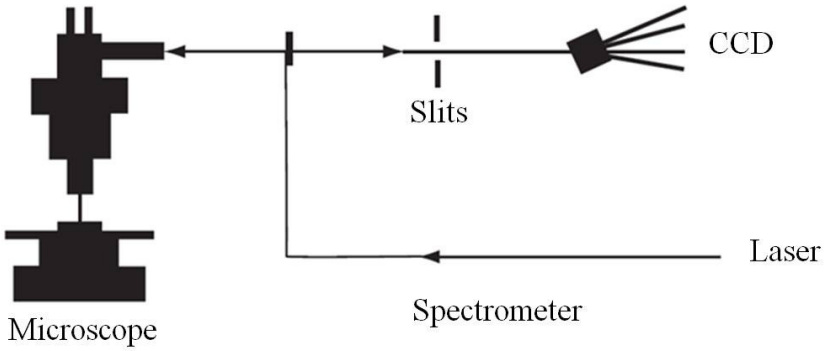

Figure 2-16 Raman spectrometer with microscope, visible laser, notch filter and CCD detector.[30]

In the confocal arrangement, the laser is focussed through a pinhole, which enables only light focussed on the plane containing the sample to be collected efficiently and a plasma filter is employed to remove any other radiation apart from the main exciting line in the laser. The radiation is then arranged to hit a notch filter. These interference filters work well when the beam is perpendicular to the plane of the filter. Hence when coming into contact with the filter, the laser radiation is entirely reflected into the microscope, while the scattered radiation gets transmitted, because it is at the ideal angle for the filter. Once transmitted, the scattered radiation then passes into the monochromator and onto the CCD detector.

Raman spectroscopy requires the minimum of sample handling and preparation. For the analysis of samples described in this thesis, a small amount of ground powders from reacted pellets have been compacted inside a small O-ring (0.5 cm in diameter) sealed on to a glass slide. The glass slide was then put under the microscope lens in the Raman spectrometer and powders were examined directly by Raman spectroscopy at room temperature. (The glass slide did not interfere with the analysis since glass scatters weakly in Raman spectroscopy.[32]) Raman spectra were measured using a Horiba LabRAM HR confocal microscope system with a 532 nm green laser (Laser Quantum Ventus 532, 150

mW). A hole aperture of 50 µm, 600 gr mm^{-1} grating and a Synapse CCD detector were used for the experiment.

Raman spectroscopy is commonly used in materials chemistry, since Raman-active modes can be found for crystals that show symmetry by using the appropriate character table for that symmetry group and this provides a fingerprint to indentify the sample. When radiation interacts with the material, it induces vibrations through the whole lattice and these can form along the direction of propagation of the radiation (longitudinal or L modes) or at right angles to it (transverse or T modes). Each of these modes consist of a very large number of vibrations of similar energy which occupy a band of energies in the material. These bands are called lattice modes and can be used in Raman spectroscopy for a vast range of studies. Raman spectroscopy, for instance, has been used to investigate a series of SiC films.[33] These SiC thin layers were deposited on different substrates using a solid gas phase epitaxy method involving carbon monoxide. Different polytype structures (3C, 6H, 4H) were grown on 6H-SiC and Raman spectroscopy made it possible to differentiate between them.

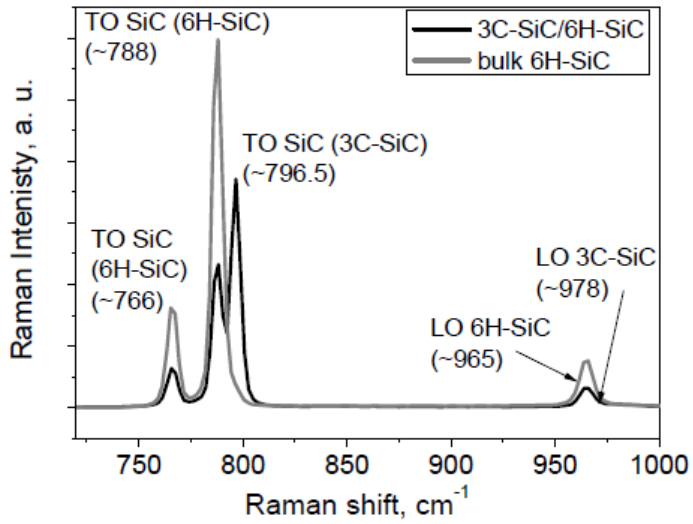

Figure 2-17 Raman spectra of bulk 6H-SiC and 3C-SiC layer on 6H-SiC substrate.[33]

The Raman spectra of bulk 6H-SiC and 3C-SiC layer on 6H-SiC substrate is shown in Figure 2-17 and the grey line represents the hexagonal modes for the 6H-SiC substrates. These three peaks are indicated as Transverse Optical phonon mode (TO), TO_2 at ~766 cm^{-1} and ~788 cm^{-1}, TO_1 at ~797 cm^{-1}, and one Longitudinal Optical phonon mode (LO) at ~965 cm^{-1}. After deposition, two strong peaks belonging to 3C-SiC appeared, one at ~978

cm^{-1}, assigned to the LO mode, and another at ~796.5 cm^{-1} assigned to the TO phonon mode.

2.3.4 Scanning Electron Microscopy (SEM) and Energy Dispersive Analysis of X-rays (EDX)

When an electron beam impinges on a sample, several types of signals are produced: secondary electrons, backscattered electrons, Auger electrons, characteristic X-rays, and photons with various energies. These signals are obtained from specific emission volumes within the sample and used in scanning electron microscopy[34] (SEM) to extract information such as composition, particle size, crystal morphology and surface defects. For instance, the intensity of the backscattered electrons (BSE) signal is strongly related to the atomic number Z of the elements in the sample; hence BSE images can provide information about the distribution of different elements. Also, when the electron beam removes an inner shell electron from an element contained in a sample, a higher energy electron fills the vacancy and releases energy in the form of characteristic X-ray radiation. This is used to give both qualitative identification and quantitative compositional information and the technique associated with this process is known as energy dispersive spectroscopy (EDS) or energy dispersive analysis of X-rays (EDAX or EDX). Finally, as the finely focused electron beam sweeps across the specimen, the secondary-electron emission (see below), coming from a volume near the beam's impact area, is used to give a map of the surface topography of samples.

The basic components of the SEM are the lens system, electron gun, electron collector, visual and recording cathode ray tubes (Figure 2-18).

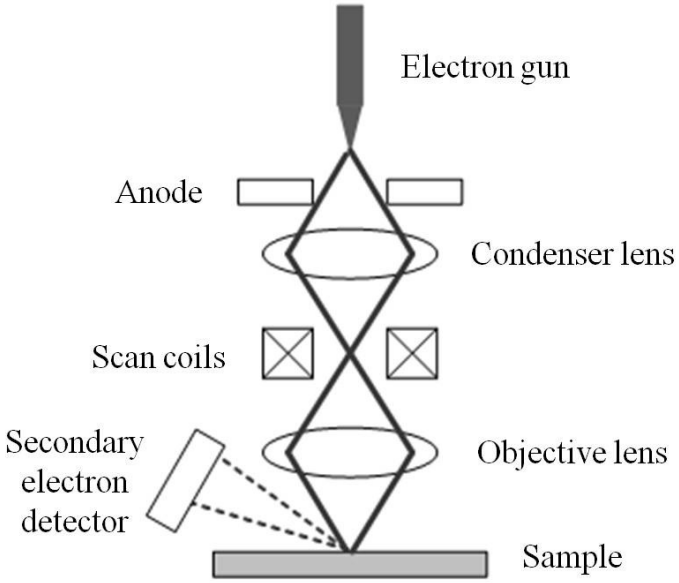

Figure 2-18 Schematic representation of a SEM microscope.

The electron column consists of an electron gun and two or more electron lenses, all under vacuum, where the electron gun provides a large, stable current in a small electron beam (with energy range of 1 - 40 keV).[34] Since beam diameter produced directly by the conventional electron gun is too large to generate a sharp image at high magnification, electron lenses are used to reduce the diameter of the electron beam and focus the beam on the specimen. The sharpness, contrast and depth of field in SEM images are dependent upon the three major electron beam parameters:[34]

- the spot size d_p, defined as the diameter of the final beam at the specimen (electron probe),
- electron-probe current i_p, defined as the current in the final probe which impinges upon the specimen and generates the various imaging signals and
- the electron-probe convergence angle α_p, defined as the half-angle that the cone of electrons at the specimen makes with the centreline of the beam.

It is important to note that the spot size, d_p, must be as small as possible to achieve the highest resolution image while for the best image quality and for X-ray microanalysis, i_p should be as large as possible and for the best depth of field, where a large range of heights on the specimen appear in focus at the same time, α_p must be as small as possible. Unfortunately, i_p is reduced when d_p and α_p are made small and this means that the microscope controls must be adjusted each time to produce the desired result depending if the microscopy mode is set for high resolution, high depth-of-field, or microanalysis.

The actual formation of a contrast image requires a scanning system to construct the image point by point across the sample surface. Two pairs of electromagnetic deflection coils (scan coils) are used to generate and control a rectangular raster of the beam on both the specimen and the viewing screen. Depending on which signal is analysed, the SEM microscope will be equipped with different detectors. The secondary electrons (SEs) are collected by an electron detector consisting of a scintillator, a light pipe, and a photomultiplier tube, located to the side of the specimen, with the specimen usually tilted towards it. Backscattered electrons (BSEs) are most efficiently and selectively collected with a detector positioned on top of the sample, which is either a semiconductor or a scintillator-photomultiplier detector.

The most fundamental part of the instrument is the electron gun and two types of electron source can be found in SEM microscopes: thermionic and field emission.[34] They vary in the amount and stability of the emitted current, the size and the lifetime of the source. When the emitter material (the source of electrons) is heated to a high temperature, the small fraction of electrons in the highest energy state, the Fermi level, acquires enough energy to overcome the work-function energy barrier, E_w, of the material and escape into the vacuum. The cathode current density obtained from the filament in the thermionic emission is strongly affected by the temperature and the work function, E_w. Since it is desirable to operate the electron gun at the lowest possible temperature to reduce evaporation of the filament, materials of low work function are desired. The most common electron gun is the triode electron gun and it consists of a tungsten filament serving as the cathode, the grid cap, and the anode. The typical tungsten filament is a bent hairpin wire maintained at a high negative potential that is heated resistively. At the operating temperature, the tungsten wire emits electrons in all directions that are accelerated by the anode potential and a grid cap is used to focus electrons inside the gun and control the amount of electron emission. A hole in the anode allows a fraction of these electrons to continue down the column towards the lenses. Tungsten filaments, although characterized by low brightness, are commonly employed as cathodes in electron microscopy (SEM and TEM) because of their advantages such as reliability, well understood properties and relative low cost. In particular for SEM applications, where high brightness is not necessary at low magnifications or where stable high currents are required, as in EDX, the thermionic tungsten filament still represent the best choice.[34]

When it is essential to improve image resolution and therefore reduce the electron-probe size without causing a loss of current in the probe, increasing the electron gun brightness is

required. The cathode current density, and hence the brightness may be increased by lowering the work function E_w. As E_w is in the exponent, the effect of this can be dramatic. Of the many oxides and borides that behave as low-workfunction emitters, the most successful has been lanthanum hexaboride, first investigated by Lafferty.[35] A block of lanthanum hexaboride (LaB_6) heated to thermionic emission is the most common high-brightness source. It offers about 5-10 times more brightness and a longer lifetime than tungsten, but requires better vacuum conditions. In this case heating is achieved by thermal contact of the LaB_6 block with a supporting tungsten wire. Another important aspect is that a constant beam current is required for microscopy and microanalysis since all information is recorded as a function of time. As the filament current is increased, the beam current eventually reaches a point where there is no further increase, a condition called saturation. Saturation ensures that a small increase or decrease in the filament heating current will not change the electron beam current.

The latest improvement in the SEM field is field emission scanning electron microscope (FESEM) that incorporates a cold cathode field emission gun and ultra high vacuum to achieve high resolution and high quality images. LaB_6 filaments offer a high current, but the brightness is three orders of magnitude lower than that of field emission guns (FEGs).[37] FEGs operates on the principle of electron tunnelling from the tip to vacuum following the application of a strong electric field ($\sim 10^9$ V m^{-1}) generating a very large electric field gradient at the tip of the cathode. This high field results in a very narrow potential barrier allowing tunnelling of the electrons from a low-workfunction metallic tip to vacuum. FEGs consist of pointed tungsten wires and a potential gradient of several kilovolts relative to an electrode causing emission of electrons induced by an external electromagnetic field (called field electron emission). The only issues arise because the total current is small and the long-term current stability poor. This is balanced however by the many advantages of FEGs such as long lifetime, small energy spread and greater brightness compared to conventional thermionic emitters. Hence the signal-to-noise ratio, spatial resolution and reliability of the emitter are increased compared to thermionic devices.[37]

For the characterisation of sample in this work, field emission scanning electron microscopy (FESEM) was conducted under high-vacuum conditions using a Hitachi S4700 microscope with 10 kV accelerating voltage and secondary electron detection to study the morphology of the sample. Samples for FESEM were prepared by depositing powder on to a carbon tab and at times gold coatings have been used to stop charge building up on the surface of the sample.

2.3.5 Transmission Electron Microscopy (TEM)

In TEM, a thin sample (~200 nm) is subjected to a high energy, high intensity beam of electrons, which pass through it and are detected to create a two-dimensional projection of the sample.[36] Because the electrons pass through the sample, TEM images the bulk structure, detecting possible crystal defects such as phase boundaries and stacking faults. Along their path through the specimen, many electrons undergo elastic or inelastic processes, which can be used for other analysis. Relaxation processes that lead to the emission of characteristic X-rays, Auger electrons, or light make chemical analysis of materials possible in the TEM and the instrument can be operated in different modes. [37] The ultimate aim of TEM is to analyze the nanostructure of materials with high spatial resolution and an electron source and electron optic components capable of producing intense beam currents and detectors capable to collect the various analytical signals generated from the interaction of the atoms with incident electrons are needed. The requirements and different types of electron sources are the same as the ones used in the SEM and have been already discussed in the previous section.

Due to their electric charge, electrons can be deflected by electric or magnetic fields, hence TEMs are equipped with round magnetic lenses used both for focusing the electron beam onto the object and to magnify the image.[38] These lenses suffer from severe aberration, which is the most important resolution-limiting factor in TEMs. As an incident electron beam enters a thin specimen, some of its electrons pass through the sample without any interaction, other electrons are diffracted by a set of crystallographic planes. The transmitted and diffracted beams are deflected by the objective lens (see Figure 2-19, 2-19). The transmitted beam passes through the origin of the back focal plane, while the diffracted beam to a spot *g* forming an inverted image of the specimen on the first image plane. If a film or a sensor is placed at the back focal plane, a diffraction pattern can be recorded.

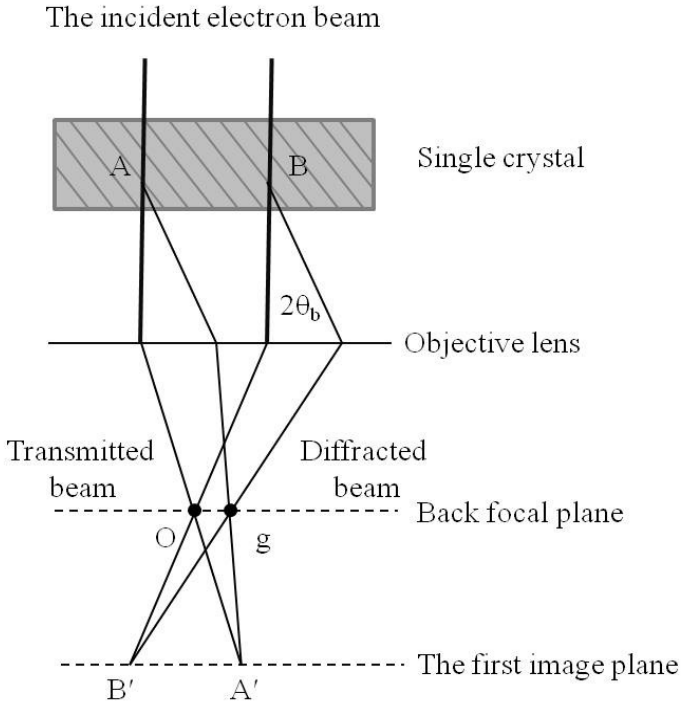

Figure 2-19 Diagram illustrating the formation of a diffraction pattern.

If the d-spacing of an (hkl) plane, responsible for the Bragg diffraction, is d and the distance between the diffracted beam (diffraction spot) and the transmitted beam (the direct spot) on the diffraction pattern is R, then:

$$L\lambda = Rd \qquad \textbf{(2-18)}$$

Where λ is the wavelength of the electron beam, and L is a constant called the camera length. Using a selected-area aperture, placed at the first image plane, an area can be selected from which the diffraction pattern is taken. If the selected area contains polycrystalline grains, the diffraction pattern consists of Debye rings. If only a single crystalline grain is included in the selected area aperture, a pattern of diffraction spots is obtained.

In the standard TEM operating mode, commonly referred to as diffraction contrast imaging, only a fraction of those electrons that have passed through the sample are used to form the highly magnified final image. Most of the scattered (or diffracted) electrons are prevented from reaching the image plane by positioning an objective aperture, Figure 2-20. This aperture thus serves to determine the image contrast and when only the transmitted beam contributes to the image, bright field (BF) imaging is employed. While if the

objective aperture is moved to allow only the diffracted beam to pass, a dark field (DF) image is obtained.[39] Deviation from an exact Bragg condition, possibly caused by different crystal orientations, crystal structure and defects, is used to create contrast from one position to another within a specimen.

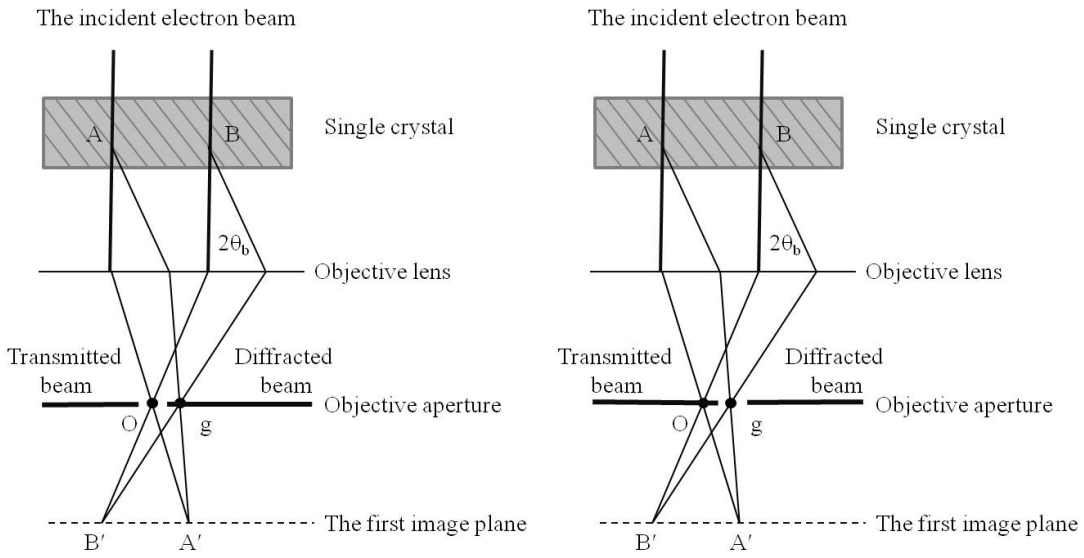

Figure 2-20 Diagram illustrating the formation of a: (a) bright-field (BF) image; (b) dark-field (DF) image.

Transmission electron microscopy was performed by Dr. Ian MacLaren from the School of Physics of the University of Glasgow, using a FEI Tecnai T20 (FEI, Eindhoven, Netherlands) operated at a 200 kV acceleration voltage using a LaB_6 filament with images recorded using a Megaview III CCD camera (Olympus SIS GmbH, Garching, Germany). Conventional bright field and dark field diffraction contrast imaging was used in combination with selected area diffraction to characterize the nanostructure and relate this to the crystallography of the nanofibres. Samples for TEM were prepared by sonicating the powders in ethanol and then pipetting drops of the suspension onto holey carbon film Cu grids.

2.3.6 Thermal analysis coupled with mass spectrometry

Thermal analysis studies the physical and chemical properties of materials as a function of temperature. Two thermal analysis techniques, namely thermogravimetric analysis (TGA) and differential thermal analysis (DTA) were employed simultaneously, using the same instrument to probe the free carbon content of crosslinked x-aerogel samples after

microwave reaction (see Chapter 5) because of differences in the oxidative stability of carbon in respect to silicon carbide.

TGA continuously records the change in weight of a sample as a function of either temperature or time during a temperature programme, while DTA measures the difference in temperature, ΔT, between a sample and an inert reference material undergoing the same temperature treatment and allows quantitative measure of the heat content changes occuring to the sample during the analysis (for instance melting, changing crystal structure or decomposing) as a function of either temperature or time during a temperature programme.[40] In thermogravimetry the change in weight is recorded continuously on a graph. As an example, Figure 2-21 depicts a typical single step reaction, such as a decomposition or loss of CO_x species by oxidation. The material analysed is heated at a constant rate, ranging from 1 to 20 °C min^{-1}, and has a constant weight W_i until it begins to decompose or oxidise at temperature T_i. The sample continues to lose weight up to a final temperature, T_f, where it reaches a second constant weight plateau, corresponding to the residual weight, W_f. The difference in weight ΔW can be used for quantitative calculations of compositional changes and in this study ΔW will represent the free carbon content in the sample.

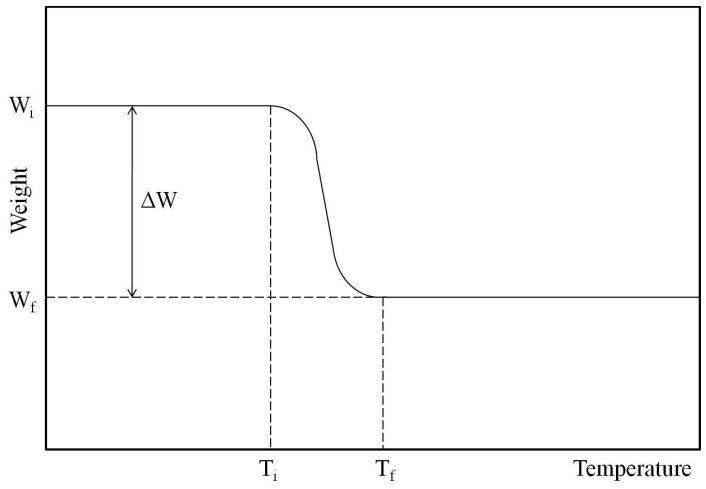

Figure 2-21 Schematic thermogram for a single step decomposition reaction.

Mass spectrometry (MS) has been employed in combination with TGA to analyse the gas products coming from a TGA experiment. By heating in an oxidising atmosphere, the carbide sample will produce CO_x species as it is oxidised. These gases are transferred to the MS where the components are ionized and then identified. The most common way to

produce a radical cation from a compound (M) from which the signal can be followed on the spectrum is by electron impact (19):

$$M + e^- \rightarrow M^{+\bullet} + 2e^- \qquad \textbf{(2-19)}$$

The radical cation $M^{+\bullet}$ produced has the same mass as the molecular weight of the compound M from which it is was produced and it is therefore called a molecular ion. In the recorded spectrum the ion appears at a mass to charge ratio of m/z, where the charge z is often 1. Carbon naturally exists as a mixture of the isotopes ^{12}C and ^{13}C; mass 12 was chosen here to follow the signal of carbon oxidative species of CO and CO_2, since the relative abundance of ^{12}C and therefore the relative intensity ratio of isotopes is 98.9 %.[41]

For PAN-crosslinked and carbon-coated silica aerogel monoliths, the free carbon content of samples post microwave synthesis was determined by Andy Monaghan (School of Chemistry, University of Glasgow) using differential scanning calorimetry/thermogravimetric analysis (TGA/DSC, SDT Q600 TA Instruments) coupled to mass spectroscopy (MS, ESS evolution model). A few milligrams in weight of the material were usually charged into an alumina pan that is placed on a precision balance inside a furnace. The furnace follows a programmed temperature profile and the mass of the sample is monitored during the experiment while a thermocouple registers the pan's temperature. All samples analysed were heated at a rate of 10 °C min^{-1} up to 800 °C, and held at this temperature for 5 h in a 2 % O_2/Ar atmosphere. The percentage weight changes have been recorded using TGA and gases coming from the exhaust have been analysed using MS. In particular, signals identified as CO_x from the products were simultaneously followed.

[1] D. K. Agrawal, *Curr. Op Solid State Mater*. Sci., 1998, **3**, 480.

[2] http://taksreview.wikispaces.com/file/view/electro_wave.gif/139624117/electro_wave.gif (last access 26/8/2011)

[3] E. T. Thostenson and T. - W. Chou, *Composites: Part A*, 1999, **30**, 1055.

[4] M. Oghbaei and O. Mirzaee, *J. Alloys Compd.*, 2010, **494**, 175.

[5] R. Meredith, *Engineers' handbook of industrial microwave heating*, 1st Edition, Short run press Ltd, Exeter, 1998, 250.

[6] R. Meredith, *Engineers' handbook of industrial microwave heating*, 1st Edition, Short run press Ltd, Exeter, 1998, 123-5.

[7] R. Meredith, *Engineers' handbook of industrial microwave heating*, 1st Edition, Short run press Ltd, Exeter, 1998, 148.

[8] J. M. Osepchuk, *Microwave technology*, in Kirk-Othmer Encyclopedia of Chemical Technology, 4th ed., 16, Wiley, New York, 1995.

[9] A. C. Metaxas, Applicators for industrial microwave processing, *Microwaves: theory and application in materials processing II,* 95th Annual Meeting of the American Ceramic Society, Cincinnati, Ohio, USA, 1993, 549.

[10] S. R. Vallance, S. Kingman and D. H. Gregory, *Adv. Mater.*, 2007, **19**, 138.

[11] E. Pert, Y. Carmel, A. Birnboim, T. Olorunyolemi, D. Gershon, J. Calame, I. K. Lloyd and O. C. Wilson, *J. Am. Ceram. Soc.*, 2001, **84**, 1981.

[12] M. Nuchter, B. Ondruschka, W. Bonrath and A. Gum, *J. Green Chem.*, 2004, **6**, 128.

[13] J. M. Osepchuk, *IEEE T. Microw. Theory Tech.*, 1984, **MTT32**, 1200.

[14] L. Carassiti, A. Jones, P. Harrison, P. S. Dobson, S. Kingman, I. MacLaren and D. H. Gregory, *Energy Environ. Sci.*, 2011, **4**, 1503.

[15] L. E. Smart and E. A. Moore, *Solid state chemistry: an introduction*, CRC Press; 3rd edition, 2005.

[16] P. W. Atkins, *Physical Chemistry*, 6th Edition, Oxford University Press, Oxford, 1998, 625.

[17] M. M. Woolfson, *An Introduction to X-ray Crystallography*, 2nd Edition, Cambridge University Press, Cambridge, 1997, 1-31.

[18] http://it.iucr.org/ (last access 12/7/2011)

[19] http://www.icdd.com/ (last access 12/7/2011)

[20] W. Kraus and G. Nolze, Federal Institute for Materials Research Testing, Berlin, Germany, 1998.

[21] http://www.fiz-karlsruhe.de/icsd.html (last access 12/7/2011)

[22] H. M. Rietveld, *Acta Cryst.*, 1967, **22**, 151.

[23] H. M. Rietveld, *J. Appl. Cryst.*, 1969, **2**, 65.

[24] R. A. Young, *The Rietveld method*, Oxford University Press, Oxford, 1995, 1-38.

[25] G. Caglioti, A. Paoletti and F. P. Ricci, *Nucl. Instrum. Methods,* 1958, **35**, 223.

[26] A. C. Larson and R. B. von Dreele, *General Structure Analysis System (GSAS)*, Los Alamos National Laboratories Report LAUR 086-748, Los Alamos, 2004.

[27] B. H. Toby, *J. Appl. Crystallogr.* 2001, **34**, 210.

[28] R. S. Krishnan and R. K. Shankar, *J. Raman Spectrosc.,* 1981, **10**, 1.

[29] C. V. Raman and K. S. Krishnan, *Nature London*, 1928, **121**, 501.

[30] E. Smith and G. Dent, *Modern Raman Spectroscopy – A Practical Approach*, Wiley-Blackwell, London, 2005, 1-20.

[31] L. A. Lyon, C. D. Keating, A. P. Fox, B. E. Baker, L. He, S. R. Nicewarner, S. P. Mulvaney and M. J. Natan, *Analytical Chemistry*, 1998, **70**, 341R.

[32] R. L. McCreery, *Raman Spectroscopy for Chemical Analysis*, in Wiley Chemical Analysis Series, **157**, J. Winefordner, Ed., John Wiley, N.Y., 2000, Chapter 5, p.90.

[33] J. Wasyluk, T. S. Perova, S. A. Kukushkin, A. V. Osipov, N. A. Feoktistov and S. A. Grudinkin, *Mater. Sci. Forum*, 2010, **645-648**, 359.

[34] J. Goldstein, D. E. Newbury, D. C. Joy, Charles E. Lyman, P. Echlin, E. Lifshin, L. Sawyer and J.R. Michael, *Scanning Electron Microscopy and X-ray Microanalysis*, Springer; 3rd edition, 2003.

[35] J. M. Lafferty, *J. Appl. Phys.*, 1951, **22**, 299.

[36] D. B. Williams and C. B. Carter, *Transmission electron microscopy: Basics*, **1**, Springer, New York, 2009.

[37] G. Botton, *Science of Microscopy*, 2007, **1**, 273.

[38] W. Sigle, *Annu. Rev. Mater. Res.*, 2005, **35**, 239.

[39] H. Saka, *Carbon Alloys*, 2003, Springer Tracts in Modern Physics, 223.

[40] A. R. West, *Solid State Chemistry and its Applications*, John Wiley and Sons, Norwich, 1984.

[41] K. Downard, *Mass Spectrometry: A Foundation course*, Royal Society of Chemistry, Cambridge, 2004.

3 Microwave synthesis studies in the Si-C system

3.1 Introduction

A number of articles have been published providing alternative synthesis methods for the energy intensive process involved in the commercial production of silicon carbide and these have been reported in a literature review in Chapter 1 (section 1.4.3). This section will be focused on the synthesis of silicon carbide starting from its elemental constituents, silicon and carbon.

Li's group have reported the synthesis of silicon carbide using a controlled mechanical activation step followed by a combustion method.[1,2] Powders of Si, activated carbon and a small amount of milling promoter, have been milled from 2 to 16 h and subsequently ignited using different approaches.[1,2] As the milling time is increased, an increase in the amorphous degree of reactant powders and a simultaneous increase in reactivity has been reported. In air, the mechanically activated powders were ignited successfully depending on their preheating time. Successful reactions were achieved without the aid of a preheating treatment, employing an inert atmosphere of nitrogen. The surface of the product was mainly composed of SiO_2, residual Si and a minor amount of SiC, while the bulk of the samples were composed of SiC with minor impurities of Si_2N_2O and in some cases Si_3N_4.

Several papers are already present in the literature describing the synthesis of silicon carbide through direct carburisation of silicon and carbon powders using microwave irradiation. Rao's group synthesised monophasic β-SiC starting from silicon and charcoal powders in a commercial microwave oven operating at 2.45 GHz and power levels up to 980 W for 10 min.[3] The reactions were carried out using either air or iodine vapours. When the reaction is carried out in air, impurity peaks corresponding to silica or silicon are present and removed by leaching the products with dilute acid, HF + HNO_3 for silicon and HF for silica. The presence of residual amorphous C could not be detected by diffraction. An iodine atmosphere has been reported to prevent oxidation and leads to the formation of only β-SiC. The temperatures of these reactions were measured by inserting a thermocouple in the reaction mixture immediately after the microwave power is turned off and the silicon-carbon reaction has been reported to occur below 1250 K, instead of 1673 K required in the conventional processes.

In 2001, Binner *et al.* published the results of the microwave initiated self-propagated high-temperature synthesis (SHS) of SiC.[4] The pellets used were composed of a stoichiometric amount of Si and C powders and heated in a multimode cavity operating at 2.45 GHz under Ar at ambient pressure. Different microwave powers were used up to 5 kW. Ramesh *et al.* synthesised the carbide using silicon and amorphous carbon powders in a 1:2 ratio at 1300 °C under Ar in less than 5 min in a 2 kW tubular microwave furnace.[5] A purifying step was required (650 °C in air for 8 h to remove excess carbon present in the product). In contrast to bulk preparations, silicon carbide nanowires have been prepared from silicon powder and phenolic resin.[6] The synthesis using microwaves was carried out at 800 °C for 1 h and 1300 - 1400 °C for 0.5 - 2 h in a static argon atmosphere, which was maintained at a constant pressure of 0.1 MPa.

Previous MW synthesis work has showed that the SiC synthesis time can be cut by orders of magnitude over the Acheson process.[3-6] These methods represent a significant improvement on the reaction time compared to conventional syntheses. However, among the challenges that remain to be overcome are:

- to remove subsequent purification steps,
- to design reactions that do not require reactive or cover gas environments,
- to reduce synthesis times (and energy expenditure) still further so that energy-efficient, continuous manufacturing becomes a possibility.

Previous studies performed in the group have shown that it is possible to prepare refractory and superconducting transition metal carbides in air over second timescales using high power MWs.[7,8,9] This chapter will cover the work carried out on the synthesis of silicon carbides in the Si-C system. In particular, the results on the synthesis of β-SiC in air from Si and C using a multimode microwave cavity (MMC) and singlemode microwave cavity (SMC) will be shown and emphasis will be given to the study of the products. In addition to the phase purity being a priority, the importance of changes in morphology and properties of samples processed using microwave irradiation has also been investigated showing how each is influenced by the reaction parameters.

3.2 Experimental synthesis of silicon carbide

Carbon is well known as a good microwave absorber. Either in the form of graphite or activated carbon, carbon materials reach temperatures of over 1000 °C in less than 2 min, when heated in a common domestic microwave oven,[10] and posses loss tangent values of up to 2.95 at room temperature.[11] This is due to a combination of conduction and dipolar heating mechanisms (Chapter 1, section 1.3.1), where the limited free π-electrons in carbon materials move in response to the electric field. The inability of electrons to follow the electric field changing in phase causes energy to be dissipated as heat.[11] Silicon, on the other hand, is expected to behave as a low absorber with a loss tangent value of approximately 0.002 at room temperature.[12] In this case, only a small amount of microwave energy is absorbed while most of it is transmitted through the material.

Several experimental approaches were adopted, considering the reactant behaviour and were improved using a trial and error approach. The heating of the reactant pellet alone was unsuccessful and adding susceptors, such as carbon, were generally ineffective if silica flour was not used to surround the reaction vessel and ensure thermal insulation. Synthesis was attempted in multimode cavity (MMC) microwave reactors (Chapter 2, section 2.2.1) and single mode cavity (SMC) reactors (Chapter 2, section 2.2.2). A single mode cavity offers many advantages compared to a multimode cavity (Chapter 2, section 2.1). While in a MMC reactor the power is fixed at 800 W, in the SMC reactor it was possible to achieve a power input of up to 9 kW in these experiments.

The majority of work concentrated around synthesis of the carbide from the elemental powders. All reactions were performed combining a stoichiometric amount of Si with activated carbon or graphite. Pellets were pressed using a small amount of distilled water as a binder, surrounded by a graphite powder MW susceptor and placed in an open silica tube immersed in a bed of silica flour contained within the MMC (Chapter 2, section 2.2.1). The shape of samples heated in a microwave reactor can be critical. The sphere is the ideal shape as heating will concentrate in the centre of the sphere and radiate outwards by conduction. In this thesis, the samples were pressed to make cylindrical pellets as the next best shape in terms of heating performance.[13] High power MW reactions were conducted following a similar procedure and using the experimental set-up described in Chapter 2, section 2.2.2.

In the case of the SMC studies, the reactor used was a Sairem 3 -15 kW GMP 150SM microwave generator, connected through a WR430 waveguide to an automatic E-h tuner for impedance matching purposes. The reaction vessel used during reactions was placed in the centre of the cavity, while in the multimode tests the reaction vessel was always positioned in the same location within the cavity to keep the experimental parameters as constant as possible.

Various characterisation techniques were used to investigate the resultant products. Powder X-ray diffraction (PXD, Chapter 2, section 2.3.1.3) (Bruker D8 Advance diffractometer, Cu $K_{\alpha 1}$ radiation) was carried out on all products in a glass capillary mounted at the centre of the Debye-Scherrer camera. Samples were routinely scanned for 1 h and a select number of samples scanned for 12 h so that structural refinement could be carried out (Chapter 2, section 2.3.2). Initially, routine 1 h scan data were used to identify product phases by reference with known structures downloaded from the Inorganic Crystal Structure Database (ICSD)[14] using the PowderCell 2.3 software[15] and 12 h scans used to derive cell parameters for Si-C phases by least squares fitting. Crystallographic parameters and quantitative phase fractions of crystalline components were obtained by Rietveld refinement against powder XRD data (collected for 2-12 h over a range of $5 \leq 2\theta$ / ° ≤ 85 with a step size of 0.017° 2θ) for each dataset (using GSAS and EXPGUI packages[16,17]).

In addition, specific samples were characterised using Raman spectroscopy to determine whether any amorphous phase fraction (e.g. of carbon) was present (Chapter 2, section 2.3.3). Raman spectra were collected at room temperature using a Horiba LabRAM HR confocal microscope system with a 532 nm green laser (Laser Quantum Ventus 532, 150 mW). A hole aperture of 50 μm, a 600 gr mm^{-1} grating and a Synapse CCD detector were used for the experiment.

The morphology and elemental composition of samples were determined by SEM and EDX respectively (Chapter 2, section 2.3.4). Field emission scanning electron microscopy (FESEM) was conducted under high-vacuum conditions using a Hitachi S4700 microscope with a 10 kV accelerating voltage and secondary electron detection to study the morphology of the sample. Samples for SEM of sufficient thickness were prepared by depositing powder on to a carbon tab. Transmission electron microscopy (Chapter 2, section 2.3.5) was performed using a FEI Tecnai T20 microscope (FEI, Eindhoven, Netherlands) operated at 200 kV acceleration voltage using a LaB_6 filament with images recorded using a Megaview III CCD camera (Olympus SIS GmbH, Garching, Germany).

Conventional bright field and dark field diffraction contrast imaging was used in combination with selected area diffraction (SAED) to characterize the nanostructure and relate this to relevant sample crystallography. Samples for TEM were prepared by sonicating the powders in ethanol and then pipetting drops of the suspension onto holey carbon film Cu grids. The TEM/SAED experiments were performed in the School of Physics and Astronomy by Dr. Ian MacLaren.

3.2.1 Experimental details

3.2.1.1 MMC synthesis

Stoichiometric amounts of silicon (Sigma-Aldrich 99 %) and activated carbon (MAST Carbon Ltd.[18]) (1:1 molar ratios; typical sample total mass 0.265 g) were ground in a ball mill (Retsch PM100, 450 rpm) for 8 h. Selected samples underwent the same procedure other than activated carbon was replaced with graphite (Aldrich, powder, < 20 μm, synthetic). The milled powders were mixed with distilled water (either 0.15 ml or 0.2 ml) and cold pressed uniaxially in an 8 mm pellet die (Specac, 5 Tons, 10 minutes). The pressed pellets were embedded in graphite (acting as a MW susceptor) in an open, 10 mm silica tube which was surrounded with low dielectric loss silica flour (Aldrich, 99.6 %) (see Figure 2-9).

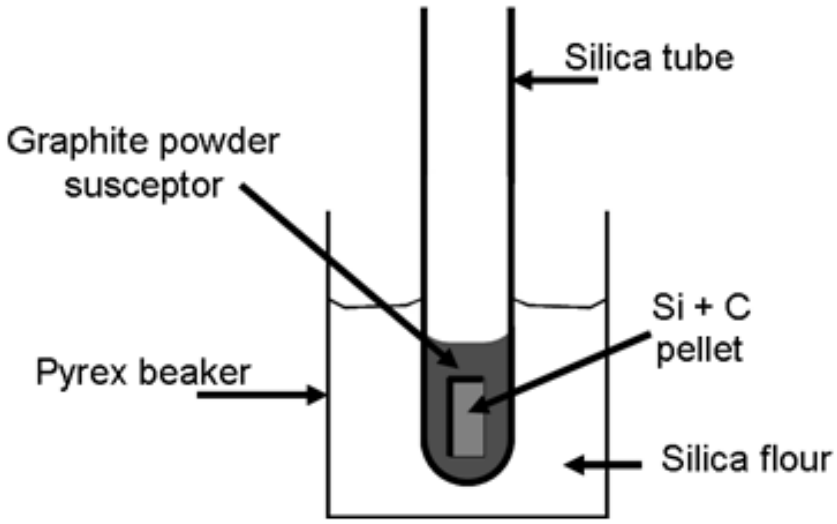

Figure 3-1 Schematic representation of MMC reaction set-up.[19]

Synthesis was conducted in a MMC fed with an 800 W magnetron and operating at 2.45 GHz. No impedance matching device was employed due to the very small sample to cavity volume ratio. All preparations were performed at ambient pressure in air.

Sample identifier	Carbon reagent	Irradiation time / min	Added water volume / ml
1	Activated carbon	1	0.15
2	Activated carbon	2	0.15
3	Activated carbon	3	0.15
4	Activated carbon	5	0.15
5	Activated carbon	10	0.15
6	Activated carbon	1	0.2
7	Activated carbon	2	0.2
8	Activated carbon	3	0.2
9	Activated carbon	5	0.2
10	Activated carbon	10	0.2
11	Activated carbon	15	0.2
12	Activated carbon	20	0.2
13	Activated carbon	25	0.2
14	Graphite	3	0
15	Graphite	15	0
16	Graphite	30	0

Table 3-1 Summary of all experiments carried out on the Si-C system in a MMC.

Ex-situ phase analysis from PXD and other techniques as a function of reaction time, revealed information on possible reaction mechanisms.

3.2.1.2 SMC synthesis

Elemental powders of Si (Sigma-Aldrich 99 %) and graphite (Sigma-Aldrich, powder, < 20 μm, synthetic) (1:1 ratios; 0.25 g total) were ground together and pressed into 8 mm diameter pellets which were set in powdered graphite susceptor in an open, 10 mm diameter quartz tube. The tube was placed in a silica beaker and packed with ground silica sand in order to maintain the tube in an upright position, this can be seen in the schematic of the setup in Figure 3-2. A series of synthesis experiments was run in a TE_{10n} single mode cavity. A single mode cavity differs from a traditional MMC as the presence of only 1 mode gives rise to very high and localized electric field intensities which are well defined in space. This definition allows the sample to be placed in the point of highest electric field. The field pattern is created by the superposition of incident and reflected

waves and is achieved through careful adjustment of a short circuit beyond the applicator. Impedance matching, required to minimize reflected power was performed using a SAIREM automatic E-H tuner. The cavity was excited using a 3 - 15 kW SAIREM GMP 150SM microwave generator operating at 2.45 GHz. The generator was adjusted to produce 3 kW of microwave power over the duration of the treatments.

In-situ temperature measurements were taken using an optical pyrometer (LAND System4 Thermometer M1 600/1600 °C; ± 1 °C accuracy) with a 5 mm diameter spot centred on the sample surface. The wavelength (1μm) of the instrument was deliberately selected to minimize errors.

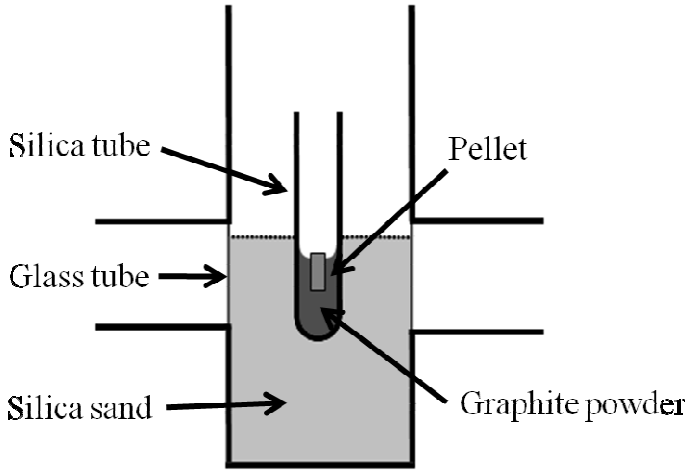

Figure 3-2 Schematic set-up of reaction using a Sairem 0 – 2 kW generator. [19]

Sample identifier	Carbon reagent	Irradiation time (s)	Power (kW)
17	Activated carbon	20	3
18	Activated carbon	25	3
19	Activated carbon	30	3
20	Activated carbon	32	3
21	Activated carbon	40	3
22	Activated carbon	45	3
23	Graphite	10	3
24	Graphite	20	3
25	Graphite	30	3
26	Graphite	40	3
27	Graphite	13	9

Table 3-2 Summary of all experiments carried out on the Si-C system in a SMC.

3.3 Results and Discussion

3.3.1 Multimode cavity (MMC) microwave syntheses of SiC

3.3.1.1 Synthesis and PXD studies

The pellets from initial reactions were visibly cracked with the constituent powders relatively loosely bound. The colour of the pellet changed from dark grey to grey/green, already reported as symptomatic of the successful synthesis of SiC.[2, 20] PXD of activated carbon samples with the least added water binder (Figure 3-3) are dominated by five peaks that match well with the reflections from the (111), (200), (220), (311) and (222) planes of the cubic modification of silicon carbide. Figure 3-3 illustrates that close to single phase β-SiC (97 wt % by Rietveld refinement, see section 3.3.1.2) can be synthesized in air after only 2 min (Figure 3-3b, sample **2**). At 5 min and above, samples **4-5**, however, it is possible to produce β-SiC as a single phase material. The shoulder near the (111) plane of β-SiC suggests the existence of stacking faults in the as-produced powders.

It should be also noted, that graphite reflections are almost certainly from surrounding susceptor powder that was not successfully removed from the product pellet. In fact, control experiments in which activated carbon was heated alone did not yield graphite by PXD. Furthermore, even though the reactions were performed in air, no silica reflections were evident at any irradiation times.

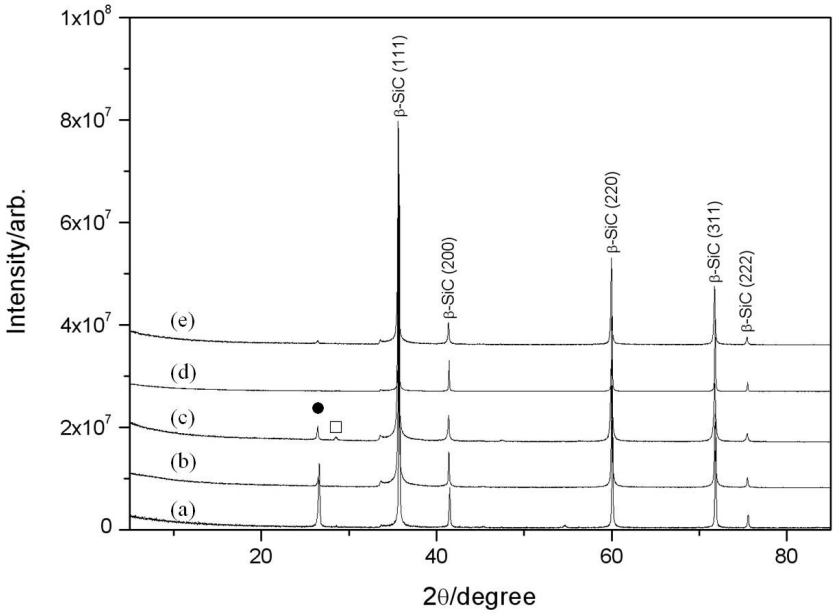

Figure 3-3 PXD patterns of samples synthesised in a MMC from Si + activated carbon with 0.15 ml of water added: (a) 1 (1 min); (b) 2 (2 min); (c) 3 (3 min); (d) 4 (5 min); (e) 5 (10 min). Reflections from graphite (●) and silicon (□) are also indicated.

If the water volume added as a binder to the stoichiometric mixture is increased, it can be seen from the PXD patterns the conversion to silicon carbide takes longer. While in the previous sets of reactions peaks belonging to β-SiC are visible for reaction times as low as 1 minute (sample **1**), in this case there is no trace of silicon carbide below 3 minutes. Beyond this reaction time, however, it is possible to yield single-phase β-SiC and if the power is maintained for times as long as 25 minutes (sample **13**) the product does not oxidise or change in terms of phase composition or crystallinity.

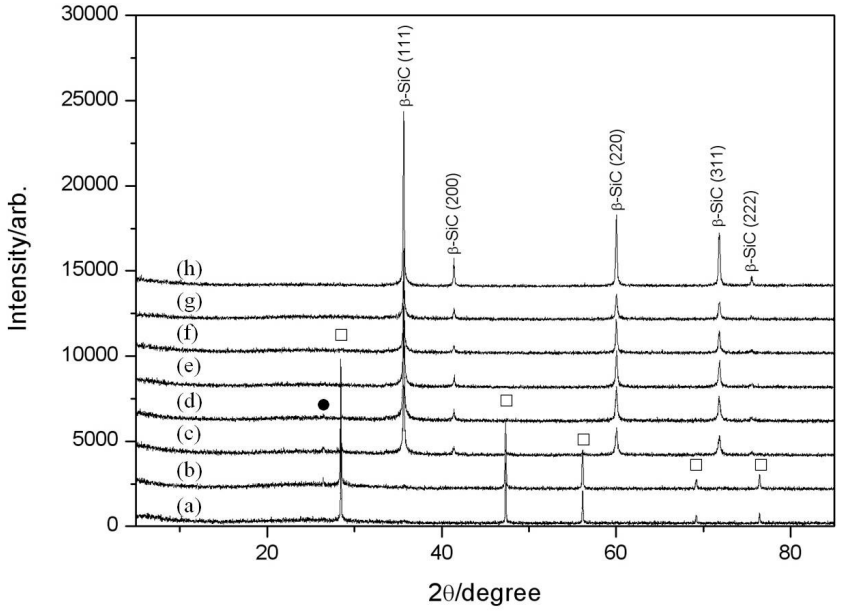

Figure 3-4 PXD patterns of samples synthesised in a MMC from Si + activated carbon with 0.2 ml of water added: (a) 6 (1 min); (b) 7 (2 min); (c) 8 (3 min); (d) 9 (5 min); (e) 10 (10 min); (f) 11 (15 min); (g) 12 (20 min); (h) 13 (25 min). Reflections from graphite (●) and silicon (□) are also indicated.

With graphite as a carbon source, dry-pressed powders proved to be the only way of obtaining pellets that maintained their integrity during pressing; addition of any volume of water in these cases (even < 0.15 ml) produced thin suspension-like slurries which could not be contained adequately in the pellet die. Even dry samples, however, were difficult to press. From the PXD studies (Figure 3-5), when graphite replaces activated carbon as carbon source, although after 3 minutes it is possible to yield silicon carbide (**14**), after 15 min (**15**), it is clear peaks belonging to silicon are present in the product. At 30 min (**16**) from the PXD pattern (Figure 3-5c), β-SiC is present again as a single phase material. Comparing this set of reactions (Figure 3-5) with the previous ones (Figure 3-3 and Figure 3-4), it is clear that the evolution in SiC phase fraction with time is more predictable using activated carbon and single phase β-SiC can be produced using activated carbon for irradiation times of 5 minutes and beyond. The better yield of β-SiC from reactions starting from activated carbon could be due to contributing factors such as the better dielectric

properties of activated carbon over graphite and the added influence of water added to the reaction mixture, as will be discussed later in the chapter.

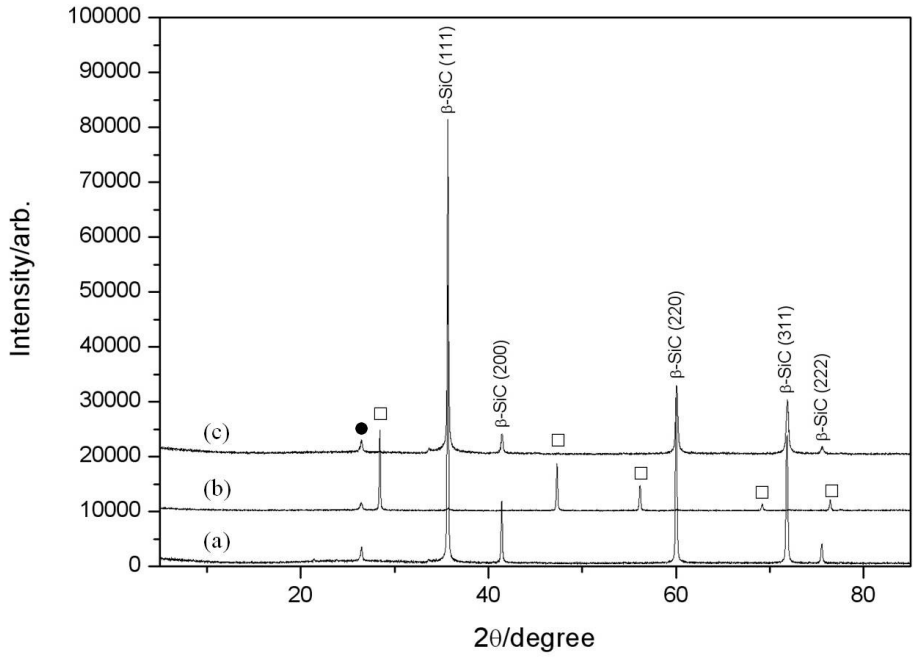

Figure 3-5 PXD patterns of samples synthesised in a MMC from Si + graphite: (a) 14 (3 min); (b) 15 (15 min); (c) 16 (30 min). Reflections from graphite (●) and silicon (□) are also indicated.

3.3.1.2 Rietveld refinement data

Rietveld refinements for the Si plus activated carbon samples, **1–5**, were performed using the zinc blende structure of β-SiC as a starting model. The background was modelled using a reciprocal intercalation function (function 8 within GSAS). Scale factor, zero point and cell parameters were also refined in initial cycles. Peak widths and profile coefficients (peak shape was modelled using the Thompson-Cox-Hastings pseudo Voigt function; peak shape function 2 within GSAS) and isotropic temperature factors were subsequently refined. Ensuring that all observed reflections were fitted, graphite was input as a secondary phase where relevant and phase fractions refined. Attempts to include oxygen or nitrogen on the C site of the β-SiC phase produced physically meaningless values and did not improve the quality of the fit. All refinements converged smoothly in final cycles. Data for **1–4** clearly demonstrate that the structure and stoichiometry of the carbide are invariant with time (e.g. Table 3-3 for **1**, **2** and **4**; Figure 3-6).

The cubic lattice parameters for samples for **1**, **2** and **4** are in excellent agreement with literature values[21] as are the Si–C distance for sample **4**, 1.8877(2) Å (Table 3-3**,** Figure 3-6c).

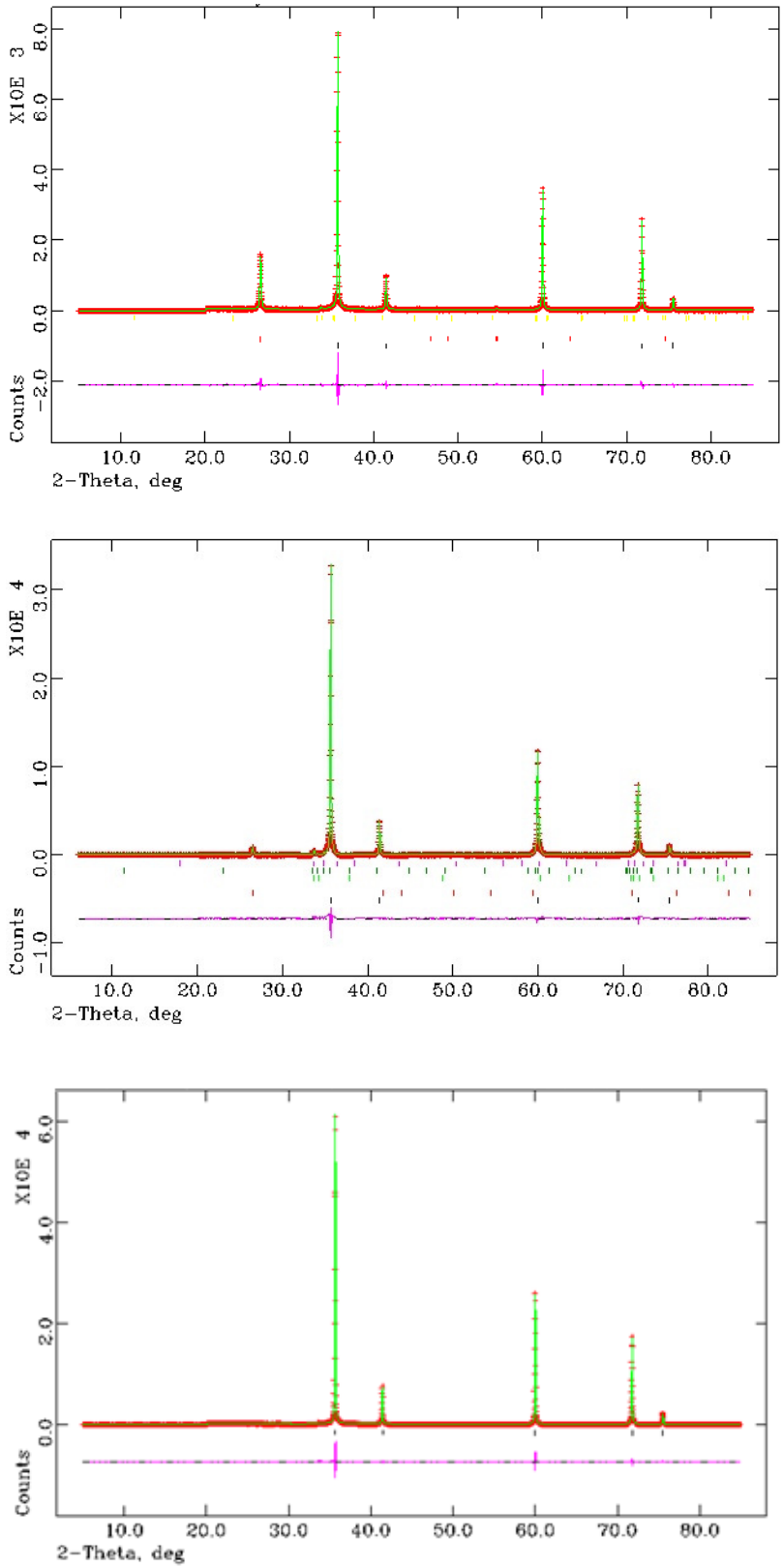

Figure 3-6 Exemplar profile plots for Rietveld refinements against PXD data. Shown are: (a) 1, (b) 2 and (c) 4 (see Table 3-1). Crosses (red) indicate observed data, the upper continuous line (green) shows the calculated profile, the lower continuous line (magenta) the difference and tick marks indicate different crystalline phases (dark blue βSiC, red graphite, yellow for a and dark green for b 6H-SiC, green 2H-SiC and magenta 4H-SiC).

Instrument, radiation	X-ray, Cu $K_{\alpha 1}$		
Nominal stoichiometry (Sample No)	β-SiC (**1**)	β-SiC (**2**)	β-SiC (**4**)
Phases, fractions / wt %	β-SiC: 82(1) % Graphite: 4(1) % 6H-SiC: 7(2) %	β-SiC: 97(1) % Graphite: 1(1) %	β-SiC: 100%
Crystal system, Space group	Cubic, F $\bar{4}$ 3 m		
Z	4		
M	160.388		
a-parameter / Å Unit cell volume / Å^3	4.3601(1); 128.6(4)	4.3583(1); 82.78(1)	4.3594(1); 82.85(1)
Calculated density, ρ_X / g cm^{-3}	3.213	3.217	3.215
Si *4a* (0,0,0), U_{iso}	6.9(4)	6.8(3)	6.8(3)
C *4c* (¼ ,¼ ,¼), U_{iso}	7.2(7)	6.3(5)	6.4(4)
Observations, parameters	3882, 46	3882, 46	3882, 32
R_p	11.31	8.78	8.18
R_{wp}	15.51	11.53	10.78
χ^2	1.88	5.20	4.03

Table 3-3 Exemplar crystallographic data from Rietveld refinements against PXD data. Shown are data for 1, 2 and 4.

Atoms bonds	Interatomic distance/ Å (at 293 K)		
Sample No	**1**	**2**	**4**
Si1 – C1 x4	1.88901 (2)	1.88720(2)	1.87739(2)
Atoms angle	Angle / º (at 293 K)		
Sample No	**1**	**2**	**4**
C1 - Si1 – C1 x4	109.471(1)	109.471(1)	109.008(8)
Si1 – C1 – Si1 x4	109.471 (1)	109.471(1)	109.008(8)

Table 3-4 Interatomic distances and bond angles for samples 1, 2 and 4.

Adding an extra volume of water as a binder, to the Rietveld refinement results, does not affect the cubic lattice parameter and samples **10-12** have lattice parameters in agreement with literature values[21] (4.3584(5) Å) ranging from a = 4.3508(6) (sample **10**) – 4.3528(9)

(sample **11**). Refinements have been performed on 1 h scans. β-SiC is the only crystalline phase present, but the curvature of the background between 20 - 30º 2θ suggests an amorphous fraction is present.

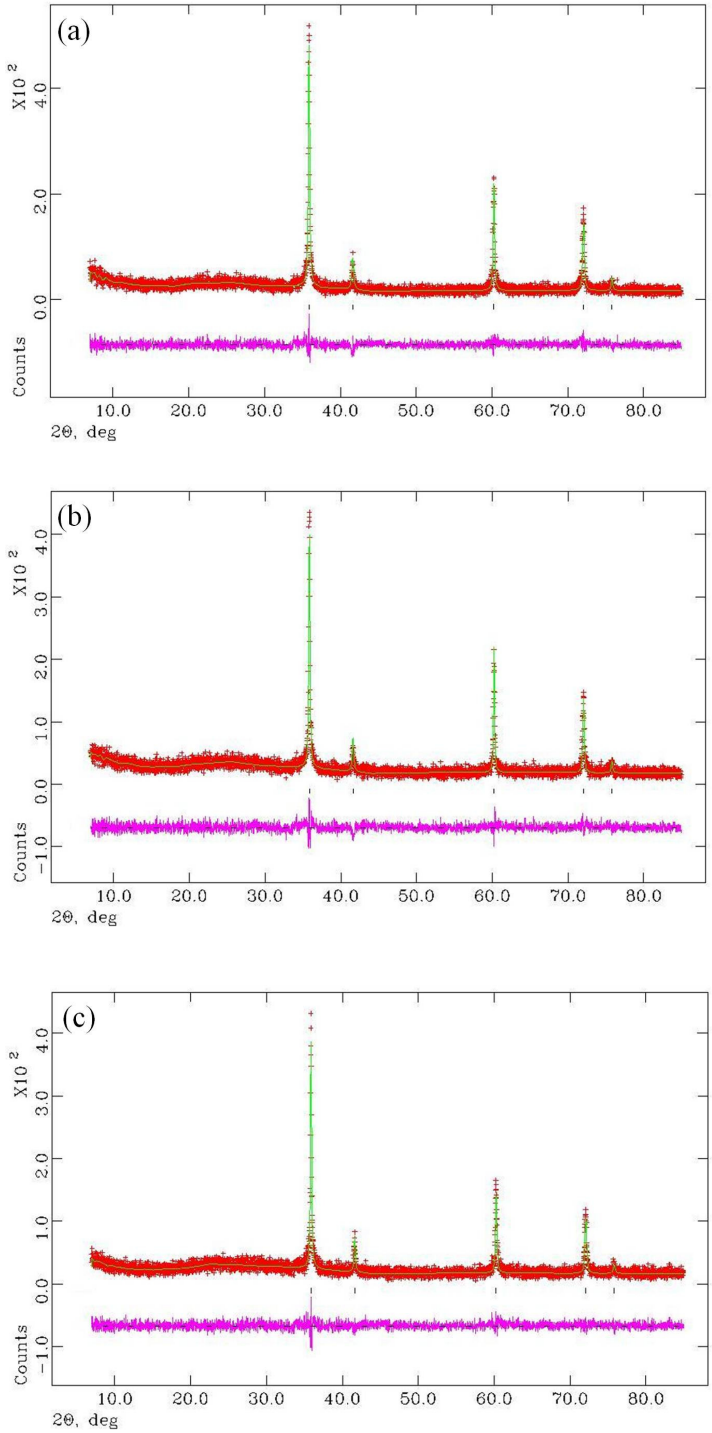

Figure 3-7 Exemplar profile plots for Rietveld refinements against PXD data. Shown are: (a) 10, (b) 11 and (c) 12 (see Table 3-1). Crosses (red) indicate observed data, the upper continuous line (green) shows the calculated profile, the lower continuous line (magenta) the difference and tick marks indicate different crystalline phases (dark blue β-SiC).

Instrument, radiation	X-ray, Cu $K_{\alpha 1}$		
Nominal stoichiometry (Sample No)	β-SiC (**10**)	β-SiC (**11**)	β-SiC (**12**)
Phases, fractions / wt %	β-SiC: 100 %	β-SiC: 100 %	β-SiC: 100%
Crystal system, Space group	Cubic, F $\bar{4}$ 3 m		
Z	4		
M	160.388		
a-parameter / Å Unit cell volume / Å^3	4.3514(7); 82.39(7)	4.3506(7); 82.35(1)	4.3507(7); 82.35(7)
Calculated density, ρ_X / g cm^{-3}	3.232	3.234	3.234
Observations, parameters	4613, 29	4613, 31	4613, 29
R_p	16.00	15.63	16.56
R_{wp}	20.62	20.02	21.16
χ^2	1.17	1.13	1.11

Table 3-5 Exemplar crystallographic data from Rietveld refinements against PXD data. Shown are data for 10, 11 and 12.

Atoms bonds	Interatomic distance/ Å (at 293 K)		
Sample No	**10**	**11**	**12**
Si1 – C1 x4	1.88424 (1)	1.88390(1)	1.88394(1)
Atoms angle	Angle/ º (at 293 K)		
Sample No	**10**	**11**	**12**
C1 - Si1 – C1 x4	109.471(3)	109.471(3)	109.471(4)
Si1 – C1 – Si1 x4	109.471(3)	109.471(3)	109.471(4)

Table 3-6 Bond angles for samples 10, 11 and 12.

3.3.1.3 Scanning electron microscopy (SEM)

SEM images for silicon plus activated carbon MMC samples show that 1 min reactions (**1**, Figure 3-8a) yield submicron sized irregular particles (of the order of 50 – 100 nm across) partially fused together to form a porous matrix. Reactions beyond 1 min yield significant

reductions in particle size and increased particle anisotropy, culminating in the growth of SiC micro- and nanofibres. Between 2-5 min, the samples are dominated by patches of nanofibres appearing to grow between clusters of nanoparticles (nanofibres from **2** are shown in Figure 3-8b). EDX data from spot and area scans suggest that all these samples (**1–5**) contain Si and C only. Evident from the SEM images of **2–5** is that the nanofibres in these samples are typically of high aspect ratio, measuring from 5 – 30 nm in diameter and exhibiting lengths of the order of 2 – 20 μm. There is neither any significant change in the yield of nanofibres nor of the structure of the nanofibres as irradiation times increase across samples **2–5**. Therefore, there is no evidence of more growth or continued growth to form longer wires for longer irradiation times.

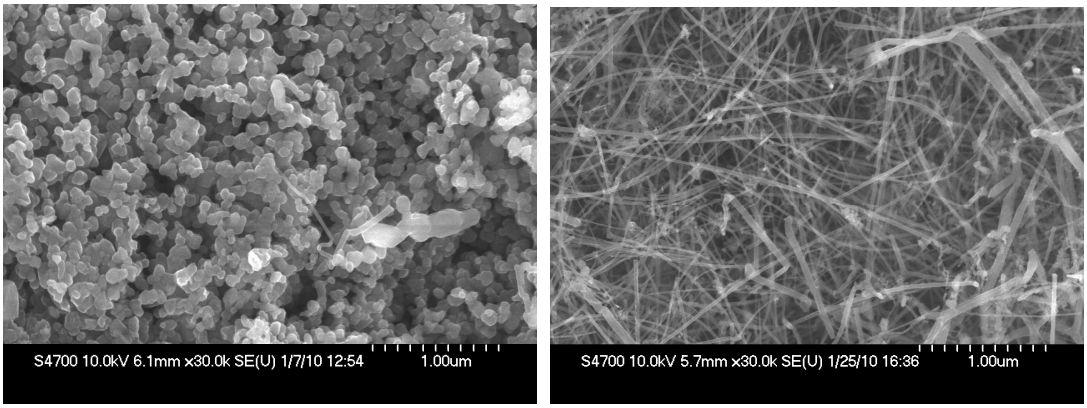

Figure 3-8 SEM micrographs of β-SiC prepared from Si + C in a MMC showing (a) nanoparticle clusters (1); (b) high aspect ratio nanofibres (2).

The influence of the amount of distilled water added to the milled powders has been studied (Figure 3-9). Increasing the water content did not influence the crystalline phases present, as graphite, Si and β-SiC were the only phases observed over the course of reaction. However, if the volume of added water is increased, it is possible to see a highly textured material after 3 minutes (sample **7**, Figure 3-9a) and by an irradiation time of 10 minutes the SEM micrograph shows the growth of nanofibres (sample **10**, Figure 3-9c). However, by contrast to **2–5**, the yields of fibres are lower and they appear to be more rod-like (lower aspect ratio), more defective and to form junctions. Both particles and fibres are of larger dimensions than those prevalent in **2–5**. The volume of water binder, therefore, appears quite critical to nanofibre growth. For longer reaction times porous structure with particles fused together can be seen, with dimensions below 1 μm (Figure 3-9d-f).

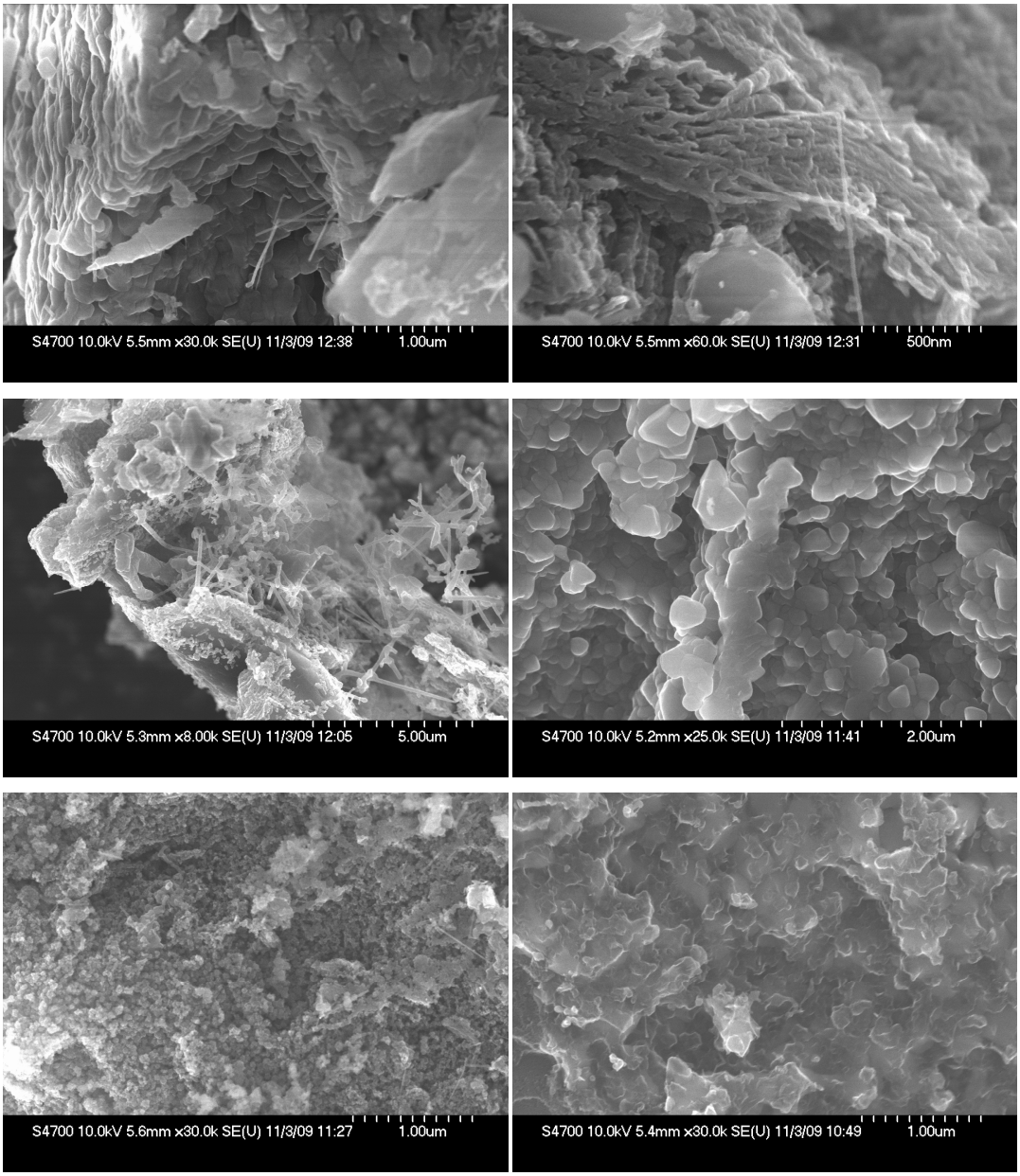

Figure 3-9 SEM micrographs of β-SiC prepared from Si + activated carbon with 0.2 ml of water added: (a) 8 (3 min); (b) 9 (5 min); (c) 10 (10 min); (d) 11 (15 min); (e) 12 (20 min); (f) 13 (25 min).

When graphite is substituted for activated carbon as the carbon source (Figure 3-10), SEM micrographs reveal that particles similar in morphology to those seen at short reaction times with activated carbon (e.g. **1**; Figure 3-8a) are formed, but in contrast to the activated carbon samples, the size distribution of the particles is not nearly as uniform and commonly the agglomerations of particles have dimension from ~ 200 nm to 1–2 μm across. Nanofibre formation is never observed in graphite samples whether from short (3 min; **14**) or long (30 min; **16**) irradiation times.

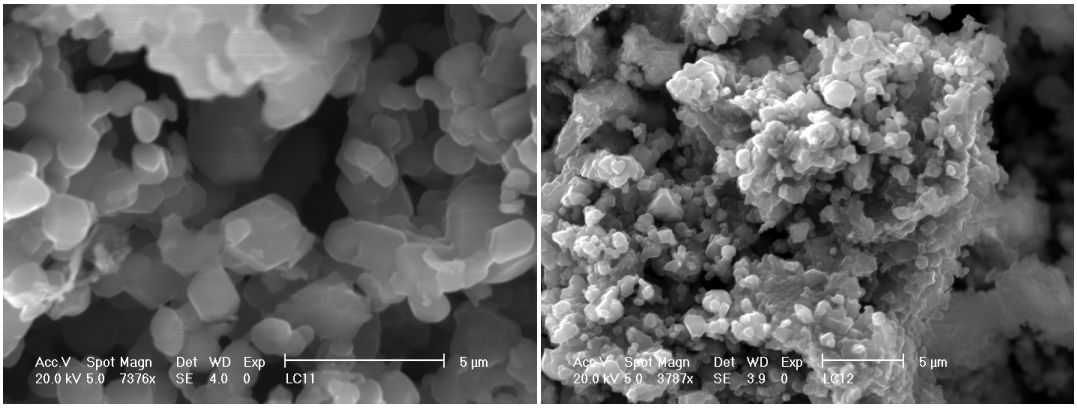

Figure 3-10 SEM micrographs of samples synthesised in a MMC from Si + graphite: (a) 14 (3 min); (b) 16 (30 min).

3.3.1.4 Raman spectroscopy

Raman spectra of products obtained from a mixture of silicon and carbon, using 0.15 ml of water as binder (sample **1-5**) exhibit a very strong band at 790 cm^{-1} and a less intense band at 970 cm^{-1} corresponding respectively to the Transverse Optical (TO) and Longitudinal Optical (LO) Raman-active mode in β-SiC (3C-polymorph; zinc blende structure).[22] As the irradiation time increases beyond 1 minute, in addition to the strong band at 790 cm^{-1} additional weaker bands appear (Figure 3-11b-c). The presence of these features has been already reported in the literature indicating the SiC products contain regions with different crystalline structures.[22,23] However, the PXD patterns show no presence of other silicon carbide polytypes beside the cubic modification β-SiC. Equally, however, such features are characteristic of β-SiC nanofibres, where a likely cause of strain in the structure could be the planar defects in the nanowire[24] (particularly those in the lower size range) as noted below in the discussion of the TEM data.

As is evidenced from the SEM micrographs, nanowires start forming after 2 minutes (sample **2-5**) and the corresponding Raman spectra show considerably broader bands and additional features. In a paper reporting the Raman spectrum of isolated nanowires, the stronger TO band has been reported as being composed of two peaks, so this could explain the asymmetry of the strong band in samples **2-5**.[23] The broad features at ~ 520-535 cm^{-1} are attributed to defect-induced acoustic (transverse and longitudinal) phonon mode scattering, while the shoulder to the strongest band (~ 780 cm^{-1}) TO phonon mode and the 820 - 980 cm^{-1} broad features are attributed to longitudinal optical (LO) phonon mode scattering.[23]

The bands at ~ 520 - 535 cm^{-1} and a shoulder on the strongest TO band (~ 780 cm^{-1}) could be collectively originating from acoustic phonon, TO and LO modes associated with stacking faults.[25,26] In the samples produced at short reaction times, the presence of broad bands at ~ 500 cm^{-1} connected to the 1050 cm^{-1} could be attributed to the first and second order Raman scattering of the TO phonon from possibly unreacted amorphous silicon.[27]

The two strong bands at higher wavenumber values are related to carbon materials. In particular the band at ca. 1350 cm^{-1} is designated as the D band and the one at 1580 cm^{-1} as the G band respectively.[28] The G band is associated with the vibration of sp^2-bonded carbon atoms belonging to graphitic layers, while the D band relates to the vibration of carbon atoms presenting a sp^3 configuration due to dangling bonds in-plane terminations or defects in disordered carbon materials.[29] The line broadening of the G band and the intensity ratio between the D and G bands (D/G) depend on the structure of the carbon,[30] although it is not easy to use Raman spectroscopy quantitatively.

According to the Raman spectra, samples **1, 2** and **5** contain a fraction of carbon, either as unreacted amorphous carbon (sample **2**, where the D band is more intense than the G band) or as graphite likely to originate from residual graphite powder susceptor and consistent with patterns obtained from PXD (Figure 3-3).[28] Additional weak and broad features at high wavenumbers, in particular the two bands observed in sample **4** at ca. 1501 cm^{-1} and ca. 1702 cm^{-1} and shifted by 20 cm^{-1} in sample **3** (at ca. 1480 cm^{-1} and ca. 1680 cm^{-1}) are almost certainly due to overtones in the second order Raman spectrum of silicon carbide.[31,32]

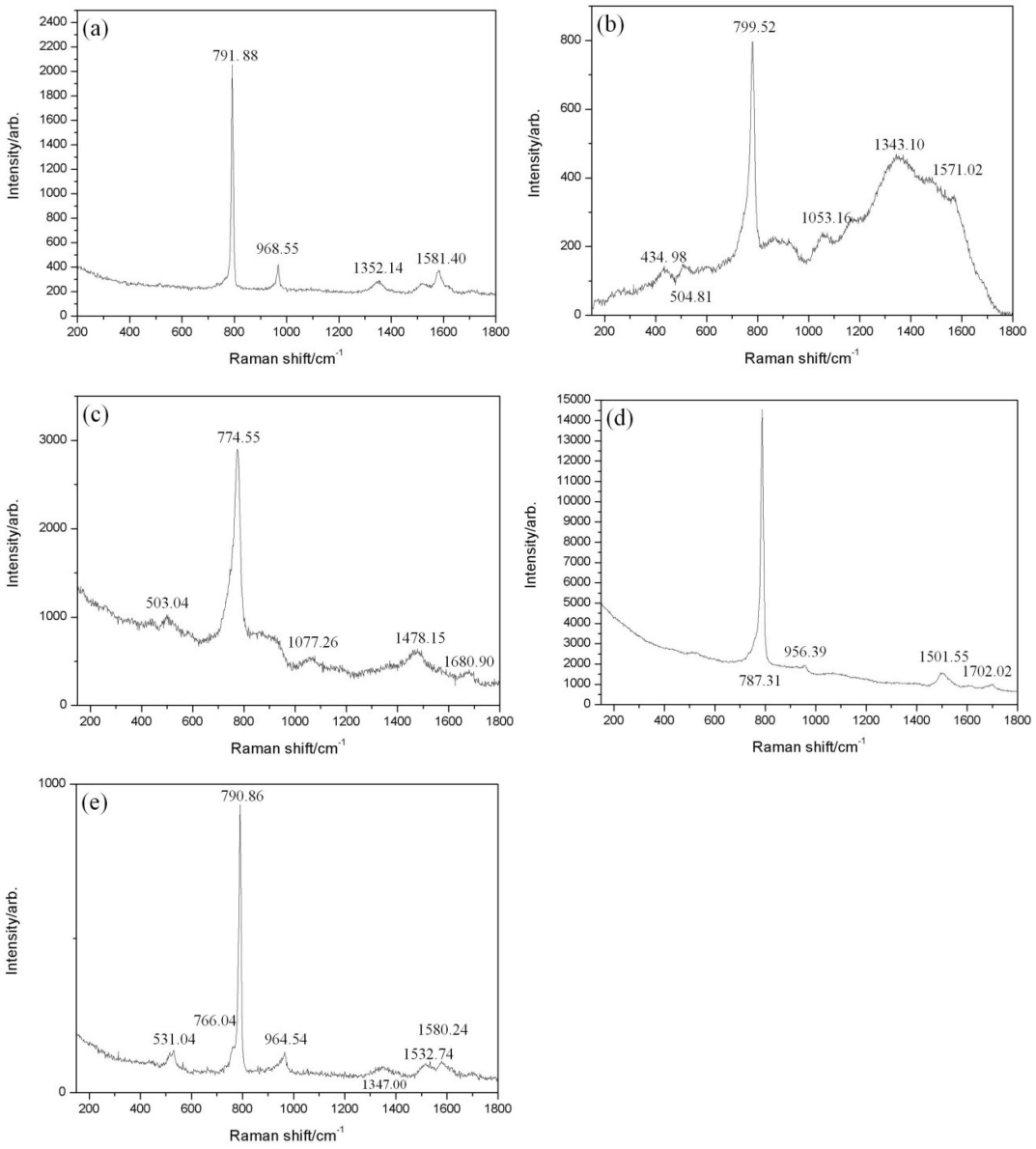

Figure 3-11 Raman spectra and observed bands for samples (a) 1 – (e) 5.

Selected samples (**9**, **11**, **13**) obtained from a mixture of silicon and activated carbon, when the added volume of water as binder is increased to 0.2 ml, have been also analysed using Raman spectroscopy. The three samples produced after 5, 15 and 25 min show some common characteristics. A strong band corresponding to the TO Raman-active mode of β-SiC is visible at ca. 790 cm^{-1}. It is interesting to note how after 5 and 15 min under MW irradiation, sample **9** and **11**, present additional weaker bands around ca. 520 - 535 cm^{-1} due to defect-induced acoustic (transverse and longitudinal) phonon mode scattering[25] and could be due to the presence of nanostructures in the product, as evidenced for instance from the SEM micrographs for sample **9**. Sample **13** instead, is manly composed of porous β-SiC (see Figure 3-9f) and both the TO and LO Raman-active modes are visible in the spectrum at ca. 790 and 970 cm^{-1} (Figure 3-12c) respectively. It is also important to note

that in the high wavenumbers region the carbon D and G bands are missing and instead overtones corresponding to the second order Raman spectrum of β-SiC can be found at ca. 1520 and 1710 cm^{-1}.[31,32]

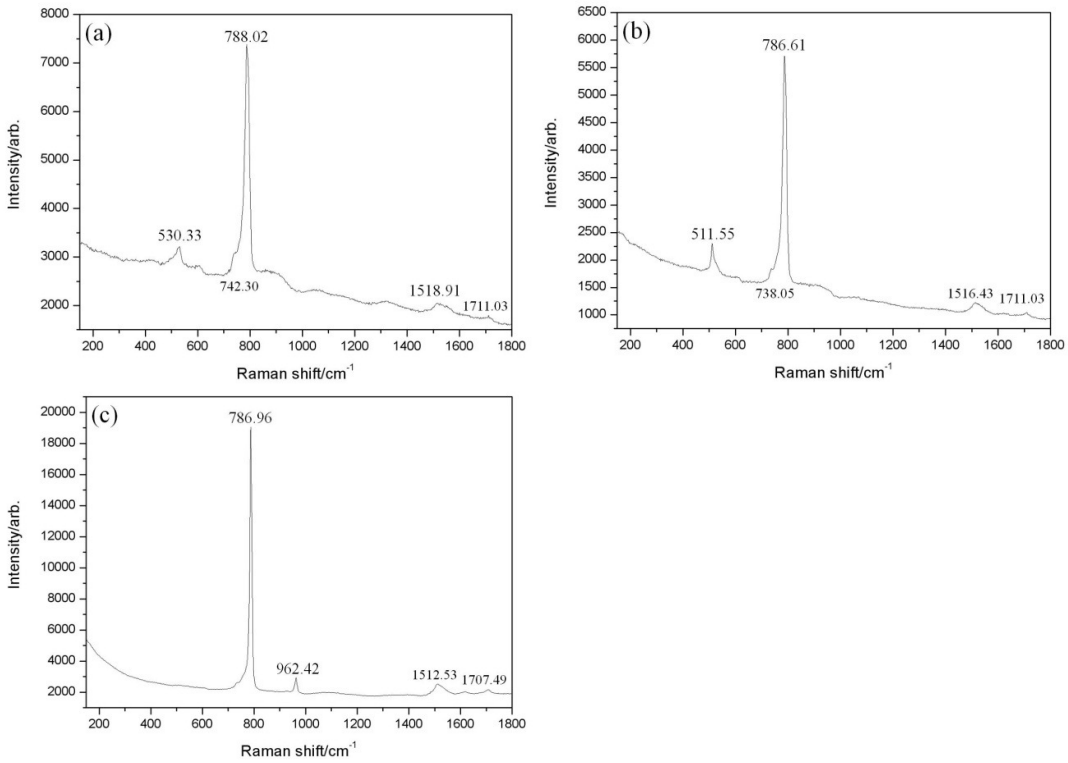

Figure 3-12 Raman spectra and observed bands for samples (a) 9, (b) 11 and (c) 13.

If graphite replaces activated carbon as a carbon source, after 3 and 30 min irradiation (**14**, **16**), the samples produced show the characteristic strong TO band of the cubic modification of silicon carbide at ca. 790 cm^{-1} and some weak features at high wavenumbers belonging to graphite at ca. 1580 cm^{-1} in the Raman spectrum (Figure 3-13). Sample **15**, produced after irradiation of the silicon + graphite mixture in the MMC for 15 min, shows bands in the Raman spectrum suggesting the presence of microcrystalline silicon, in agreement with the PXD in Figure 3-5b. The intense band at ca. 500 cm^{-1} has a small band width, suggesting it belongs to a crystalline sample.[22] The band is shifted from the usual value of 520 cm^{-1} for bulk silicon, and a shift to a lower frequency has been reported in the literature connected to microcrystalline silicon and due to a one-photon scattering process.[33] The other band at 280 cm^{-1} falls in a region of the silicon Raman spectrum where overtones of acoustic phonons are present and the band at ca. 920 cm^{-1} is due to a two TO-phonon overtone scattering for Si.[34]

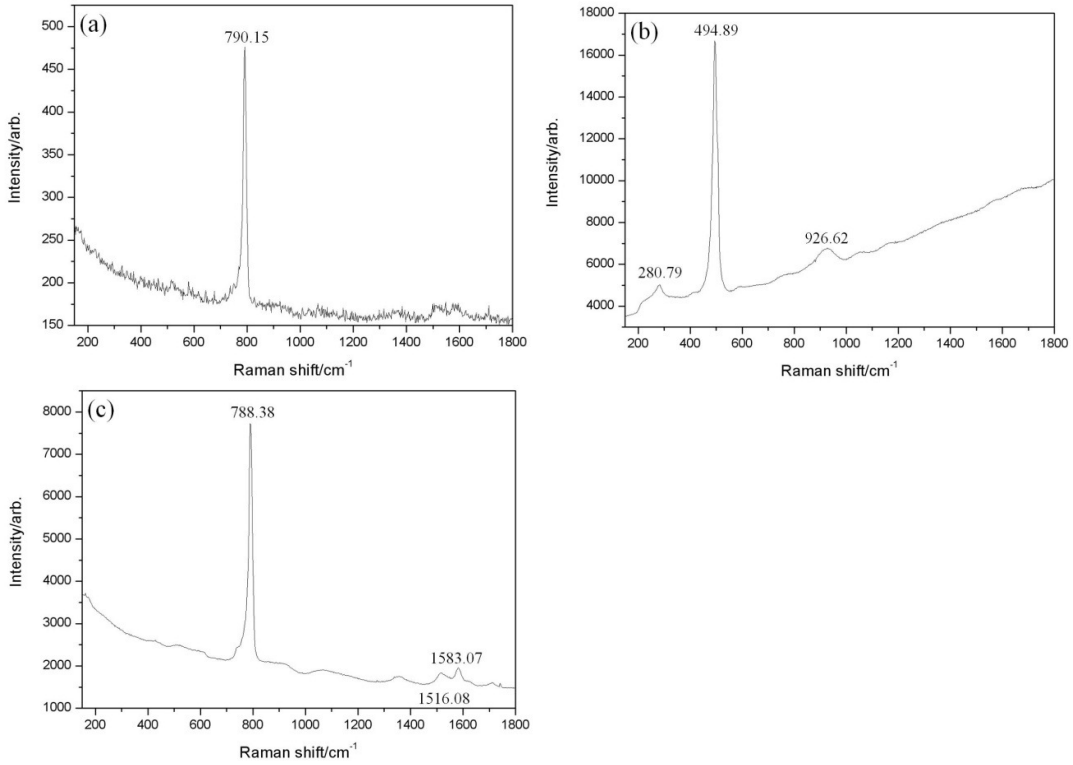

Figure 3-13 Raman spectra and observed bands for samples (a) 14, (b) 15 and (c) 16.

3.3.1.5 Transmission electron microscopy (TEM)

The detail of the nanostructure of the nanofibres from sample **2** was investigated using transmission electron microscopy (TEM) as shown in Figure 3-14. Fibres a few tens of nm in thickness are frequently observed and dark field imaging using suitable reflections frequently revealed a parallel striped structure within each wire, with the stripes having an irregular spacing of the order of a few nanometers as shown in Figure 3-14a. Comparison of the images with SAED patterns (e.g. Figure 3-14b) reveals that the stripes always run perpendicular to <111> directions. Moreover, the growth direction is always along the <111> direction. Higher magnification images, as shown in Figure 3-14c show that the stripes are a result of twinning on {111} planes of the β-SiC structure, in this case perpendicular to the growth direction. This frequent planar faulting also manifests itself as streaks in diffraction patterns perpendicular to the stripes, as shown in the diffraction pattern in Figure 3-14b. It is clear from this that the SiC forms nanowires with frequent twinning, but that the twinning is neither frequent nor regular enough that this qualifies as a specific polytype other than β-SiC. Twinning takes place when stress associated with crystal growth forces the nanowire to continue crystallization in another direction. Stacking faults and {111} twins are, in fact, relatively well documented in β-SiC nanofibres, especially in fibres of diameters of the order of tens of nm, including those that have been

synthesised previously via microwave plasma CVD or vapour transport methods.[35,36,37,38] These planar defects have been associated with the growth process itself rather than with a phase transition to one of the hexagonal SiC polytypes, irrespective of whether, for example, the carbide nanofibres grow via a Vapour–Liquid (VL) or Vapour–Liquid–Solid (VLS) mechanism.[39]

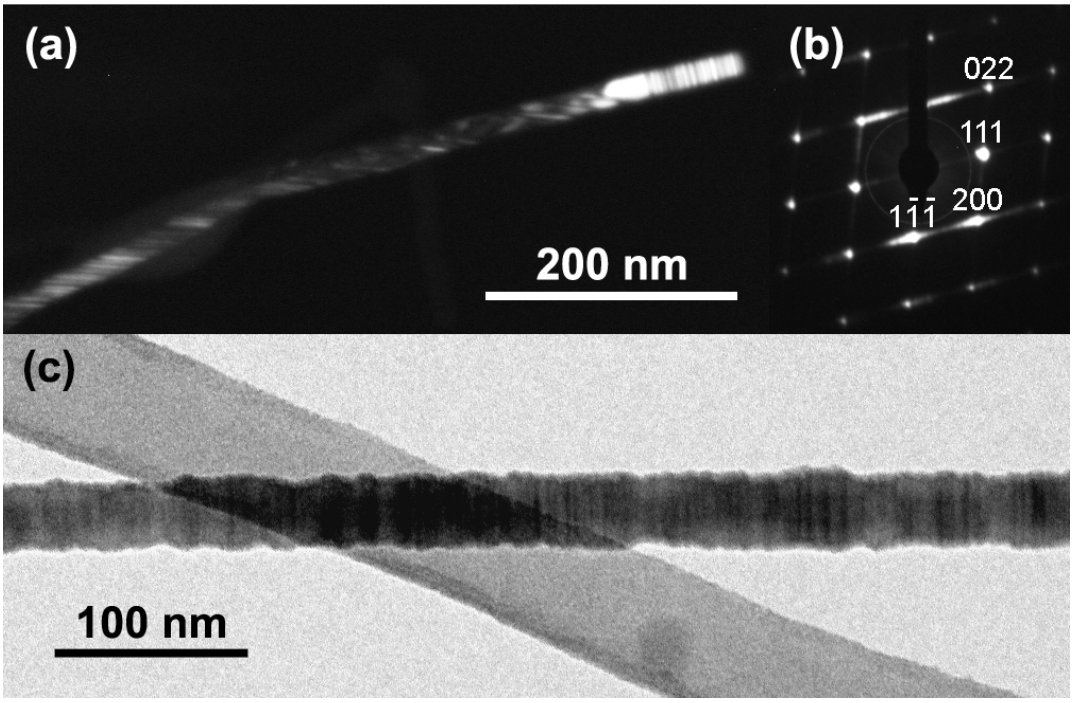

Figure 3-14 TEM micrographs of β-SiC nanofibres from sample 2 showing (a) dark field image of a nanowire showing frequent twinning (b) [$0\bar{1}1$] selected area diffraction from the right hand end of this nanowire; (c) higher magnification bright field image of a SiC nanowire showing frequent twinning perpendicular to the growth direction.

3.3.1.6 Discussion

The conversion of elemental Si and C to form SiC from is a 1-step process:

$$Si + C \rightarrow SiC \qquad \textbf{(1)}$$

The melting point of Si has been reported to occur at ca. 1400 °C,[20] a temperature likely to be reached in these experiments as the activated carbon starts absorbing microwaves.[10] Hence, a growth mechanism based on a direct liquid-solid reaction between molten silicon and carbon can be proposed. Previous reports have suggested that, reaction **(1)** conventionally proceeds via dissolution of solid carbon in liquid silicon.[35] In particular, it has been reported carbon dissolves substitutionally in Si at temperatures of 1200 - 1400 °C. The carbon diffuses through liquid silicon and β-SiC precipitates from the supersaturated

melt.[40] It is therefore possible that a similar process occurs in a microwave field, although no direct evidence can be drawn from analysis of samples at short reaction times to confirm that this is the case.

It is well established that the power dissipated in the material (or power density) is proportional to the electric field strength inside the material squared (see Chapter 1, section 1.3.1),[41] which in turn is a function of the cavity dimensions and design. The use of an MMC gives rise to the creation of power densities several orders of magnitude lower in comparison to a SMC (see following section). Electron micrographs of material processed in the MMC indicate that fibres grow at the interfaces between particles. This can be caused by the enhanced heating rates at such interfaces resulting from interfacial polarisation phenomena.[42] Such effects create highly localised and selective temperature rises which may explain the formation of the SiC nanowire structures, possibly crystallising and growing from molten silicon as carbon is dissolved as already explained above.

Considering interfacial polarisation, the use of a binder is essential to enable both reaction and nanofibre growth to occur in the MMC environment. The binder is fundamental to achieve intimate mixing and allow the intergrain void space to be minimised as a result of successful pelleting.[43] Although, for example, all syntheses involving silicon and carbon were ball milled prior to mixing, the inherent smaller particle size and higher surface area of the activated carbon over graphite (confirmed by SEM micrographs of the starting materials) also acts so as to maximise interfacial contact on mixing and pressing (see Appendix).

Hence, it is not surprising that a combination of activated carbon and binder provides the optimum conditions for nanofibre growth. Further, if a postulate of interfacial polarisation is indeed correct, one can understand how the MMC reactions employing water bound Si plus activated carbon lead to pure β-SiC in much shorter reaction times than equivalent dry pressed Si plus graphite preparations. It is even possible that water, as a polar liquid MW susceptor, acts so as to promote initial local dielectric heating at grain boundaries. The mixture of powders may then become ‘lossy’ enough to continue the heating process while water is driven out of the material by evaporation. A similar heating stage process has been proposed by Meek in the microwave sintering of oxide materials using sintering aids.[44] Interestingly if the water volume is increased then the beneficial binding effects begin to be countered (the conversion to silicon carbide is delayed, Figure 3-4). Similar detrimental

effects on reaction time and phase purity were also encountered in preliminary experiments in which other solvents of varying polarity and viscosity (e.g. acetone, ethylene glycol) replace water. These alternative solvent experiments are still under investigation for a wider range of liquids, but the role of water as primarily a binder would appear to be corroborated in that the loss tangents of ethylene glycol (1.350) and acetone (0.054) are respectively greater and less than that of water (0.123).[45] In MMC syntheses without a binder, reaction from Si and C to SiC does not proceed to completion despite the excellent and well-documented MW susceptor properties of both graphite and activated carbon.[46,40] This suggests that the power density inside the material is insufficient to enable the reaction temperature to be reached.

In MMC syntheses from Si plus C the presence of surrounding graphite is fundamental not only as a microwave susceptor[11] but also as a reductant providing a low partial pressure of O_2 in the environment surrounding the pellet. In the former context, the MW reactions are driven by the MW susceptibility of the carbon reactant and surrounding graphite; silicon being lower loss than graphite. That these reactions can be performed in air is important in terms of designing convenient and relatively inexpensive scaled-up processes.

Pellets produced with graphite, **13–16**, always fractured during reaction in the MMC reactor, tended to disintegrate and were difficult to recover. Powder patterns from these set of reactions, reported in Figure 3-5, always contained graphite peaks, even after relatively long irradiation times. Further, only at long irradiation times (e.g. **16**) was there no evidence of residual silicon. As with the activated carbon reactions above, no silica reflections were evident for any of the irradiation times employed.

3.3.2 High-power singlemode cavity (SMC) microwave syntheses of SiC

3.3.2.1 Synthesis and PXD studies

Results from syntheses performed in the TE_{10n} single mode cavity (SMC) reactor demonstrated that under these conditions graphite could be successfully used as a source of carbon and synthesis times could be improved at least ten-fold from the fastest reactions in the MMC. *In-situ* optical pyrometer measurements, taken during the course of reaction, recorded temperatures higher than 1873 K. The heating rate over the course of these reactions exceeds 500 K s^{-1}(see Appendix for optical pyrometer output).

PXD showed that phase-pure β-SiC was obtained from a dry pellet of Si plus activated carbon after only 20 s (**17**; Figure 3-15). Reactions performed for longer irradiation time (e.g. beyond 25 s, **18-22**) also produced β-SiC as single phase product. Beside the (111) plane of β-SiC, a shoulder in the PXD suggests the existence of stacking faults in the as-produced powders.

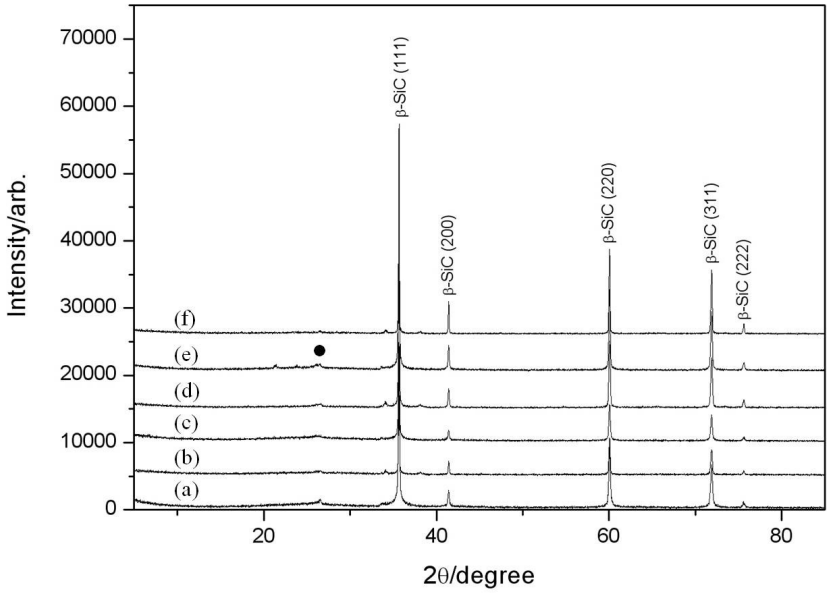

Figure 3-15 PXD patterns of samples: (a) 17 (20 s at 3 kW); (b) 18 (25 s at 3 kW); (c) 19 (30 s at 3 kW); (d) 20 (32 s at 3 kW); (e) 21 (40 s at 3 kW); (f) 22 (45 s at 3 kW). Reflections from graphite (●) are also indicated.

If graphite replaces activated carbon, PXD demonstrated that production of phase-pure β-SiC was not influenced by the carbon precursor chosen and it is possible to obtain a phase-pure product after 20 s (**24**, Figure 3-16). Reactions performed at 40 s (**26**) produced β-SiC with the presence of silicon as a minority phase (~ 14 wt %).

To study the influence of the power applied, an experiment has been performed choosing a higher power, 9 kW, applied for 13 s (**27**). The microwave energy absorbed by the pellet in 13 s at 9 kW can be compared with the energy provided to sample **26**, e.g. a power of 3 kW for 40 s applied.

From the PXD (Figure 3-17) it can be seen that there was not full conversion of the starting materials to β-SiC and reflections belonging to unreacted silicon are still visible in the diffraction pattern.

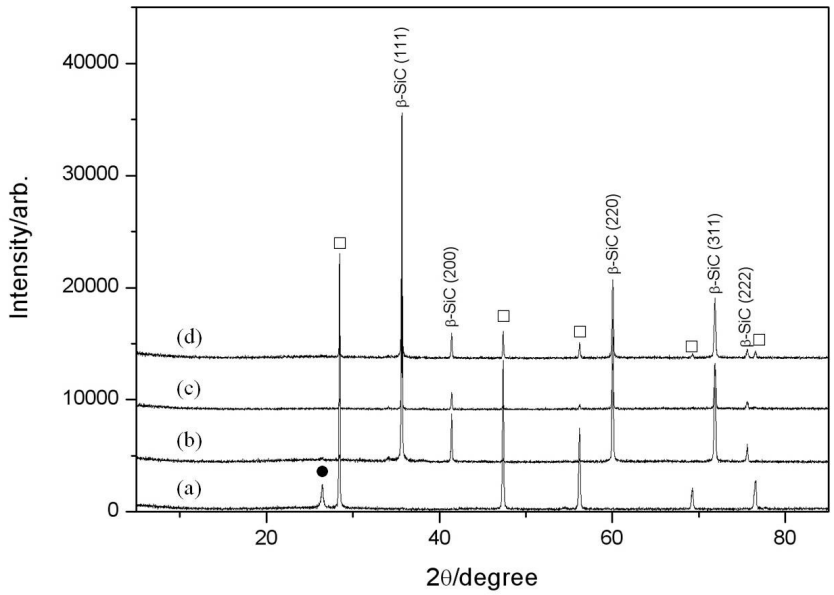

Figure 3-16 PXD patterns of samples synthesised: (a) 23 (10 s at 3 kW); (b) 24 (20 s at 3 kW); (c) 25 (30 s at 3 kW); (d) 26 (40 s at 3k W). Reflections from graphite (●) and silicon (□) are also indicated.

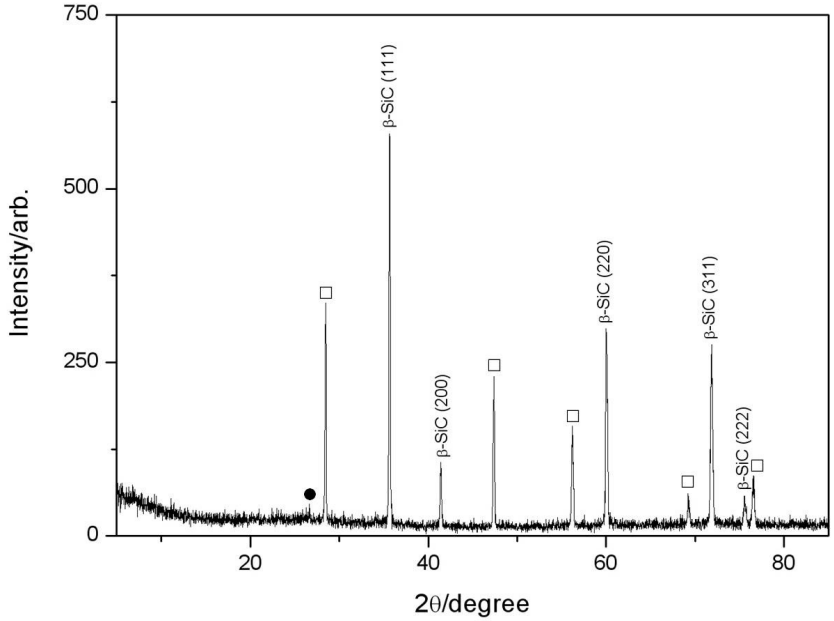

Figure 3-17 PXD patterns of sample 27 synthesised for 13 s at 9 kW. Reflections from graphite (●) and silicon (□) are also indicated.

3.3.2.2 Rietveld refinement data

Rietveld refinements on 1 h scans (Figure 3-18, Figure 3-19) for the as-produced sample starting from a mixture of Si and activated carbon/graphite (selected samples **17**, **21**, **24** and **26**) were performed using the zinc blende structure of β-SiC as a starting model. The background was modelled using a linear interpolation function (function 7 within GSAS). Scale factor, zero point and cell parameters were also refined in initial cycles. Peak widths and profile coefficients (peak shape was modelled using the Thompson-Cox-Hastings

pseudo Voigt function; peak shape function 2 within GSAS) were subsequently refined. Ensuring that all observed reflections were fitted, graphite was input for samples **17**, **21** and **24** as a secondary phase were relevant and phase fractions refined. For samples **24** along with graphite, 6H-SiC and Si were added as secondary phases. In sample **26** after the reflections from the β-SiC phase were fitted, Si was added as an additional phase. All refinements converged smoothly in final cycles. Data for **1–5** clearly demonstrate that the structure and stoichiometry of the carbide are invariant with time (e.g. Table 3-3 for **1**, **2** and **4**; Figure 3-6).

The cubic lattice parameter for the selected samples are in excellent agreement with literature values[21] as are the Si–C distances that have values between 1.88457(6) Å for sample **17** and 1.88597(4) Å for sample **24** (Table 3-8 and Table 3-10, Figure 3-18a and Figure 3-19a respectively).

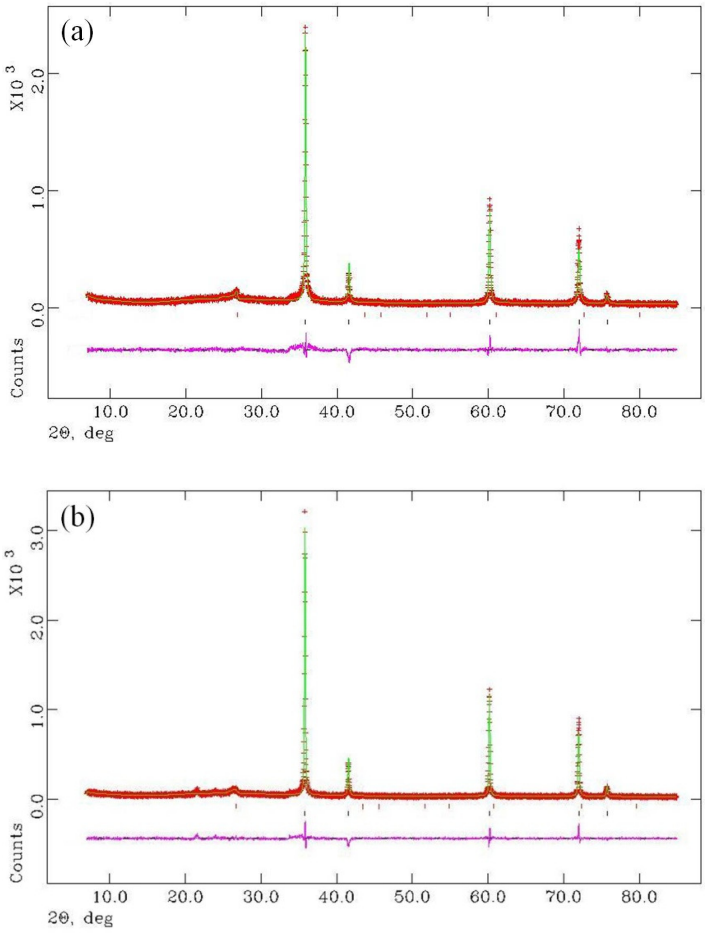

Figure 3-18 Exemplar profile plots for Rietveld refinements against PXD data. Shown are: (a) 17 and (b) 21 (see Table 3-2). Crosses (red) indicate observed data, the upper continuous line (green) shows the calculated profile, the lower continuous line (magenta) the difference and tick marks indicate different crystalline phases (dark blue β-SiC, red graphite).

Instrument, radiation	X-ray, Cu $K_{\alpha 1}$	
Nominal stoichiometry (Sample No)	β-SiC (**17**)	β-SiC (**21**)
Phases, fractions / wt %	β-SiC: 83(4) % Graphite: 16(6) %	β-SiC: 87(7) % Graphite: 12(3) %
Crystal system, Space group	Cubic, F $\bar{4}$ 3 m	
Z	4	
M	160.388	
a-parameter / Å Unit cell volume / $Å^3$	4.3522(4); 82.44(1)	4.3531(5); 82.49(2)
Calculated density, ρ_X / g cm^{-3}	3.231	3.229
Observations, parameters	4612, 26	4612, 25
R_p	11.78	12.35
R_{wp}	15.48	16.11
χ^2	1.62	1.486

Table 3-7 Exemplar crystallographic data from Rietveld refinements against PXD data. Shown are data for 1, 2 and 4.

Atoms bonds	Interatomic distance/ Å (at 293 K)	
Sample No	**17**	**21**
Si1 – C1 x4	1.88457 (6)	1.88497(4)
Atoms angle	Angle/ º (at 293 K)	
Sample No	**17**	**21**
C1 - Si1 – C1 x4	109.471(2)	109.471(1)
Si1 – C1 – Si1 x4	109.471(2)	109.471(1)

Table 3-8 Interatomic distance and bond angles for samples 17 and 21.

Longer period reactions (e.g. 20 s, **24**) using graphite as C source, yielded β-SiC with 6H-SiC (α-SiC) present as a secondary phase (17 wt % from Rietveld refinement against PXD data for **24**, for example).

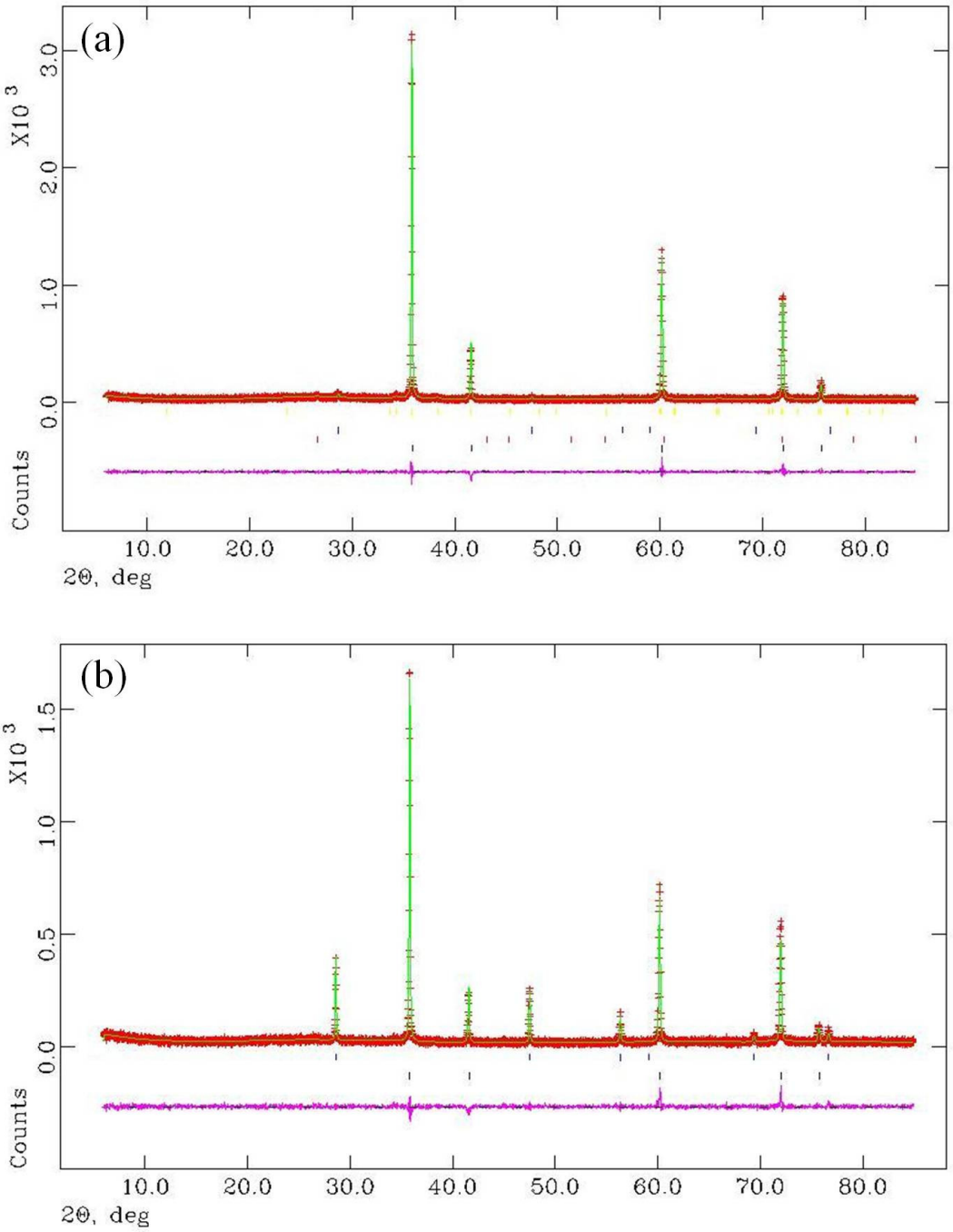

Figure 3-19 Exemplar profile plots for Rietveld refinements against PXD data. Shown are: (a) 24 and (b) 26 (see Table 3-2). Crosses (red) indicate observed data, the upper continuous line (green) shows the calculated profile, the lower continuous line (magenta) the difference and tick marks indicate different crystalline phases (dark blue β-SiC, red graphite, blue Si, yellow 6H-SiC).

Instrument, radiation	X-ray, Cu $K_{\alpha 1}$	
Nominal stoichiometry (Sample No)	β-SiC (**24**)	β-SiC(**26**)
Phases, fractions / wt %	β-SiC: 80(2) % Graphite: 2(1) % Si: 0.8(1) % 6H-SiC: 17(2) %	β-SiC: 86(7) % Si: 14(3) %
Crystal system, Space group	Cubic, F $\bar{4}$ 3 m	
Z	4	
M	160.388	
a-parameter / Å Unit cell volume / Å^3	4.3554(6); 82.62(3)	4.3550(5); 82.60(1)
Calculated density, ρ_X / g cm^{-3}	3.223	3.224
Observations, parameters	4671, 48	4671, 47
R_p	11.52	13.22
R_{wp}	15.40	17.32
χ^2	1.088	1.122

Table 3-9 Exemplar crystallographic data from Rietveld refinements against PXD data. Shown are data for 24 and 26.

Atoms bonds	Interatomic distance/ Å (at 293 K)	
Sample No	**24**	**26**
Si1 – C1 x4	1.88597(4)	1.88579 (5)
Atoms angle	Angle/ ° (at 293 K)	
Sample No	**24**	**26**
C1 - Si1 – C1 x4	109.471(1)	109.471(3)
Si1 – C1 – Si1 x4	109.471(1)	109.471(3)

Table 3-10 Interatomic distance and bond angles for samples 24 and 26.

3.3.2.3 SEM

The SEM micrographs of the sample synthesised from dry pellets of silicon and activated carbon in the SMC show that for reaction times up 40 s (samples **17-21**, Figure 3-20) the microstructure is essentially invariant. Irregular particles with sizes up to few microns across from the SEM images in Figure 3-20 a-e look partially fused together to form a

porous matrix. Reactions beyond 45 s, **22** (Figure 3-20f), yield a significant increase in the particle size and SiC faceted crystallites 5 – 10 μm or more across.

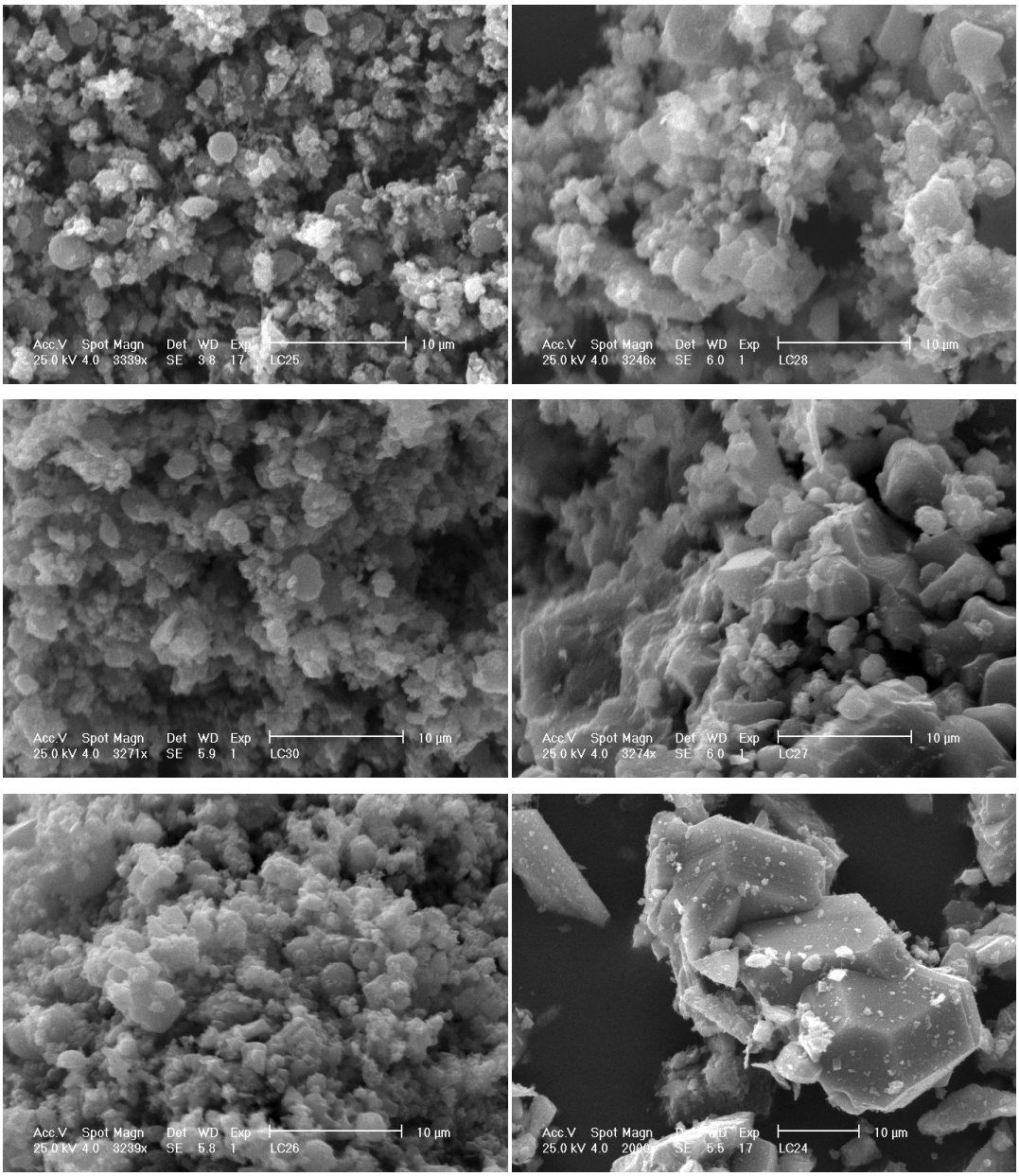

Figure 3-20 SEM micrographs of sample: (a) 17 (20 s at 3 kW); (b) 18 (25 s at 3 kW); (c) 19 (30s at 3 kW); (d) 20 (32 s at 3k W); (e) 21 (40s at 3 kW); (f) 22 (45 s at 3k W) (see Table 3-2).

When using a SMC microwave setup and starting from graphite as carbon precursor, a striking difference can be noticed for SiC products compared to the microstructure of the samples made in the MMC (Figure 3-10a) or the ones synthesised using the same setup but employing dry pellets of silicon plus activated carbon (Figure 3-20). SEM images of **23-24** (Figure 3-21a-b) shows that after only 10 s irradiation (Figure 3-21a) products composed of well-formed, faceted crystallites sized 5 – 10 μm or more across can be achieved.

Increasing the irradiation time leads to further crystal growth; crystallites of **25 - 26** were typically few μm across. Furthermore, while at short irradiation times (samples **23**, **24**) cubic crystallites are present, when irradiated for 30 – 40 s samples (**25**, **26**) show hexagonal faceted crystallites. Comparing the microstructure of the samples made in the MMC (Figure 3-10a) suggests that the strongly contrasting heating rate in the different cavities causes the formation of different product morphologies.

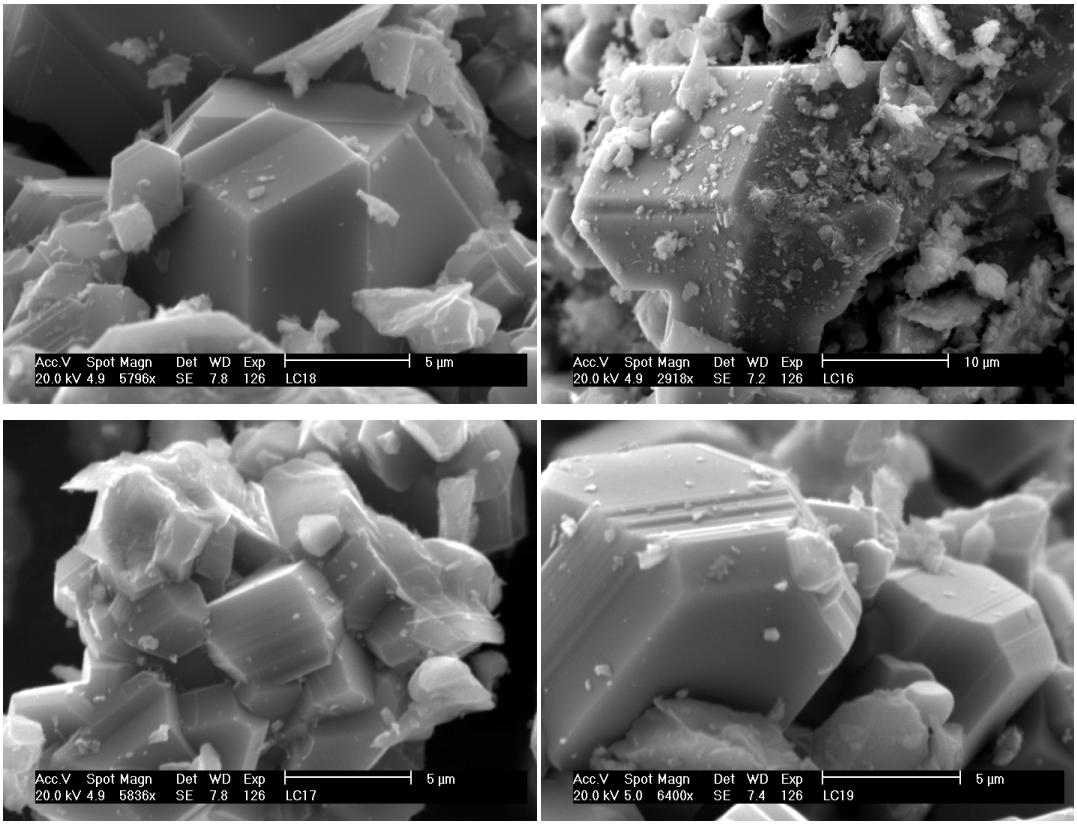

Figure 3-21 SEM micrographs of sample: (a) 23 (10 s at 3 kW); (b) 24 (20 s at 3 kW); (c) 25 (30 s at 3 kW); (d) 26 (40 s at 3k W).

The SEM micrograph of sample **27** synthesized after 13 s with a power applied of 9 kW confirms a very crystalline silicon carbide product can be achieved using graphite in a SMC (Figure 3-22).

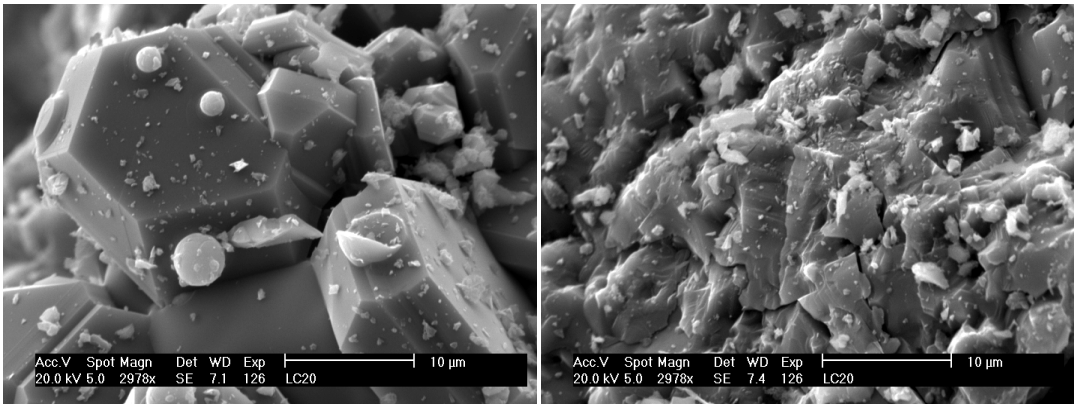

Figure 3-22 SEM micrographs of sample 27 synthesised for 13 s at 9 kW.

3.3.2.4 Raman spectroscopy

Raman spectra of products obtained after irradiating for times of up to 45 s in a SMC using activated carbon (selected samples **17**, **19**, **21**, **22**) are reported in Figure 3-23. After only 20 s irradiation (**17**) the Raman spectrum exhibits a very strong band at 780 cm^{-1} and a less intense band at 940 cm^{-1}. These are the Transverse Optical (TO) and Longitudinal Optical (LO) Raman-active mode in β-SiC and are slightly shifted with respect to the usual bulk values.[22] The bands at ca. 1330 and 1560 cm^{-1} can be assigned to the D and G bands from graphite and at high wavenumbers it is possible to find weak bands related to the second order Raman spectrum of β-SiC (ca. 1478 cm^{-1}).[31,32] Samples **19** and **21**, produced respectively after irradiation for 30 and 40 s, are very similar and just three bands are visible; the TO band from β-SiC and the two bands (D and G) attributable to carbon. As already noted from the SEM micrographs, sample **22** (45 s irradiation) differs from the products synthesised at shorter times. From the micrograph in Figure 3-20f it can be seen that **22** is highly crystalline with increased crystallite sizes relative to the other samples. The Raman spectrum of **22** has bands widths which are narrower due to this high crystallinity. Both the TO and LO Raman-active modes of β-SiC can be seen at ca. 790 and 960 cm^{-1} along with overtones in the high wavenumber region (1500-1700 cm^{-1}). The band at ca. 500 cm^{-1} is believed to be due to residual silicon. The presence of silicon has already been indicated in the Rietveld refinements of samples irradiated for long times (sample **26**, Figure 3-19b).

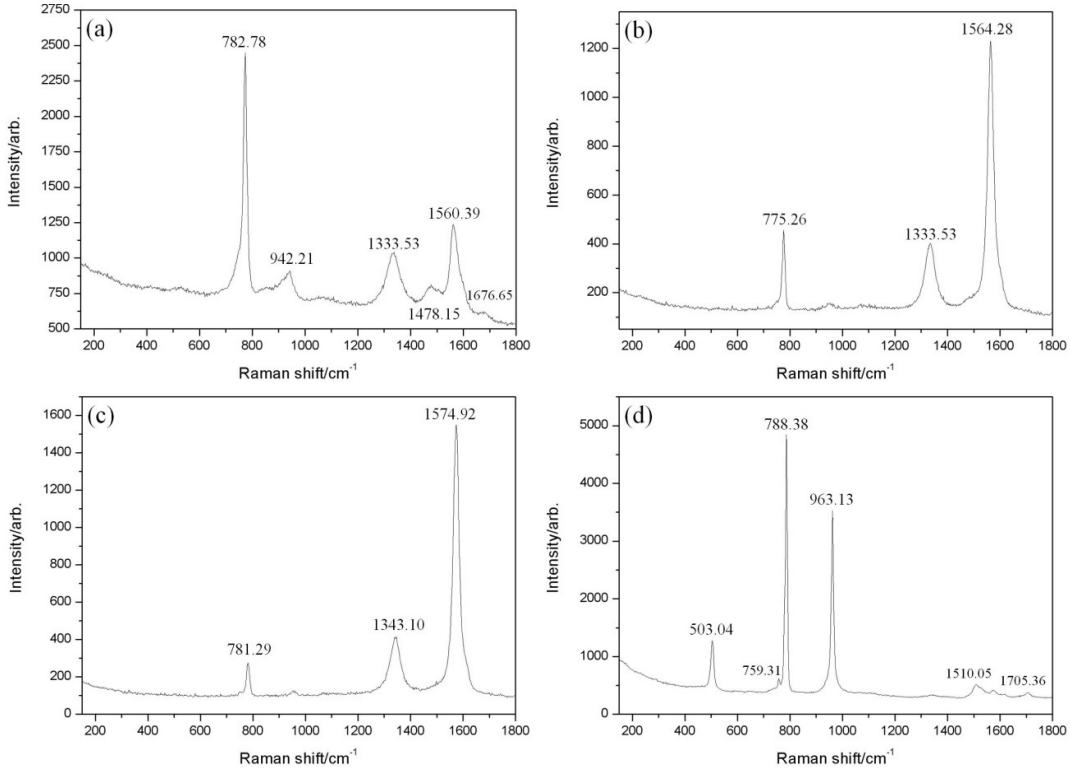

Figure 3-23 Raman spectra and observed bands for samples (a) 17, (b) 19, (c) 21 and (d) 22.

Samples produced starting from a mixture of silicon and graphite in a SMC show very narrow bands after only 20 s of irradiation (Figure 3-24). The bands present in each sample belong to the TO and LO modes of β-SiC respectively at 790 and 960 cm^{-1}, and the narrow band width suggests the products are well crystallised, in agreement with the SEM micrographs in Figure 3-10. In the low wavenumber region, in samples **25** and **26** a sharp band at ca. 500 cm^{-1} is visible, likely to be attributed to silicon. This is in agreement with the Rietveld refinement of sample **26** (Figure 3-19b) which indicated the presence of 14 wt% of silicon. Due to the temperature of the reaction, that exceeds the maximum temperature recorded by the optical pyrometer used of 1600 °C, it is possible that the silicon comes from recrystallisation from gas rather than from unreacted material. The high wavenumber region of the spectra is dominated either by carbon bands (**24** and **26**, D and G bands at ca. 1330 and 1560 cm^{-1} respectively) or by β-SiC overtones (**25**).

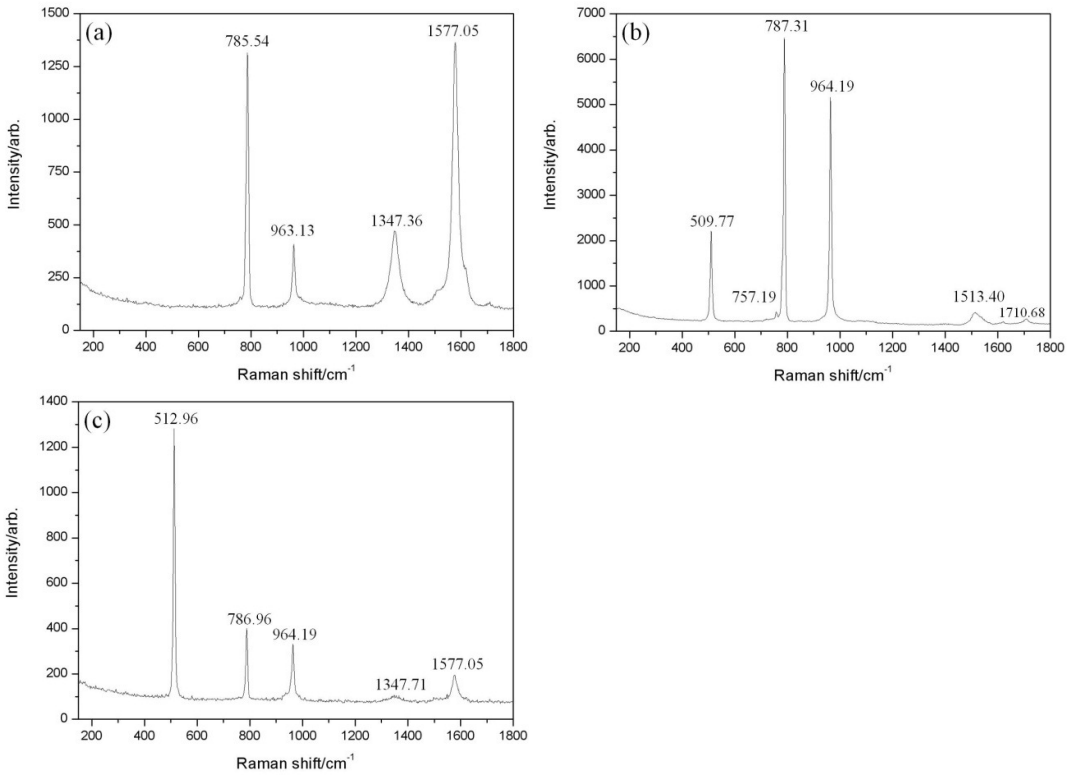

Figure 3-24 Raman spectra and observed bands for samples (a) 24, (b) 25 and (c) 26.

In agreement with the PXD of sample **27** (Figure 3-17), which shows a partially reacted sample, the Raman spectrum of sample **27** (Figure 3-25) presents a dominant peak at ca. 514 cm^{-1} due to a one-photon scattering process in microcrystalline silicon.[33] The other band at 290 cm^{-1} falls in a region of the silicon Raman spectra where overtones of acoustic phonons are present. The remaining two bands originate from the TO and LO Raman active mode of β-SiC (at ca. 780 and 960 cm^{-1}).

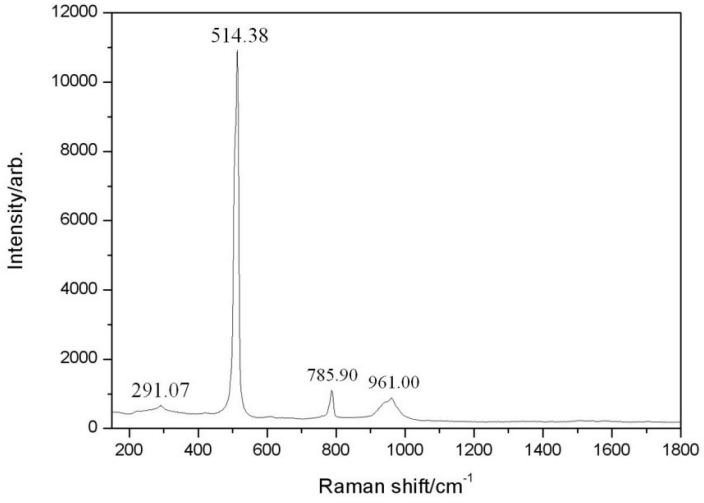

Figure 3-25 Raman spectra and observed bands for sample 27.

3.3.2.5 Discussion

Results from syntheses performed in the TE_{10n} SMC reactor demonstrated that under these conditions both activated carbon and graphite could be successfully used as a source of carbon and synthesis times could be improved at least ten-fold from the fastest reactions in the MMC.

Consideration of the effect of the carbon source on the SMC reactions leads to two interesting observations. First, when using activated carbon, the crystallite size of the carbide product appears reproducibly smaller compared to samples synthesised from graphite, for approximately equivalent irradiation times. No nanocrystalline products, either particles or fibres, are observed, however, for any durations (in contrast to MMC reactions; see previous section). Second, for longer irradiation times (for example samples **20-22**) SiC products contain not only β-SiC (i.e. 3C-SiC) but also appreciable 6H-SiC as a secondary phase (~20 wt %). Optical pyrometry evidenced that both the heating and cooling rates in the SMC Si plus activated carbon reactions were extremely high (see Appendix). Activated (disordered, amorphous) carbon typically couples more efficiently to MWs than graphite, achieving higher heating rates and peak temperatures.[46,40] It seems likely that these factors favour the formation of metastable 6H-SiC. Increasing the applied power and/or optimising the cavity could therefore be exploited to maximise the heating rate and the reaction temperature and, in principle, enable hexagonal polymorphs of SiC (α-SiC) to be prepared in preference to the cubic polytype.

As in the MMC reactions (reported in section 1.3.1), the reactions to form SiC from elemental Si are relatively straightforward and proceed via reaction **(1)**. Previous reports have suggested that reaction **(1)** conventionally proceeds *via* the dissolution of carbon in liquid Si and precipitation of SiC from the supersaturated melt.[40] Si melts at 1687 K and the optical pyrometer measurements would concur that it is possible that a similar process occurs in a TE_{10n} reactor. The PXD results suggest β-SiC is produced with an eventual transition to α-SiC polymorphs, hence a peak temperature in excess of 2373 K is plausible.[47] The samples synthesised using both MMC and SMC are likely to contain amorphous carbon, but its presence has not been studied quantitatitely.

It is well established that the power dissipated in the material (or power density) is proportional to the electric field strength inside the material squared[41] (equation **(1-4)** Chapter 1, section 1.3.1), which in turn is a function of the cavity dimensions and design.

Complete reaction in the SMC is possible both using graphite and without a binder. This would agree with the supposition that higher reaction temperatures are achieved in the SMC due to the creation of power densities several orders of magnitude higher than the MMC counterpart. During experiments it was noted that the reflected power was high during the initial 1-2 s of the experiment. However, after 2 s reflected power dropped to essentially zero indicating that the dielectric loss had increased to the point that very high coupling efficiency occurred. Almost certainly this is consistent with melting of the materials present and the inducement of thermal runaway in the material. Even in the SMC reactions surrounding graphite was fundamental both as a MW susceptor and also as a reductant providing a low partial pressure of O_2 in the atmosphere surrounding the pellet.

3.4 Conclusions

In summary, the synthesis of high purity β-SiC in air in timescales from 5 min to 20 s has been reported. The selection of Si and C sources, the use of water as a binder and the choice of applied MW source (power, cavity) are variables that can be used successfully to control carbide purity and processing time. In particular, synthesis of β-SiC has been achieved on minute timescales (≤ 5 min), by designing synthesis experiments that did not require reactive or cover gas environments. Furthermore for the first time, subsequent purification steps were not needed as the reactions can lead to nearly phase-pure SiC (an unknown amount of amorphous carbon is likely to be present).

Significantly, the mode and therefore rate of MW heating can be exploited to dictate carbide morphology from nanowires to large crystallites. By using more sophisticated higher power MW methods (like single mode cavity systems), reaction can be accomplished in air over second timescales reducing synthesis times and energy expenditure still further than MMC methods. Beyond the improvements in product purity, reduction of processing complexity (and cost) and reduction of processing times, it has been clearly demonstrated how the morphology of the products from MW syntheses can be controlled *via* the mode of heating.

These results can be understood generally in terms of the reaction chemistry and microwave interactions. It is clear that in order to gain complete control over phase formation, crystal growth and to achieve further understanding of the reaction mechanism, it will be necessary to develop state-of-the-art *in-situ* measurement techniques. Those are capable of characterisation over short time scales and under extreme conditions, offering a

way to progress towards energy-efficient, continuous manufacturing. The fact that these reactions can be performed in air is important in terms of designing convenient and relatively inexpensive scaled-up processes.

[1] Y. Yang, Z.-M. Lin and J.-T. Li, *J. Eur. Ceram. Soc.*, 2009, **29**, 175.

[2] G. Liu, K. Yang and J. Li, *J. Phys. Chem.*, 2008, **112**, 6285.

[3] P.D. Ramesh, B. Vaidhyanathan, M. Ganguli and K. J. Rao, *J. Mater. Res.*, 1994, **9**, 3025.

[4] J. Peng, J. Binner and S. Bradshaw, *J. Mater. Synth. Proces.,* 2001, **9**, 6.

[5] L.N. Satapathy, P.D. Radamesh, D. Agrawal and R. Roy, *Mat. Res. Bul.*, 2005, **40**, 1871.

[6] B. Lu, J.X. Liu, H.W. Zhu and X.H. Jiao, *Mat. Sci. For.*, 2007, **561-565**, 1413.

[7] S. R. Vallance, S. Kingman and D. H. Gregory, *Adv. Mater.*, 2007, **19**, 138.

[8] S. R. Vallance, S. Kingman and D. H. Gregory, *Chem. Commun.*, 2007, **7**, 742.

[9] S. R. Vallance, D. M. Round, C. Ritter, E. J. Cussen, S. Kingman and D. H. Gregory, *Adv. Mater.*, 2009, **21**, 4502.

[10] K. J. Rao, B. Vaidhyanathan, M. Ganguli, and P. A. Ramakrishnan, *Chem. Mater.* 1999, **11**, 882.

[11] J. A. Menendez, A. Arenillas, B. Fidalgo, Y. Fernandez, L. Zubizarreta, E. G. Calvo and J. M. Bermúdez, *Fuel. Process. Technol.*, 2010, **91**, 1.

[12] J. Krupka, J. Breeze, A. Centeno, N. Alford, T. Claussen and L. Jensen, *IEEE Trans. Microw. Theory Tech.*, 2006, **54**, 3995.

[13] T. Ohlsson and P. O. Risman, *J. Microw. Power Electromagn. Energy*, 1978, **13**, 303.

[14] http://www.fiz-karlsruhe.de/icsd.html (last access on 8/07/2011)

[15] W. Kraus and G. Nolze, Federal Institute for Materials Research Testing, Berlin, Germany, 1998.

[16] A. C. Larson and R. B. von Dreele, *The General Structure Analysis System*, 2000, Los Alamos National Laboratories, Report LAUR 086-748, LANL, Los Alamos.

[17] B. H. Toby, *J. Appl. Crystallogr.*, 2001, **34**, 210.

[18] S. R. Tennison, *Appl. Catal. A: General*, 1998, **173**, 289-311.

[19] L. Carassiti, A. Jones, P. Harrison, P. S. Dobson, S. Kingman, I. MacLaren and D. H. Gregory, *Energy Environ. Sci.*, 2011, **4**, 1503.

[20] L. Shi, H. Zhao, Y. Yang, Z. Li and C. Tang, *Pow. Tech.*, 2006, **169**, 71.

[21] T. Kawamura, *Mineralog. J.*, 1965, **4**, 333.

[22] S. Nakashima and H. Harima, *Phys. Stat. Sol. a*, 1997, **162**, 39.

[23] S. G. Sundaresan, A. V. Davydov, M. D. Vaudin, I. Levin, J. E. Maslar, Y.-L. Tian and M. V. Rao, *Chem. Mater.*, 2007, **19**, 5531.

[24] S. Rohmfeld, M. Hundhausen, L. Ley, L., *Phys. Status Solidi B*, 1999, **215**, 115.

[25] J. C. Burton, L. Sun, M. Pophristic, S. J. Lukacs, F. H. Long, Z. C. Feng and I. T. Ferguson, *J. Appl. Phys.*, 1998, **84**, 6268.

[26] J. C. Burton, F. H. Long and I. T. Ferguson, *J. Appl. Phys.*, 1999, **86**, 2073.

[27] C. Meier, S. Lüttjohann, V. G. Kravets, H. Nienhaus, A. Lorke, H. Wiggers, *Physica E*, 2006, **32**, 155.

[28] M. J. Matthews, M. A. Pimenta, G. Dresselhaus, M. S. Dresselhaus and M. Endo, *Phys. Rev. B*, 1999, **59**, 6585.

[29] H. Li, Y. Zhu, Z. Mao, J. Gu, J. Zhang and Y. Qian, C*arbon,*, 2008, **47**, 328.

[30] D. S. Knight and W. B. White, *J. Mater. Res.*, 1989, **4**, 385.

[31] W. Windl, K. Karch, P. Pavone, O. Schutt, D. Strauch, W. H. Weber, K. C. Hass, and L. Rimai, *Phys. Rev. B*, 1994, **49**, 8764.

[32] D. Olego and M. Cardona, *Phys. Rev. B*, 1982, **25**, 1151.

[33] R. J. Nemanich, E. C. Buehler, Y. M. Legrice, R. E. Shroder, G. N. Parsons, C. Wang, C. Lucovsky and J.B. Boyce, *J. Non-Cryst. Solids*, 1989, **114**, 813.

[34] P. A. Temple and C. E. Hathaway, *Phys. Rev. B*, 1973, **7**, 3685.

[35] J. Narayan, R. Raghunathan, R. Chowdhury and K. Jagannadham, *J. Appl. Phys.*, 1994, **75**, 7252.

[36] S. M. Pickard, B. Derby and E. A. Feest, *J. Mater. Sci.*, 1991, **26**, 6207.

[37] W.-S. Seo and K. Kuomoto, *J. Am. Ceram. Soc.*, 1996, **79**, 1777.

[38] S. Honda, Y.-G. Baek, T. Ikuno, H. Kohara, M. Katayama, K. Oura and T. Hirao, *Appl. Surf. Sci.*, 2003, **212–213**, 378.

[39] L. Wang, H. Wada and L. F. Allard, *J. Mater. Res.*, 1992, **7**, 148.

[40] A. R. Bean and R. C. Newman, *J. Phys. Chem. Sol.*, 1971, **32**, 1211.

[41] R. J. Meredith, *Engineers' Handbook of Industrial Microwave Heating*, The Institution of Electrical Engineers, London, UK, 1998.

[42] A. R. v. Hippel, *Dielectrics and Waves*, MIT Press, Cambridge,Mass, 1954.

[43] ed. R. A. Terpstra, P. Pex and A. de Vries, *Ceramic Processing*, Chapman & Hall, London, 1995.

[44] T. T. Meek, C. E. Holcombe and N. Dykes, *J. Mater. Sci. Lett.*, 1987, **6**, 1060.

[45] B. L. Hayes, *Microwave Synthesis: Chemistry at the Speed of Light*, CEM Publishing, Matthews NC, 2002.

[46] K.J. Rao, B. V. M. Ganguli, P. A. Ramakrishnan, *Chem. Mater.* 1999, **11**, 882.

[47] S. Sugiyama and M. Togaya, *J. Am. Chem. Soc.*, 2001, **84**, 3013.

4 Microwave synthesis studies in the SiO_2-C system

4.1 Introduction

Properties and applications of silicon carbide, SiC, have been discussed in Chapter 1 and it is clear that reducing the cost of the starting materials would be a further significant advantage when considering energy-efficient routes to silicon carbide particularly on an industrial scale. SiC powder is industrially produced by the Acheson process (Chapter 1) which involves carbothermal reduction of silica using coke and other additives in an electric furnace.[1,2] Temperatures as high as 2700 °C are employed and long reaction times are needed. The Acheson process is simple and cost effective since it relies on inexpensive raw materials, but has the disadvantage that the silicon carbide so-produced varies in quality and purity depending on its location within the furnace and usually coarse powders are produced. Post-processing involving milling of the powders is therefore needed to decrease their particle sizes, but this introduces impurities into SiC and increases manufacturing costs. The aim of this Chapter is to show the viability of the microwave method already proposed (Chapter 2) to synthesise silicon carbide using inexpensive silica and carbon as starting materials. This becomes especially important since it has already been shown in the previous chapter how processing time can be cut using microwave (MW) preparations. Reducing the cost of starting materials would be an additional driver for the possibility of scaling up this method.

In the literature, a vast number of articles have been published concerning the carbothermal reduction of silica to produce silicon carbide. These mainly utilise conventional heating and have already been reported in the literature review in Chapter 1. This section briefly describes previous microwave studies on the synthesis of silicon carbide starting from bulk silica and carbonaceous materials.

In 1996, the synthesis of ultrafine SiC powder was reported in which precipitated SiO_2 was reduced and carburised with various forms of C in a cylindrical multimode cavity (2.45 GHz, power unknown) in a nitrogen atmosphere.[3] A slightly higher ratio than 3:1 of $C:SiO_2$ was used to drive the reaction to completion. Reactants were held at temperatures up to 1350 °C for 20 minutes and post-treatment was needed to remove the unreacted starting materials. The microwave products were compared to conventionally heated ones, which underlined the advantages such as higher heating rates and, subsequently, decreased synthesis temperature and reaction times. Another study was published by the same

authors in early 1997 reporting the synthesis of ultrafine silicon carbide whiskers, but the reaction conditions do not seem to differ significantly from the previous ones and no explanation was proposed as to how the morphology from powders to whiskers can be controlled.[4]

Following a similar theme, a paper was published in 2009 on the synthesis and growth of SiC nanostructures using microwave radiation. It reported synthesis using pellets made of silica gel and either extra pure fine graphite or carbon black powders in a 1:3 ratio. The microwave heating process was performed at 2.45 GHz and 900 W for a period of 60 min in a silicon carbide crucible. The temperature reported on the optical pyrometer was 1454 °C and even in this case residual carbon needed to be removed subsequently by calcinations. The sample produced was characterized as nanosized β-SiC with different morphologies from spheres to long strand-like particles. As in the previous papers, the microwave reactions proved to be considerably faster than conventional methods and silicon carbide was reported to form at a lower temperature than the corresponding reaction in a coke-bed using an electrical tube furnace.

The synthesis of bamboo-like β-SiC nanowires by carbothermal reduction of silica using microwave irradiation was reported in 2010.[5] A sol-gel process was used to synthesise the silica employed and carbon was added to the surface of the silica in the alumina crucible used in the reaction. The microwave reaction was performed in air for 30 min at 2.45 GHz and an applied power of 800 W. The raw products were heated for 3 h in air at 700 °C and then immersed in HF for 10 h to remove excess carbon and silica respectively. After purification, no impurities were detected in the PXD pattern, but the Raman spectrum of the sample revealed bands belonging to carbon. A vapour-solid mechanism has been proposed for the formation of nanowires starting from carbon and SiO gas formed during reaction.

These synthetic studies clearly show that improvements can be achieved over conventional syntheses. However, challenges that remain to be overcome are:

- to remove subsequent purification steps,
- to reduce synthesis times (and energy expenditure) still further so that energy-efficient, continuous manufacturing becomes a possibility.

This chapter will discuss work carried out using instrumentation similar to that employed in the studies reported in the previous chapter. The following describes how SiO_2-C reactions can be performed using starting materials in the form of both pellets and loose powders. Results of the synthesis of β-SiC in air from silica and various form of C using a multimode microwave cavity (MMC) and singlemode microwave cavity (SMC) will be shown. From characterisation of the resulting products it will be demonstrated how the overall power absorbed is a key parameter in the processing.

4.2 Experimental: synthesis of silicon carbide

Either in the form of activated carbon or graphite, carbon materials have already been demonstrated to be good microwave absorbers.[6,7] By contrast, silica behaves as a transparent material when irradiated with microwaves and therefore is usually used for containing vessels and turntables in domestic microwave ovens. Initiation of heating is problematic in reactions between carbon and silica. Silica has a low dielectric loss at low temperatures (lower than that of silicon, Table 4-1), and does not generate heat while irradiated with microwaves at 2.45 GHz. As is generally valid for oxides, when the temperature of the system is raised, the dielectric properties improve and silica starts to couple more efficiently with microwaves.[8] The heating method employed here is to use graphite as susceptor to heat silica by thermal radiation to temperatures when it starts absorbing microwaves.

Material	Temp./ °C	ε′/ε″			$\delta=\tan^{-1}\varepsilon''/\varepsilon'$
		30 MHz	1 GHz	2.45 GHz	
Fused quartz	25	3.78/<0.001	3.78/<0.001	3.78/<0.001	$1.52\ 10^{-2}$
Silicon, semiconductor grade	25	-	4.3/<0.05	-	$6.\ 66\ 10^{-1}$
Silicon carbide	20	-	-	30/11	20.14

Table 4-1 Dielectric properties of silica, silicon and silicon carbide.[9]

It has been found in the literature that the dielectric losses of sintered or fused silica are low even at 1000 – 1200 °C and that preheating should be at temperatures close to 1700 °C. At that temperature silica is near its melting point and the ionic conduction losses

become sufficient to maintain silica in a molten state without the aid of further thermal radiation.[10]

Several experimental configurations were tried and improved, and clearly since silica is not a good microwave absorber, even in these sets of reactions, graphite has been used as susceptor to take advantage of the heat radiated by it in the first stage of reaction. Silica flour was applied around the reaction vessel to ensure thermal insulation. Regardless of the type of microwave applicator used, all experiments were performed on pellets and powders containing a stoichiometric amount of silica and carbon (1:3) to yield SiC according to equation (1):

$$SiO_2\ (s) + 3\ C\ (s) \rightarrow SiC\ (s) + 2\ CO\ (g) \qquad (1)$$

and reactions were repeated to ensure reproducibility. Since the carbothermal reaction mechanism involves evolution of harmful gas intermediates, such as CO, all reactions were carried out in a fumehood for safety reasons. In these studies a fixed power of 800 W was used for the multimode cavity syntheses. Activated carbon was chosen as carbon precursor since it has been shown (in the previous Chapter) that it successfully couples in a multimode cavity. The singlemode cavity reactor used, in collaboration with Prof. Kingman at the University of Nottingham, offered a tunable 0 - 2 kW microwave generator. Both MMC and SMC reactors were operated at 2.45 GHz. In SMC experiments, the carbon precursor of choice was graphite given the ease with which one can make pellets. In order to ensure experimental reproducibility, the reaction vessel was either placed in the centre of the single mode cavity, or for multimode reactions was always placed at the same position within the cavity.

After reaction, products were characterised using powder X-ray diffraction (PXD, Chapter 2, section 2.3.1.3) (PANalytical X'pert MPD, Cu $K_{\alpha 1}$ radiation). The data obtained were initially used to identify product phases by reference to the ICDD PDF database using the PANalytical program X'pert HighScore Plus.[11] A selected number of samples were scanned for 12 h (over a range of $5 \leq 2\theta\ /\ ° \leq 85$ with a step size of 0.017° 2θ) so that the data collected could be used to derive cell parameters by least squares fitting and quantitative phase fractions of crystalline components could be determined by Rietveld refinement (Chapter 2, section 2.3.2) using GSAS and EXPGUI packages.[12,13] Raman spectra (Chapter 2, section 2.3.3) were collected at room temperature to corroborate PXD results and to determine whether any amorphous phases were present. Experiments were performed using a Horiba LabRAM HR confocal microscope system with a 532 nm green

laser (Laser Quantum Ventus 532, 150 mW). A hole aperture of 50 μm, 600 gr mm^{-1} grating and a Synapse CCD detector were used for the experiment. The morphological changes of the starting material were observed and analysed by field emission scanning electron microscopy (FESEM) operating under high-vacuum conditions using a Hitachi S4700 microscope with 10 kV accelerating voltage and secondary electron detection. Samples for SEM of sufficient thickness were prepared by depositing powder on to a carbon tab.

4.2.1 MMC experimental details

Stoichiometric amounts of SiO_2 (Aldrich, -325 mesh, 99.6 %) and activated carbon (MAST Carbon Ltd.[14]) (1:3 molar ratio; typical sample total mass 0.265 g) were ground in a ball mill for 8 hours (Retsch PM100, 450 rpm). The milled powders were mixed with distilled water (0.2 ml) and cold pressed uniaxially in an 8 mm pellet die (Specac, 5 Tons, 10 minutes). The pressed pellets were embedded in graphite (acting as a MW susceptor) in an open, 10 mm silica tube which was surrounded with low dielectric loss silica flour (Aldrich, 99.6 %) (Figure 4-1).

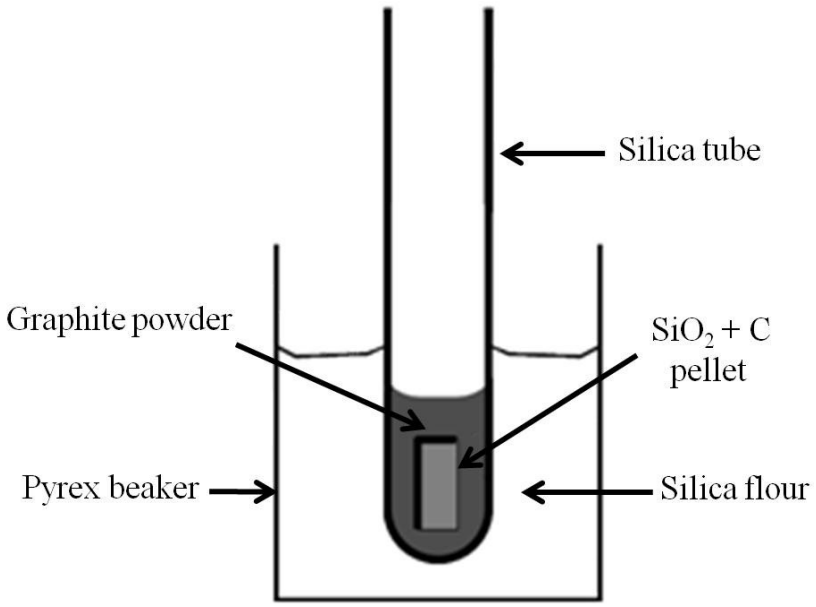

Figure 4-1 Schematic representation of MMC reaction set-up.

Synthesis was conducted in a multimode cavity (MMC) fed with an 800 W magnetron and operating at 2.45 GHz. No impedance matching device was employed due to the very small sample to cavity volume ratio. All preparations, reported in Table 4-2, were performed at ambient pressure in air.

Sample identifier	Carbon reagent	Irradiation time / min	Added water volume / ml
1	Activated carbon	3	0.2
2	Activated carbon	5	0.2
3	Activated carbon	10	0.2
4	Activated carbon	15	0.2

Table 4-2 Summary of experiments carried out on the SiO_2-C system in a MMC.

4.2.2 SMC experimental details

4.2.2.1 Pellets

Elemental powders of SiO_2 (Aldrich, -325 mesh, 99.6 %) and graphite (Sigma-Aldrich, powder, < 20 μm, synthetic) (1:3 ratios; 0.25 g total) were ground together and pressed into 8 mm diameter pellets which were set in powdered graphite susceptor in an open, 10 mm diameter quartz tube. The tube was placed in a silica beaker and packed with ground silica sand in order to maintain the tube in an upright position and to provide thermal insulation (Figure 4-2).

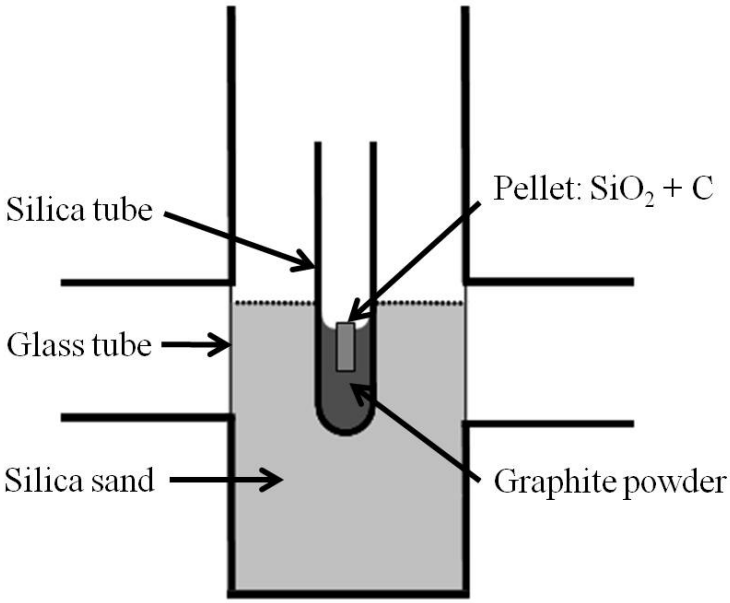

Figure 4-2 Schematic representation of SMC reaction set-up using SiO_2 + C pellets.

These tests were carried out at 600 W and repeated at 1.8 kW, shortening the time of irradiation in the latter case. The irradiation times reported were mainly dictated by the behaviour of the mixture. When arcing was observed, reactions were stopped promptly in

order to protect the integrity of the magnetron. The SMC reactor used in these studies was a 0 - 2 kW microwave generator produced by Sairem and operating at 2.45 GHz (Chapter 2, section 2.2.2). The system is also equipped with a s-team Homer autotuner. The autotuner had the advantage over the previously used 3 stub tuner to allow the best heating profile automatically. Temperature readings were taken *in-situ* using an optical pyrometer (LAND System4 Thermometer M1 600/1600 °C; ± 1 °C accuracy) with a 5 mm diameter spot centred on the sample surface. A series of synthesis experiments were run, as reported in Table 3-2.

Power applied (W)	Sample identifier	Irradiation time (s)
300	**5**	150
	6	240
	7	480
450	**8**	105
	9	300
	10	320
600	**11**	120
	12	240
900	**13**	160

Table 4-3 Summary of all experiments carried out on SiO_2-C (graphite) pellets in a SMC.

4.2.2.2 Powders

Since the pelleted mixture coupled satisfactorily in the single mode cavity even at low powers (300 to 900 W), several experiments were also performed using 1 g of loose silica and carbon powders (Table 4-4) to determine whether synthesis of SiC could be performed successfully without the need of a graphite susceptor. Using a susceptor has been found to be fundamentally crucial for all the reactions up to now, but it is clear that a big step towards improving the simplicity of the process would be using mixture of powders alone.
Loose silica and carbon powders were inserted in the open 12 mm diameter quartz tube *without the use* of a susceptor. Silica flour was placed around the quartz tube as a thermal insulator. Tests have been performed using the same single mode cavity system desbribed in the previous section (0 - 2 kW Sairem microwave generator, 2.45 GHz frequency, equipped with an s-team Homer autotuner). Two sets of powers have been applied; a low power fixed at 600 W and a high power of 1.8 kW and in each case (whenever possible

since the samples sometimes exhibited arcing), the same total energy (espressed in W x s) was supplied to the sample, to make reasonable comparisons possible.

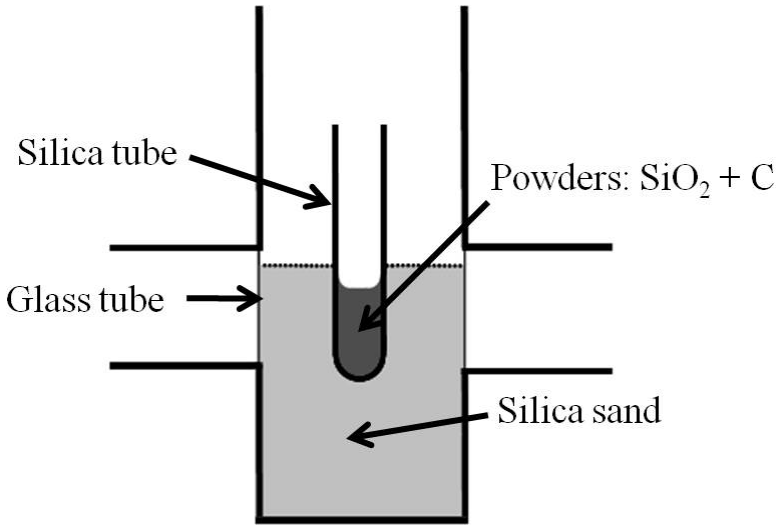

Figure 4-3 Schematic representation of SMC reaction set-up using SiO_2 + C powders.

The reactions performed on mixture of loose powders are reported in the following table (Table 4-4):

Carbon reagent	Power applied (W)	Sample identifier	Irradiation time (s)
Activated carbon	600	**14**	162
	1800	**15**	54
Graphite	600	**16**	162
	1800	**17**	68

Table 4-4 Summary of experiments carried out on SiO_2-C powders in a SMC.

4.3 Results

4.3.1 Multimode cavity (MMC) microwave syntheses of SiC from SiO_2 + activated C pellets

4.3.1.1 Synthesis and PXD studies

Several reactions were performed starting from a mixture of dry pressed powders, but all proved unsuccessful. When a water binder was added to silica and activated carbon powder mixtures, pressed samples were most easily handled when the amount of added water was

in a ratio of 0.2 ml : 0.25 g of powders. During the course of reactions **1–4**, it was immediately clear that pellets fractured extensively, at times violently. Furthermore, the observation of plasma in the open tubes also strongly suggested that gaseous products might be released. In rare cases where pellets remained intact after reaction, the pellet volume decreased after microwave irradiation, and this is likely due to the change in density from reactants to products.[15] SiC has a higher density (3.22 g cm^{-3}) than silica (0.05 g cm^{-3}) and activated carbon (1.80 – 1.86 g cm^{-3}).[15] Carbon loss is expected from reaction (1) by conversion to CO.

From the PXD patterns collected (Figure 4-4), it can be seen that after 3 minutes (**1**), β-SiC is accompanied by unreacted SiO_2 (both quartz and cristobalite), but by 5 minutes (**2**), all silica phases are almost negligible. It is interesting to note that at extended irradiation times (**3**, **4**) the silicon dioxide phases (both quartz and cristobalite) increase in phase fraction and the phase fraction of carbide diminishes, possibly due to the disproportion of SiO at longer irradiation times.

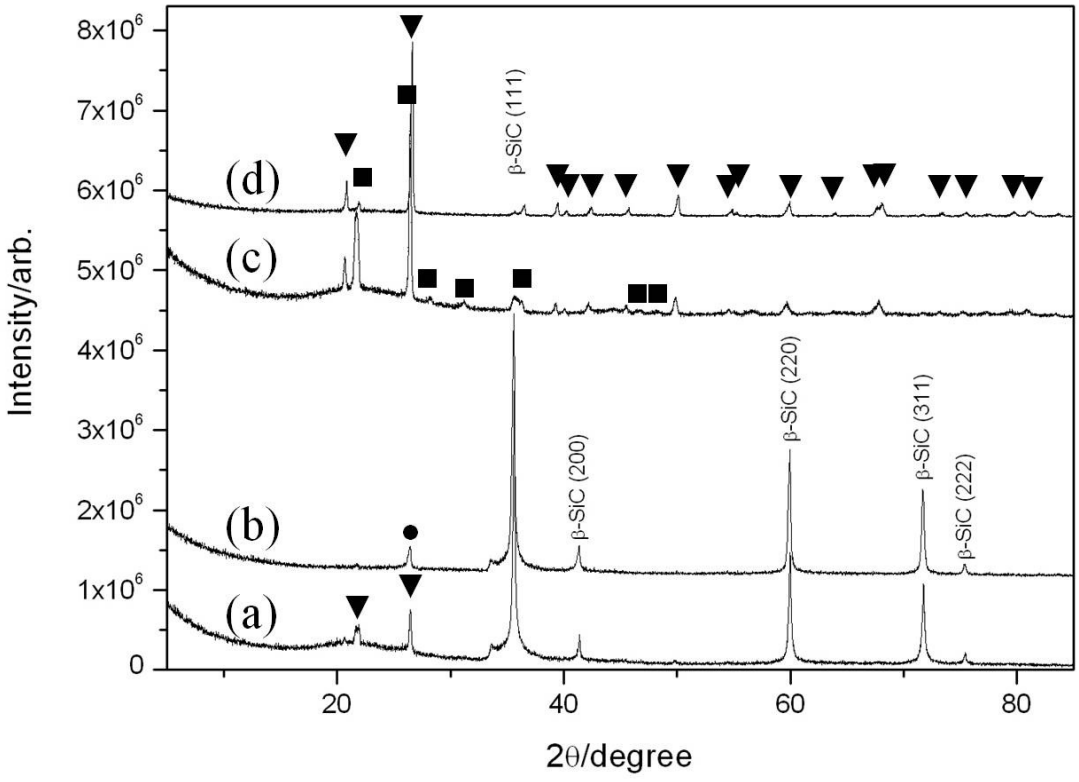

Figure 4-4 PXD patterns of samples synthesised:(a) 1 (3 min irradiation time); (b) 2 (5 min); (c) 3 (10 min); (d) 4 (15 min). Reflections from graphite (●), quartz (▼) and cristobalite (■) are also indicated.

4.3.1.2 Rietveld refinement data

Rietveld refinements were performed using 1 h PXD scans for samples **1–2** (Figure 4-5a-b) using the zinc blende structure of β-SiC as a starting model. During the initial cycles, the background was modelled and refined using a reciprocal interpolation function (function 8 within GSAS); scale factor, zero point and cell parameters were then refined. Peak widths and profile coefficients (peak shape was modelled using the Thompson-Cox-Hastings pseudo Voigt function; peak shape function 2 within GSAS) were subsequently refined. Once all SiC observed reflections were fitted and the refinement converged, cristobalite and quartz for sample **1** and graphite for sample **2** were input as secondary phases and phase fractions refined. All refinements converged smoothly in final cycles. The cubic lattice parameter in Table 4-6 and the Si–C distances reported in Table 4-5 for samples for **1** and **2** are in excellent agreement with literature values.[16] The same procedure was repeated for samples **3** and **4**, with the exception that the most prominent crystalline phases are quartz and cristobalite (Figure 4-5c-d). The first crystalline phase introduced for samples **3-4** was silica, either as cristobalite (for sample **3**) or quartz (in the case of sample **4**). β-SiC reflections were also successfully refined in sample **3**. The possible reason why the phase fraction of β-SiC decreases as the reaction progresses will be discussed in section 1.4 of this chapter. At the atmospheric pressure and at room temperature, the stable form of silica is quartz, while from 1470 °C to the melting point of silica (1713 °C), cristobalite is stable polymorph.[17] Data for **3–4** clearly shows how the relative phase fraction of quartz and cristobalite decreases from sample **3** to sample **4** as the silicon carbide phase fraction decreases, suggesting the temperature in the system is below 1713 °C, possibly due to the absence of a good microwave absorber such as SiC (e.g. Table 4-6 for **3** and **4**; Figure 4-5).

Atoms bonds	Interatomic distance/ Å (at 293 K)		
Sample No	**1**	**2**	**3**
Si1 – C1 x4	1.88927(8)	1.88956(8)	1.88004(3)
Atoms angle	Angle / ° (at 293 K)		
Sample No	**1**	**2**	**3**
C1 - Si1 – C1 x4	109.471(2)	109.471(2)	109.471(2)
Si1 – C1 – Si1 x4	109.471 (2)	109.471(2)	109.471(2)

Table 4-5 Interatomic distances and bond angles for samples 1, 2 and 3.

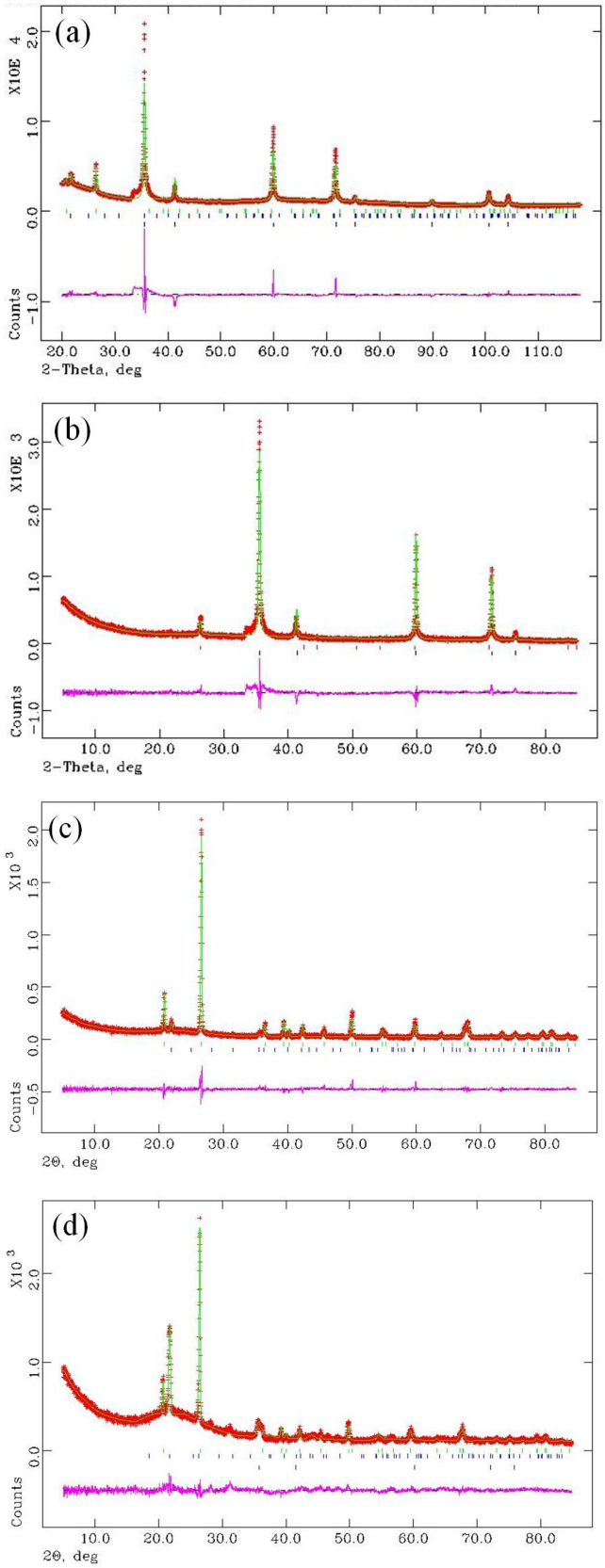

Figure 4-5 Exemplar profile plots for Rietveld refinements against PXD data. Shown are: (a) 1, (b) 2, (c) 3 and (d) 4 (see Table 4-2). Crosses (red) indicate observed data, the upper continuous line (green) shows the calculated profile, the lower continuous line (magenta) the difference and tick marks indicate different crystalline phases (dark blue β-SiC, red graphite, blue cristobalite, green quartz).

Instrument, radiation	X-ray, Cu $K_{\alpha 1}$			
Nominal stoichiometry (Sample No)	β-SiC (**1**)	β-SiC (**2**)	β-SiC (**3**)	Cristobalite (**4**)
Phases, fractions / wt %	β-SiC: 87(1) % Cristobalite: 4(6) % Quartz: 8(4) %	β-SiC: 90(8) % Graphite: 9(2) %	β-SiC: 43(1) % Cristobalite: 29(5)% Quartz: 27(4) %	Cristobalite: 5(0)% Quartz: 95(0) %
Crystal system, Space group	Cubic, F $\bar{4}$ 3 m			
Z	4			
M	160.388			
a-parameter, Å; Unit cell volume, Å^3	4.3630(7); 83.05(7)	4.3637(5); 83.09(6)	4.3417; 81.843	-
Calculated density, ρ_X / g cm^{-3}	3.207	3.205	3.254	-
Observations, parameters	5864, 12	4786, 26	4786, 41	4787, 41
R_p	6.61	10.58	6.67	12.01
R_{wp}	10.63	14.48	9.17	16.14
χ^2	15.43	3.26	2.07	1.71

Table 4-6 Exemplar crystallographic data from Rietveld refinements against PXD data. Shown are data for 1 and 2.

4.3.1.3 Scanning electron microscopy (SEM)

SEM micrographs of samples produced starting from a mixture of silica and carbon (**1**–**2**) show no evidence for nanofibre formation as has been observed in some cases from Si + C reactions (Chapter 3, section 3.3.1.3) (Figure 4-6). Rather, agglomerates of particles typically 1 – 5 μm across are observed at short irradiation times, such as 3 min for sample **1** and 5 min for sample **2**. In particular, in sample **2**, it is possible to note more faceted particles (Figure 4-6 b).

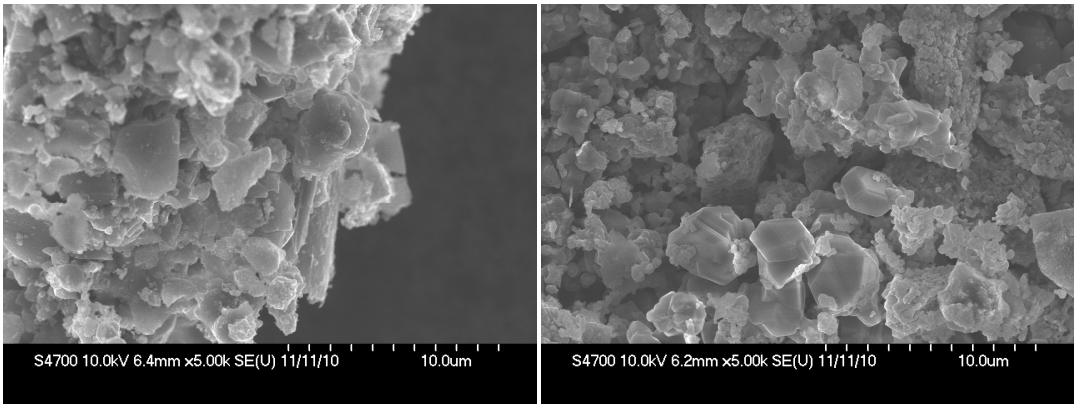

Figure 4-6 SEM micrographs of β-SiC prepared from SiO_2 plus activated carbon in a MMC after: (a) 1 (3 min) and (b) 2 (5 min).

4.3.1.4 Raman spectroscopy

The Raman spectrum of the product after 3 minutes of irradiation (sample **1**, Figure 4-7a) is quite complex and shows bands relative to both the starting materials and product. In particular the sample exhibits bands in the low wavenumber region of the spectrum (below ca. 400 cm^{-1}) due to torsional vibrations and O-Si-O bending modes of silica.[18,19] Peaks observed at higher wavenumbers in the samples, ca. 1350 cm^{-1} and 1580 cm^{-1}, are typically diagnostic of the presence of carbon materials and are named as the D band and G band.[20,21] The intensity ratio between these two bands (D/G) depends on the structure of the carbon.[22] Given the absence of graphitic peaks in the PXD and considering the relative intensity of the D and G band in sample **1** (the D band at ca. 1330 cm^{-1} has a higher intensity than the G band at ca. 1580 cm^{-1}), the presence of unreacted activated carbon in the product is highly likely. The initial formation of β-SiC can be detected from characteristic bands at 790 cm^{-1} corresponding to the Transverse Optical (TO) [23] Raman-active modes and a less intense band at ~1000 cm^{-1} probably due to an overtone combination of TO and Transverse Acoustic mode (TA) reported in the literature at ca. 1032 cm^{-1}.[24] The reason why the β-SiC TO band is broad is believed to be due to the overlap with silica bands, i.e. the band at 850 cm^{-1} corresponding to Si-O stretching modes from the silica framework present above 600 cm^{-1}.[19,25]

If the irradiation time is extended to 5 minutes (sample **2** Figure 4-7b), only bands due to β-SiC can be seen, along with peaks from residual graphite powder susceptor (~ 1330 cm^{-1} and 1580 cm^{-1}, the latter band being more intense). Furthermore, the very strong band at ca. 785 cm^{-1} in the Raman spectra of sample **2** (Figure 4-7b) is quite sharp indicating the products are more crystalline,[26,27] as confirmed from the SEM micrographs where faceted crystalline particles start appearing (Figure 4-6b). As the irradiation time increases, in agreement with the PXD patterns (samples **3** and **4**, Figure 4-7c-d) the Raman spectra

appear dominated by the unreacted activated carbon peaks in the high wavenumber region. Bands associated with silica are also present at low wavenumbers (ca. 200 cm^{-1}) and a broad band between 380 and 480 cm^{-1} which can be attributed to the motions of O in Si-O-Si symmetric stretching-bending modes. The range where this band sits matches the value expected for tetrahedra forming six-membered rings, such as in the case of quartz and cristobalite.[19]

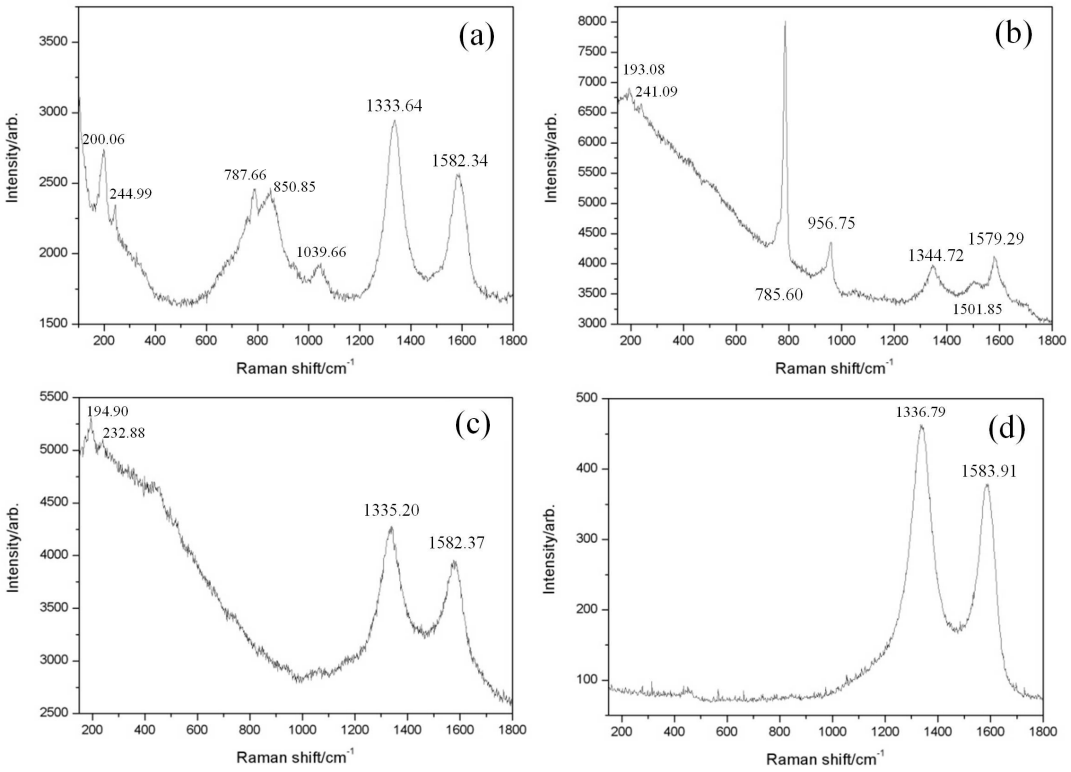

Figure 4-7 Raman spectra and observed bands for samples (a) 1 – (d) 4.

4.3.2 SMC microwave syntheses of SiC from SiO_2 + graphite pellets

4.3.2.1 Synthesis and PXD studies

From the PXD analysis (Figure 4-10) it can be seen that samples irradiated at 300 W for 150 and 240 s (**5** and **6** respectively**)** and a sample irradiated at 450 W for 105 s (**8**) were not successful and only reflections belonging to the starting materials could be seen (Figure 4-8). This means at short times and low powers the power density inside the samples is not sufficient for the reaction to take place.

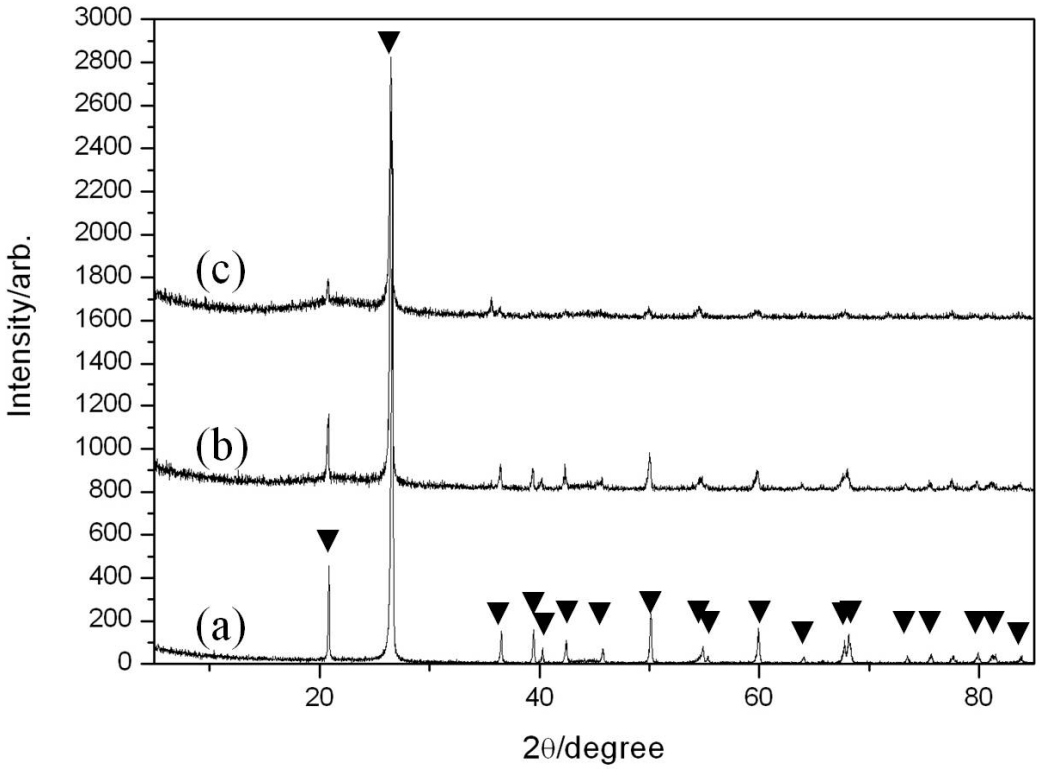

Figure 4-8 PXD patterns of samples: (a) 5; (b) 6 and (c) 8 (see Table 4-3). Reflections from quartz (▼) are also indicated.

Even when intermediate reaction times and powers were applied, as in the case of samples **7** and **10**, where the pellets have been irradiated at 450 W for 5 minutes and 600 W for 6 minutes respectively, the reactions did not proceed to completion and PXD patterns show a mixture of β-SiC and unreacted starting materials are present (see Table 4-3).

The temperature reached during reactions and measured on the optical pyrometer was above 1100 °C (Figure 4-9c). The silica ampoule emitted white light during the reaction, as can be seen in Figure 4-9 a and b.

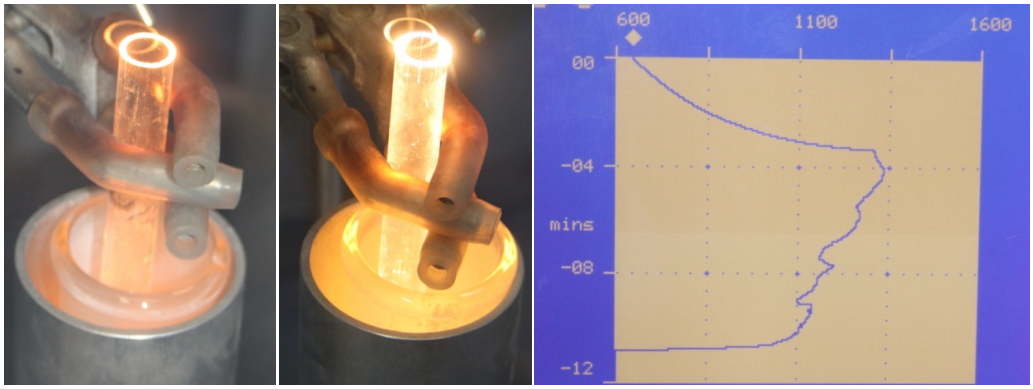

Figure 4-9 Photos of reaction (a) within 5 s and (b) beyond 5 s, and (c) optical pyrometer output for sample 7.

PXD studies (Figure 4-10) confirmed that for the operating conditions used for samples **7**, **10**, **12** and **13**, β-SiC is the main product of reaction. Graphitic peaks can also be clearly seen in samples **7** and **10** (Figure 4-10 a and b) and probably originate from the susceptor. At high applied powers (sample **13**, Figure 4-10 d), peaks belonging to Si appear, probably due to a reaction involving SiO gas. This will be discussed later in this section.

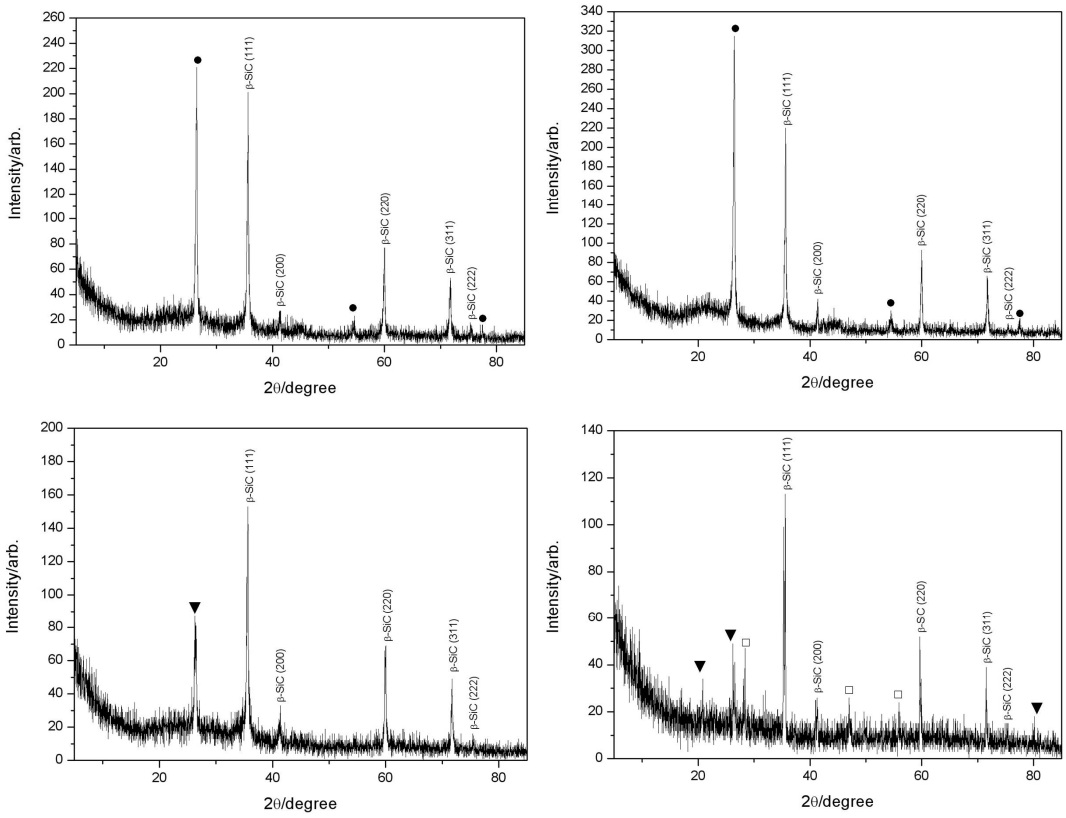

Figure 4-10 PXD patterns of samples synthesised:(a) 7, (480 s at 300 W); (b) 10 (320 s at 450 W); (c) 12 (240 s at 600 W); (d) 13 (160 s at 900 W). Reflections from graphite (●), quartz (▼) and silicon (□) are also indicated.

4.3.2.2 Raman spectroscopy

As previously mentioned, sample **5** represents an unreacted mixture of starting materials according to PXD analysis (Figure 4-8). Its Raman spectrum is included below as reference since only silica bands around 434 cm^{-1} (due to the motions of O in Si-O-Si symmetric stretching-bending modes)[19] and the characteristic carbon bands at ~1300 (D) and 1500 cm^{-1} (G) are present.[21]

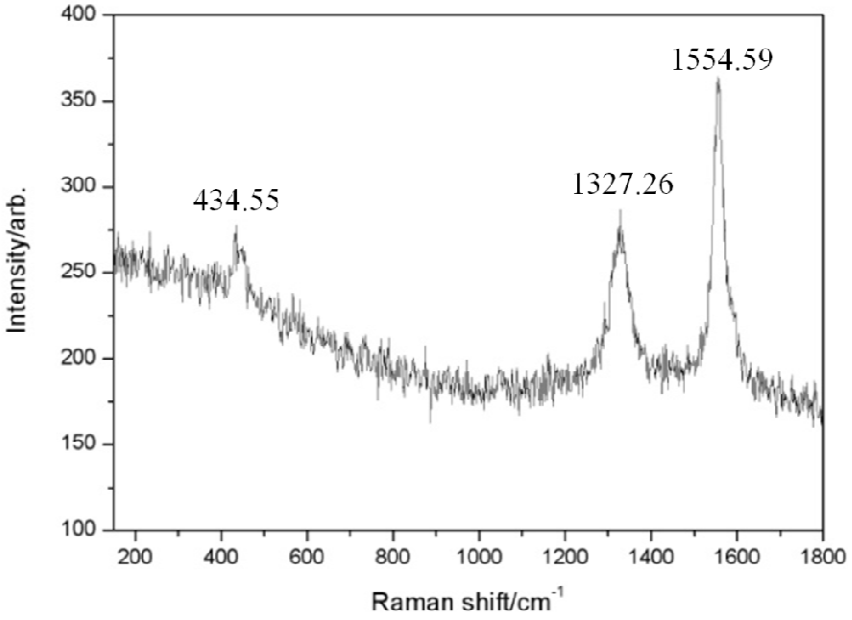

Figure 4-11 Raman spectrum for unreacted sample 5.

The Raman spectrum of the product after 8 minutes at 300 W (sample **7**, Figure 4-12a) shows a strong band around 760 cm^{-1} that corresponds to the Transverse Optical Raman-active mode (TO) in the cubic polytype of silicon carbide. In sample **12** (Figure 4-12c), irradiated for 2 minutes at 600 W, the TO band is also accompanied with a broad band around 920 cm^{-1} corresponding to the Longitudinal Optical (LO) Raman-active mode of β-SiC.[23] As is already evidenced from the PXD pattern (Figure 4-10b), sample **10** shows bands corresponding to partially unreacted silica - carbon mixture. In particular, bands in the low wavenumber region of the spectrum (200-800 cm^{-1}) are due to silica,[18] and the peaks around 1350 cm^{-1} and 1580 cm^{-1} originate from carbon.

If the power applied is increased to 900 W, in agreement with the PXD pattern (Figure 4-10 d), the Raman spectrum of sample **13** shows bands attributable to silicon (at ca. 270 and 490 cm^{-1}) and silicon carbide (at ca. 730 cm^{-1}). The small band width and the shift to lower wavenumbers from the usual value (520 cm^{-1}) for bulk silicon, suggests the band at ca. 500 cm^{-1} is due to the presence of microcrystalline silicon.[28] While the band at ca. 500 cm^{-1} is due to a one-photon scattering process, the other band at 280 cm^{-1} falls in a region of the silicon Raman spectra were overtones of acoustic phonons are present and the band at ca. 920 cm^{-1} is due to a two TO-phonon overtone scattering.[29]

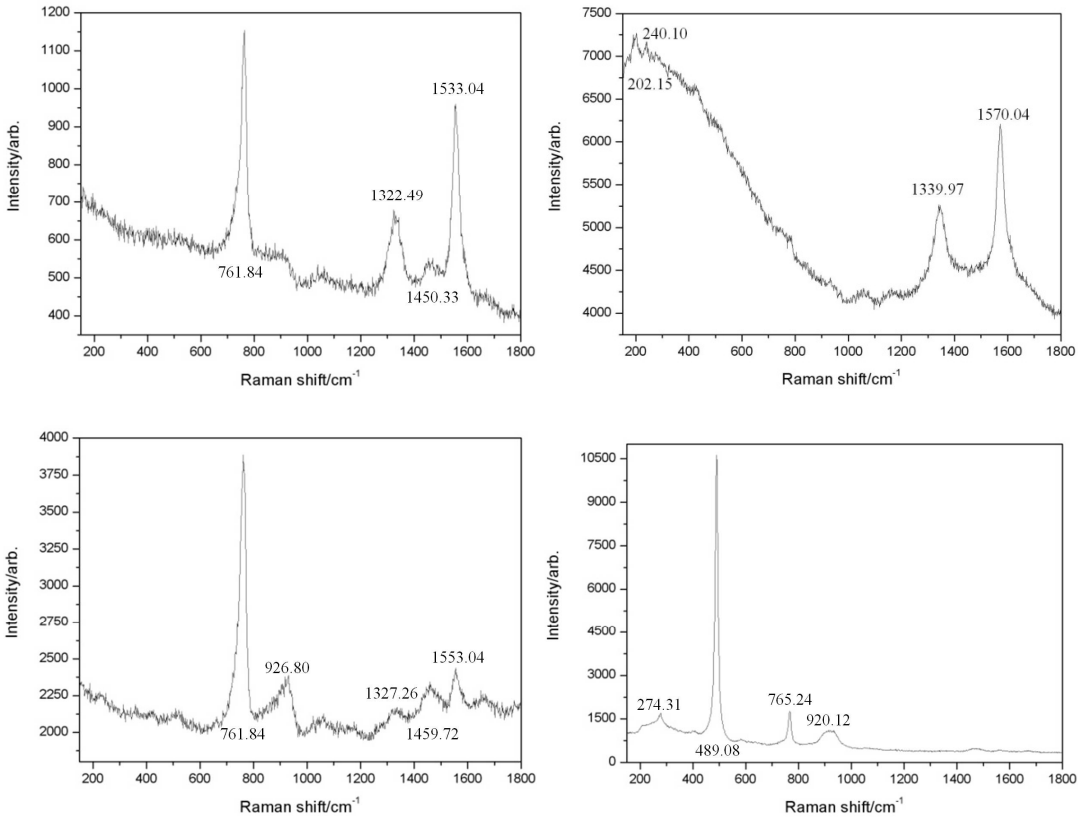

Figure 4-12 Raman spectra and observed bands for samples having the same overall power absorbed (a) 7, (b) 10, (c) 12 and (d) 13.

4.3.2.3 Scanning electron microscopy (SEM)

Analysis of the morphology of the samples produced was performed using scanning electron microscopy (SEM). The studies show (Figure 4-13) that the samples contain agglomerates of particles of both spherical and irregular shapes. While the samples irradiated up to 600 W show very similar morphologies, when increasing the power applied to 900 W, from the micrographs of sample **13** (Figure 4-13 d), it can be seen particles are now faceted and a better sintering of the sample is achieved.

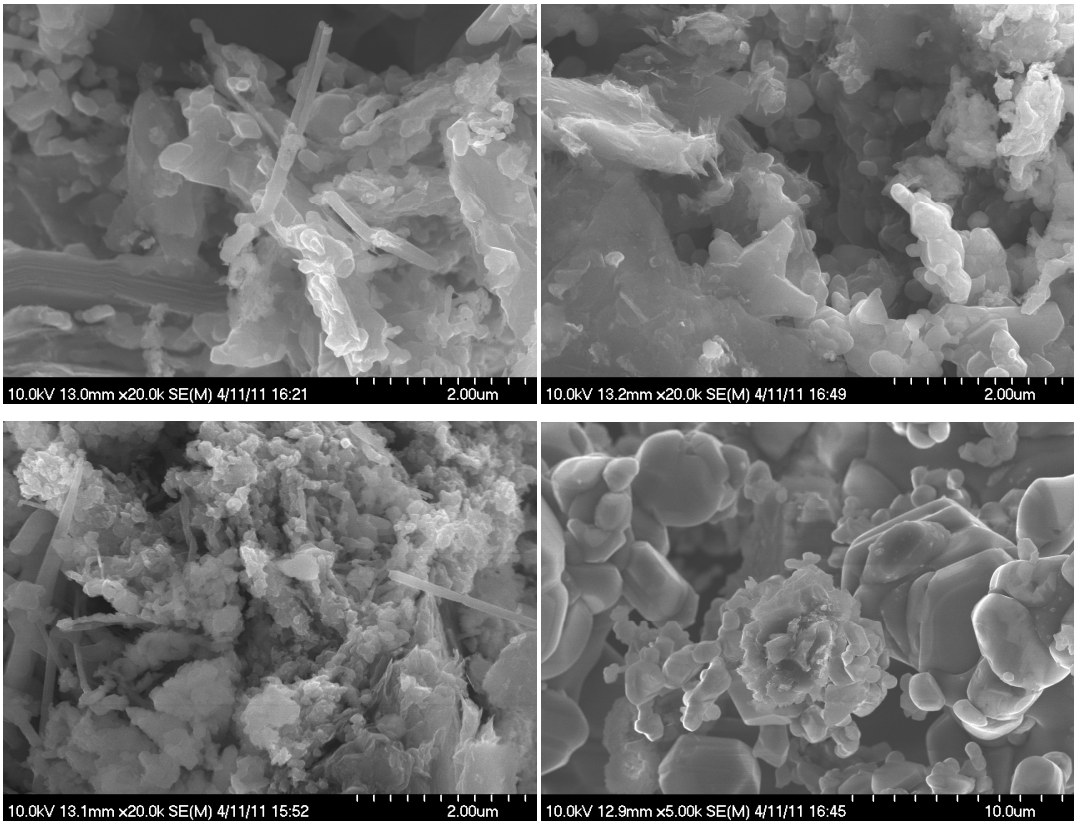

Figure 4-13 SEM micrographs of β-SiC samples prepared from SiO_2 plus activated carbon pellets in a SMC: (a) 7, (b) 10, (c) 12 and (d) 13.

4.3.3 SMC microwave syntheses of SiC from SiO_2 + C powders

4.3.3.1 Synthesis and PXD studies

Mixtures of powders starting from silica and carbon both as graphite and activated carbon have been used. From the optical pyrometer readings, all the reactions (apart from sample **17**) reached temperatures close to 1600 °C (see optical pyrometer outputs in Appendix).

When activated carbon replaces graphite, in the case of sample **14**, irradiated for 162 s at 600 W and sample **15**, irradiated for 54 s at 1.8 kW, β-SiC is always the predominant reaction product. For sample **14** extra reflections due to graphite, probably crystallized from activated carbon during the reaction, are present and in sample **15** silicon peaks appear.

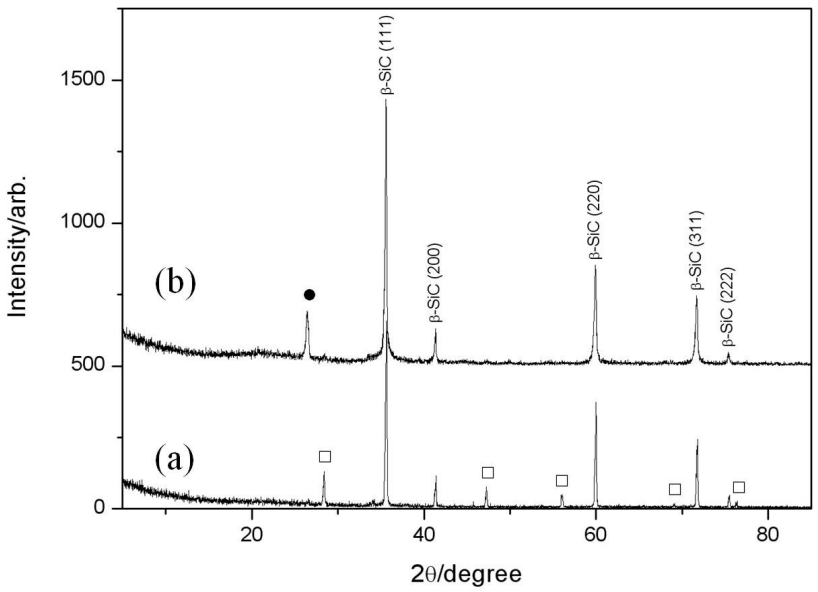

Figure 4-14 PXD patterns of β-SiC synthesised from SiO_2 + activated C powders in a SMC for (a) 14 (600 W and 162 s) and (b) 15 (1.8 kW and 54 s). Reflections from graphite (●) and silicon (□) are also indicated.

From the PXD analysis (Figure 4-15), it can be seen the products synthesised starting from silica and graphite powders, namely sample **16**, irradiated for 162 s at 600 W and sample **17**, 68 s at 1.8 kW resulted in the conversion to the cubic form of silicon carbide. In both products the silicon carbide is close to pure but small reflections belonging to graphite and silicon are present.

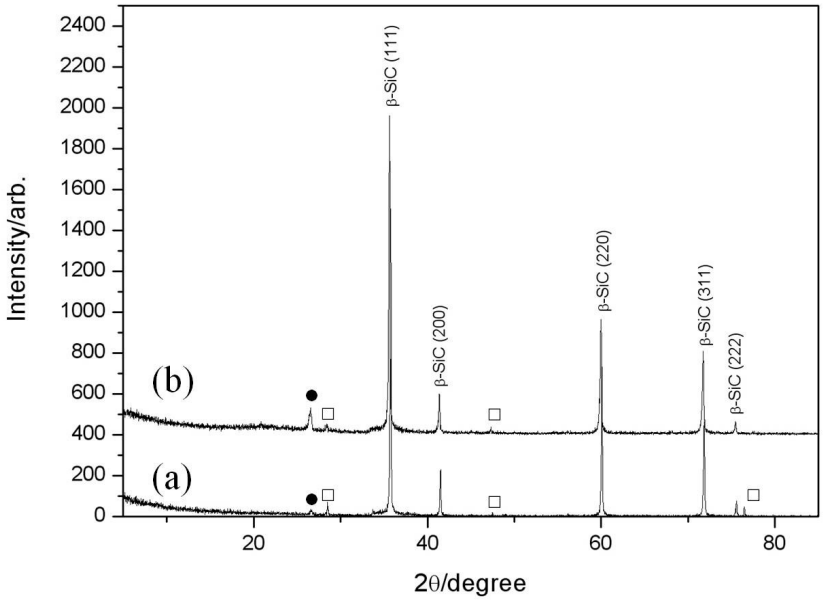

Figure 4-15 PXD patterns of β-SiC synthesised from SiO_2 + graphite powders in a SMC for (a) 16 (600 W and 162 s) and (b) 17 (1.8 kW and 68 s). Reflections from graphite (●) and silicon (□) are also indicated.

4.3.3.2 Rietveld refinement data

Rietveld refinements for the Si plus activated carbon samples, **14–17**, were performed using 1 h PXD scans. A procedure similar to the one described in section 3.3.1.2 was followed. β-SiC observed reflections were fitted first, then secondary phases, such as silicon and/or graphite were input depending on the sample. Peak profiles and phase fractions were refined and refinements converged smoothly in final cycles. Data for **14–17** shows that conversion higher than 74 % were achieved in each experiment and nearly phase pure β-SiC was synthesised after 162 s at 600 W. (e.g. Table 4-7; Figure 4-16). The presence of Si as a secondary phase will be discussed in section 4.4.

Instrument, radiation	X-ray, Cu $K_{\alpha1}$			
Nominal stoichiometry (Sample No)	β-SiC (**14**)	β-SiC (**15**)	β-SiC (**16**)	β-SiC (**17**)
Phases, fractions / wt %	β-SiC: 89(3) % Si: 12(7) %	β-SiC: 74(1) % Graphite: 25(9) %	β-SiC: 95(9) % Graphite: 3(2) % Si: 0.9(5) %	β-SiC: 85(0) % Graphite: 14(0) % Si: 0.8(7) %
Crystal system, Space group	Cubic, F $\bar{4}$ 3 m			
Z	4			
M	160.388			
a-parameter, Å; Unit cell volume, $Å^3$	4.3672(1); 82.29(4)	4.3703(1); 83.47(1)	4.3668(5); 83.27(3)	4.3634(6); 83.07(9)
Calculated density, ρ_X / g cm^{-3}	3.197	3.191	3.198	3.206
Observations, parameters	4782, 38	4786, 24	4723, 35	4785, 35
R_p	18.04	17.81	18.75	16.89
R_{wp}	25.60	23.95	27.51	23.58
χ^2	1.36	1.78	1.55	1.72

Table 4-7 Exemplar crystallographic data from Rietveld refinements against PXD data. Shown are data for 1 and 2.

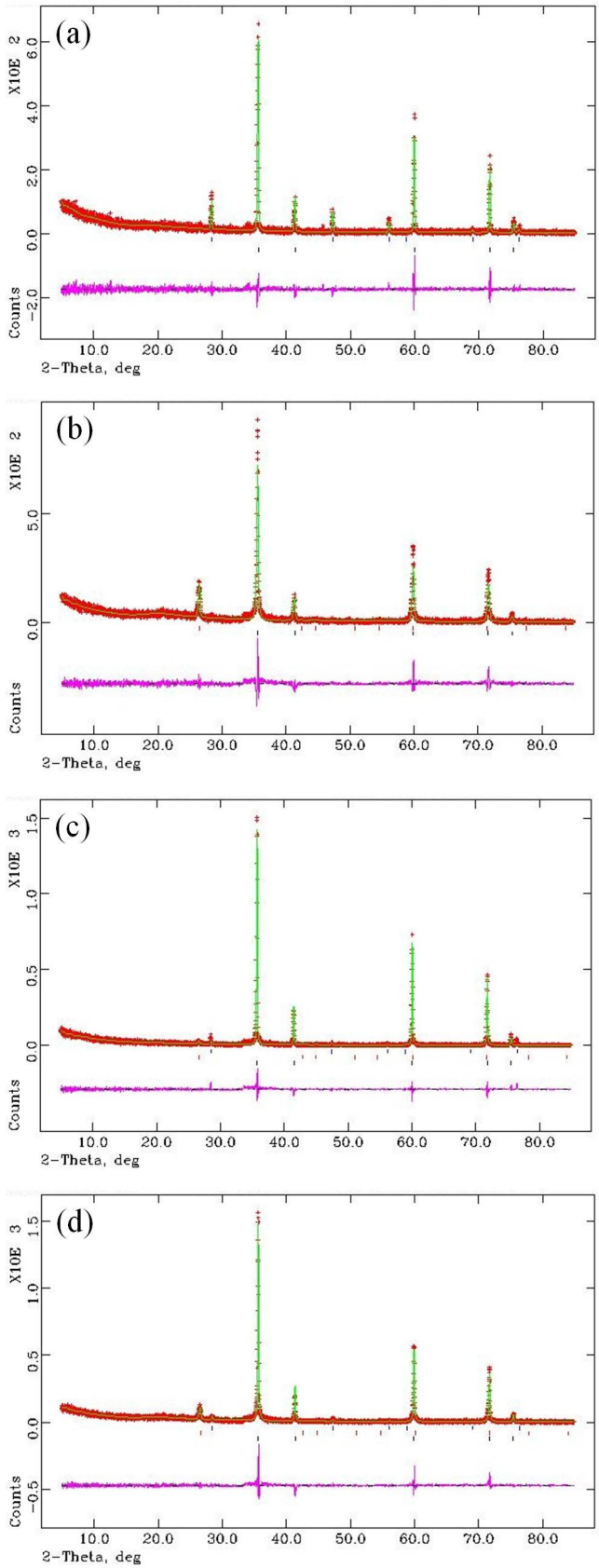

Figure 4-16 Exemplar profile plots for Rietveld refinements against PXD data. Shown are: (a) 14 to (d) 17 (seeTable 4-4). Crosses (red) indicate observed data, the upper continuous line (green) shows the calculated profile, the lower continuous line (magenta) the difference and tick marks indicate different crystalline phases (dark blue β-SiC, red graphite, blue Si).

Atoms bonds	Interatomic distance/ Å (at 293 K)			
Sample No	**14**	**15**	**16**	**17**
Si1 – C1 x4	1.89106(7)	1.89240(1)	1.89090(4)	1.88943(6)
Atoms angle	Angle / º (at 293 K)			
Sample No	**14**	**15**	**16**	**17**
C1 - Si1 – C1 x4	109.471(2)	109.471(3)	109.471(1)	109.471(2)
Si1 – C1 – Si1 x4	109.471 (2)	109.471(3)	109.471(1)	109.471(2)

Table 4-8 Interatomic distances and bond angles for samples 14 - 17.

4.3.3.3 Scanning electron microscopy

The morphology of the samples has been analysed using scanning electron microscopy (SEM). Products starting from a mixture of silica and either activated carbon or graphite show similar morphologies. Noticeable is the constant presence of both nanowires and well defined crystallites in each sample (Figure 4-17 and Figure 4-18). In particular in one micrograph of sample **14** (Figure 4-17b), wires are observed to grow from an apparent melt located on silicon carbide faceted particles.

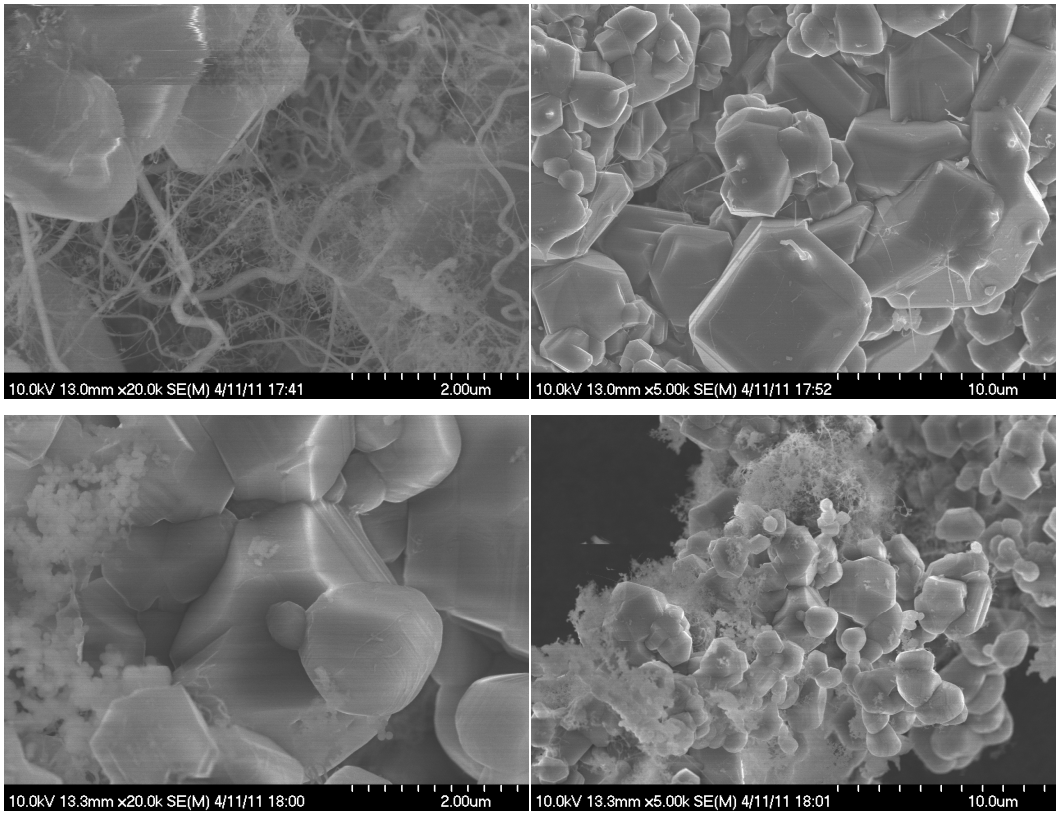

Figure 4-17 SEM micrographs of samples prepared from SiO_2 plus activated carbon powders for (a) – (b) 14 (600 W and 162 s) and (c)-(d) 15 (1.8 kW and 54 s) in a SMC. In (b) a nanowire growing from a melt on a crystallite is highlighted.

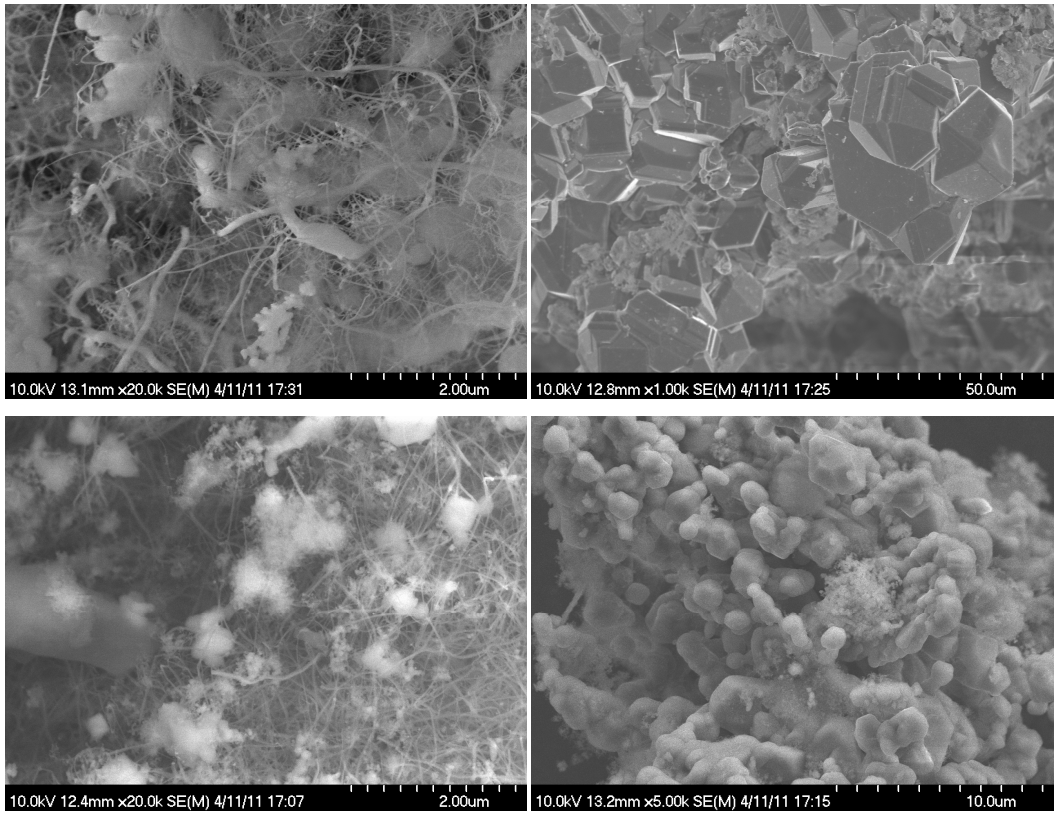

Figure 4-18 SEM micrographs of samples prepared from SiO_2 plus graphite powders for (a) –(b) 16 (600 W and 162 s) and (c)-(d) 17 (1.8 kW and 68 s) in a SMC.

4.3.3.4 Raman spectroscopy

The Raman analysis of samples **15** and **16** (Figure 4-19 b and c) shows the presence of the TO and LO band of β-SiC.[23] For sample **15**, irradiated for 54 s at 1.8 kW, along with the characteristic silicon carbide bands, additional weaker bands appear due to overtones in the second order Raman spectrum of silicon carbide.[24] The intensity ratio of the D/G bands suggests the sample also contains a fraction of graphite, probably due to carbon crystallisation during reaction.[22] Raman spectra of sample **17** (Figure 4-19 d) show bands indicating the presence of silicon, in excellent agreement with the PXD pattern (Figure 4-15b). Silicon is also present in sample **14**, as evidenced in the Raman spectrum by a very sharp peak at ca. 500 cm^{-1} (Figure 4-19c) and additional features at 272 cm^{-1} and 931 cm^{-1} related respectively to the overtones of acoustic phonons and to two TO-phonon overtone scattering.[29]

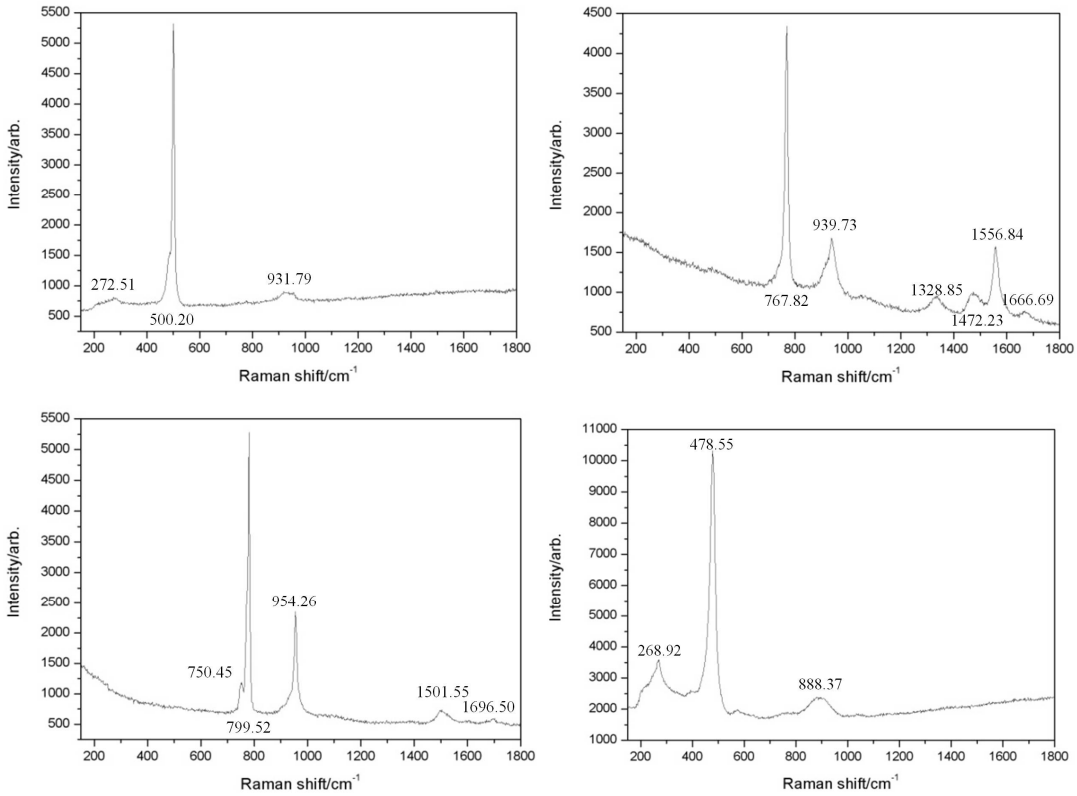

Figure 4-19 Raman spectra and observed bands for samples (a) 14 – (d) 17.

4.4 Discussion

In contrast to reactions to produce silicon carbide involving silicon and carbon (Chapter 3) which involves a straightforward solid-state reaction between the two elemental reactants,

the reaction of silica and carbon is more complex. Given that the carbothermal reaction of silica is the most economic way to produce silicon carbide, the reaction has been discussed extensively in the literature.[30,31] The overall reaction is represented by equation (1) but the process is proposed to follow two consecutive steps involving the gaseous intermediate SiO:[32]

$$SiO_2\ (s) + C\ (s) \leftrightarrow SiO\ (g) + CO\ (g) \qquad (2)$$

$$SiO\ (g) + 2\ C\ (s) \leftrightarrow SiC\ (s) + CO\ (g) \qquad (3)$$

Since silica melts above 1450 °C, the first step is a solid-solid or a liquid-solid reduction reaction leading to the formation of gaseous silicon monoxide (SiO) and carbon monoxide and the second a gas-solid reduction–carburisation. The direct contact between silica and carbon particles in the starting mixture is a key feature in reaction (2) and in the microwave case, as opposed to conventional heating, there is an added issue due to the fact that at the boundaries between the silica and carbon grains both the dielectric behaviour and thermal conductivity changes drastically. Further, each step requires the evolution of gaseous products; SiO, CO in reaction (2) and CO in reaction (3), therefore both reactions depend on the temperature and partial pressure of SiO and CO.

From PXD analysis (Figure 4-4) of reactions performed in a MMC, it is apparent that despite initial fast formation of β-SiC by reactions (2) and (3) (samples **1** and **2**), at longer irradiation times the relative yield of the carbide diminishes significantly (samples **3** and **4**). This effect is well established in the literature when conventional heating is employed.[33,34] For longer heat treatments at 1400 °C, in fact, when the majority of carbon has been consumed, a side reaction can occur in the solid state between remaining silica and SiC as it forms (4):

$$SiC\ (s) + 2\ SiO_2\ (s) \rightarrow 3\ SiO\ (g) + CO\ (g) \qquad (4)$$

This reaction consumes the silicon carbide produced by producing more SiO which can cause the condensation of silicon materials in the products, such as silica and silicon. Another possible reason for diffraction patterns dominated by SiO_2 (and crystalline carbon phases absent) at long irradiation times could be the oxidation of SiO in air. Despite the surrounding graphite, the high localised gas pressures (from SiO and CO) generated very quickly in the MMC cause the pellet to disintegrate and scatter graphite susceptor. This could cause the sample to be exposed to air and subsequently SiO to oxidise to SiO_2. A similar effect is also observed in the SMC reaction from pellets (i.e. sample **12**, Figure

4-10), where the heating rates are higher. Synthesis of SiC in the MMC from SiO_2 in air could be more challenging than starting from silicon due to the difference in reaction temperature depending on the starting materials. In fact, while silicon and graphite react together through a solid-state reaction at a temperature of ca. 1150 ºC (using a conventional heating method), a mixture of silica and carbon yields silicon carbide through a vapour phase reaction at ca. 1450 ºC. As already reported in the literature, however, the form of the carbide product is not influenced by the choice of starting materials and the cubic modification of silicon carbide (β-SiC) is always favoured.[35] The importance of controlling the gaseous environment and especially the SiO and CO partial pressures is crucial[36] and to have an insight into the reaction mechanism *in-situ* techniques should be perfomed.

As in the reactions starting from silicon (Chapter 3), the shoulder present next to the β-SiC plane (111) reflection is believed to be due to the presence of stacking faults in the 3C-silicon carbide structure. These can give rise to diffraction effects similar to the ones due to those in hexagonal modifications of SiC (where the cubic structure is distorted by rotating the tetrahedra in alternate sheets along the diagonal axis (111) of the cube, in a way that the tetrahedra end up laying in parallel and anti-parallel directions).[35]

When performing the reactions in a SMC from a mixture of silica plus carbon, the product presents different morphologies (Figure 4-17 and Figure 4-18). This result has been already reported in the literature as a sign indicating various reactions might have co-existed in the synthesis of silicon carbide.[37] Spherical particles have been reported as formed by a solid-solid or solid-liquid reaction (3) and it has been noted the particle sizes of the product increase as the reaction time increases.[37] Studies reporting the formation of wires during the silica plus carbon carbothermal reaction, usually refer to static atmosphere operating conditions, where the build-up of saturated gases is possible and a gaseous growth mechanism can possibly produce wires.[32]

The transient accumulation of SiO and CO in the carbothermal reaction, in fact, could lead to the reaction of these two gases to give silicon carbide wires following the reaction:[32]

$$SiO\ (g) + 3\ CO\ (g) \rightarrow SiC\ (s) + 2\ CO_2\ (g) \qquad (5)$$

Followed instantly by the Boudouard reaction where the excess of carbon present in the system will control the ratio between CO and CO_2 gases:[38]

$$CO_2\ (g) + C\ (s) \rightarrow 2\ CO\ (g) \qquad (6)$$

Given the high heating rates achievable in the SMC used here in these experiments (compared to those from a MMC system), this mechanism is perhaps likely due to the fast building up of CO and SiO pressures even though dynamic conditions are met (Figure 4-17 and Figure 4-18). The SEM micrograph reported in Figure 4-17 b suggests the growth of more uniform, rigid and possibly less defective wires under these conditions could also be due to a growth from the melt as already mentioned in Chapter 3.

The presence of silicon has been observed in various samples from analysis of both PXD (Figure 4-10 d, Figure 4-14 a and Figure 4-15) and Raman data (Figure 4-12 d, Figure 4-19 a, d). According to the literature, Si formation can be justified on the basis of two possible reactions,[32] the former being a solid-gas reaction between silicon carbide and SiO and the latter a disproportionation of gaseous SiO:

$$SiC\ (s) + SiO\ (g) \rightarrow 2\ Si\ (s) + CO\ (g) \qquad (7)$$

$$2\ SiO\ (g) \rightarrow Si\ (s) + SiO_2\ (s) \qquad (8)$$

From the thermodynamic data found using the online version of FactWeb,[39] while reaction (7) presents a positive ΔG of 19.188 kJ even at temperatures as high as 2000 K, reaction (8) has negative Gibson energy in the range of temperatures involved in the reaction (add 1100 – 1700 K).

Reaction (8) therefore is the one usually accounted for the presence of both Si and silica in the PXD pattern (Figure 4-10 d). High temperature gradients are an important issue in the reaction system (as might be expected in the MMC), where the evaporation of SiO in regions of higher temperatures would cause condensation of either silicon or silica and silicon in the regions of lower temperatures.[40]

In these experiments, given the open reaction conditions, in one sense a route is provided for CO removal that hinders the formation of silicon carbide through reaction (3). From the PXD analysis it seems purity of the final product is improved starting from graphite, this seems to confirm the conclusions already drawn in the paper written by Vix-Guterl *et al.* In the above mentioned paper, it is stated that in the case of a non-graphitised precursor, such as activated carbon, the partial pressure of CO is higher due to the desorption of oxygen complexes on the surface.[32] Furthermore the choice of carbon precursor seems to be crucial since the first reaction for the production of silicon carbide during the carbothermal

reaction is an interfacial interaction between silica and carbon (reaction (3)) to achieve a better purity of silicon carbide.

Being able to synthesise β-SiC with purities of up to 96 % (Table 4-7, sample **16**) starting only from the starting mixture, i.e. *without* a need for a graphite susceptor, represents a major step towards simple industrial flow processing. A model for heating of ceramics in the microwave field was proposed by Meek,[41] while studying a two phase system composed of alumina particles and air, who showed that more power would be deposited in the less dense region and the penetration depth would also be greater where the density was lower. This could explain why the powders have been heated in the SMC system faster than using dense mixtures in pellets.

While for the reaction perfomed using pellets embedded in graphite, the absence of oxide formation can be due to the presence of an excess of graphite that ensures reducing conditions are met, when only powders are employed the absence of oxide formation could be explained by the CO evolution during reaction, acting as an inert atmosphere. In fact, the setup used while performing reactions is composed by a tall silica tube filled by 20 % with powders; having air and CO nearly the same density, the exchange between these two gases is slow.

The temperature of the heated sample has been estimated above 1600 ºC with an optical pyrometer. The measured sample temperature corresponds to a surface temperature which is smaller than the internal temperature in microwave heating. This makes an accurate comparison of reaction temperature with conventional methods difficult given the inversion of the temperature gradient.[10]

4.5 Conclusions

In summary, although the selection of silica and carbon sources might be cost-effective, in a multimode cavity system the high temperature gradients and the gaseous products involved as intermediates in the reaction are difficult to control under dynamic conditions (i.e. in a open vessel). When the equivalent reactions using pellets are performed in a single mode cavity higher crystallinity samples have been produced but the purity has been limited by the partial conversion and formation of silicon and silica. Despite these issues, β-SiC up to 90 wt. % phase pure (based on Rietveld refinements, samples are likely to

contain an unknown amount of amorphous material) has been synthesised in a MMC in timescales from 3 - 5 minutes without the use of an inert atmosphere.

Morphology control has been achieved to a certain extent and while the product from pellets synthesised in a MMC revealed to be porous with agglomeration of particle, when silicon carbide was produced using a SMC, both nanowires and a higher level of sintering has been achieved. This demonstrates once again how the influence of the experimental parameters is crucial.

The development of *in-situ* techniques is crucial to understand the mechanism of the reaction and to be able to control the process, especially when gaseous intermediates are involved, such as in the carbothermal reaction.

More importantly, very encouraging results relating to scale up of the process have been found when performing the reaction in a SMC starting from loose powders without the use of graphite as susceptor. Reactions have yielded more than 95 % of silicon carbide in less than 3 minutes and the ability to achieve nearly phase pure SiC without the use of a susceptor fulfilled a major objective of this thesis work.

[1] F. Cardarelli, *Materials Handbook A Concise Desktop Reference*, 2008, Springer-Verlag, London, 2nd ed., Chapter 10, 626.

[2] G.S. Gupta, P. V. Kumar, V. R. Rudolph and M. Gupta, *Metall. Trans. A,* 2001, **32**, 1301.

[3] C. Dai, X. Zhang, J. Zhang, Y. Yang, L. Cao and F. Xia, *J. Mater. Sci.*, 1997, **32**, 2469.

[4] C. Dai, X. Zhang, J. Zhang, Y. Yang, L. Cao and F. Xia, *J. Am. Ceram. Soc.*, 1997, **80**, 1274.

[5] M. Lu, A. Li, T. Wang, D. Wang and W. Qin, *J. Nanosci. Nanotechnol.*, 2010, **10**, 2135.

[6] K. J. Rao, B. V. M Ganguli and P. A. Ramakrishnan, *Chem. Mater.*, 1999, **11**, 882.

[7] J. A. Menendez, A. Arenillas, B. Fidalgo, Y. Fernandez, L. Zubizarreta, E.G. Calvo and J.M. Bermúdez, *Fuel. Process. Technol.*, 2010, **91**, 1.

[8] S. A. Nightingale, *Ionics*, 2001, **7**, 327.

[9] R. J. Meredith, *Engineers' Handbook of Industrial Microwave Heating*, The Institution of Electrical Engineers, London, UK, 1998, Table 2.4, 28.

[10] A. J. Berteaud and J. C. Badot, *J. Microwave Power Electromag. Energ.*, 1976, **11**, 315.

[11] http://www.icdd.com/ (last access 12/7/2011)

[12] A. C. Larson and R. B. von Dreele, *The General Structure Analysis System*, 2000, Los Alamos National Laboratories, Report LAUR 086-748, LANL, Los Alamos.

[13] B. H. Toby, *J. Appl. Crystallogr.* 2001, **34**, 210.

[14] S. R. Tennison, *Appl. Catal. A: General*, 1998, **173**, 289.

[15] S. J. Kim, S.–M. Yun and Y.-S. Lee, *J. Indust. Eng. Chem.*, 2010, **16**, 273.

[16] Kawamura, T. *Mineralog. J.* 1965, **4**, 333.

[17] V. Swamy, S.K. Saxena, B. Sundman et al., *J. Geophys. Res.*, 1994, **99**, 11787–11794.

[18] A. Bachmatiuk, F. Börrnert, M. Grobosch, F. Schäffel, U. Wolff, A. Scott, M. Zaka, J. H. Warner, R. Klingeler, M. Knupfer, B. Büchner and M. H. Rümmeli, *ACS Nano*, 2009, **3**, 4098.

[19] K. J. Kingma and R. J. Hemley, *Am. Mineral.* 1994, **79**, 269.

[20] H. Li, Y. Zhu, Z. Mao, J. Gu, J. Zhang and Y. Qian, C*arbon,*, 2008, **47**, 328.

[21] M. J. Matthews, M. A. Pimenta, G. Dresselhaus, M. S. Dresselhaus and M. Endo, *Phys. Rev. B*, 1999, **59**, 6585.

[22] D. S. Knight and W. B. White, *J. Mater. Res.*, 1989, **4**, 385.

[23] S. Rohmfeld, M. Hundhausen and L. Ley, *Phys. Status Solidi B*, 1999, **215**, 115.

[24] D. Olego and M. Cardona, *Phys. Rev. B*, 1982, **25**, 1151.

[25] T. Woignier, C. Fernandez-Lorenzo, J. L. Sauvajol, J. F. Schmit, J. Phalippou and R. Sempere, *J. Sol-Gel Sci. Techn.*, 1995, **5**, 167.

[26] S. Nakashima and H. Harima, *Phys. Stat. Sol. (a)*, 1997, **162**, 39.

[27] S. G. Sundaresan, A. V. Davydov, M. D. Vaudin, I. Levin, J. E. Maslar, Y.-L. Tian and M. V. Rao, *Chem. Mater.*, 2007, **19**, 5531.

[28] R. J. Nemanich, E. C. Buehler, Y. M. Legrice, R. E. Shroder, G. N. Parsons, C. Wang, C. Lucovsky and J.B. Boyce, *J. Non-Cryst. Solids*, 1989, **114**, 813.

[29] P. A. Temple and C. E. Hathaway, *Phys. Rev. B*, 1973, **7**, 3685.

[30] N. Klinger, E. L. Strauss and K. L. Komarek, *J. Am. Ceram. Soc.*, 1966, **49**, 369.

[31] G. C. Wei, C. R. Kennedy and L. A. Harris, *Am. Ceram. Soc. Bull.*, 1984, **63**, 1054.

[32] C. Vix-Guterl and P. Ehrburger, *Carbon*, 1997, **35**, 1587.

[33] C. Vix-Guterl, B. McEnaney and P. Ehrburger, *J. Eur. Ceram. Soc.*, 1999, **19**, 427.

[34] E. A. Gulbransen and S. A. Jansson, *Oxid. Met.*, 1972, **4**, 181.

[35] A. Taylor and D. S. Laidler, *Br. J. Appl. Phys.*, 1950, **1**, 174.

[36] A. Jha, *J. Mater. Sci.*, 1993, **28**, 3069.

[37] W.-S. Seo and K. Koumoto, *J. Am. Ceram. Soc.*, 1996, **79**, 1777.

[38] G. Z. Yang, H. Cui, Y. Sun, L. Gong, J. Chen, D. Jiang and C. X. Wang, *J. Phys. Chem.*, 2009, **113**, 15969.

[39] http://www.sgte.org/reacweb.htm (last access 08/11/2011)

[40] V. D. Krstic, *J. Am. Ceram. Soc.*, 1992, **75**, 170.

[41] T. T. Meek, *J. Mater. Sci. Letters,* 1987, **6**, 638.

5 Microwave synthesis studies using x-aerogel precursors

5.1 Introduction

Porous SiC ceramics have attracted recent interest as supports in catalysis, as good alternative to commercial oxide and carbon based supports and catalysts.[1] The powders produced commercially using the Acheson process are coarse and require further milling and purification to be used for advanced porous SiC ceramics. Even when particles are fine in size, it is extremely difficult to sinter SiC to monoliths due to the highly covalent Si-C bond, which gives rise to low diffusion coefficients in SiC. Various techniques have been applied to sinter SiC powders, such as pressureless sintering, hot pressing or hot isostatic pressing, but they all require temperatures in the range of 1800 - 2200 °C and sinter aids.[2]

Porous SiC monoliths have been successfully fabricated starting from natural materials. Biomorphic synthesis has been extensively studied as a renewable and relatively inexpensive process where biological carbon preforms have been fabricated by carbonising different wood structures, such as pine,[3,4] oak,[5] Tilia amurensis,[6] and beech,[7] in high-temperature pyrolysis (up to 1800 °C). The carbonised materials retain the open porous structure of the parent wood and can be used as templates for infiltration with gaseous or liquid silica. One drawback of this process is the lengthy procedure since multiple infiltrations are needed to get the stoichiometric ratio of C:SiO_2 to 3:1. The direct reaction between porous carbonised wood and silica is then successfully applied to synthesise silicon carbide porous ceramics.[8]

The widely accepted mechanism for the carbothermal reduction of silica was discussed in the previous chapter. The first step of the reaction involves the solid-state reaction between silica and carbon to give silicon monoxide (SiO) gas as an intermediate, equation (2) in Chapter 4. As a consequence, the initial stage (2) of the reaction requires the intimate contact between silica and carbon particles, which makes the reaction difficult at lower temperatures due to solid state diffusion and represents the rate-limiting step of the reaction mechanism.[9] Improving the direct contact between silica and carbon and using finer precursor particles would positively influence the final silicon carbide properties. In particular several studies have reported the size of carbon particles dictates the size of the silicon carbide produced.[10] Sol-gel methods have been employed to blend silica and carbon

sources together and enhance the homogeneous distribution of carbon within silica. The conversion of these materials to SiC has been extensively studied.[11,12,13,14,15,16,17]

The idea of using porous silica frameworks infiltrated by a form of carbon as precursors to silicon carbide was employed by Vix-Guterl *et al.* in 1999.[17] They prepared porous freeze dried gel silica pellets and infiltrated them with a phenolic resin. Later the polymer was carbonised and the so-prepared artefact was used as a starting material for the synthesis of silicon carbide. The reaction was run under either static or flowing argon at a temperature of 1550 °C using a temperature program of total length of ~ 5 hours. At the end of the reaction, powder X-ray diffraction (PXD) patterns showed a strong peak due to cristobalite which had crystallised from amorphous silica and a higher yield of silicon carbide was obtained under dynamic conditions. When the reaction is performed under static argon, a high partial pressure of CO in the reactor can suppress reaction (2) in Chapter 4 and consequently decrease the yield of SiC obtained through reaction of SiO with C (reaction (3) Chapter 4). The same approach has been reported recently, where a silica monolith infiltrated with carbon has been used to prepare equivalent porous silicon carbide monoliths.[18] The silica artefact was coated in this case either with mesophase pitch or furfuryl alcohol and then heat treated in argon at 1500 °C for several hours and the product cooled for 12 h to room temperature to avoid cracking of the monolith. Even in this case, silica had to be removed post-processing.

The quest for new materials with improved performances combined with the development of modern sol-gel techniques has led to the design of mesoporous materials such as aerogels.

The term “sol-gel” refers to a multistep process to synthesise inorganic solids (principally oxides) that employs wet chemical methods at low temperature (typically T < 100 °C).[19] The name derives from the sudden viscosity increase taking place during processing when gel formation is initiated.[20] Sol-gel methods have been used to yield either crystalline or amorphous products in different form, such as powders or monoliths.[20]

Inorganic salts in water or organometallic precursors (usually metal alkoxides) in organic solvents are the two main precursors used in sol-gel processing.[20] The most studied and used precursors are alkoxides $M(OR)_n$ where M is a metal and OR an alkoxide group (R being an alkyl group). The molecules are often present as small polymerised complexes, often in solution in their parent alcohol and the M-O bonds in the molecules are polar covalent. The first step typically involved in sol-gel processing is the hydrolysis of the metal alkoxide with a controlled amount of water in a solvent (usually alcohol) at

temperatures below 100 °C.[20] During hydrolysis, the OR groups in the alkoxide are replaced by OH groups and acid or base catalysts are often added to increase the reaction rate.[19]

A polymerisation stage occurs next where condensation reactions occur between adjacent molecules with the elimination of H_2O and ROH and the formation of M-OH-M or M-O-M bridges.[19] In this step a colloidal suspension is formed called a sol. The colloidal nanoparticles forming the sol are independent and dispersed in the solvent presenting an internal structure densely crosslinked due to polymerisation (Figure 5-1a).[19]

Subsequently, called gelation, a catalyst is added to promote the link of these colloidal particles with each other to form a 3-D network throughout the liquid (Figure 5-1b).[19] The 3-D assembly of colloidal nanoparticles is rigid and is called a gel. Allowing more time for gelation increases the aggregation of smaller polymer units in the main framework. The solvent and products of the condensation reactions (e.g. water and alcohol) are still present at this stage in the open pore structure of the gel. To remove water and alcohol from the system, different drying techniques can be used at moderate temperatures depending on the desired type of product.[20]

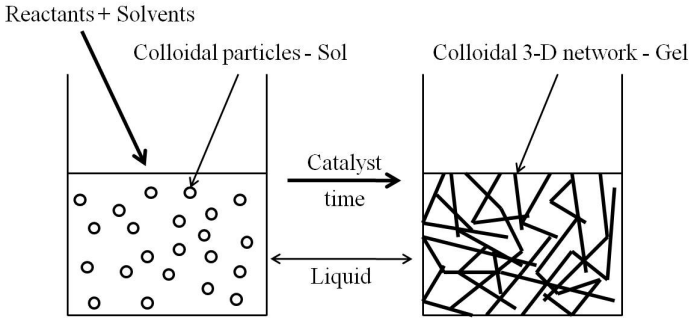

Figure 5-1 The sol-gel process: (a) sol, (b) gel (after [19]).

In 1932, Kistler first used supercritical drying to evacuate the liquid from the wet gels and named the resulting highly porous framework an "aerogel".[19,21] Aerogels retain the open, three dimensional assemblies of nanoparticles which they had in the wet gel stage and although there is no official definition, it is common to use the term "aerogels" only if the pores occupy above 90 % of the sample volume.[20] Silica aerogels have been extensively studied[19] and the silicon alkoxides employed are in the form of $Si(OR)_4$ where R is commonly either an alkyl CH_3 group, in which case the precursor is named tetramethylorthosilicate, or TMOS, or R is an ethyl C_2H_5 group and the corresponding precursor is tetraethylorthosilicate, or TEOS. The synthesised silica aerogel monoliths are

very fragile due to interparticle necks and to overcome this disadvantage, coating with a conformational polymer can reinforce the monolithic structure.[22] Recently such coated monoliths have been synthesised in a one pot process and successfully converted to monolithic silicon carbide aerogels by conventional pyrolysis in argon by Leventis *et al*..[23]

In this chapter, samples of silica aerogels conformally coated (crosslinked) with polyacrylonitrile supplied by Prof. Leventis (Missouri University of Science and Technology) have been studied as precursors for the conversion to silicon carbide using microwave irradiation in air. In the synthesis process used by Prof. Leventis to synthesise the material, two solutions were prepared and added together. The first solution, named A, was prepared by mixing Si-AIBN (4,4′-(diazene-1,2-diyl)bis-(4-cyano-*N*-(3-triethoxysilil)propyl)pentanamide), methanol, tetramethylorthosilicate (TMOS) and AN (acrylonitrile), while a second solution (Solution B) was made of a mixture of methanol, AN, distilled water and NH_4OH. Solution B was added to solution A to form the sol and this mixture gelled within 10 - 15 min and was then transferred in moulds. Aging lasted 24 h at room temperature, then the wet gels were exposed to UV light for 300 s, heated at 55 °C for 12 h and solvent exchanged with ethanol first and then toluene (the first solvent is used to remove gelation water and the second to remove free polyacrylonitrile (PAN) present in the pores).[23] The resulting samples were dried to form PAN-crosslinked aerogels using supercritical fluid (SCF) CO_2 drying. The schematic in Figure 5-2 summarises the reaction scheme.

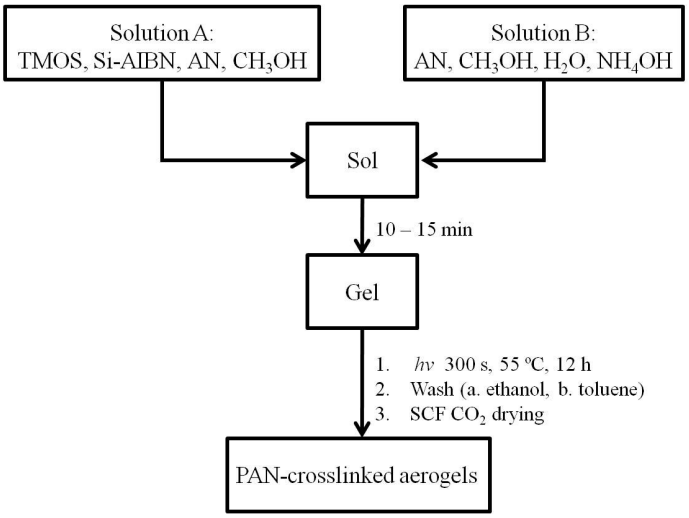

Figure 5-2 Flowchart for the one-pot reaction to synthesise PAN-crosslinked aerogels (after [23]).

Mesoporous monolith silica was coated (cross-linked) in Leventis' group with PAN in one pot using Si-AIBN as free-radical initiator to start the surface initiated free-radical polymerisation (SIP) of acrylonitrile (AN, the monomer) according to Figure 5-3. Gelation and cross-linking have been successfully carried out in the same vessel because the gelation of TMOS takes place at room temperature and does not interfere with the cross-linking process that is triggered while the wet gel is aging.[23]

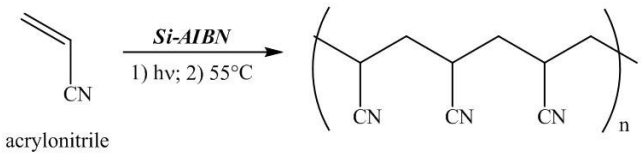

Figure 5-3 Reaction to give PAN (after [23]).

Conversion of the polymer PAN to carbon requires two subsequent temperature treatments. The temperature and time of the treatments were selected in order to prevent the cracking of the samples. The structural rearrangement of the polymer during conversion to carbon creates stresses on the silica framework.[23] The first thermal treatment has been called "aromatisation" and is induced oxidatively by heating the polymer at 225 °C for up to 36 h (Figure 5-4).[23] During this treatment, the open-chain structure of the polyacrylonitrile layer, covering the silica aerogel was converted to a closed-chain arrangement. The dangling nitrile groups of the polymer undergo cyclisation giving rise to an aromatised structure.

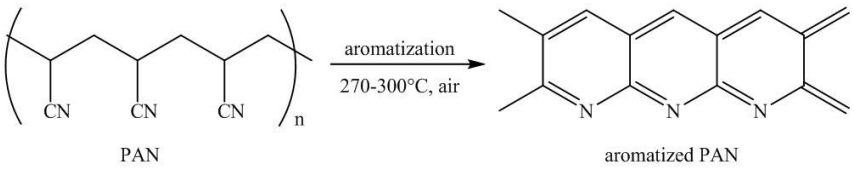

Figure 5-4 Aromatisation of PAN-crosslinked aerogels (after [23]).

The second temperature treatment to convert the PAN to carbon is performed at 800 °C in argon to produce an extended graphitic structure (Figure 5-5).

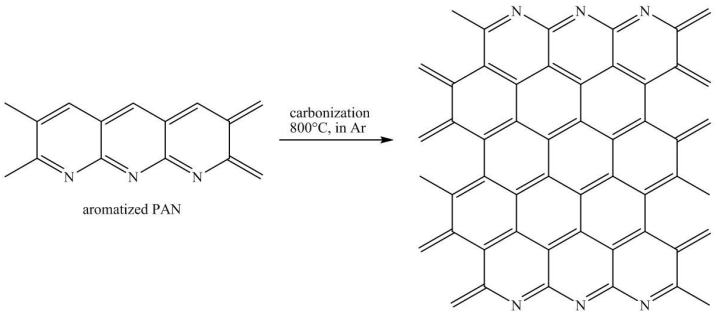

Figure 5-5 Carbonisation of aromatised PAN-crosslinked aerogels (after [23]).

Trial conversion to form porous silicon carbide monoliths is then achieved via pyrolysis at 1600 °C for 72 h. A post synthesis temperature treatment at 600 °C in air removes unreacted carbon.[23]

The advantages of using such composite materials as porous silicon carbide precursors centre on (1) the better homogeneity and intimate mixing of the reactants during the sol-gel method compared to traditional solid state powder methods[20] and (2) the possibility to mimic and preserve the silica aerogel porous framework.[23] The aims of the studies in this chapter are to probe whether it is possible to synthesise porous silicon carbide using microwaves and in so doing both shorten the processing time while retaining the porous microstructure of the precursor.

5.2 Experimental synthesis of silicon carbide

Samples taken from intermediate stages of the precursor synthesis process[23] have been sent by Prof. Leventis and represent the samples tested in this study as potential SiC precursors. These precursors are: (A) PAN-crosslinked silica aerogels, (B) aromatised aerogels and (C) carbon-coated aerogels and the following flowchart (Figure 5-6) shows how these three samples are linked to each other.

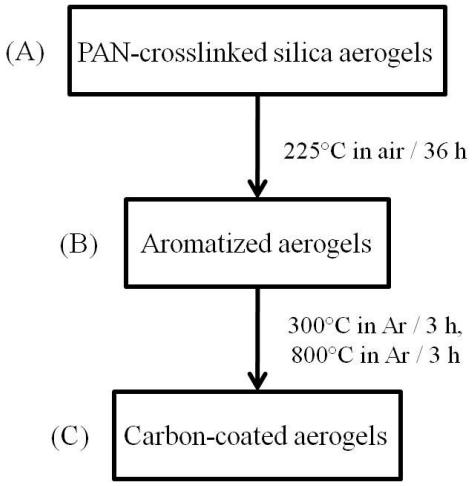

Figure 5-6 Flowchart of the three samples studied as SiC precursors (after [23]).

For the conventional synthesis of SiC pursued by Leventis, the carbothermal reduction to SiC was performed on the carbon-coated aerogels in flowing argon over a period of 36 to 140 h. The crude silicon carbide aerogel monolith produced was successively purified by heating to 600 °C for 5 h to burn off the residual carbon still present in the sample.

5.2.1 Experimental details

5.2.1.1 MMC and SMC syntheses

In this study all reactions were performed using a whole monolith of aerogel taken at different stages (A, B, C in Figure 5-6) in the carbon coated aerogel process. Since the polymeric fraction of the carbon-coated silica aerogels (C) has been already converted into inorganic matter by various temperature treatments (Figure 5-6), they represent the closest analogy to the mixture of silica and carbon powders studied in the previous chapter. The carbothermal reduction was attempted for each sample in a multimode cavity microwave oven (MMC) operating at a frequency of 2.45 GHz frequency and fixed power of 800 W (Chapter 2, section 2.2.1) always positioning the reaction vessel in the same location. A single mode cavity reactor (Chapter 2, section 2.2.2) was also used in reactions with PAN-crosslinked aerogels with a power input of 450 W. In this case the reaction vessel was placed in the centre of the cavity.

During singlemode cavity (SMC) experiments, temperature measurements were taken *in-situ* using an optical pyrometer (LAND System4 Thermometer M1 600/1600 °C; ± 1 °C accuracy) with a 5 mm diameter spot centred on the sample surface. From a trial experiment in the SMC, it was discovered all the silica aerogel samples used as silicon

carbide precursors in this study do not couple directly with microwaves, hence graphite was used as a susceptor in each experiment.

In the case of carbon-coated samples (C), monoliths were immersed in a beaker of distilled water for a certain time in each case. Samples were then embedded in graphite powder and placed in an open silica tube surrounded by silica flour. When starting from aromatised silica aerogels (B) or PAN-crosslinked silica aerogels (A), samples were reacted without use of water using the same set up as above (shown in Figure 5-7). Since the polymeric fraction is still present, water was found to be counterproductive, possibly due to the hydrolysis of the polymer at high temperatures.[24]

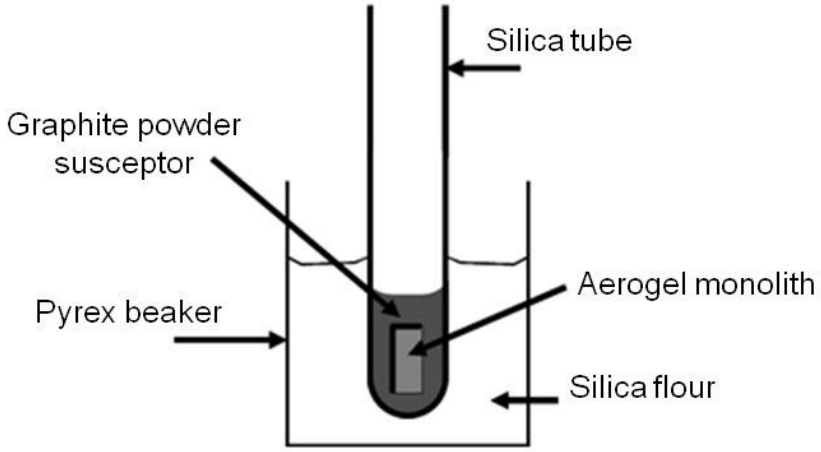

Figure 5-7 Schematic representation of MMC reaction set-up.

All preparations were performed at ambient pressure in air and were performed as described in the following table (Table 5-1).

Sample identifier	Precursor	Precedent soaking in water	Type of cavity	Power / W	Irradiation time / min
1	Carbonised (C)	x	MMC	800	20
2	Carbonised (C)	x	MMC	800	20
3	Aromatised (B)	-	MMC	800	1
4	Aromatised (B)	-	MMC	800	1.5
5	Aromatised (B)	-	MMC	800	2
6	Aromatised (B)	-	MMC	800	3
7	Aromatised (B)	-	MMC	800	4
8	Aromatised (B)	-	MMC	800	5
9	Aromatised (B)	-	MMC	800	10
10	Aromatised (B)	-	MMC	800	15
11	PAN-x-linked silica (A)	-	MMC	800	10
12	PAN-x-linked silica (A)	-	MMC	800	15
13	PAN-x-linked silica (A)	-	SMC	450	3
14	PAN-x-linked silica (A)	-	SMC	450	3.5

Table 5-1 Summary of all experiments carried out on using different kind of aerogels as precursors.

The samples were characterised using Powder X-ray diffraction (PXD) to study the structural evolution from likely amorphous materials to crystalline silicon carbide. PXD (PXD, Chapter 2, section 2.3.1.3) (PANalytical X'Pert MPD, Cu $K_{\alpha 1}$ radiation) was carried out routinely using 1 hour scans in flat plate Bragg Brentano geometry to identify product phases by reference to the ICDD PDF database[25] using the PANalytical program Xpert HighScore Plus. Specific samples were also characterised using Raman spectroscopy (Chapter 2, section 2.3.3) to complement the PXD data and determine whether any phases were present that were amorphous to X-rays (Chapter 2, section 3.3). Raman spectra were collected at room temperature using a Horiba LabRAM HR confocal microscope system with a 532 nm green laser (Laser Quantum Ventus 532, 150 mW). A hole aperture of 50 μm, a 600 gr mm^{-1} grating and a Synapse CCD detector were used for the experiment.

Fragments belonging to the products were examined using scanning electron microscopy (SEM) to study the morphological changes starting on treating the samples with microwave irradiation. Field emission scanning electron microscopy (FESEM) was conducted under high-vacuum conditions using a Hitachi S4700 microscope with a 10 kV

accelerating voltage and secondary electron detection to study the morphology of the sample. Samples for FESEM were prepared by depositing samples on to carbon tabs.

For the carbon-coated silica aerogel and (C, **1-2**) PAN-crosslinked (A, **12-14**) monoliths, the free carbon content of samples post microwave synthesis was determined using differential scanning calorimetry/thermogravimetric analysis (TGA/DSC, SDT Q600 TA Instruments, Chapter 2, section 3.6) coupled to mass spectroscopy (MS, ESS evolution model). All samples analysed were heated at a rate of 10 °C min^{-1} up to 800 °C, and held at this temperature for 5 h in a 2 % O_2/Ar atmosphere. The percentage weight changes have been recorded using TGA and signals identified as CO_x from the products were simultaneously followed using MS. Samples were collected after TGA analysis and analysed by PXD.

5.3 Results and discussion

5.3.1 Carbonised silica aerogels (C) as SiC precursors

5.3.1.1 Synthesis and PXD studies

Initially a trial experiment was run in which 0.2 ml of water was added to a piece of a carbon-coated silica aerogel (C) ground with a mortar and pestle. A pellet was pressed from the ground powder and irradiated in an MMC for 25 min. The PXD pattern (Figure 5-8) reveals peaks belonging to graphitic layers; in particular strong peaks at 2θ ~ 26.7º and 2θ ~ 55º corresponding to the (002) and (004) plane of graphite respectively.[26] β-SiC reflections from (111), (220) and (311) planes demonstrate that it is possible to form silicon carbide from x-aerogel samples. After this trial experiment, subsequent samples were not ground with the aim of preserving their monolithicity. Water was introduced in the subsequent samples by soaking the monoliths in a beaker of distilled water.

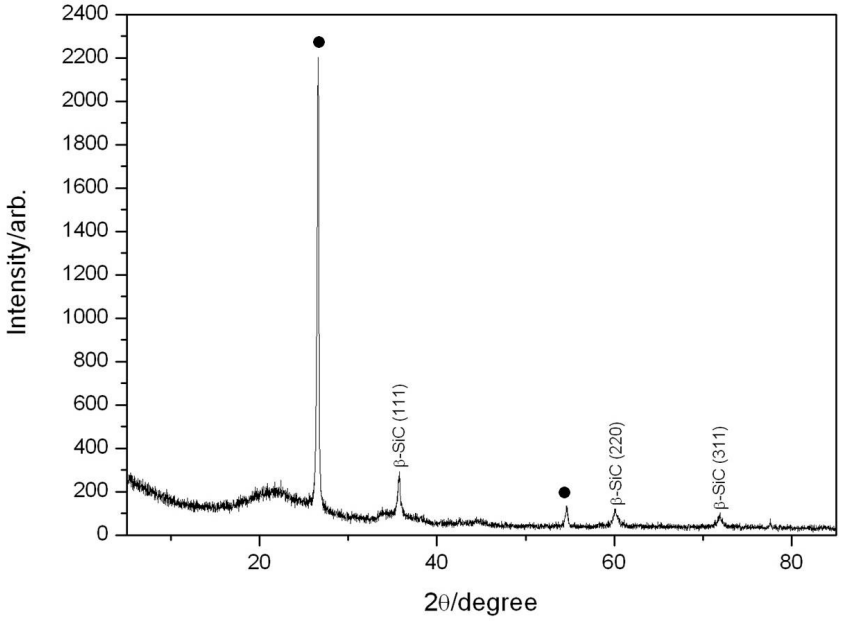

Figure 5-8 PXD pattern from a pellet pressed from a ground carbon-coated silica aerogel. Reflections from graphite from susceptor (●) are also indicated.

A piece of the carbonised sample (**1**) was soaked in water for 1 h, embedded in graphite and then reacted in a MMC. After 20 min, as can be seen in the PXD pattern (Figure 5-9), β-SiC is the most prominent phase. The noisy background along with a broad feature at ca. 23° 2θ suggests that the sample is not composed completely of crystalline phases and amorphous silica or carbon is still present.

If sample from stage C is soaked in distilled water for 24 h (**2**), while keeping other reaction parameters constant, higher crystallinity products are obtained manifested by the flatter, smoother background of the PXD pattern and sharp diffraction peaks. It was observed that soaking the sample in water for a longer duration increases the brittleness of the β-SiC product. The graphitic peaks present on the pattern are believed to belong to the susceptor used in the reaction due to the difficulty in cleaning the sample after the reaction.

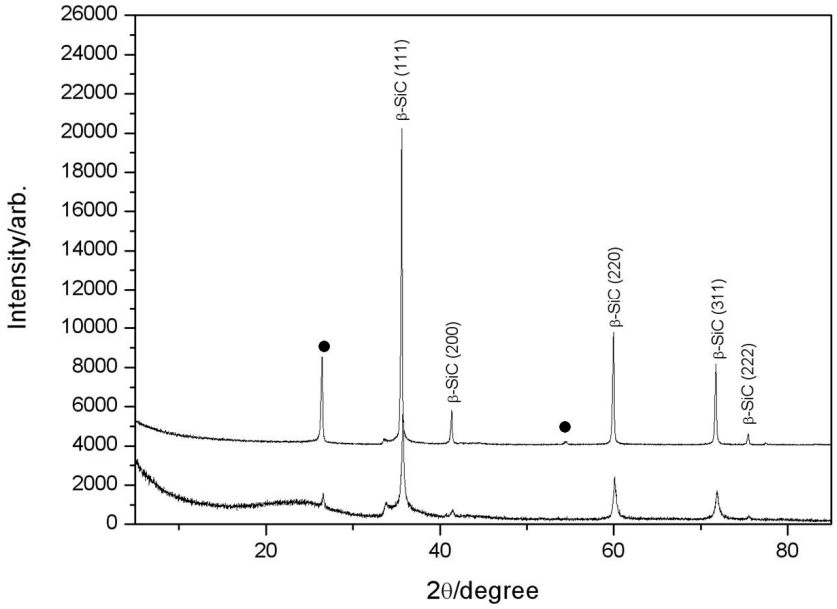

Figure 5-9 PXD patterns of products synthesised from carbonised silica aerogels in an MMC for 20 min after the monolith has been soaked for (a) 1 (1 h); (b) 2 (24 h) in distilled water. Reflections from graphite (●) are also indicated.

5.3.1.2 Scanning electron microscopy (SEM)

SEM micrographs reveal that for samples produced from carbon-coated silica aerogels, the length of the treatment in water does not appreciably affect the morphology of the products. After 20 min reactions (samples **1** and **2**) a porous matrix of submicron sized irregular particles (of the order of 50 – 100 nm across) is formed whether the monoliths have been soaked in water for 1 h (**1**, Figure 5-10) or 24 h (**2**, Figure 5-11). The monoliths appeared visibly cracked after reaction (Figure 5-10b).

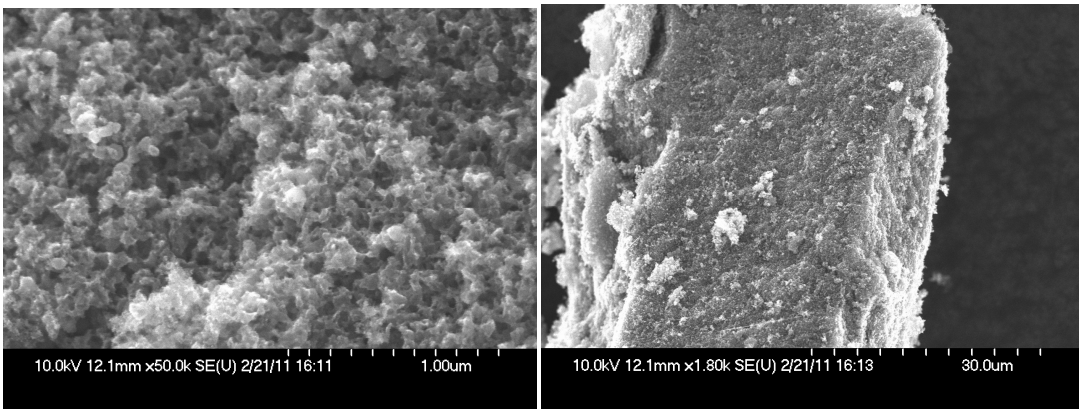

Figure 5-10 SEM micrographs of samples (a)-(b) 1 (1 h soaked in water, 20 min in MMC).

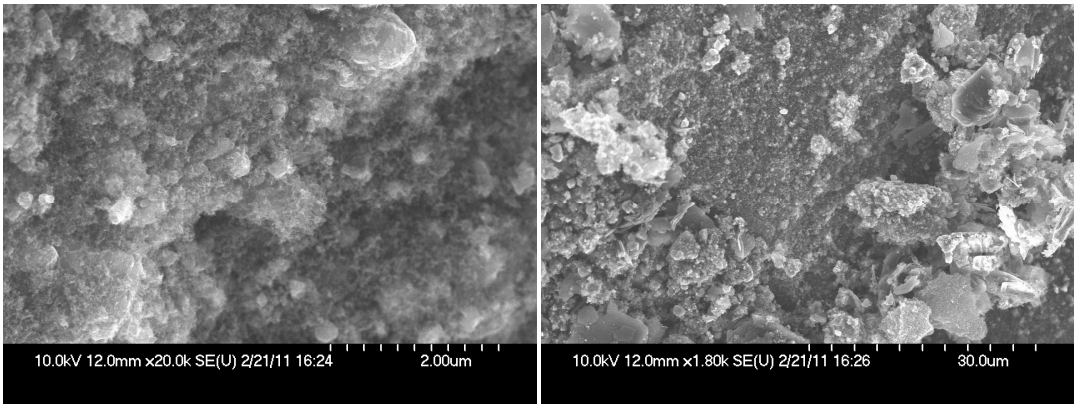

Figure 5-11 SEM micrographs of samples (a)-(b) 2 (24 h soaked in water, 20 min in MMC).

5.3.1.3 Raman spectroscopy

The Raman spectra of **1** and **2** (Figure 5-12) exhibit a band at 790 cm^{-1} corresponding to the Transverse Optical (TO) Raman-active mode in β-SiC (3C-polymorph; zinc blende structure).[27] The weak feature present in sample **1** at ~ 434 cm^{-1} is associated with Si-O-Si symmetric stretching-bending modes arising from residual silica. Bands between 380 - 480 cm^{-1} have been assigned to silicates such as quartz, cristobalite and tridymite in which tetrahedra form six-member rings.[28] Intense diagnostic bands originating from carbon are observed in both samples **1** and **2** at higher wavenumbers: ca. 1340 cm^{-1} and 1570 cm^{-1}. These can be assigned to the D and G band respectively.[29] The G band is associated with the vibration of sp^2-bonded carbon atoms belonging to graphitic layers, while the D band relates to the vibration of carbon atoms presenting a sp^3 configuration due to dangling bonds, in-plane terminations or defects in disordered carbon materials.[30] As already mentioned in Chapter 3, the line broadening of the G band and the intensity ratio between the D and G bands (D/G) depends on the structure of the carbon. In particular the G bandwidth is related to the disorder within the carbon sheets and the intensity ratio D/G depends on the order of the structure, being zero for natural graphite crystals and highly ordered pyrolytic graphite (HOPG).[31] According to the Raman spectra of samples **1** and **2** (Figure 5-12) and in agreement with patterns obtained from PXD, it can be said that while sample **2** contains mostly amorphous carbon, in sample **1** the stronger G band is likely to originate from graphite (probably graphite susceptor).

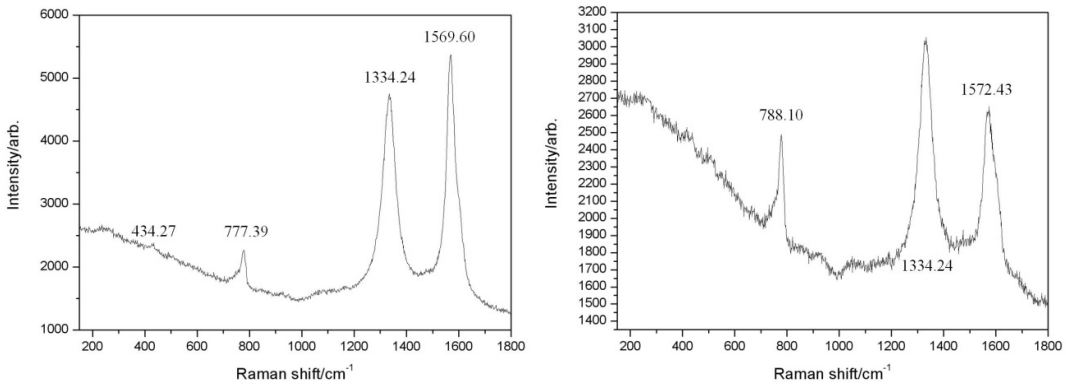

Figure 5-12 Raman spectra and observed bands for samples (a) 1 and (b) 2.

5.3.2 Aromatised silica aerogels (B) as SiC precursors

In this batch of samples, the dangling nitrile groups of the polyacrylonitrile layer covering the silica aerogel were converted to aromatised structures by temperature treatment (see Figure 5-4). Samples irradiated with microwaves for times above 5 min always fractured in the MMC reactor and the pieces collected were extremely brittle. Extended reaction times ranging from 10 - 15 minutes (samples **9** and **10**) caused the monoliths to disintegrate and fragments were difficult to recover from the graphite susceptor. PXD demonstrated that β-SiC was obtained from an aromatised silica aerogel after 5 minutes (Figure 5-14a). One additional peak can be seen around 33° 2θ in the PXD pattern next to the (111) peak of the cubic phase which is an indication of stacking faults in the structure.

Powder patterns from samples obtained after longer irradiation times (samples **8-10**) always contained graphite peaks, as a reflection of the fact that it is difficult to recover the broken fragments from the susceptor powder. Further, the flat background around 20° 2θ indicates no evidence of amorphous residual silica for any of the irradiation times employed.

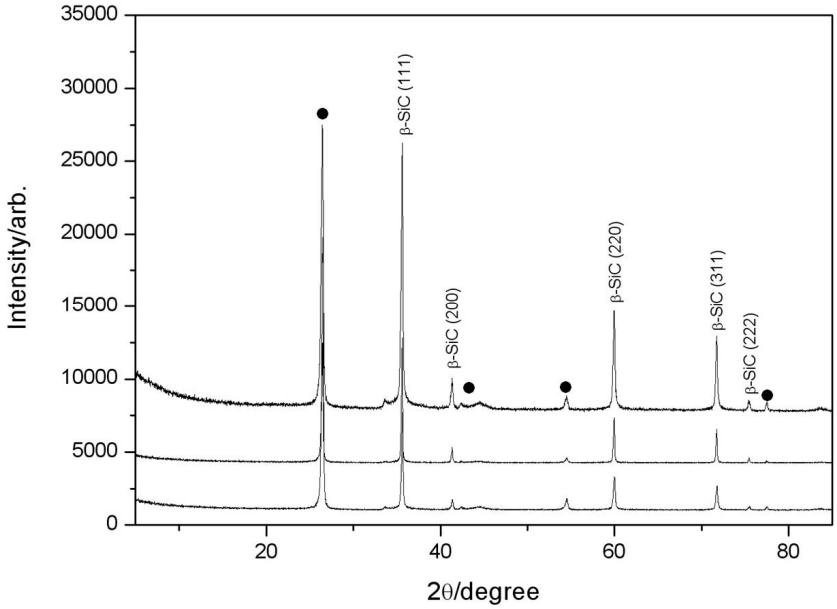

Figure 5-13 PXD patterns of β-SiC synthesised from aromatised silica aerogels in an MMC for (a) 8 (5 min); (b) 9 (10 min) and (c) 10 (15 min). Reflections from graphite (●) are also indicated.

Shorter irradiation times were employed to see if β-SiC could still be produced while preserving monolithicity. Below 5 min irradiation, samples **3-7**, it is already possible to produce β-SiC and the extent of cracking on the monoliths is reduced. Figure 5-14 shows the PXD patterns of the samples produced from aromatised silica aerogels from reaction times ranging from 1 - 4 minutes (samples **3-7**). Peaks belonging to β-SiC are observed after only 1 minute along with a broad peak around 23° 2θ that could be tentatively assigned to amorphous silica and/or carbon. As the reaction time increases, it is clear that peaks belonging to cubic silicon carbide increase in intensity and the background of the pattern flattens to suggest that amorphous components have decreased and perhaps therefore, that residual silica has fully reacted. Even in these products a shoulder at 2θ ca. 33° adjacent to the (111) reflection of β-SiC suggests the existence of stacking faults in the as-produced powders. The graphitic peak present at 2θ ~ 26° has a relative intensity that is not obviously irradiation time-dependent and it is believed to originate from the graphite powder used as the susceptor in the reaction.

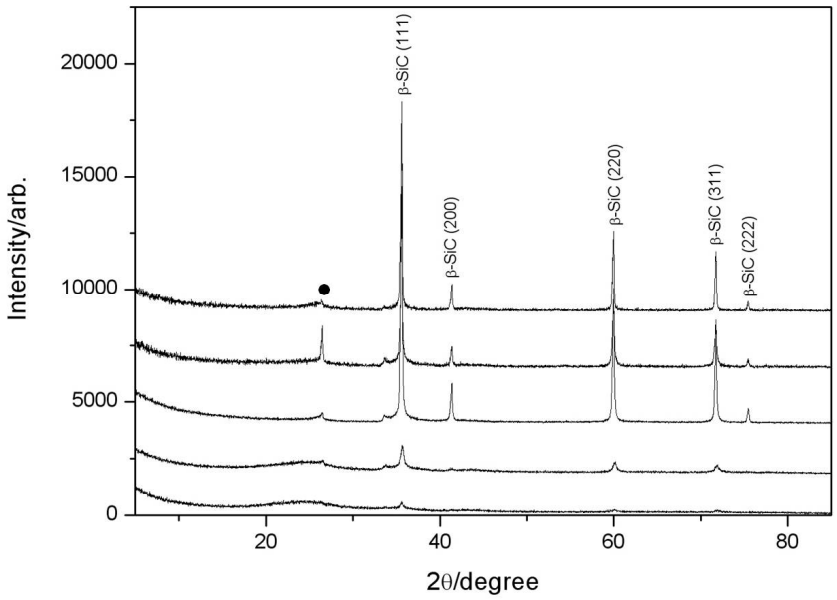

Figure 5-14 PXD patterns of β-SiC synthesised from an aromatised silica aerogel in an MMC for (a) 3 (1 min); (b) 4 (1.5 min); (c) 5 (2 min); (d) 6 (3 min); (e) 7 (4 min). Reflections from graphite (●) are also indicated.

The samples of reactions after 1, 2 and 4 minutes (samples **3**, **5** and **7** respectively) were also analysed using scanning electron microscopy (SEM) and Raman spectroscopy to study the changes in structure and morphology as a function of irradiation time.

5.3.2.1 Scanning electron microscopy (SEM)

A SEM micrograph of the PAN cross-linked silica aerogel, taken in Leventis' lab and reproduced with the permission of Prof. Leventis, is shown in Figure 5-15.

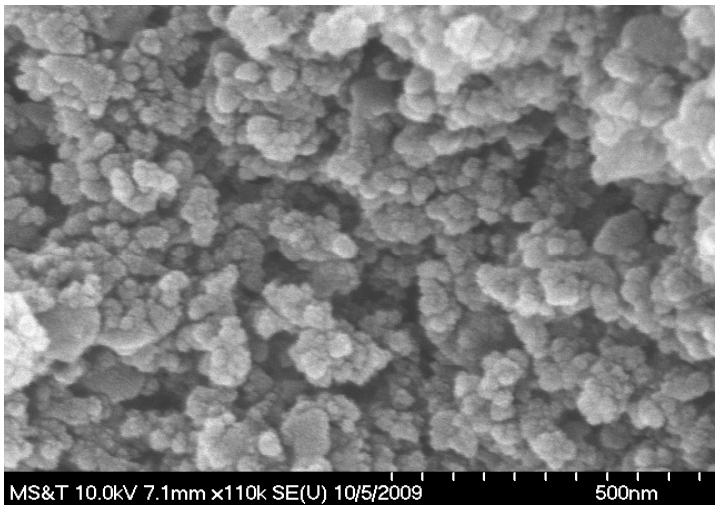

Figure 5-15 SEM image of aromatised PAN cross-linked silica aerogels, taken by Leventis' group.

Comparing this image with the SEM images of the samples after microwave irradiation (Figure 5-16-17), the difference in morphology can be seen as the reaction progresses. After 1 minute of irradiation the micrograph (Figure 5-16a) shows that submicron sized irregular particles (of the order of 50 – 100 nm across) are partially fused together to form a porous matrix, a morphology similar to that of the starting material. As the irradiation time increases, the SEM micrographs show an increasing amount of well-formed, faceted crystallites appearing, while agglomerations of irregular shaped nanoparticles are clearly observed for reaction times shorter than 4 minutes. Further, while the size distribution of the particles is still not uniform, a significant increase in the particle size can be noted with crystalline SiC particles of the order of microns present after 2 minutes (particles from **5** are shown in Figure 5-16c). It is interesting to note that the crystallites are embedded in a matrix composed of very fine material (Figure 5-17a-b). Looking at the progression in the morphology of the sample with irradiation time, a net contrast can be seen in the sintering and density of samples made in the MMC. The low magnification micrographs show, in fact, increased sintering as the irradiation time increases, as one might expect.

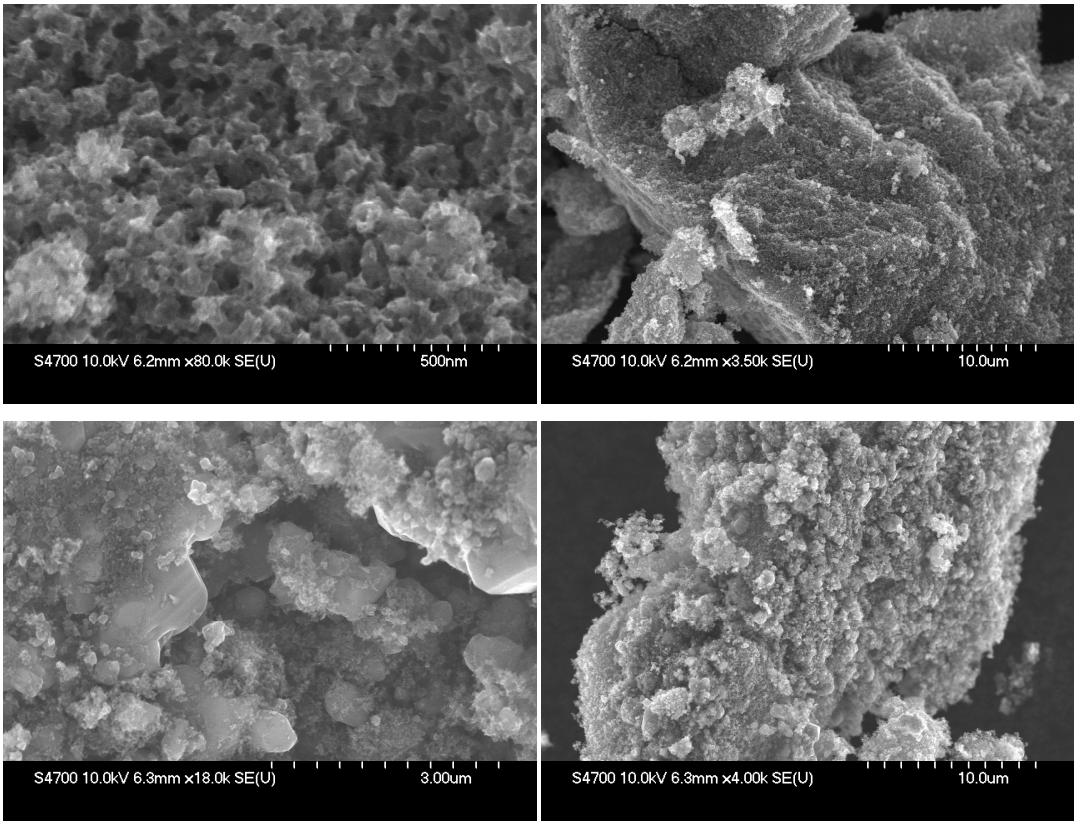

Figure 5-16 SEM micrograph of samples (a)-(b) 3 (1 min) and (c)-(d) 5 (2 min) (Table 5-1).

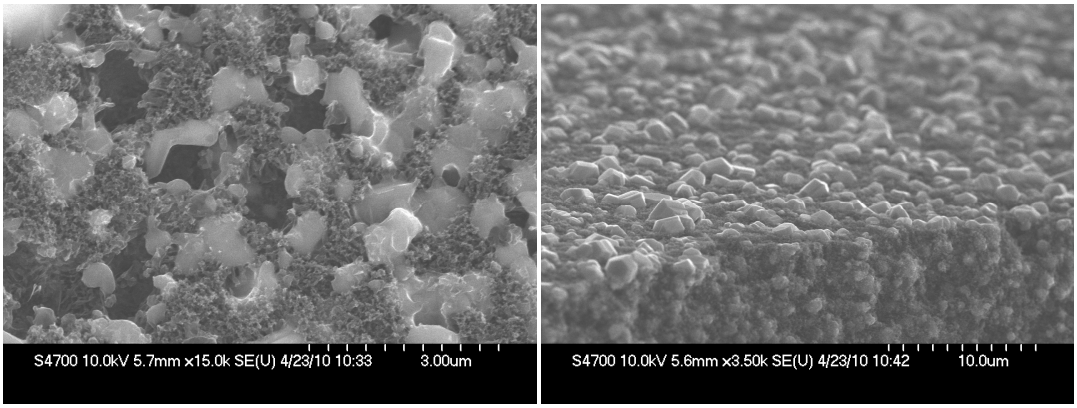

Figure 5-17 SEM micrograph of samples (a)-(b) 7 (4 min)(Table 5-1).

5.3.2.2 Raman spectroscopy

As is already evidenced from the PXD pattern (Figure 5-14a), sample **3** irradiated with microwaves only for 1 minute shows a Raman spectrum representing in all likelihood, mainly the unreacted starting materials. The two main peaks are considerably broad and their Raman shifts (ca. 1330 cm^{-1} and 1580 cm^{-1} respectively) match well to the D and G bands for carbon materials. In fact, although the common values for D and G bands for glassy carbon are ca. 1350 cm^{-1} and 1590 cm^{-1},[31] the possibility for shifted values for both bands has been already reported in the literature.[32] The relative intensity of the D and G bands suggests that after 1 minute irradiation, carbon is still mainly unreacted. Additional weak features present in the low wavenumber region of the Raman spectra are most likely to belong to silica[33,34] and only one very broad and weak feature around 760 cm^{-1} can be considered to represent silicon carbide. Raman spectra of samples **5** and **7** (Figure 5-18) exhibit a very strong band at ca. 770 cm^{-1} corresponding to the Transverse Optical (TO) Raman-active mode in β-SiC.[27] As the irradiation time increases, the strong band at 780 cm^{-1} (Figure 5-18b-c) becomes sharper indicating the products are more crystalline,[35,36] as confirmed from the SEM micrographs where faceted crystalline particles start appearing (Figure 5-17).

For sample **7**, irradiated for 4 min, weaker bands appear in addition to the strong band at 780 cm^{-1} (Figure 5-18c). The presence of these features is reported in the literature indicating the presence of strain in the SiC structure possibly associated with stacking faults often indicating the formation of the 4H polytype of α-SiC.[37,38] The additional weak and broad features at high wavenumbers (above 800 cm^{-1}) are due to overtones in the second order Raman spectrum of silicon carbide.[39]

Given that the D band is either of higher intensity or comparable intensity to the G band for **5** and **7**, it is likely that these samples contain a significant fraction of unreacted amorphous carbon.[31]

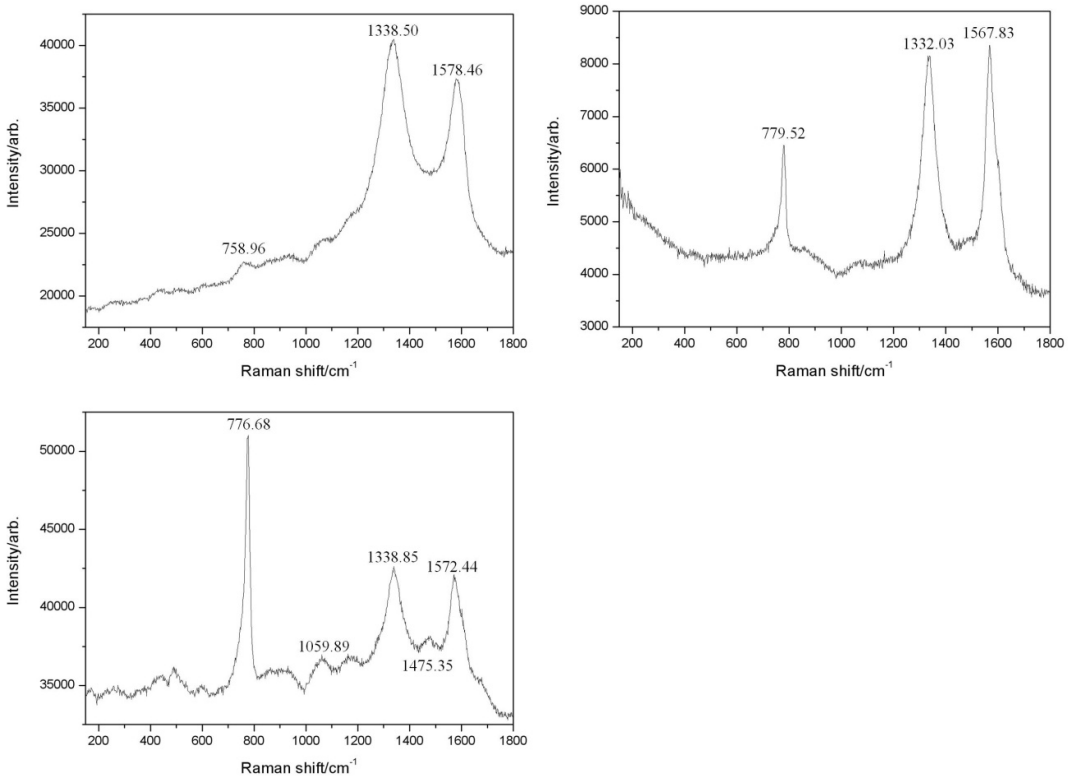

Figure 5-18 Raman spectra and observed bands for samples (a) 3; (b) 5 and (c) 7 (Table 5-1).

5.3.3 PAN-crosslinked silica aerogels (A) as SiC precursors

5.3.3.1 Synthesis and PXD studies

The main difference between these last samples and those studied in the previous sections (carbon-coated silica aerogels and aromatised silica aerogels) is the fact that the porous silica framework is coated with polyacrylonitrile, whereas for the other precursors all the organic species are oxidised during temperature treatments (see Introduction and Figures 2 and 6). The PXD patterns of samples produced after 10 and 15 minutes of irradiation using graphite as a susceptor in a MMC are shown in Figure 5-19. Between 20-30° 2θ the background is not flat, suggesting the samples contain amorphous phases. After 15 minutes the main cubic silicon carbide reflections are prominent with a well defined peak at ca. 33° 2θ originating from stacking faults in the structure. The only indication of a crystalline

impurity present is the (002) reflection from graphite belonging to the susceptor at ca. 26° 2θ.

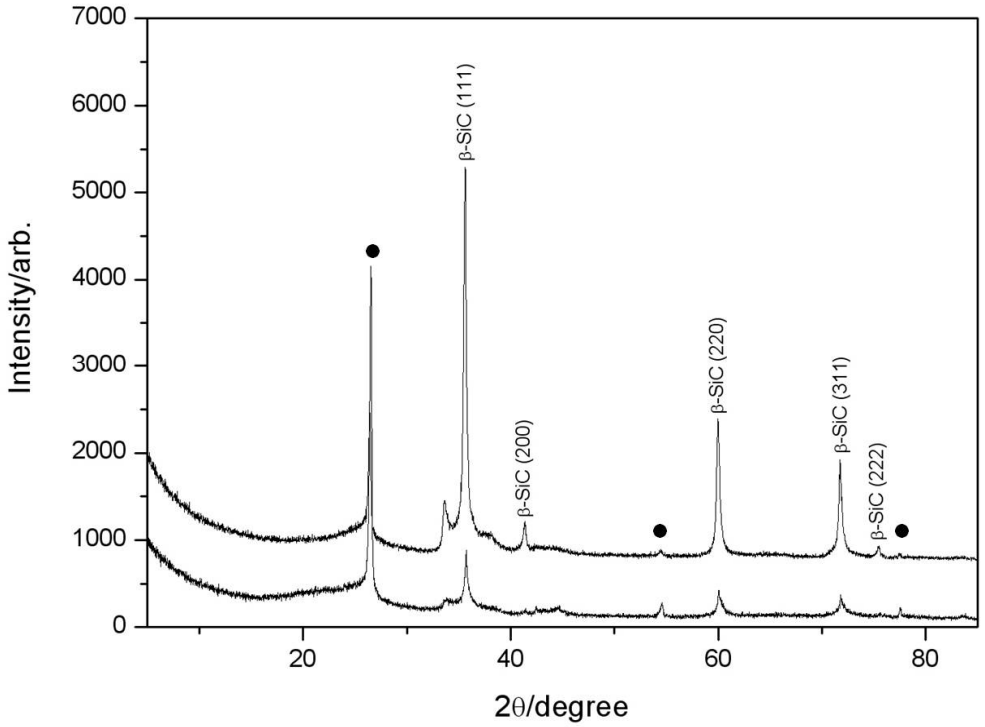

Figure 5-19 PXD patterns of products synthesised from PAN-crosslinked silica aerogel in a MMC at (a) 10 min (11) and (b) 15 min (12). Reflections from graphite (●) are also indicated.

Experiments were also run in an SMC to evaluate the influence of a more homogenous heating profile on the samples. An SMC synthesis experiment without the use of a graphite susceptor was attempted and was unsuccessful. Therefore even in the SMC, surrounding graphite was crucial as a MW susceptor.[40]

In-situ optical pyrometer measurements taken during the course of reaction recorded temperatures of approximately 1400 K (see Appendix for optical pyrometers output). The PXD patterns (Figure 5-20) of two samples irradiated at 450 W for 3 minutes and 3.5 minutes (samples **13** and **14** respectively) show a profound change in reaction outcome over a 30 s period. Single phase β-SiC can be synthesised in less than 4 minutes using an SMC.

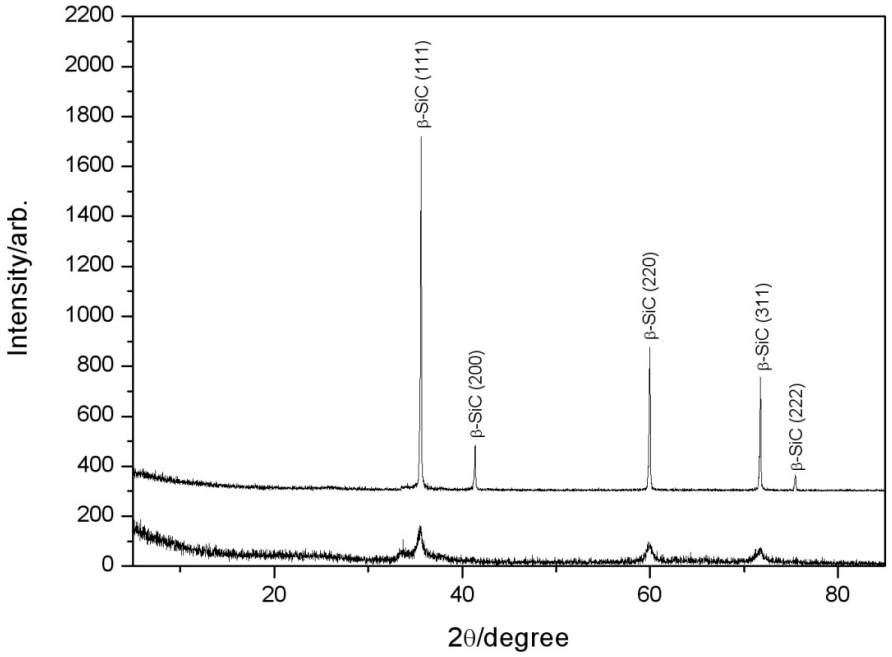

Figure 5-20 PXD patterns of β-SiC synthesised from an PAN-crosslinked silica aerogel in a SMC at (a) 3 min (13); (b) 3.5 min (14).

5.3.3.2 Scanning electron microscopy (SEM)

The SEM analysis (Figure 5-21) shows the inhomogeneous morphology of a sample synthesised in an MMC (**15**), which is composed of nanowires and agglomerations of nanoparticles.

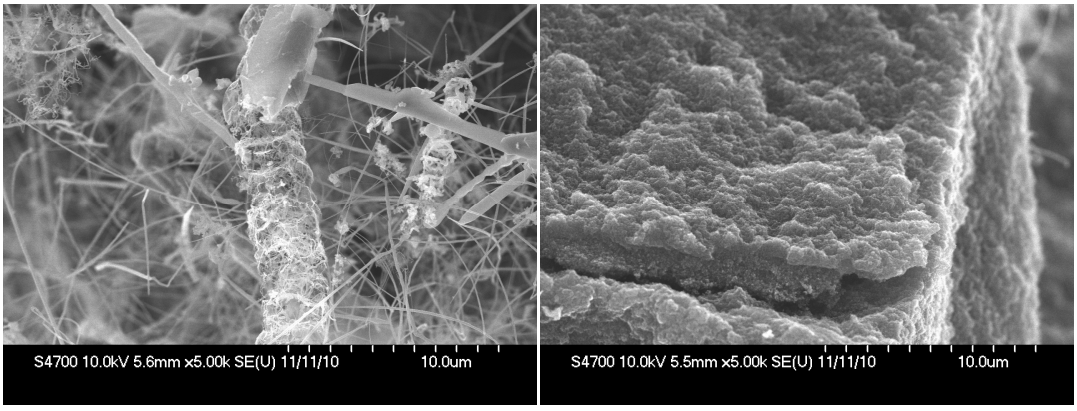

Figure 5-21 SEM micrographs (a) - (b) of sample 12 (Table 5-1).

By contrast, the SEM micrographs (Figure 5-22) of samples **13** and **14** confirm the high degree of crystallinity of the samples synthesised in a SMC. In particular sample **14** (Figure 5-22c) at low magnification shows a product composed of well-formed faceted particles with sizes ranging from few microns to many tens of μm in size. In comparison with the samples synthesised using a MMC (Figure 5-21), it can be noted the samples

synthesised in a SMC is composed only of particles showing different particle size distribution.

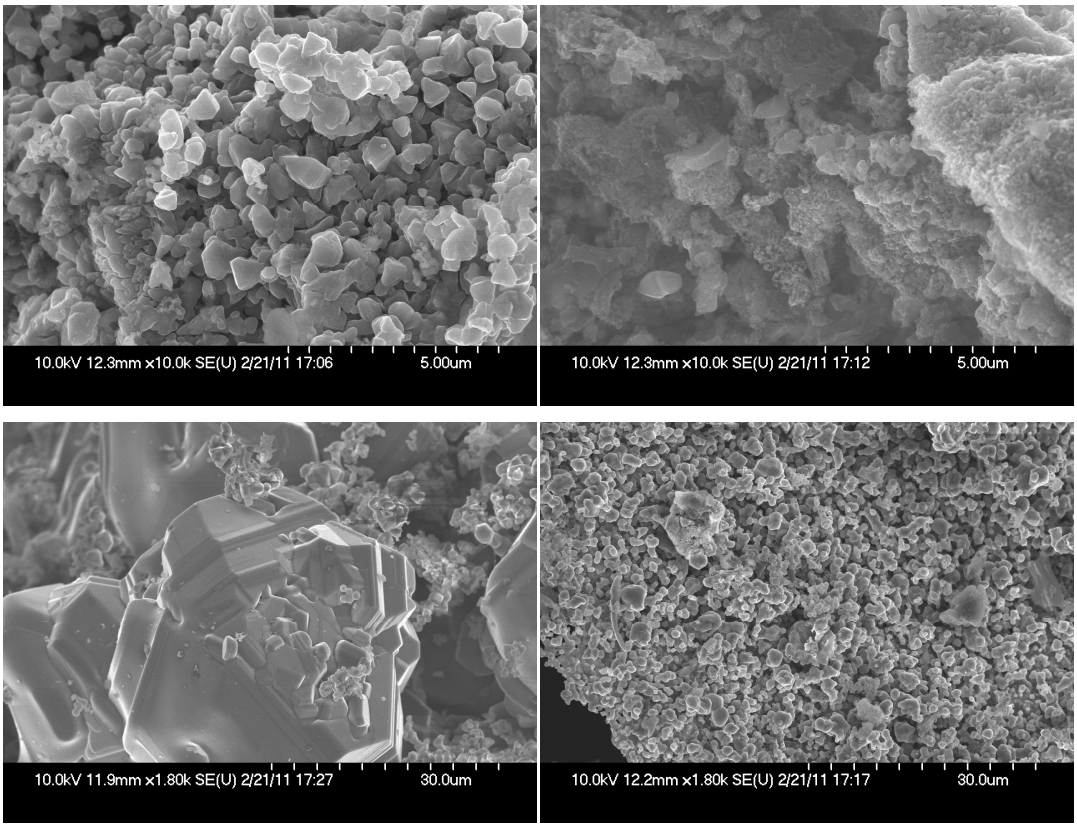

Figure 5-22 SEM micrograph of samples (a)-(b) 13 and (c)-(d) 14 (Table 5-1).

5.3.3.3 Raman spectroscopy

The Raman spectrum of sample **12** obtained starting from PAN cross-linked silica aerogels (A) and irradiated with microwaves in a MMC setup is reported in Figure 5-23. From the SEM micrographs (Figure 5-21), nanowires are present along with agglomeration of particles in sample **12** and the corresponding Raman spectra show considerably broader bands and additional features compared to the equivalent irradiated in the SMC setup (Figure 5-24). As already reported in the literature for the case of isolated nanowires, the strong TO band of cubic silicon carbide in Figure 5-23 is actually composed of two peaks, hence the asymmetry of the band in the Raman spectrum.[36] In particular, the main diagnostic peak at 773.85 cm^{-1} shows a shoulder at 743.71 cm^{-1} attributed to defect-induced TO phonon mode scattering.[36]

The defective structure is also confirmed by the Raman analysis that presents weak and broad features at ~ 500 cm^{-1} attributed to defect-induced acoustic (transverse and longitudinal) phonon mode scattering.[36] The broad features above 800 cm^{-1} are instead

relating to the second order Raman spectrum of silicon carbide.[39] The relative intensity of the D and G bands at high wavenumbers (1328.22 and 1578.46 cm^{-1} respectively) belonging to carbonaceous materials, indicate that amorphous carbon dominates over graphitic material and is likely unreacted carbon from the aerogel precursor.[31]

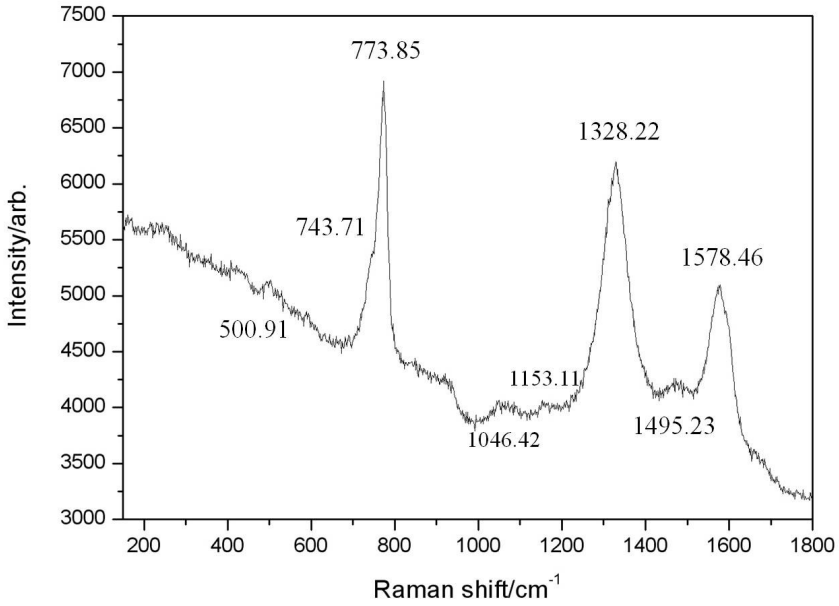

Figure 5-23 Raman spectra and observed bands for sample 12 (Table 5-1).

The Raman spectra of samples **13** and **14** synthesised in an SMC confirmed the high crystallinity of these products. The main TO band of cubic silicon carbide (at ~ 780 - 790 cm^{-1}) in particular appears very sharp.[35,36] Despite the PXD pattern of sample **13** (Figure 5-20) showing broad peaks, the Raman spectrum of the sample irradiated for 3 min in a SMC exhibit a very strong band at 780 cm^{-1}, suggesting that in parts of the sample, β-SiC is already well crystallised. Signs that the reaction is not complete can be found in the low wavenumber region where a silica band at ca. 200 cm^{-1} is present28 and the presence of unreacted amorphous carbon is strongly suggested by a broad and relatively intense D band at 1330 cm^{-1} compared to the G band at 1580 cm^{-1}.[31]

As already noted from the results from the SEM analysis of sample **14** (Figure 5-22b) and in agreement with the PXD of the sample (Figure 5-20b), the Raman spectrum of the sample suggests improved crystallinity and increased crystallite sizes. The Raman analysis in fact shows the band widths in the spectrum are narrower for the sample irradiated for the longer time again suggesting higher crystallinity.[35,36] Furthermore a very strong band at 790 cm^{-1} (with a shoulder at ca. 760 cm^{-1}) and a less intense band at 990 cm^{-1} are present, corresponding respectively to the Transverse Optical (TO) and Longitudinal Optical (LO)

Raman-active mode in β-SiC,[35] along with overtones in the high wavenumbers region of 1500 - 1700 cm^{-1} (respectively at ca. 1500 cm^{-1} and 1700 cm^{-1}).[39]

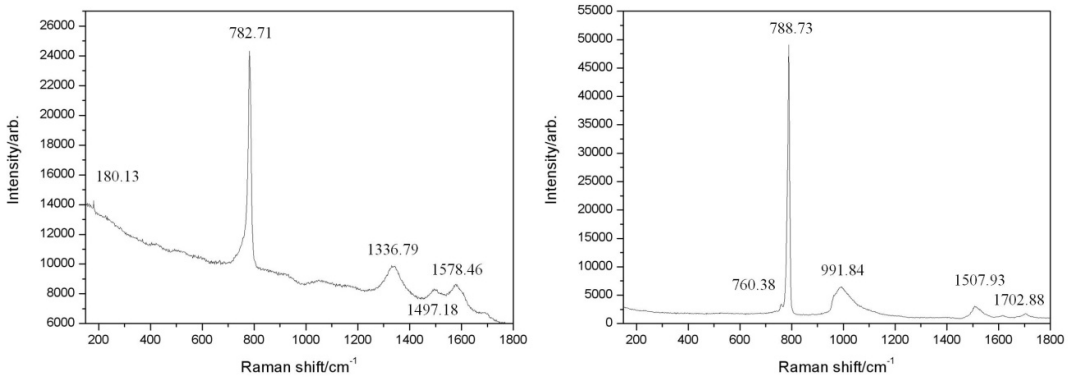

Figure 5-24 Raman spectra and observed bands for samples (a) 13 (3 min) and (b) 14 (3.5 min) (Table 5-1)

5.3.4 Study on the surface area and free carbon content

Surface areas were determined by Andrew Monaghan (School of Chemistry, University of Glasgow) for carbon-coated (C) and PAN-crosslinked (A) samples from nitrogen adsorption at -78 °C using the BET equation (Table 5-2). Samples **1** and **2** yielded specific surface areas of 184.0 and 106.5 $m^2 g^{-1}$ respectively. When silicon carbide is synthesised from PAN-crosslinked silica aerogels, the organic volatile species evolved in the carbonisation process increase the content of pore and therefore the surface area of the product was higher than **1** and **2** for sample **12**. Furthermore, sample **12** has had no previous heat treatments like aromatised (B) or carbon-coated (C) samples. A significant decrease in the specific surface area occurs for sample **13**, which reflects the increased sintering induced by the SMC. In sample **14** the silicon carbide specific surface area is reduced still further as the sintering of the product becomes even greater.

Sample	**1**	**2**	**12**	**13**	**14**
$m^2 g^{-1}$	184.0	106.5	212.9	72.9	11.1

Table 5-2 BET specific surface areas of carbon-coated (C) and PAN-crosslinked (A) samples.

The content of "free" carbon in the products after reaction has been studied using thermogravimetric analysis (TGA). The weight loss below 100 °C is attributed to evaporation of physically adsorbed water and is notable in sample **2**, which was soaked for 24 h in distilled water (1.5 % weight loss starting at 113 ºC). Above that temperature, in

the oxidizing atmosphere (2 % O_2/Ar), the main weight loss in the TG curve derives from the oxidation of the remaining carbon, as suggested by the MS, and varies from sample to sample. The slight increase in weight after all carbon has been removed is probably due to the oxidation of nanostructured silicon carbide, less resistant to oxidation compared to silicon carbide particles of micrometer sizes.[41] The presence of silica has been proved from the PXD analysis of sample **2** after TGA (Figure 5-26b). Most of the samples start to lose weight at around 640 – 650 ºC. The exceptions are sample **2** that shows a higher resistance to oxidation (weight loss initiates at 770 ºC) and sample **13** which begins to lose mass from ca. 610 ºC. The highest mass loss recorded is 34 % for sample **12**, not surprising since the sample pre-TGA showed a high presence of carbon, both as graphitic reflections in the PXD (Figure 5-19) and as amorphous carbon in the Raman spectrum (Figure 5-23). Furthermore, sample **12** is also the sample with the highest specific surface area (Table 5-2), providing an increasing active surface area for oxidation. The presence of a high fraction of carbon can also be seen in the TGA curve of sample **2**. In this case, as opposed to sample **12**, the higher temperature of oxidation and the fact that the sample is still losing weight after 5 h at 800 ºC it is likely originating from a different form of carbon, such as graphite, undergoing oxidation. It is known graphite has a higher oxidation resistance than activated carbon,[42] furthermore the specific surface area for sample **2** is half the one from sample **12**. Overall, the TGA analysis suggests the purest silicon carbide sample produced starting from PAN cross-linked silica aerogels is sample **14**, with 8 % of free carbon and good crystalline properties of the sample (see following characterisation analyses). This is not surprising, seeing that the sample pre-TGA shows no sign of a significant presence of carbon both in the PXD (Figure 5-20) and Raman spectrum (Figure 5-24) and the SEM micrographs of sample **14** (Figure 5-22) show a very sintered sample, in agreement with a very low specific surface area (Table 5-2).

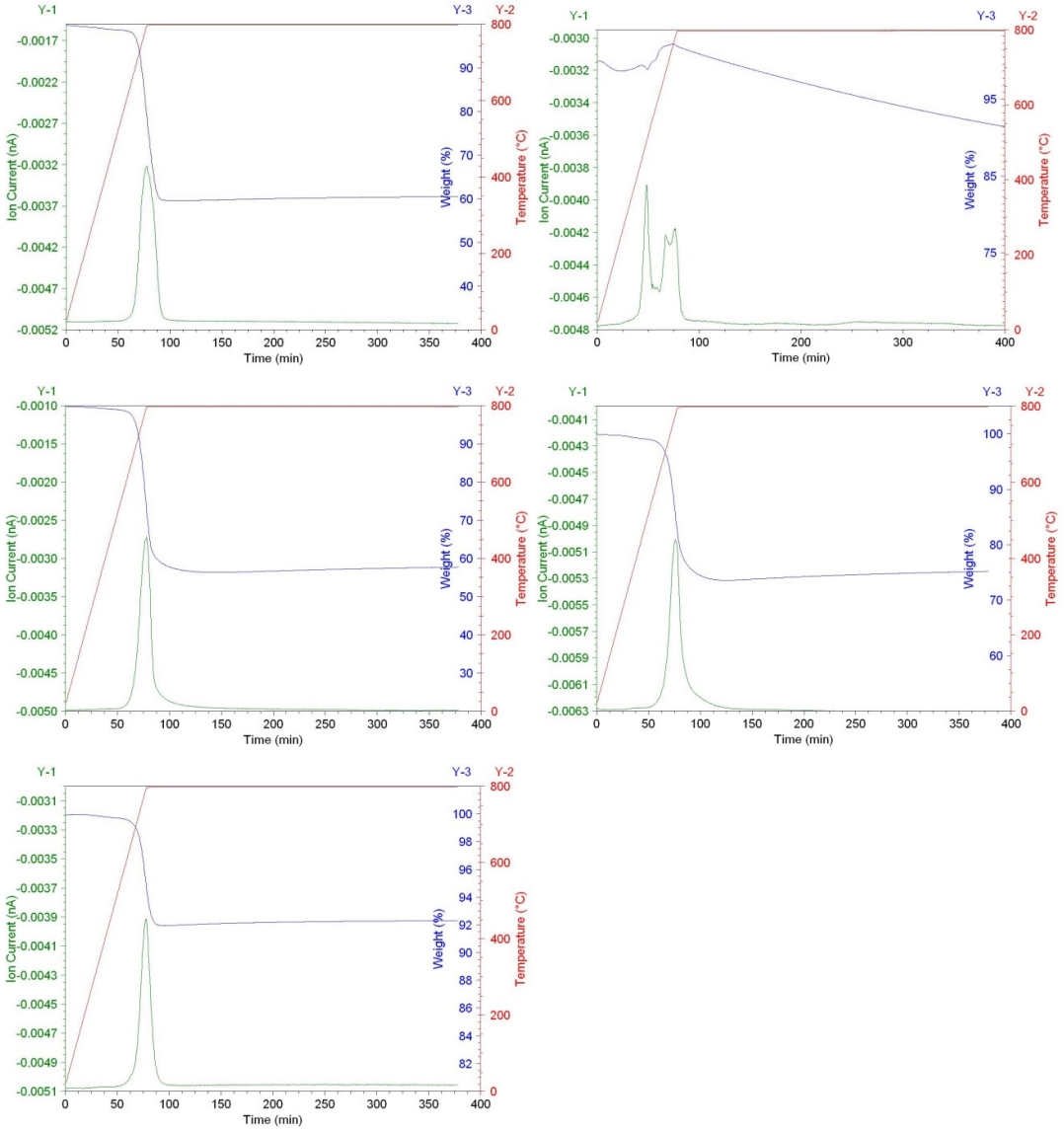

Figure 5-25 TGA analyses and MS signals from CO_2 for samples (a) 1; (b) 2; (c) 12;(d) 13 and (e) 14 (Table 5-1)

Due to the scarce quantity of samples recovered after TGA, the PXD analysis was performed on the back of a glass flat plate, by dispersing powders on vacuum grease. From the data acquired over 14 h scans, it can be seen two broad peak are present below 30º 2θ belonging to the grease and the glass slide used. While in sample **1** after TGA it is possible to see the common β-SiC reflections from (111), (220) and (311) planes (Figure 5-26a), sample **2** shows a complex patterns. It is very difficult to assign reflections due to the overlapping of peaks and poor quality of the data. One set of reflections can be tentatively assigned to silicon although this is difficult to rationalise given the absence of Si in the sample before TGA and the oxidising atmosphere of the TGA experiment. Ideally, it would have been useful to perform another oxidative analysis on samples of **2**. The pattern

also matches the reflections from an α-polytype of SiC, 141R rhombohedral polytype (Figure 5-26b).[43]

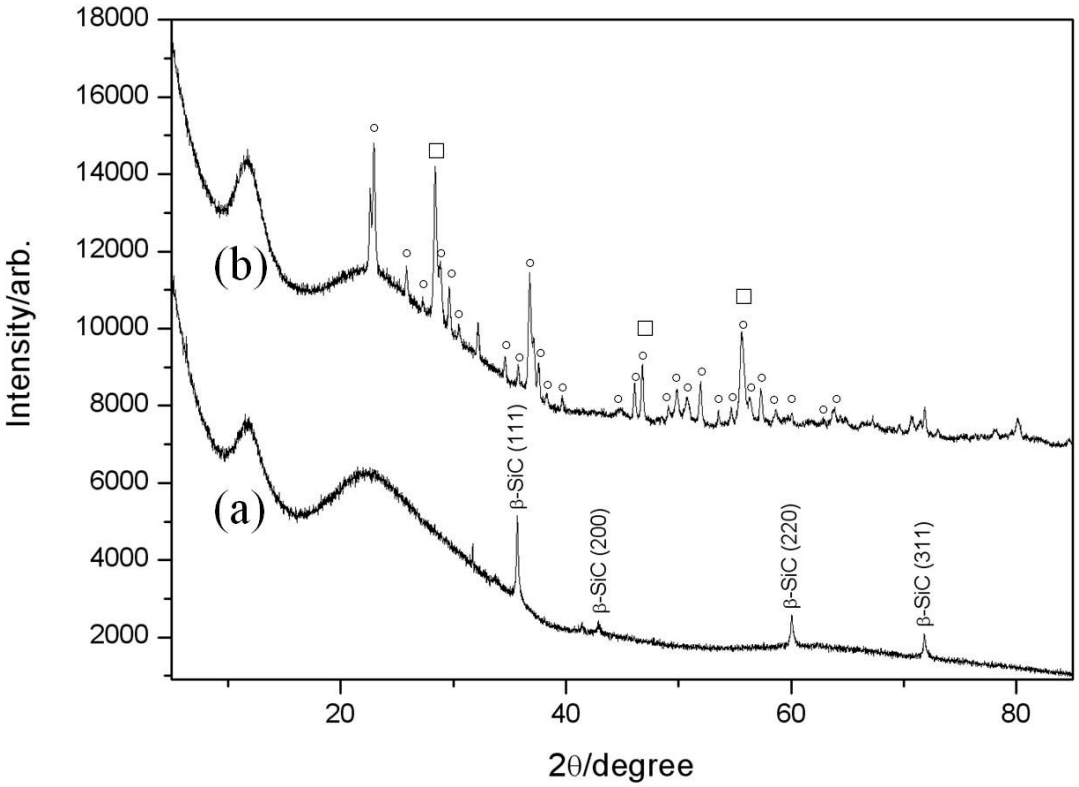

Figure 5-26 Post-TGA PXD patterns of products from carbonised silica aerogels in an MMC for 20 min after the monolith has been soaked for (a) 1 (1 h); (b) 2 (24 h) in distilled water. Reflections from 141R-SiC (◦) and silicon (□) are also indicated.

The PXD for post-TGA samples synthesised starting from PAN cross-linked silica aerogel (A) show a broad peak around ca. 23º 2θ probably originating from the glass slide used and the characteristic peaks of β-SiC (Figure 5-27a-c). Interesting to note, there is no evidence in the PXD patterns reported in both Figure 5-26 and Figure 5-27 for silicon carbide oxidation and no evidence for the graphitic reflections seen in samples **2** and **12**, before temperature treatment. The latter result meaning that all carbon present has been oxidised.

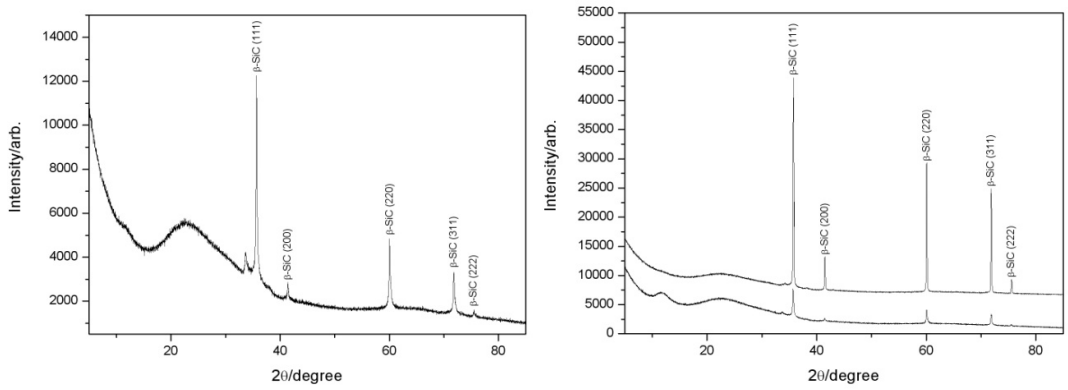

Figure 5-27 Post-TGA PXD patterns of products synthesised from PAN-crosslinked silica aerogel in a MMC (a) 12 (15 min); in a SMC for (b) 13 (3 min, 450 W) and (c) 14 (3.5 min, 450 W).

Several notable observations can be made on the basis of the SEM data. For instance, while SEM micrographs of samples **1** and **2** after microwave irradiation (i.e. pre-TGA) showed a similar microstructure (Figure 5-10-11), after TGA the purified samples 1 and 2 show very different nano/microstructures and from EDX measurements contain only Si and C in a 1:1 ratio. While sample **1** shows a very fine composition (Figure 5-28a), sample **2** presents a homogenous agglomeration of particles each a few microns in dimension (Figure 5-28b).

The TGA/MS graph of sample **2** (Figure 5-25b) suggests no oxidation of silicon carbide takes place as the sample does not increase in weight and only carbon is removed during temperature treatment. Therefore, comparing the micrographs of sample **2** before and after purification (respectively Figure 5-10b-c and Figure 5-28b), it can be suggested the fine porous material surrounding the silicon carbide particles is composed of carbon (Figure 5-10b-c, dark areas), as already stated by Leventis *et al.*.[23] Furthermore, since carbon acts as dispersant and barrier to prevent neck growth adhesion of the silicon carbide particles, if removed agglomeration of the sample could occur (Figure 5-28b).[44] Similar to **2**, sample **12** post-TGA (Figure 5-28c) exhibits an agglomeration of particles with sizes below 1 μm, but what it is important to note is that nanowires are still present suggesting they are made of a material with better oxidative resistance than carbon, and almost certainly silicon carbide as also evidenced by the EDX measurements reporting a 1:1 ratio of Si and C (see Chapter 3). SEM micrographs of samples **13** and **14** after TGA (Figure 5-28d-e) show larger crystallites (of a few microns in size) than any of the MMC samples similar to the same samples pre-TGA (Figure 5-22).

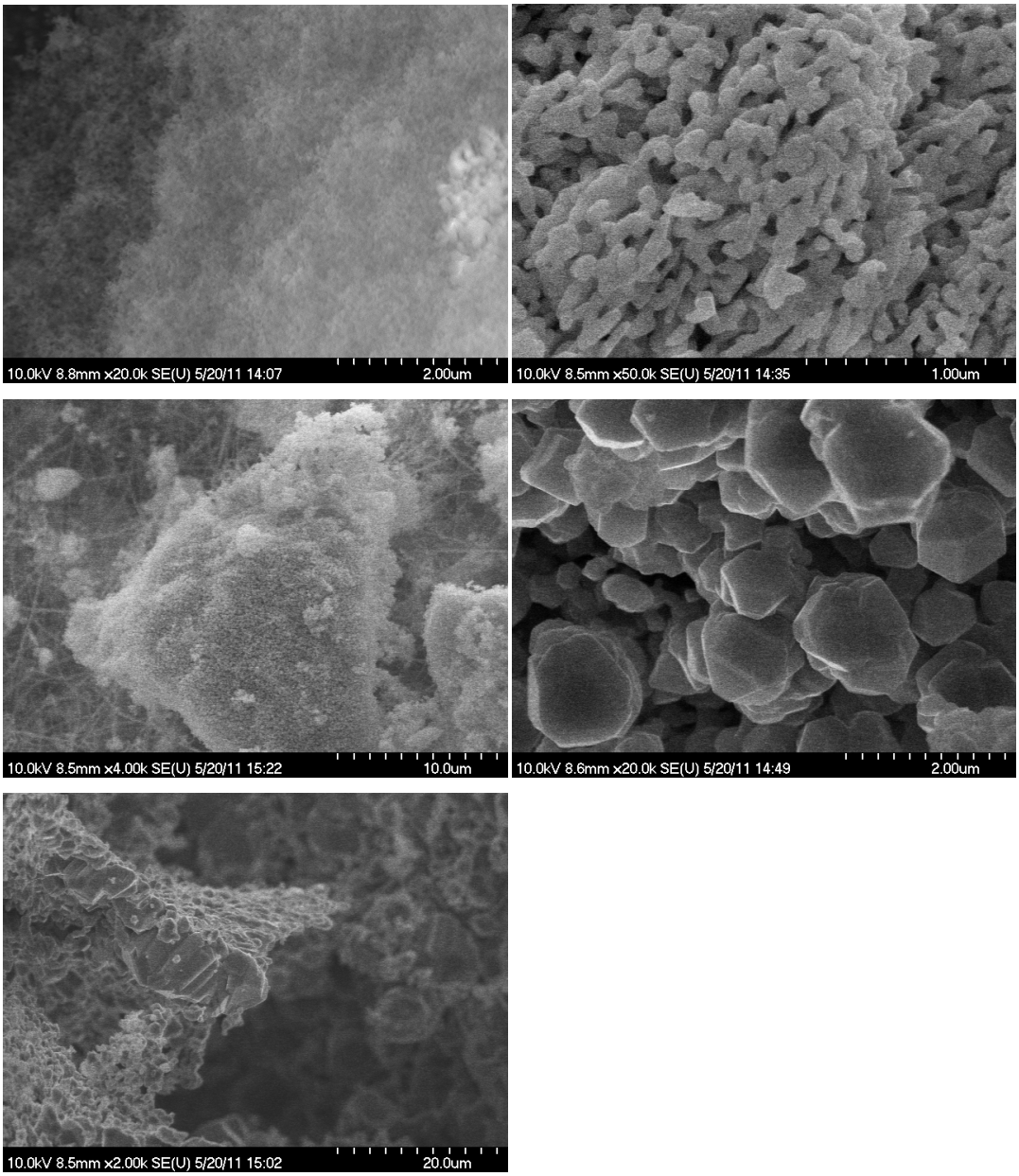

Figure 5-28 SEM micrograph of samples (a) 1; (b) 2; (c) 12;(d) 13 and (e) 14 (Table 5-1).

Confirming the results from TGA, from the Raman spectra of samples post-TGA (Figure 5-29) it is noticeable that the D and G bands relating to the carbon content in the sample are essentially absent for most of the samples, apart from a very broad feature for sample **12** and possibly sample **13**, where also second order Raman features of silicon carbide can be found in the same region (Figure 5-29c-d). Along with the a decrease in intensity of the carbon bands, the main silicon carbide band due to Transverse Optical (TO) Raman-active mode in β-SiC considerably sharpens and shifts to the common value of 780 - 790 cm^{-1}. The Longitudinal Optical (LO) band of β-SiC is also present at 990 cm^{-1},[35] along with an overtone in the high wavenumber region at ca. 1500 cm^{-1}.[39] Broad and weak features in the low wavenumber region are most likely to be connected to the presence of Si-O bonds due

to a possible slight (surface) oxidation of silicon carbide during the TGA analysis in the flowing oxidising gas mixture.[28]

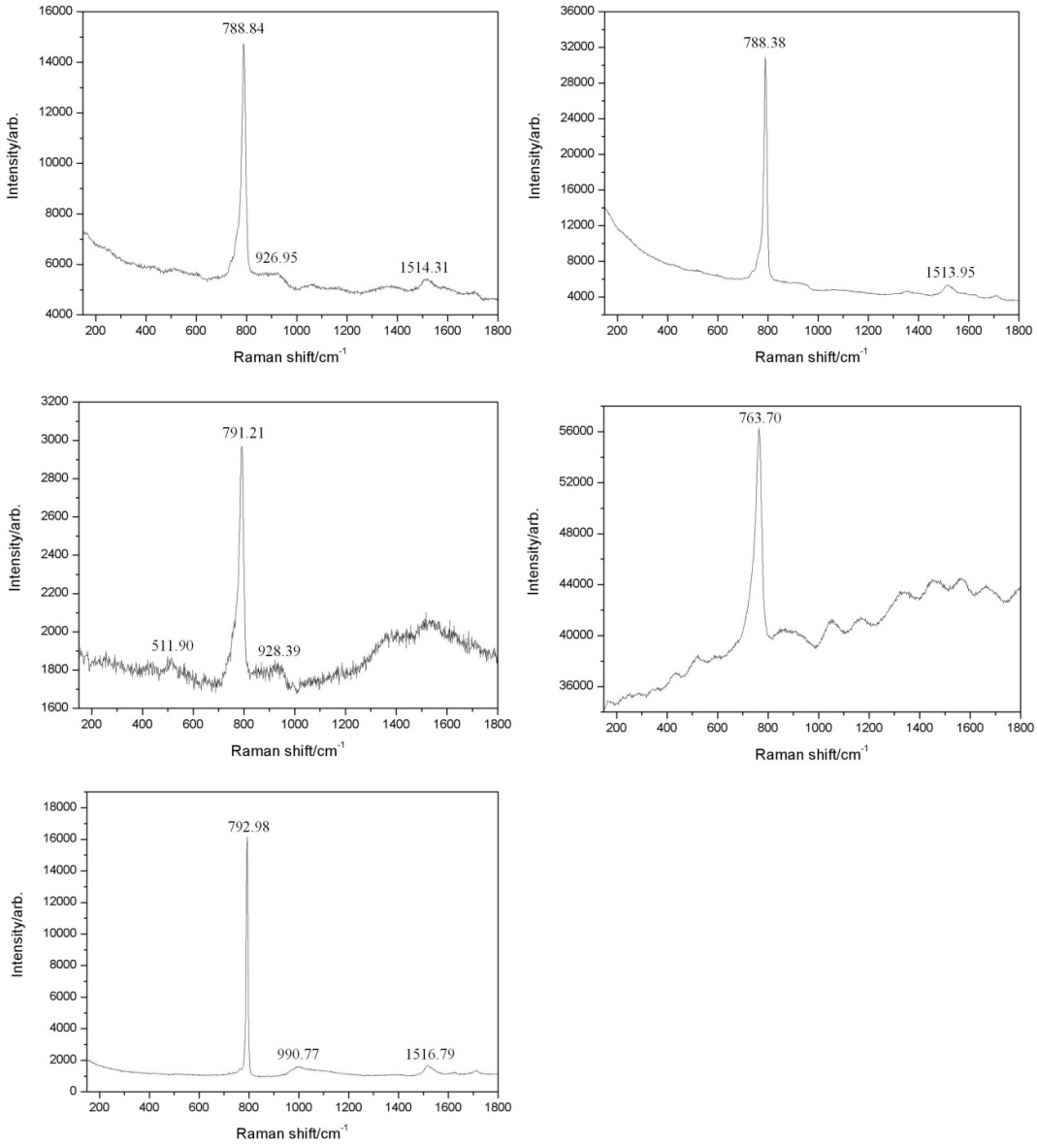

Figure 5-29 Raman spectra and assignments for samples (a) 1; (b) 2; (c) 12; (d) 13 and (e) 14 (Table 5-1).

5.3.5 Discussion

These studies have shown β-SiC can be synthesised starting from carbon coated silica aerogels (stage C of the Leventis process) in air after 20 min (PXD Figure 5-9). The length of the soaking treatment in distilled water prior to microwave irradiation influences the reaction. The longer the samples are soaked in water, the more crystalline the product is (as

evidenced from a flat PXD background in Figure 5-9b). Graphite reflections present in sample **2** are in fact believed to be due to the surrounding susceptor powder that was not completely physically removed from the product. The enhanced crystallinity in water soaked samples can be explained considering interfacial polarisation during the microwave heating process, in fact water, as already mentioned in Chapter 3, is a polar liquid and can act as MW susceptor, to promote initial local dielectric heating of the carbon coating.[45] Once the carbon coating has reached higher temperatures, it becomes "lossy" enough to subsequently continue the heating process independently, while water evaporates and leaves the system. A similar multistep heating process has been proposed by Meek in the microwave sintering of oxide materials using sintering aids.[46] One drawback of increasing the length of the soaking time is that it also increases the brittleness of the sample, in fact it is believed that by increasing the soaking stage, water has enough time to infiltrate the structure causing stress and increase pressure inside the pores when it evaporates.

Results from syntheses performed starting from monoliths of aromatised PAN crosslinked on silica aerogels (stage B of the Leventis process) demonstrate that at irradiation times as short as 1.5 min, the monoliths could be successfully used as silicon carbide precursors. Even when aromatised PAN cross-linked silica aerogels monoliths can be employed as precursors without the aid of water, the monoliths crack and fragment into small pieces during microwave reactions, making it difficult to recover only products without the graphite used as susceptor. The persistent cracking is due to the high heating rates achievable in a microwave oven and the evolution of gases involved in the carbothermal reaction mechanism (see mechanism of formation later in this section). Extensive cracking has been reduced by reducing the irradiation time and, as it can be seen from the PXD patterns in Figure 5-14, β-SiC showing good crystalline properties can be produced after only 2 minutes in an MMC, making it possible to treat and recover sizeable monoliths from susceptor contamination (Figure 5-14a-e). The morphology of the product can be tuned depending on the irradiation time. It can be noted from the SEM micrographs reported in Figure 5-17, that prolonging the irradiation time leads to enhanced sintering and an increase of particles size. In fact, while after 1 minute the product retains the morphology and size of the agglomerated nanoparticles of the starting materials (Figure 5-16a-b), once silicon carbide crystallites are formed, they start agglomerating (as it can be seen from Figure 5-17a) and growing in particle size. After 4 minutes, the sample carbide produced is almost pure single phase SiC (Figure 5-14e) and presents large monocrystalline particles in the range of micrometers (Figure 5-17b). A mechanism for bulk diffusion in SiC has been

reported by Kevorkijan *et al.* important at temperatures above 1500 °C, and these conditions are possibly met in the MMC during reaction.[10]

The morphologies of resulting SiC products can be very different when PAN cross-linked silica aerogel samples (stage A of the Leventis process) are used as precursors. For example, nanowires are found in sample **12** along with agglomerations of nanoparticles, By comparison, the silicon carbide sample produced by Leventis *et al.*[23] in a conventional oven at 1600 ºC in a dynamic flow of Ar does not show the presence of such nanostructures. While in the conventional case the PAN polymer undergoes several structural changes due to temperature treatments, in the microwave case the decomposition of PAN happens *in-situ* due to the fast heating rate of microwave processing. A common formation mechanism proposed for the synthesis of SiC nanowires is a vapour growth process where the gaseous species SiO and CO formed during reaction yield nanowires.[47] The generation of CO coming from the decomposition of PAN polymer could be the driving force behind the formation of nanowires in the microwave reactions here.

Consideration of the effect of the type of cavity used in the reactions leads to two interesting observations:

- First, despite a lower power applied, 450 W in the SMC vs. 800 W in the MMC, the reaction was nearly five times faster.
- Second, the crystallinity and density of the samples produced is higher in the SMC.

These results correlate directly to the type of cavity used and are in agreement with the results found in the previous chapters. In particular, it has already been mentioned how the power dissipated in the material (or power density) is a function of the cavity dimensions and design (through the relationship with the electric field strength inside the material squared).[48] This would agree with the supposition that higher reaction temperatures are achieved in the SMC due to the creation of power densities several orders of magnitude higher than the MMC counterpart and explain why the SEM micrographs of material processed in the SMC shows large, well-formed crystallites (Figure 5-22).

When it comes to the formation mechanism, it has been already mentioned in the introduction to this chapter how critical it is to ensure intimate contact between silica and carbon for the carbothermal reaction to be successful. PAN cross-linked aerogels have been specifically designed to achieve that and their structures represent effectively a composite material where the core is a porous silica aerogel covered by a carbon layer. Therefore the reaction can be explained in terms of the same carbothermal reaction steps

already discussed in the previous chapter where the precursor to silicon carbide is a mixture of silica and carbon powders. One issue arises when using PAN cross-linked silica aerogels as opposed to powders. While with the powders silica and carbon are mixed relatively homogeneously, when using the aerogel precursor once silicon carbide is synthesised at the contact point between the silica aerogel and the carbon coating, the process should stop. This does not happen and Leventis *et al.* have proposed the continued conversion of silica to silicon carbide to progress by the following solid – solid reaction:[23]

$$SiC\ (s) + 2\ SiO_2\ (s) \rightarrow 3\ SiO\ (g) + CO\ (g) \qquad (\mathbf{1})$$

This would ensure the regeneration of SiO gas at the interface between the silica core and the freshly formed silicon carbide layer (**1**). The SiO gas subsequently diffuses through the synthesised silicon carbide layer and reacts with the outer carbon coating, ensuring a complete conversion of silica to silicon carbide (**2**).

$$SiO\ (g) + 2\ C\ (s) \rightarrow SiC\ (s) + CO\ (g) \qquad (\mathbf{2})$$

In one sense, comparing the results in this chapter with those in Chapter 4, although essentially the same carbothermal reaction is employed for the synthesis of silicon carbide, the process could be considered less attractive for scale-up, because the precursors would cost more. Furthermore, while Leventis *et al.* managed to preserve monolithicity and porosity, justifying the choice of a more expensive precursor, the retention of microstructure and integrity has proven more difficult when using microwave irradiation. The SiC product often cracks during reaction and emerges brittle. As stated in the introduction, porous silicon carbide has raised a lot of interest in the past years as a potential replacement for oxide catalysts[1] and as has also been shown in the methods in previous chapters, it is possible to prepare porous SiC from appropriate precursors under optimum experimental conditions.

A crucial point of this thesis has been the removal of purification steps needed after reaction to produce SiC. The nature of the aerogel processing leads to excess carbon in the product after reaction as proven by the TGA/MS analysis (Figure 5-25). While the PXD analysis is able only to asses the crystalline fraction of the sample and has been suggesting graphite from the susceptor is present, Raman spectroscopy has been used to probe the presence of amorphous phases and suggested the presence of unreacted amorphous carbon after SiC formation.

A purification temperature treatment has been followed by TGA/MS proving the only gaseous species leaving the system are the oxidative products coming from the removal of the excess of carbon. Looking at the SEM micrographs pre and post-TGA one can note the absence of porous material after TGA, yielding well-formed, faceted crystallites with an atomic ratio in agreement with silicon carbide (as evidenced by the EDX measurements). The successful removal of carbon has been further evidenced by the Raman spectra of the post-TGA samples, which show only silicon carbide overtones band in the high wavenumber region. The fact silica is not detected at any point in the microwave process by Raman spectroscopy suggests that the carbon present in samples should be due to a higher carbon : silica ratio than would be ideal for carbothermal reduction and carburisation. Other evidence that suggests even though reactions have been performed in air, no silica reflections exist in PXD patterns for any irradiation times. The reaction temperature would be high enough to permit the recrystallisation of the silica aerogel (that melts completely at temperatures below 1050 ºC, the sintering temperature reported in[49]).

5.4 Conclusions

In summary, samples from the three different stages of Leventis process (A, B and C) have been successfully converted to β-SiC, significantly reducing processing time compared to the conventional process (Figure 5-6). In fact, the synthesis of β-SiC can be achieved from PAN coated silica aerogels without previous temperature treatments, in air and in less than 4 minutes in a single mode cavity system. The mode and rate of microwave heating has once again proven crucial for the improvements in product purity, reduction of processing complexity (and cost) and reduction of processing times. Furthermore, the morphology and porosity of the silicon carbide products can be controlled *via* mode of heating and it has been shown how SMC syntheses lead to dense, sintered, single crystalline products.

Ultimately, aerogels offer a good possibility for making porous SiC in a controlled way. Given the high surface area of the gels, choosing appropriately high power and temperature, it is possible to achieve very rapid sintering and produce two different silicon carbide products. Porous silicon carbide produced at low power using a MMC, could be potentially used in catalysis. Instead, a well sintered material (achievable applying high power in a SMC) could be good for structural application.

One of the remaining challenges is achieve monolithic preservation. More tests should be performed using SMC systems with tunable applied powers to understand the feasibly of microwave processing in the synthesis of monolithic silicon carbide using polymer coated silica aerogels. Controlling a key condition such as the power applied would help to control the heating rate and allow further understanding of the reaction mechanism. Such experiment would probe whether a lower power applied could be capable of preserving the structure.

[1] A.-M. Alexander and J. S. J. Hargreaves, *Chem. Soc. Rev.*, 2010, **39**, 4388.

[2] R. Riedel, G. Passing, H. Schonfelder and R. J. Brook, *Nature*, 1992, **355**, 714.

[3] K. Vyshnyakova, G. Yushin, L. Pereselentseva and Y. Gogotsi, *Int. J. Appl. Ceram.Technol.*, 2006, **3**, 485.

[4] J. Locs, L. Berzina-Cimdina, A. Zhurinsh and D. Loca, *J. Eur. Ceram. Soc.*, 2009, **29**, 1513.

[5] J. Qian, J. Wang and Z. Jin, *Mater. Sci. Eng. A*, 2004, **371**, 229.

[6] J.-M. Qian, J.-P. Wang, G.-J. Qiao and Z.-H. Jin, *J. Eur. Ceram. Soc.*, 2004, **24**, 3251.

[7] A. Herzog, R. Klingner, U. Vogt and T. Graule, *J. Am. Ceram. Soc.*, 2004, **87**, 784.

[8] H. Sieber, C. Hoffmann, A. Kaindl and P. Greil, *Adv. Eng. Mater.*, 2000, **2**, 105.

[9] G.C-T. Wei, *Am. Ceram. Soc. Comm.*, 1983, **66**, C-111.

[10] V. M. Kevorkijan, M. Komac and D. Kolar, *J. Mater. Sci.*, 1992, **27**, 2705.

[11] G. Hasegawa, K. Kanamori, K. Nakanishi and T. Hanada, *Chem. Mater.*, 2010, **22**, 2541.

[12] Y. Shi, F. Zhang, Y.-S. Hu, X. Sun, Y. Zhang, H. I. Lee, L. Chen and G. D. Stucky, *J. Am. Chem. Soc.*, 2010, **132**, 5552.

[13] G.-Q. Jin, X.-Y. Guo, *Micropor. Mesopor. Mater.*, 2003, **60**, 207.

[14] K. Sonnenburg, P. Adelhelm, M. Antonietti, B. Smarsly, R. Nöske and P. Strauch, *Phys. Chem. Chem. Phys.*, 2006, **8**, 3561.

[15] V. Raman, G. Bhatia, A.K. Mishra, S. Bhardwaj and K. N. Sood, *Mater. Lett.*, 2006, **60**, 3906.

[16] X. Li, X. Chen and H. Song, *Mater. Sci. Eng. B*, 2011, **176**, 87.

[17] C. Vix-Guterl, B. McEnaney and P. Ehrburger, *J. Eur. Ceram. Soc.*, 1999, **19**, 427.

[18] K. Sonnenburg, P. Adelhelm, M. Antonietti, B. Smarsly, R. Noske and P. Strauch, *Phys. Chem. Chem. Phys.*, 2006, **8**, 3561.

[19] A. C. Pierre and G. M. Pajonk, *Chem. Rev.*, 2002, **102**, 4243.

[20] C. N. R. Rao ed., *Chemistry of Advanced Materials*, Blackwell Scientific Publications, Oxford, 1993.

[21] S. S. Kistler, *J. Phys. Chem.*, 1932, **36**, 3941.

[22] N. Leventis, C. Sotiriou-Leventis, S. Mulik, V. Patil, D. Mohite, Y. Zhang and H. Lu, *Polym. Preprints*, 2008, **49**, 504.

[23] N. Leventis, A. Sadekar, N. Chandrasekaran and C. Sotiriou-Leventis, *Chem. Mater.*, 2010, **22**, 2790.

[24] M. Prince and J. Hornyak, *J. Polymer Sci. A*, 1967, **5**, 161.

[25] http://www.icdd.com/ (last access 12/7/2011)

[26] Z.Q. Li, C.J. Lu, Z.P. Xia, Y. Zhou and Z. Luo, *Carbon*, 2007, **45**, 1686.

[27] S. Rohmfeld, M. Hundhausen and L. Ley, *Phys. Status Solidi B,* 1999, **215**, 115.

[28] K. J. Kingma and R. J. Hemley, *Am. Mineralogist*, 1994, **79**, 269.

[29] M. J. Matthews, M. A. Pimenta, G. Dresselhaus, M. S. Dresselhaus and M. Endo, *Phys. Rev. B*, 1999, **59**, 6585.

[30] H. Li, Y. Zhu, Z. Mao, J. Gu, J. Zhang and Y. Qian, C*arbon,*, 2008, **47**, 328.

[31] D. S. Knight and W. B. White, *J. Mater. Res.*, 1989, **4**, 385.

[32] R. O. Dillon, J. A. Woollam and V. Katkanant, *Phys. Rev. B*, 1984, **29**, 3482.

[33] C. Vix-Guterl, B. McEnaney and P. Ehrburger, *J. Eur. Ceram. Soc.*, 1999, **19**, 427.

[34] E. A. Gulbransen and S. A. Jansson, *Oxid. Met.*, 1972, **4**, 181.

[35] S. Nakashima and H. Harima, *Phys. Stat. Sol. (a)*, 1997, **162**, 39.

[36] S. G. Sundaresan, A. V. Davydov, M. D. Vaudin, I. Levin, J. E. Maslar, Y.-L. Tian and M. V. Rao, *Chem. Mater.*, 2007, **19**, 5531.

[37] J. C. Burton, L. Sun, M. Pophristic, S. J. Lukacs, F. H. Long, Z. C. Feng and I. T. Ferguson, *J. Appl. Phys.*, 1998, **84**, 6268.

[38] J. C. Burton, F. H. Long and I. T. Ferguson, *J. Appl. Phys.*, 1999, **86**, 2073.

[39] D. Olego and M. Cardona, *Phys. Rev. B*, 1982, **25**, 1151.

[40] J. A. Menendez, A. Arenillas, B. Fidalgo, Y. Fernandez, L. Zubizarreta, E. G. Calvo and J. M. Bermúdez, *Fuel. Process. Technol.*, 2010, **91**, 1.

[41] G. Hasegawa, K. Kanamori, K. Nakanishi and T. Hanada, *Chem. Mater.*, 2010, 22, 2541.

[42] V. Z. Shemet, A. P. Pomytkin and V. S. Neshpor, *Carbon*, 1993, **31**, 1.

[43] R. S. Mitchell, *J. Chem. Phys.*, 1954, **22**, 1977.

[44] S. Pan, J. Zhang, J. Yang and G. Song, *Ceram. Int.,* 2008, **34**, 391.

[45] A. R. v. Hippel, *Dielectrics and Waves*, MIT Press, Cambridge,Mass, 1954.

[46] T. T. Meek, C. E. Holcombe and N. Dykes, *J. Mater. Sci. Lett.*, 1987, **6**, 1060.

[47] C. Vix-Guterl, B. McEnaney and P. Ehrburger, *J. Eur. Ceram. Soc.*, 1999, **19**, 427.

[48] R. J. Meredith, *Engineers' Handbook of Industrial Microwave Heating*, The Institution of Electrical Engineers, London, UK, 1998.

[49] G. W. Scherer, S. Calas and R. Sempéré, *J. Non-Cryst. Solids*, 1998, **240**, 118.

6 Conclusions

In the production of advanced ceramic powders, along with the continuous studies of chemical routes able to control product properties, the development of processes that are also energy efficient and sustainable has become a high priority. Traditionally, the processing of ceramics has been energy intensive, demanding extreme temperatures and long treatment times and leads to a products presenting different grades. Microwave processing is a viable alternative approach to synthesise carbides due to the excellent microwave susceptor properties of carbon in the starting materials.

Silicon carbide, SiC, is arguably the most industrially important non-oxide ceramic. Since its first synthetic production at the end of the 18th century, the potential of silicon carbide was immediately recognised as a structural material due to its mechanical and thermal properties. Nowadays, it is still emerging as a highly promising and versatile material for applications such as heterogeneous catalyst support and in power electronics. All these applications rely on chemical routes that allow precise control of both crystal structure and nanostructure.

In all systems examined, the successful synthesis in air of silicon carbide was achieved with good purity in less than 15 minutes even for low power multimode cavity setups. By using single mode cavity systems not only was pure SiC produced in second timescales, but also that the morphology of the sample has been proved to be highly dependent on the form of the microwave cavity and the incident microwave power.
While performing reactions in a multimode cavity system, the use of a graphite susceptor was essential to initiate reactions. By absorbing microwaves, the graphite powders raised the temperature of the system to a point where the sample itself started acting as a microwave absorber and the formation of silicon carbide took place.

When the synthesis of silicon carbide was attempted from a mixture of silicon and carbon powders, it was found that one can switch between high aspect ratio nanofibres (from 5 nm in diameter) using water as a binder and porous silicon carbide to crystallites many microns across, primarily as a function of heating rate and reaction temperature. In fact, the power density at the sample is proportional to the electric field strength squared, therefore the choice of the cavity type is fundamental and generally speaking the high power density reached in a SMC system was revealed to be crucial both in more rapid product formation but also in the production of samples with increased particle sizes.

Reactions from starting powder mixtures of silica and carbon were studied to explore the possibility of employing more cost effective starting materials, even though a more difficult reaction initiation was expected due to the worse dielectric properties as compared to a mixture of silicon and carbon. Furthermore, while the reaction containing silicon implied a straightforward solid reaction between silicon and carbon, when using silica the reaction mechanism was more complex involving gaseous intermediates in an open reaction vessel. Nonetheless, synthesis of porous silicon carbide was achieved starting from pellets embedded in a graphite susceptor at short reaction times (5 min) in a MMC and when employing a SMC the successful synthesis of silicon carbide starting from mixtures of powders with no susceptor once again proved the choice of cavity is a key point. This result was certainly important when considering the ease of process towards a potential industrial scale up.

Finally, the last system examined in this thesis was composed of silica aerogel covered with a layer of polymer. In fact, since the first step of the reaction between silica and carbon relies on an intimate contact between the powders, samples prepared by Prof. Leventis seemed very interesting to study also in the view of mimicking the silica aerogel porous structure. Indeed synthesis in a controlled way has been achieved and depending on the cavity used, porous SiC was synthesised in a MMC and when employing a high power in SMC very rapid sintering of the silicon carbide product could be achieved. The two different forms of silicon carbide produced could be used for catalyst support and the latter for structural ceramics, especially if the matrix of sintered SiC could be infiltrated with Co.

Ultimately, microwave processing has been demonstrated to be an advantageous and successful experimental procedure to achieve silicon carbide products with different purity level, density, porosity and microstructures; that can be exploited for different applications. The combination of different parameters, such as the choice of applied MW source (applied microwave power and cavity), the use of water as binder and susceptor have been found to be key parameters in controlling the reaction product.

Appendix

1. Microwave synthesis studies in the Si-C system

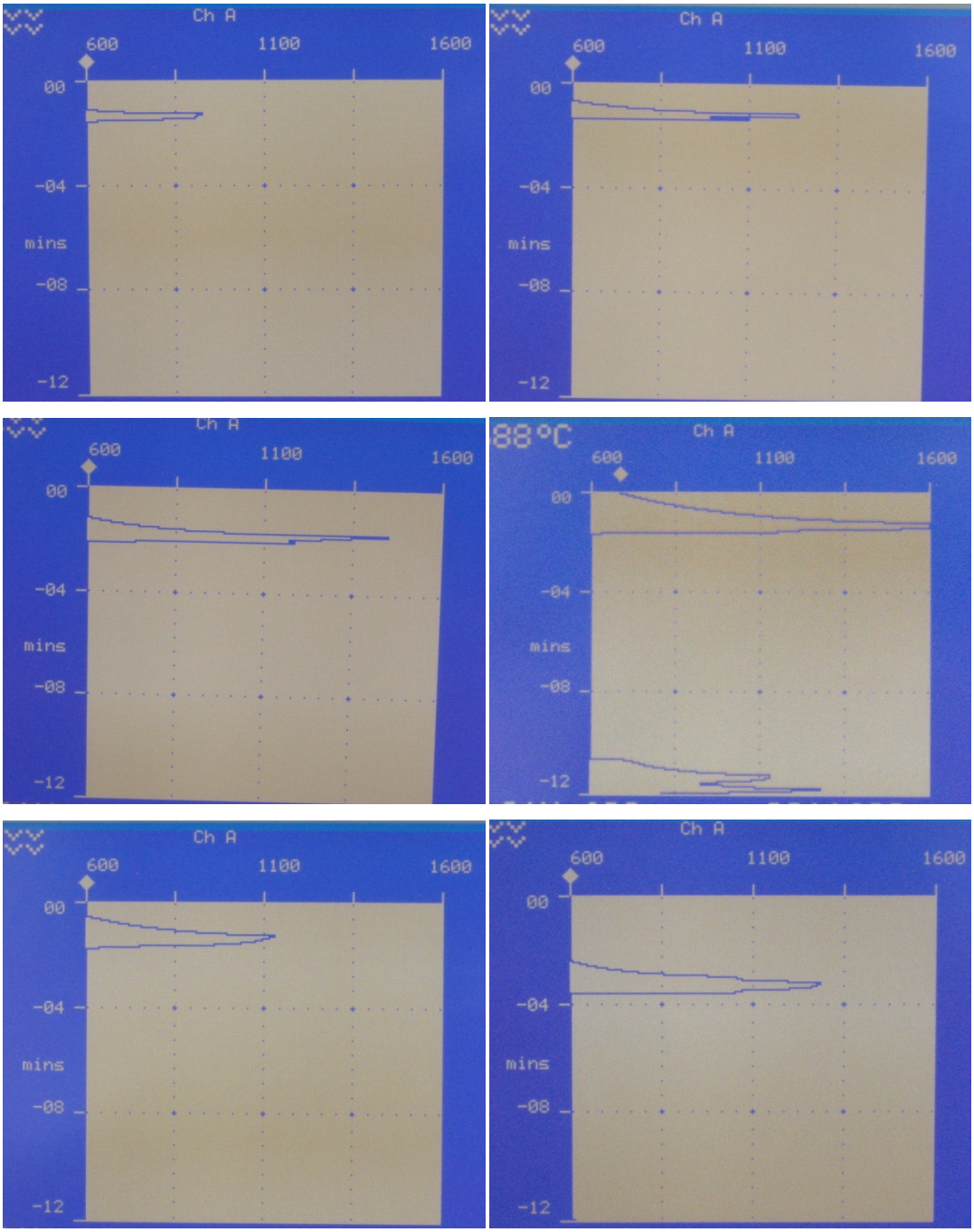

Figure 0-1 Optical pyrometer output during reactions in a SMC at 3 kW from Si + activated C. The images are relevant to samples (a) 17 to (f) 22.

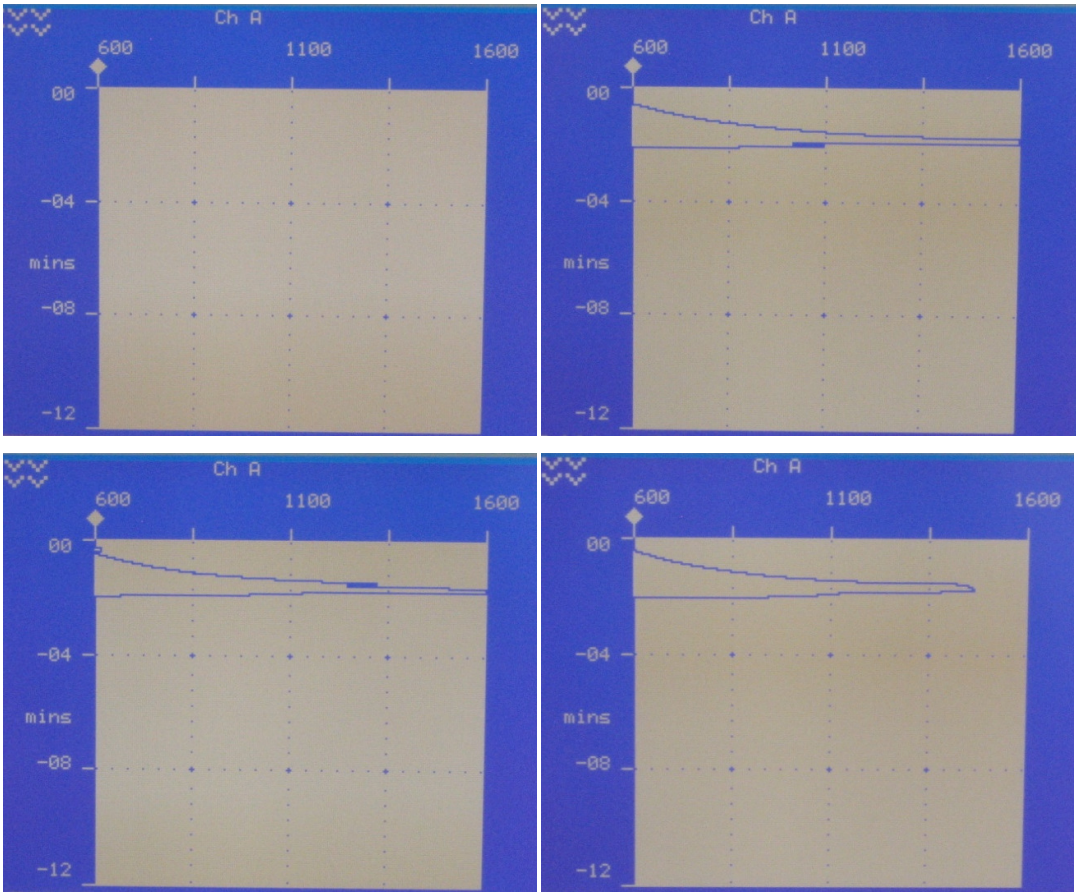

Figure 0-2 Optical pyrometer output during reactions in a SMC at 3 kW from Si + graphite. The images are relevant to samples (a) 23 to (d) 26.

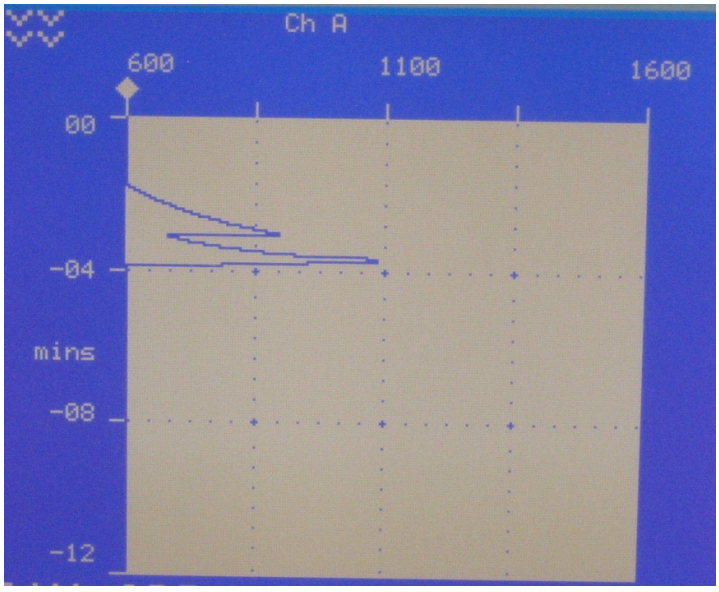

Figure 0-3 Optical pyrometer output in a SMC at 9 kW during 13 s reaction from Si + graphite (27).

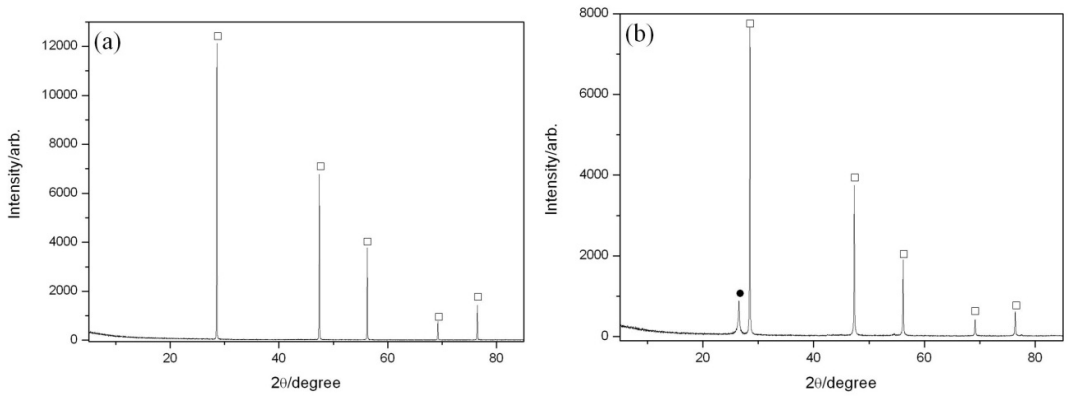

Figure 0-4 PXD patterns of mixtures of Si + C prior to reaction where C is (a) activated carbon and (b) graphite. Reflections from graphite (●) and silicon (□) are also indicated.

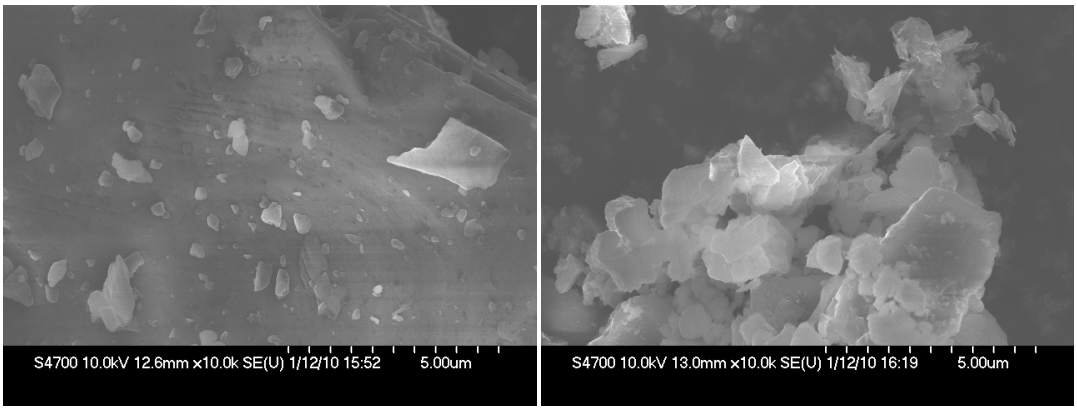

Figure 0-5 SEM micrographs of mixtures of Si + C prior to reaction where C is (a) activated carbon and (b) graphite. The micrographs show the smaller particle sizes in the case of activated carbon.

2. Microwave synthesis studies in the SiO_2-C system

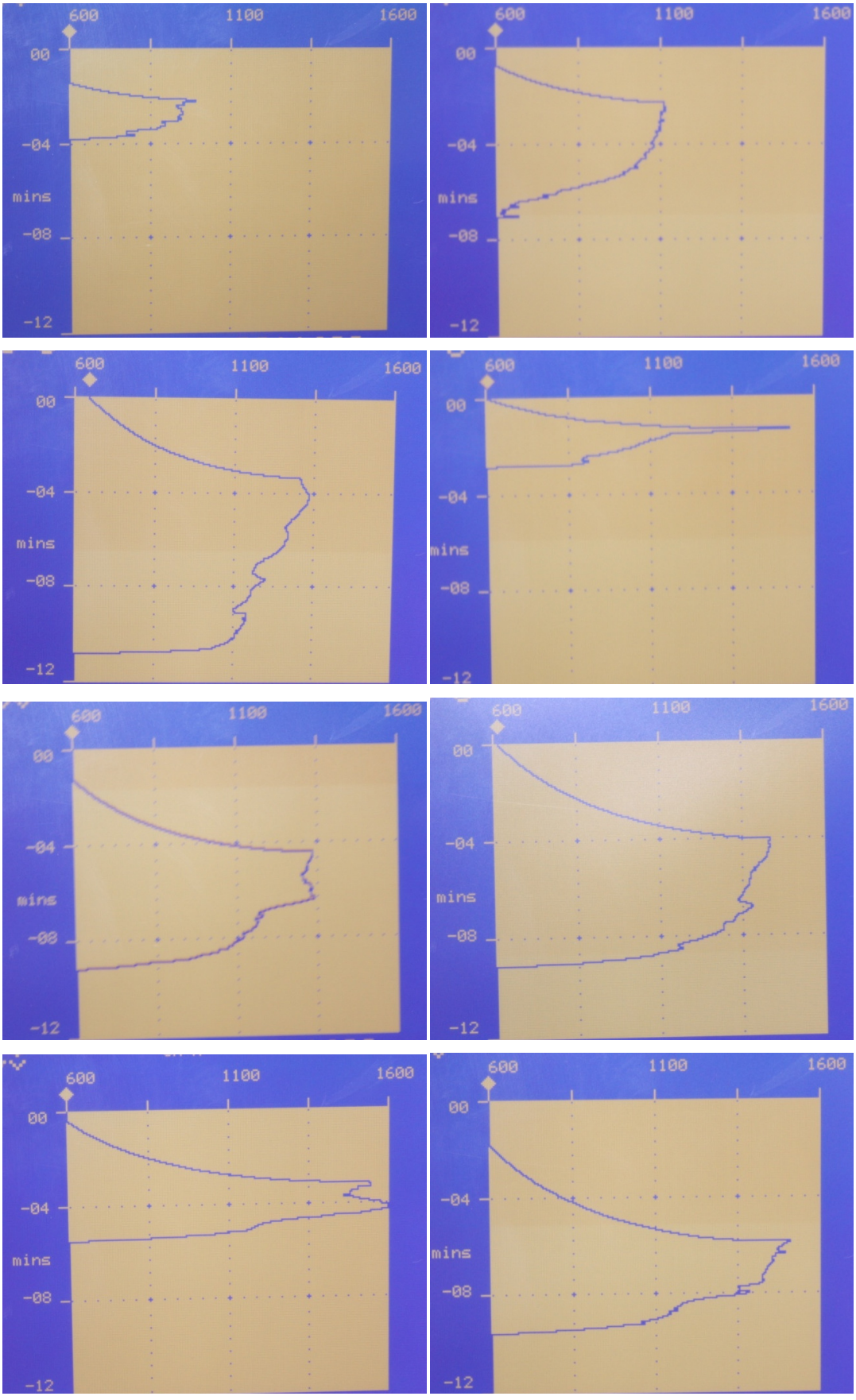

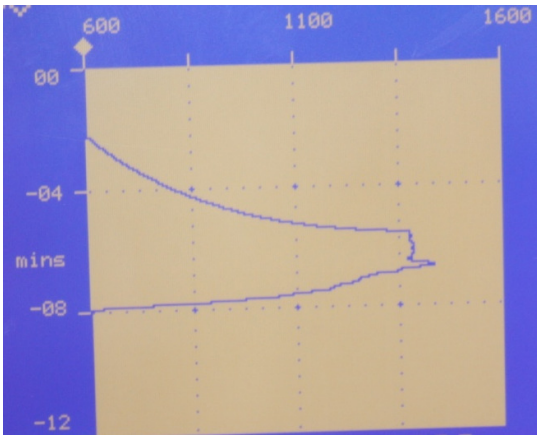

Figure 0-6 Optical pyrometer output during reactions in a SMC from SiO_2 + graphite. The images are relevant to samples (a) 5 to (j) 13 (see Table 3, Chapter 4).

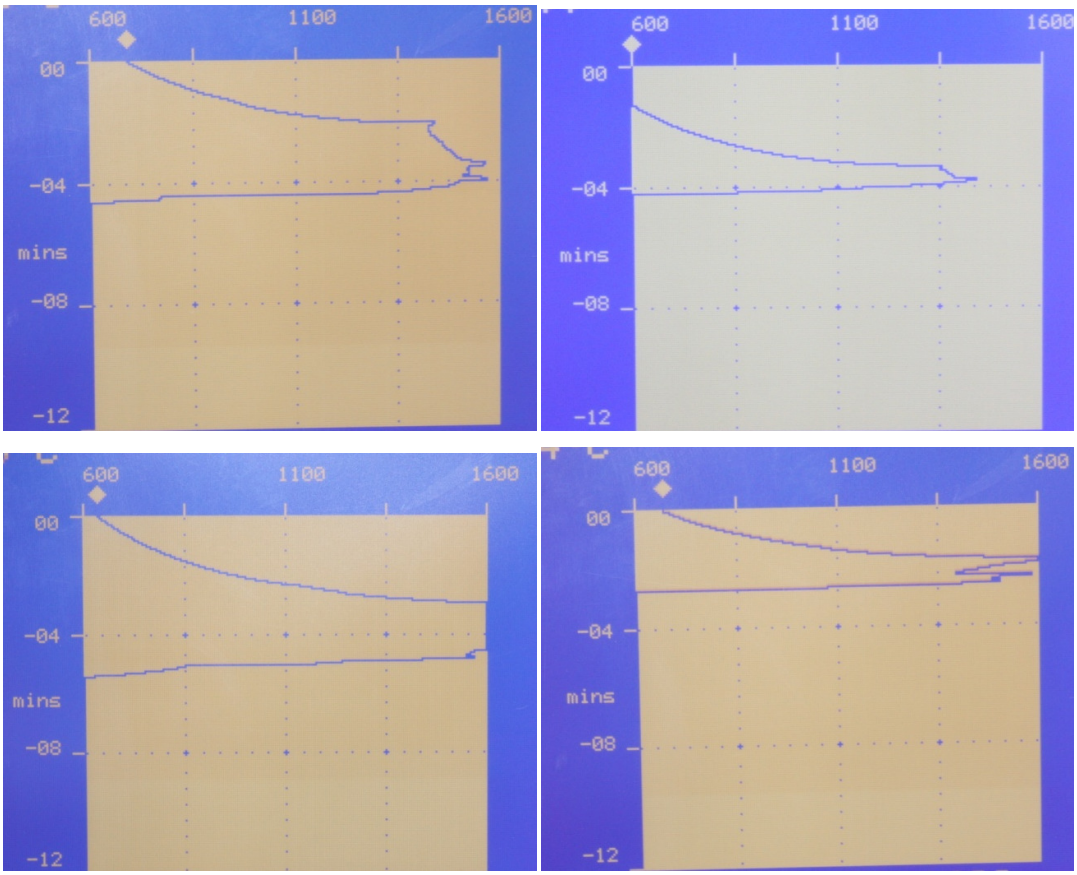

Figure 0-7 Optical pyrometer output during reactions in a SMC: (a) Si + activated C at 600 W for 2:42 s (14), (b) Si + activated C at 600 W for 0:54 s (15), (c) Si + graphite at 600 W for 2:42 s (16), (b) Si + graphite at 600 W for 1:08 s (17).

3. Microwave synthesis studies using x-aerogel precursors

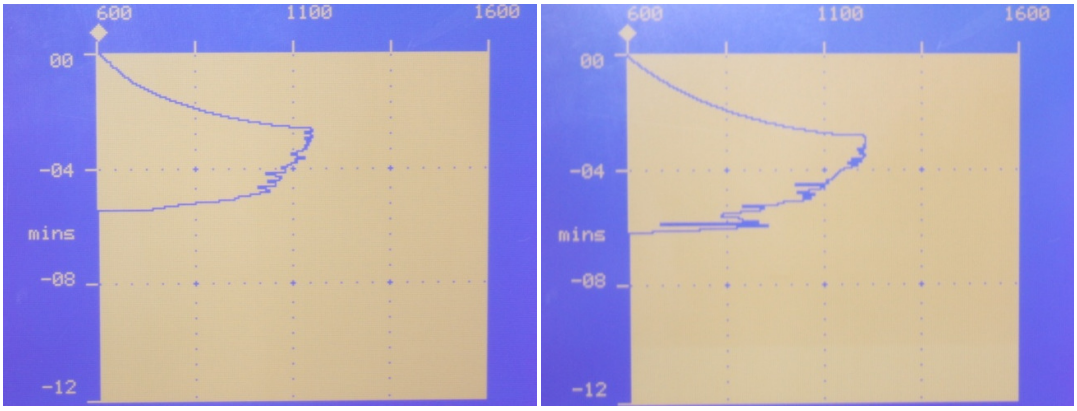

Figure 0-8 Optical pyrometer output during reactions of PAN-crosslinked silica aerogel in a SMC at 450 W for (a) 3 min (13) and (b) 3.5 min (14).